NORTHWESTERN UNIVERSITY

Internal and External State Preparation of a Single Molecule

A DISSERTATION

SUBMITTED TO THE GRADUATE SCHOOL
IN PARTIAL FULFILLMENT OF THE REQUIREMENTS

for the degree

DOCTOR OF PHILOSOPHY

Field of Physics

By

James Benson Dragan

EVANSTON, ILLINOIS

December 2022

ABSTRACT

Internal and External State Preparation of a Single Molecule

James Benson Dragan

The vibrational and rotational degrees of freedom in a molecule add complexity that complicate optical cycling and state preparation procedures. However, the same additional degrees of freedom also make molecules suitable candidates for tests of physics beyond the standard model. A precision measurement of the transition energy between two vibrational levels can set a limit on the time variation of the proton-to-electron mass ratio. If that experiment is made in an ion trap, spectroscopy using quantum logic techniques can be employed. These methods allow for the internal state of the molecule to be mapped onto a shared motional mode between the molecule and an auxiliary atomic ion. This is only possible when the motional modes are first cooled to the ground state. Typically the auxiliary atom is used for sympathetic cooling and state readout, as the molecule lacks a closed optical transition to laser cool on.

Preparation of the motional modes can become challenging when the two ions have different masses, and only one ion is actively Doppler cooled. Reduction of the second ion's thermal motion by sympathetic cooling is less efficient and the two ion crystal is more susceptible to heating sources that can potentially thermalize the ions and interrupt data collection. This thesis outlines the experimental control needed to fully prepare a two ion crystal with a mass ratio of 1:3, when only one ion is Doppler cooled. A scheme in which the ion crystal is fully and automatically prepared in several seconds after melting, including

the appropriate trap settings and additional lasers is discussed.

Ground rovibrational state preparation of the SiO^+ molecule is achieved by optical pumping on the $X^2\Sigma^+$-$B^2\Sigma^+$ transition. It is estimated that 68(6)% of the population is pumped into N=0, with the remaining population in N=1, where N is the spinless rotational quantum number. Obtaining ground rovibrational state preparation is the first step towards survey and precision spectroscopy of vibrational overtone transitions in the $X^2\Sigma^+$ state. The optical pumping process of SiO^+ by driving the X-B transition is modeled using rate equations and the intervening $A^2\Pi$ state is found to be vital by providing a pathway for state parity to change. The simulation results suggest that the B-A transition strength is larger than the highest level calculations predict. In addition, calculations of the transition dipole moments (TDMs) show that the excited B state is more likely to decay on vibrational cooling transitions than on heating ones. To gain insight, a simple model is introduced and the results show that a combination of terms lead to a stronger TDM for vibrational cooling decays. The same terms fortuitously cancel and lead to a lower TDM for vibrational heating decays. The result is that optical cycling on the X-B transition naturally leads to vibrational cooling.

In a first step towards nondestructive state readout of a molecule, a two ion crystal of Ba^+ and SiO^+ are cooled to the ground motional state in three dimensions using EIT sideband cooling. Along the axial direction, the resulting ground state occupations are $\bar{n}_{oi,z} = 0.06(3)$ and $\bar{n}_{op,z} = 0.08(3)$. With ground state cooling operational, the attempts at the first demonstration of Photon Recoil Readout (PRR) are shown. This state dependent heating technique works by synchronizing photon recoils from stimulated absorption in the molecule, with a specific motional mode. If this transition is driven, momentum is coherently added to a given motional mode, which pumps population out of the ground motional state. The theory behind PRR, initial attempts and potential improvements are discussed.

Acknowledgements

Physics is a team sport
Martin Disla

You know how they say that it takes a village to raise a child? Well that is especially true for myself, as I have been in school my entire life. A first and special thank you to Mr. Levy, my 11th and 12th grade Physics teacher who sparked my initial interest and encouraged me to pursue an undergraduate Physics degree. His teaching and kindness really started it all.

At Stony Brook University I was fortunate to meet and work with many great people. Much of my life was shaped at Stony Brook where I met lifelong friends in Blake, Mike and Suhaib. I would never have passed any of my classes without the help of Alex, Stefan, Wes and my other classmates of '14. Rob Regan was a dear friend who had a natural talent for teaching physics and mathematics. He was always eager to help explain and make sure that you developed an intuition for the concept. Rob was a special kind of friend, an especially brilliant mind and I am fortunate to have gotten more time with him at Northwestern.

My life was forever changed after I took the class Waves & Optics with Prof. Hal Metcalf. His engaging and fantastic teaching style made me want to learn as much as I possible could from him. I will never forget when we were talking after class one day and I asked "what do you do for research?" to which he replied "I use lasers to push atoms". That was the moment I became an AMO physicist. Hal was generous enough to accept me into his research group, fund my summer research and send me to my first conferences. All of those were formidable experiences and learning opportunities. I am forever indebted to Hal for opening the door and welcoming me in.

In Hal's group I was fortunate to work with Yuan, John, Brian and Chris all of whom

were always friendly and happy to help a young researcher. Working with John I learned what it takes to be a graduate researcher. When experiments don't work and every day is a struggle he exemplified the patience and diligence needed to push through. Hal taught us that if there is a knob to turn, you turn it and see what happens. His guidance on how to conduct experimental research is fundamental to the scientist I became.

I am forever grateful to the Physics Department at the University of Connecticut, who was the only graduate school to accept me at the time. I can say that now right? Fortunately for me it was a year where the UConn Physics department admitted a historically high number of students, many of whom I am close with to this day. I was lucky to join UConn with a fellow SBU alum Alex Sage, who found us an amazing townhouse in a retirement community which turned out to be a gem. Living with Alex and Ben Commeau, we were a little family and got each other through a lot in those two years. Those two, and that townhouse, will always have a special place in my heart. There is nothing like having a community pool and hiking trails right outside your door. A special thanks to my dear friends Erin, Jeremy, Jon, Luke and Martin. We were, and still are, a family who got eachother through homework, tests, prelims, and daily life as a graduate student. I am forever grateful to have met them. There are many others, really our entire class was close, and I am thankful to everyone's kindness and friendship during my time in Storrs. The entire staff and faculty were so also kind. Lunches playing basketball with the crew was the best mental break from graduate work.

It was a pleasure working in Prof. George Gibson's lab. He was kind enough to take me on as a student, encourage me to develop novel research ideas and write fellowship applications. While I may not have gotten those fellowships — I'm not mad — it showed the character of George that he would so readily help a new student and guide him into what was a new

field of research for me. George was the one professor that I actually sat with and took data with in the lab. Thank you to Dale and Katya both of whom made the Gibson lab a warm and welcoming place. I am grateful to Dale's wife for having their child during the summer, which gave me prime time to operate the experiment and take data that was later published. I am very fortunate for my time in the Gibson lab. When I transferred to Northwestern, George was nothing but supportive and encouraging in the transition and I grateful for his help in that transition.

I will never forget the first time I met Brian Odom, to whom I owe so much. Transferring to Northwestern and moving to Chicago is entirely thanks to Brian's kindness and understanding. I am forever thankful of the opportunity he gave me. Brian welcomed me into the group immediately and has always been kind and supportive throughout the ups and downs of graduate school. In our first conversation Brian said "what we do in this lab is hard, and takes a lot of time". That was definitely the case. No matter what, I know that Brian is always there to support me and eagerly help guide the research and work. Graduate research is challenging enough and never once did I feel pressure from Brian to rush/force progress. Brian fosters an engaging and productive group through his warmness and brilliance. Without needing to be told so, everyone under Brian works hard and strives for success. Collectively we aim to see the group and research excel.

My time at Northwestern has been a joy thanks to the help of everyone in the group who became my family. Thank you to Yen-Wei Lin who early on encouraged me to learn Python. Quickly Vincent Carrat and I bonded and I am very fortunate to have met him. Vincent is a kind and generous person who will eagerly teach and help you learn something. Working with Pat Stollenwerk and helping build the ion trap resonator and control electronics for him was the perfect introduction to an ion trapping group. Pat has always been quick to help,

eager to chat and I am grateful to call him a friend. Zeke Tung was there to teach me about op-amps and help debug circuit errors. Everyone in the Odom lab at the time of the lab move was a family who made it all happen. Joseph Cordero-Mercado and Panpan Huang were always so kind and funny and I am so grateful to have gotten to know them. When I joined the single ion experiment, Mark Kokish was the best senior graduate student one could ask for. He has been a great friend and mentor and I am thankful for his friendship. Rebuilding an experiment is challenging but the help of Greg Robelo made it much more fun and enjoyable. I am forever grateful to Qiming Wu who had so much patience in aligning 1.762 μm light in the dark for hours on end. His hard work led us to achieving quadrupole shelving in Ba^+ .

In my later years it somehow ended up just being Sruthi Venkataramanabu, Ivan Antonov and myself left in the group. I am so grateful for their help in teaching me molecular physics and being there to talk to day in and day out. Their friendship kept me sane and they both gave me the opportunity to pursue research that I was not originally involved in. Thank you also to the other Odom Lab members: Jiafeng, Skye, Hadiseh, Jacob, Carissa, Scott and Chandler all of whom made the lab a friendly and engaging place to work. I value the time we all shared together and getting to know everyone.

Thank you to everyone in the Center for Fundamental Physics for making school feel like home. Conversations in the hallway with Andra, Benedict, Chloe, Cris, Eduardo, Nathaniel, Nia, Xing and everyone else broke up the daily grind and helped make the CFP a warm and friendly place to work. A special thank you to Laura Nevins and the rest of the Northwestern Department of Physics and Astronomy staff that did all the background work, made our lives easier, and planned awesome events.

Thank you to my two committee members, Prof. Andy Geraci and Prof. Tim Kovachy.

It has been a pleasure getting to know you both and watching your labs grow. From the attitude of your students it is clear you are both warm and encouraging advisors. You both have always been so helpful every time I have approached either of you with questions about physics or asking to borrow equipment. It is a joy watching the CFP grow with you, Brian and Jerry at the helm.

A special thank you to my family: my parents Jeff and Hilma, my sister Elizabeth and my in-laws Jack, Elaine, Blake and Jameson for all their support, throughout all my schooling. Maybe they never understood what I was doing for research but they always were there to offer encouragement and support or help put things into perspective. Thank you for not asking "when are you going to graduate?" too often.

A million thank you's, the deepest and most sincerest gratitude goes to my wife Mackenzie. We have been together since undergrad day one. She has seen every up and down, late night and early morning, success and failure that follows PhD research. She may be the happiest that I am finally graduating. Certainly you deserve an honorary PhD for your help and patience throughout this process. I could not have done this without your support. Thank you Mackenzie for literally everything, you do so much to enrich and support our lives and your the best part of my day, making all of this hard work worth it. I love you.

To everyone else whom I may not have specifically mentioned and have been apart of my life I am thankful to you. Everyone throughout my life has been kind, friendly and supportive during this journey. I am extremely fortunate to have so many special people in my life and am grateful to each of you.

Dedication

To my brother Evan, the strongest person I know.

TABLE OF CONTENTS

LIST OF FIGURES

LIST OF TABLES

CHAPTER 1

Introduction: State Prepared Molecules and What They Can Tell Us About the Universe

The universe is always
stranger than you think
James S. A. Corey
"Tiamat's Wrath"

1.1 The Growing M in AMO

Laser cooling and optical control has most easily been achieved in atoms with a single valence electron, which is true for alkali atoms or singly-ionized alkali earth atoms. These systems contain a strong dipole-allowed transition and cycling involves only two to three states (not including sublevels) and require at most that many lasers. This focus on 'simple' structure — which reduces experimental complexity — led to the famous "a diatomic molecule is one atom too many!" comment made by Arthur Schawlow [1]. With the addition of vibrational and rotational degrees of freedom it would appear too many lasers or microwaves are needed to gain any type of optical control over molecules.

Despite the perceived challenge, the use of molecules in AMO labs has grown significantly over the past twenty plus years. Currently, optical control has led to studies of ultracold chemistry [2]–[7], quantum information processing [8]–[13], tests of fundamental physics [14]–[31] and metrology [32]–[36]. In fact the field has gotten over any fears of diatomic molecules and expanded into experiments with triatomic [37], [38] and polyatomic molecules [39]–[42]

leading to the idea that "a diatomic molecule is one atom too few" [1].

The focus in our lab has been to find and demonstrate molecular ions that are amenable to optical cycling and state preparation [43]–[46]. With a state prepared molecule, we can conduct spectroscopy in a sample far from equilibrium [47], study reaction rates [48] or probe new physics [19].

1.2 Drifting Fundamental Constants

One interesting area where the use of molecules can potentially excel over atomic samples is in study of fundamental physics. This may be best exemplified in the limits set on the electron electric dipole moment (eEDM) obtained in experiments with diatomic molecules [16], [18]. Here the strong internal electric field inherent to a polar molecule greatly eases the experimental complexity. In our lab, we are interested in the potential for fundamental constants to drift in time [49]. Specifically, we are interested in the time variation of the proton-to-electron mass ratio $\dot{\mu} = \frac{d}{dt}(m_p/m_e)$ [19]. Since the value of μ is not defined in any physical theory, there is no standard that sets the value as constant in time. Any indication of a nonzero $\dot{\mu}$ would imply physics beyond the Standard Model. It is interesting to look at both linear and sinusoidal variations. Linear terms may hint at variations over cosmic time scales [49]. Sinusodial variations may hint at, among other things, dark matter (DM). For example, if DM is ultralight and below a certain mass, it is necessarily bosonic [17] and then may interact with matter as a classical field. In one example, if the DM is a spin 1 particle then this field's interaction would cause mass ratios to oscillate and thus the energy of transitions to oscillate. Scalar DM particles can also induce variations in μ and so it is of great interest to measure $\dot{\mu}$ and potentially set limits on DM masses and couplings.

Molecules play an exciting role in this measurement because of the inherent dependence

vibrational energies have on μ [19]. A measurement made of a given vibrational transition energy $\hbar\nu$ can be made at different times and then analyzed to constrain a time variation of μ. Molecules have an advantage over atoms since the vibrational energy spacing of molecules can be much larger than the hyperfine energy spacing of atoms. This leads to a higher obtainable precision and ultimately a lower uncertainty placed on any possible temporal variations. Despite the apparent advantage, the best limit set on a variation of μ is from using an atomic sample and set the variation of $(\mathrm{d}\mu/\mathrm{dt})/\mu < 8(36) \times 10^{-18}$ / yr [50]. The best limit set using a molecular sample in the lab determines $(\mathrm{d}\mu/\mathrm{dt})/\mu < 0.3(1.0) \times 10^{-14}$ / yr [51]. The large difference here is that the atomic probe using Yb^+ atoms measures an ultra-narrow optical transition while the work of Ref. [51] utilizes a near degeneracy in the KrB molecule to obtain high sensitivity to $\dot{\mu}$. The atomic probe however is limited by the small hyperfine energy splittings where a μ variation would present itself, while molecules can possess vibrational transitions in the optical. In the Odom lab, we aim to improve the molecular measurement by probing a vibrational transition at optical energies in a single molecule.

1.3 State Preparation

State preparation is a desirable component to any precision measurement. If achieved, one can obtain the maximal possible signal and gain sensitivity to low noise sources. State preparation also provides a method to study or mitigate systematic effects. For example, precision measurements in a polar molecule are ideally made for a molecule prepared in its first rotational level since scalar polarizability shifts from adjacent rotational levels cancel out [19]. Additionally, Zeeman shifts are canceled by probing the stretch sublevels in an alternating manner, which requires optical pumping to prepare the species in either state.

State preparation is especially necessary if only a single particle is probed. While limiting the achievable statistics, a single ion can be prepared near it's zero point motional energy and probed in a near zero field environment [52]. By obtaining a frequency uncertainty below 10^{-18}, the Al^+ clock at NIST has shown the amazing potential that a single ion clock offers. Utilizing a scheme known as Quantum Logic Spectroscopy (QLS), the internal state of the Al^+ ion is mapped to a normal mode of motion which is then read out using an auxiliary ion. This scheme requires both the internal state of the spectroscopy ion prepared and the external states of the ions cooled to the ground state of motion. Working in an ion trap is advantageous because the large motional frequencies ($\sim$ MHz) can be spectrally resolved and addressed allowing for motional cooling [53].

Extending a QLS-like scheme to a single molecule has the potential to achieve precision spectroscopy and tests of fundamental physics. Full state preparation of a single molecule is still an ongoing effort, with some groups using projective methods [34] or achieving $\sim$20% state purity in seconds [54]. Nondestructive readout schemes of a single molecular ion is also a current focus with the NIST group achieving $\sim$ kHz resolution of molecular constants using QLS [55] without complete rotational state preparation. Other groups have demonstrated state dependent heating schemes [56]–[58].

1.4 Summary of Thesis

In this thesis I will outline the ongoing effort to demonstrate a new nondestructive state readout method, called Photon Recoil Readout (PRR), and the progress made towards it. Photon Recoil Readout makes use of the same laser that achieves molecular optical pumping, to also motionally heat a molecule in a state dependent way. The technique is meant to be slightly simpler to achieve than QLS, a bit more general, but requires the presence of an

optical cycling transition. As with QLS, an auxiliary 'logic' ion is needed for state readout and sympathetic cooling.

The fundamentals of ion traps are described in Chapter 2. The normal mode structure of two ions of different masses is vital to the operation of this experiment. The experimental apparatus and the control system is outlined in Chapter 3. Details of the atomic and molecular ions used in this experiment, Ba^+ and SiO^+ , are found in Chapter 4 and Chapter 5 respectively. In each chapter, the relevant lasers to address each species are described. In Chapter 5 theoretical modeling of the population dynamics that lead to rotational state optical pumping and some interesting conclusions are discussed. These results are currently being prepared into a manuscript. Data regarding the reaction rates of SiO^+ with H_2 are also being prepared for publication. Chapter 6 goes into the several sideband cooling techniques used to cool two ion crystals to the ground motional state. Finally, Chapter 7 outlines the theory and experimental set-up to achieve PRR. A publication detailing the complete experimental procedure and results of internal and external state preparation for a two-ion crystal of Ba^+ and SiO^+ will also be made.

1.4.1 Note on Atomic/Molecular Physics

I refer the reader to core atomic [59], [60] and molecular [61]–[63] textbooks for discussions of Doppler cooling, Rabi Oscillations, derivation of atomic and molecular states, etc.

CHAPTER 2

Ion Traps: Where the Magic Happens

It's not magic, it's physics
The Expanse
Season 3, Episode 11

2.1 Introduction

Trapping of free particles is a useful tool for experiments in which researchers are able to reduce thermal motion and confine matter to a small volume of space. The low kinetic energy of the particles are nearly free of Doppler shifts and the pathway to precision measurements is opened. By confining matter, long interrogation times lead to measurements made with reduced uncertainty. Ion traps have experimental footprints that are typically much smaller than gas beam experiments and therefore also have value as in quantum sensors as well.

Trapping of charged particles using (static or oscillatory) electric and static magnetic fields has served as the core apparatus in many experiments, some of which have achieved record breaking precision [16], [50], [64], [65]. Ion traps also serve as a dominant platform in quantum computing [66]. Since confinement is solely based on charge to mass ratio a wide variety of samples can be trapped and studied such as atoms and molecules as well as particles that do not have optical cycling and cooling transitions such as electrons, protons, anti-matter and highly-charged ions.

2.2 Fundamentals

In this chapter I will discuss the fundamentals and operation of a linear Paul Trap. The core design is based off a quadrupole mass filter [67] with a static field applied at both ends to cap the system. There are several ways to design the electrode geometry of radio frequency and DC electric fields to achieve confinement. One dominant way involves segmented electrodes [68], [69]. In our case, we achieve DC biasing using four compensation rods that sit at a larger outer radius than the trapping RF rods. This geometry is described below.

Earnshaws Theorem details why a three-dimensional minimum cannot be created from electrostatic fields alone. A minimum is defined as sink in the field, where the divergence is negative. Gauss' Law indicates that the divergence of a force field is zero in free space, $\boldsymbol{\nabla} \cdot \vec{\mathrm{F}} = \boldsymbol{\nabla} \cdot (-\boldsymbol{\nabla} U) = \nabla^2 U = 0$. If the Laplacian operator on a function is zero at a given point in space, there exists a saddle point, as the curvature of the function in one direction cancels with the slope in another direction.

As a consequence an oscillatory field is required to maintain a stationary point. In the linear Paul trap, an RF voltage is applied to the four rods (diagonal pair of the same polarity, with the opposite pair at 180 degrees out of phase from those) or two diagonal rods with the other two grounded. The latter is the set-up used in this experiment. See Fig 2.1 for details of voltage configuration. The system exhibits cylindrical symmetric about the Z axis, defined as a line drawn that intersects the center of each endcap.

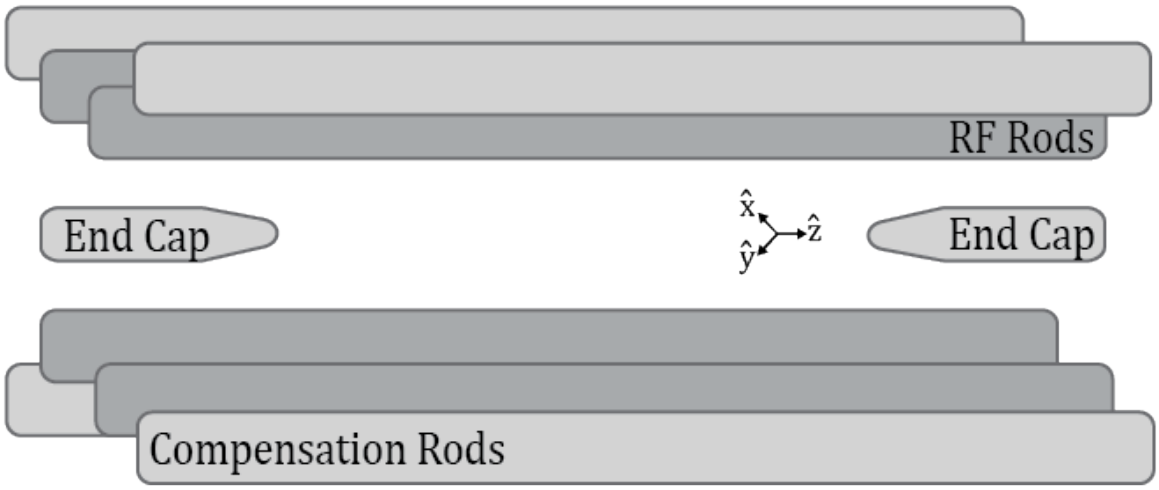

Figure 2.1: **Paul Trap:** A RF voltage is applied to two diagonal rods, while the other two are grounded. Surrounding the RF rods are DC compensation rods to cancel stray fields and reduce micromotion of the ions. A separate DC voltage is applied to the endcaps to prevent the ions from escaping along that direction.

For complete descriptions of the equation of motion and trapping voltages I refer the reader to [68], [70], [71]. I will briefly go over the relevant equations here. A potential of $V_{RF}\cos\Omega_T + V_{xy}$ is applied to diagonal rods, where V_{xy} is a DC voltage to break the degeneracy between the x and y axes. If the ion to RF electrode distance is r_0 then the potential near the trap center is approximately,

$$\Phi \cong \frac{(V_{RF}\cos\Omega_T t + V_{xy})}{2}\left(1 + \frac{x^2+y^2}{r_0^2}\right). \tag{2.1}$$

The resulting potential is described as a harmonic pondermotive potential in the x- and y-direction. If voltage of V_{ec} is applied to the static endcaps separated by $2z_0$, the potential along this direction takes the form,

$$\Phi_s = \kappa V_{ec}\left(z^2 - \frac{1}{2}(x^2+y^2)\right) = \frac{m}{2q}\omega_z^2\left(z^2 - \frac{1}{2}(x^2+y^2)\right). \tag{2.2}$$

Here, κ is a geometric screening factor, m is the ion mass, q is the ion charge and $\omega_z = \left(\frac{2\kappa q V_{ec}}{m}\right)^{1/2}$ is the oscillation frequency of a single ion along the z-direction. This is typically referred to as the 'axial' frequency.

The resulting equations of motion can be solved analytically for small oscillations near equilibrium positions where the harmonic approximation is valid [68]. The classical equations of motion are described by the Mathieu equation,

$$\frac{d^2x}{d\zeta^2} + \Big(a_x + 2q_x\cos(2\zeta)\Big)x = 0 \tag{2.3}$$

$$\frac{d^2y}{d\zeta^2} + \Big(a_y + 2q_y\cos(2\zeta)\Big)y = 0\ , \tag{2.4}$$

where,

$$\zeta = \Omega_t t/2 \tag{2.5}$$

$$a_x = \Big(\frac{4q}{m\Omega_T^2}\Big)\Big(\frac{V_{xy}}{z_0^2} - \kappa\frac{V_{ec}}{z_0^2}\Big) \tag{2.6}$$

$$a_y = -\Big(\frac{4q}{m\Omega_T^2}\Big)\Big(\frac{V_{xy}}{z_0^2} + \kappa\frac{V_{ec}}{z_0^2}\Big) \tag{2.7}$$

$$q_x = -q_y = \frac{2qV_{RF}}{\Omega_T^2 m r_0^2} \tag{2.8}$$

The solutions to Eq. 2.4 are solved using Floquet solutions. Typically the stability parameters, a_i and q_i are related by $a_i < q_i^2 \ll 1$ where $i = \{x, y\}$. The resulting equation of motion describing the position of the ion along either radial ($i = \{x, y\}$) direction is,

$$u_i(t) = A_i\Bigg(\cos(\omega_i t + \phi_i)\left[1 + \frac{q_i}{2}\cos\left(\Omega_T t\right) + \frac{q_i^2}{32}\cos\left(2\Omega_T t\right)\right] \tag{2.9}$$

$$+ \beta_i \frac{q_i}{2}\sin\left(\omega_i t + \phi_i\right)\sin\left(\Omega_T t\right)\Bigg) . \tag{2.10}$$

Here,

$$\omega_i \cong \left(\frac{\Omega_T}{2}\right)\left(a_i + \frac{q_i^2}{2}\right)^{1/2} \tag{2.11}$$

.

Commonly, the oscillation at frequency ω_i is called the 'secular' motion. The terms that oscillate at Ω_T and $2\Omega_T$ give rise to 'micromotion' coined by the small motional amplitude at this fast frequency. There are two types of micromotion, intrinsic and excess. Intrinsic micromotion is the type just described and only reduced by cooling the ion to the ground motional state [68]. Excess micromotion is caused by stray fields that displace the ion from the center of the trap. This is mitigated by applying bias fields which minimize this motion. If the relation $a_i < q_i^2 \ll 1$ holds, $V_{xy} = 0$, and the micromotion terms are neglected then the ions motion is described by a harmonic psuedopotential in the radial direction,

$$q\Phi_p = \frac{1}{2}m\omega_r^2(x^2 + y^2). \tag{2.12}$$

As a result, the defining motional frequencies for a single trapped ion are,

$$\omega_z = \left(\frac{2\kappa q V_{ec}}{m z_0^2}\right)^{1/2} \tag{2.13}$$

$$\omega_p = \frac{q V_{RF}}{\sqrt{2}\Omega_T m r_0^2} = \frac{q_x \Omega_T}{2\sqrt{2}} \tag{2.14}$$

$$\omega_x = \left(\frac{1}{2}\frac{q^2 V_{RF}^2}{\Omega_T^2 m^2 r_0^4} - \kappa\frac{q V_{ec}}{m z_0^2} + \frac{q V_{xy}}{m r_0^2}\right)^{1/2} \tag{2.15}$$

$$\omega_y = \left(\frac{1}{2}\frac{q^2 V_{RF}^2}{\Omega_T^2 m^2 r_0^4} - \kappa\frac{q V_{ec}}{m z_0^2} - \frac{q V_{xy}}{m r_0^2}\right)^{1/2}. \tag{2.16}$$

Simplifying, we can write,

$$\omega_x = \left(\omega_p^2 - \alpha\omega_z^2\right)^{1/2} = \omega_z\left(\epsilon^2 - \alpha\right)^{1/2} \tag{2.17}$$

$$\omega_y = \left(\omega_p^2 - (1-\alpha)\omega_z^2\right)^{1/2} = \omega_z\left(\epsilon^2 - (1-\alpha)\right)^{1/2}. \tag{2.18}$$

Here, $\epsilon = \frac{\omega_p}{\omega_z}$, $\alpha = \frac{1}{2}(1 - \frac{\omega_{xy}^2}{\omega_z^2})$ where $\omega_{xy}^2 = \frac{2qV_{xy}}{mr_0^2}$ describes the frequency shift from breaking the x-y degeneracy. These equations define the harmonic modes of motion for ions near the center of the trap. Interestingly, we find here that the applied field from the endcaps reduces the strength of the potential in the x- and y-directions.

It will be important in the next section to define the Lamb-Dicke Parameter, η, (for a full explanation see Ch. 6) so I will quickly do that here. This dimensionless parameter is relates the ratio of the motional state energy to the recoil energy for a transition being driven. The Lamb-Dicke Parameter is defined as,

$$\eta^2 = \frac{\omega_R}{\omega_z} = \frac{\hbar k_i^2}{2m\omega_i}, \tag{2.19}$$

where m is the mass of the ion, k_i and ω_i are the light's wavevector and motional frequency

along a certain direction with $i = \{x, y, z\}$. It is desirable that $\eta \ll 1$, in which case any energy added to the ion from photon recoils (absorption or emission) will not diabatically change the ion's motional state.

It is also important (for those reading this sequentially, whom I applaud) to introduce the concept of motional sidebands. This is all detailed in Ch.6 and Appendix A. If an atomic resonance occurs at frequency ω_a and the lifetime of the excited state is less than $\omega_{\{x,y,z\}}$ then a scan over the atomic resonance will show motional sidebands as well. Just like in RF signal mixing, the resonance at lower frequencies are found at $\omega = \omega_a - n * \omega_{x,y,z}$ and these correspond to an internal atomic transition as well as a lowering of the motional state by n. These are called the 'red sidebands' (RSB). Those at higher frequencies, where $\omega = \omega_a + n * \omega_{x,y,z}$, are known as 'blue sidebands' (BSB) and the atomic transition is paired with an increase in the ion motional state by n. This is observable when the laser k-vector (or Δk for Raman transitions) has a component along a given trap axis {x,y,z}. This makes it possible to heat the ion or cool the ion to the ground motional state of a given mode, where $n = 0$.

The relation between ω_z and ω_x defines the resulting crystal geometry. For a few Doppler cooled ions, if $\omega_x > \omega_z$ then the ions will align into a string along the z-axis. If $\omega_x < \omega_x$ then the ions line up along the radial direction. The relation between the radial and axial frequencies plays an important role in recrystallizing a mixed-species crystal back to Doppler temperatures. This is described in Sec. 3.5.8.

2.3 Two Ion Crystals

The main goal of this project is to co-trap a single molecular ion alongside one atomic ion. We can also refer to these as the 'spectroscopy' and 'logic' ions respectively. The two ions

are coupled from the Coulomb interaction which results in their motion also being coupled. In Ch.6 is a discussion of how electromagnetic radiation can couple the ions motion and internal states. If a single ion is Doppler cooled, the other ion is sympathetically cooled and reduced to Doppler temperatures as well [72]. This cooling occurs due to their mutual Coulomb interaction.

The coupling between the two ions is described the normal eigenvectors and eigenmodes of the system. While these equations can be found elsewhere [73], [74] the details are important to the work in this thesis and therefore will be outlined here as well.

For an ion of mass m_1 we can write the motional frequencies as given by Eq. 2.12, 2.16 and 2.17. We can then relate the motional frequencies of an ion with mass m_2 in terms of those equations. The resulting frequencies for ion 2 are,

$$\omega_{z,2} = \omega_{z,1}\sqrt{\frac{m_1}{m_2}} \tag{2.20}$$

$$\omega_{x,2} = \omega_{x,1}\sqrt{\frac{m_1}{m_2}}\sqrt{\frac{\frac{m_1}{m_2}\epsilon^2 - \alpha}{\epsilon^2 - \alpha}} \tag{2.21}$$

$$\omega_{y,2} = \omega_{y,1}\sqrt{\frac{m_1}{m_2}}\sqrt{\frac{\frac{m_1}{m_2}\epsilon^2 - (1-\alpha)}{\epsilon^2 - (1-\alpha)}} \tag{2.22}$$

Two ions can crystallize, by laser cooling one ion for example, which occurs when their kinetic energy becomes less than the confining potential energy. As a result, the ions align themselves equidistant from trap center, spaced a distance apart given by $z_{eq} = (\frac{ez_0^2}{32V_{ec}\pi\epsilon_0})^{1/3}$ [68]. This value is typically on the order of 5 - 10 μm.

These crystallized ions have motions described by small and coupled oscillations along the x-,y- and z-directions about their equilibrium positions. In each spatial dimension the

motion is described by a superposition of two modes: one where they move in opposite directions (out-of-phase or *op*) and one where the ions move in the same direction (in-phase or *ip*) [73]. The ions have components of the normalized eigenvectors given by $b_{1,2}$ where $b_1^2 + b_2^2 = 1$ [1]. Here, b_1 corresponds to the in-phase mode and b_2 corresponds to the out-of-phase mode. If $\mu = m_2/m_1$ then the axial and radial mode frequencies are (setting the radial modes to be degenerate, $\alpha = 0$),

$$\omega_{ip,z} = \omega_z \sqrt{\frac{1+\mu-\sqrt{1-\mu+\mu^2}}{\mu}} \tag{2.23}$$

$$\omega_{op,z} = \omega_z \sqrt{\frac{1+\mu+\sqrt{1-\mu+\mu^2}}{\mu}} \tag{2.24}$$

$$\omega_{ip,\{x,y\}} = \omega_z \sqrt{-\frac{\mu+\mu^2-\epsilon^2(1+\mu^2)-a}{2\mu^2}} \tag{2.25}$$

$$\omega_{op,\{x,y\}} = \omega_z \sqrt{-\frac{\mu+\mu^2-\epsilon^2(1+\mu^2)+a}{2\mu^2}}, \tag{2.26}$$

where $a = \sqrt{\epsilon^4(\mu^2-1) - 2\epsilon^2(\mu-1)^2\mu(1+\mu) + \mu^2(1+(\mu-1)\mu)}$. Additionally, we find the components of the eigenvectors are,

$$b_{1,z}^2 = \frac{1-\mu+\sqrt{1-\mu+\mu^2}}{2\sqrt{1-\mu+\mu^2}} \tag{2.27}$$

$$b_{1,\{x,y\}}^2 = \frac{\mu-\mu^2+\epsilon^2(\mu^2-1)+a}{2a} \tag{2.28}$$

[1] For a complete mathematical treatment see Appendix B of Ref. [74]

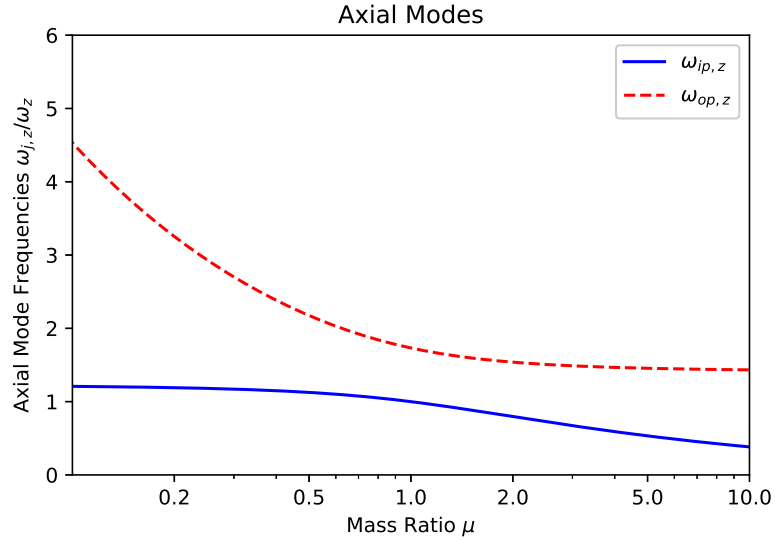

(a) **Two Ion Axial Eigenmodes:** These mode frequencies are scaled by the axial frequency ω_z of mass m_1.

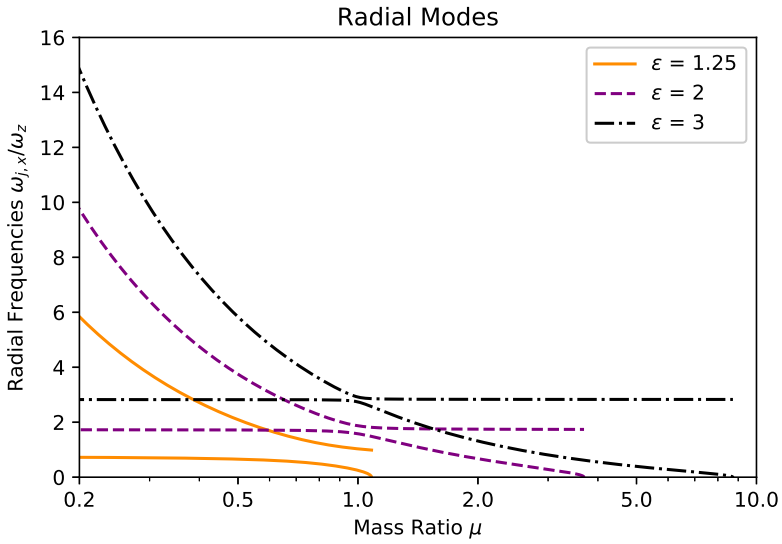

(b) **Two Ion Radial Eigenmodes:** for varying mass ratio and different values of $\epsilon = \omega_p/\omega_z$. The lines stop when $\omega_{op,x}$ goes to zero, which indicates that the crystal switches from being aligned on the axial direction to the radial direction. The top three lines reflect the radial in-phase mode while the radial out-of-phase mode is relatively unchanged for varying μ.

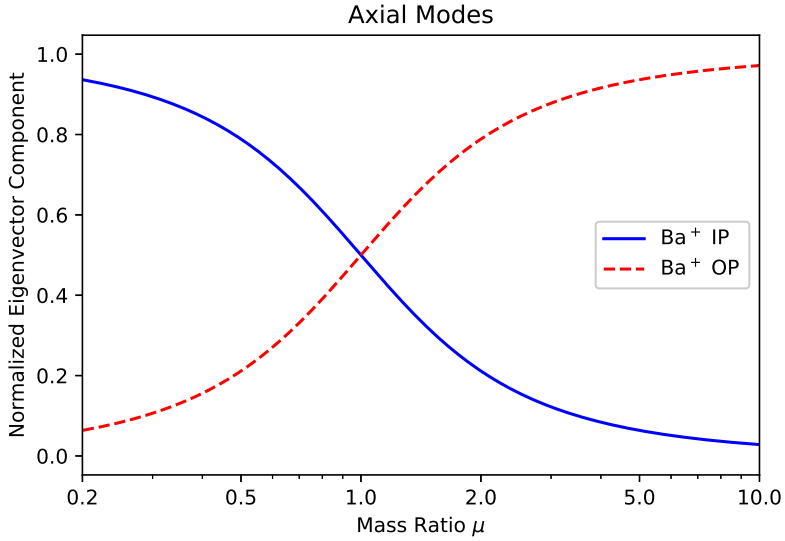

(a) **Axial Eigenmode Components:** Shown for varying mass ratio. The in-phase component, b_1 for the heavier ion is shown in blue and the out-of-phase component, b_2, is shown in red for the same ion.

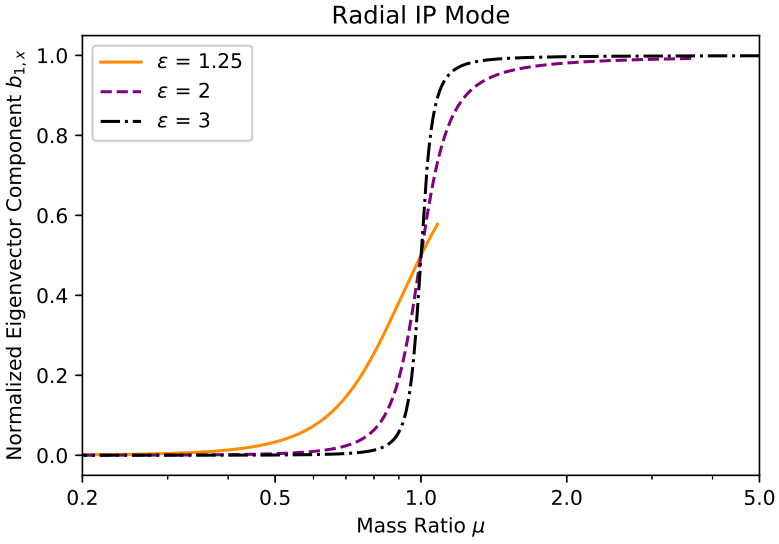

(b) **Radial Eigenmode Components:** Shown for varying mass ratio and ratio between psuedopotential and axial frequency $\epsilon = \omega_p/\omega_z$. The lines stop when $\omega_{op,x}$ goes to zero, which indicates the crystal switches from being aligned on the axial direction to the radial direction.

The dependency that the eigenmode vectors have on μ is easily seen in Fig. 2.3a. It becomes clear how different the normal mode structure becomes as the mass ratio μ changes from one. The lighter ion has the largest amplitude of motion for the highest frequency mode which is the axial out-of-phase and radial in-phase mode. The opposite is true for the heavier ion which has the largest amplitude of motion for axial in-phase and radial out-of-phase modes. From Fig. 2.3b it is clear how quickly the modes become decoupled in the radial direction as the mass ratio changes from one.

If the motional frequency can be measured, these calculations make mass spectrometry possible. For example, if one ion can be Doppler cooled, its presence in the ion trap is simply detected by an increase in photon counts and the ions position can even be imaged on a camera (see Sec. 3.5.3.2). If the second ion does not have a cycling transition due to its level structure, then it appears dark and its presence is only indicated by a displacement of the Doppler cooled ion from trap center. As discussed in Ch.6 the motional modes are dressed onto the internal transitions of the ions and can therefore be measured [75]. By finding the frequency (atomic plus motional) this occurs at, one can calculate the mass of the dark ion [75]–[78]. Less precise methods, though still sufficient, involve the application of another, typically lower frequency and voltage, RF signal to a trap electrode. When this RF frequency matches a motional mode, the ions motion will be driven and excited, heating the Doppler cooled ion which will fluoresce less light. This is the primary readout method mentioned in Ch. 5 and [46], [47].

The Lamb-Dicke parameters are also modified in the normal mode picture for two ions and become weighted by the eigenvector components of a specific mode and specific ion [2]. These value are shown in Table 2.1.

[2]See Appendix B of both [79] and [74]

Mode	Ion 1	Ion 2
z-ip	$\eta_1^{ip,z} = k_z^{(1)}\sqrt{\frac{1-\mu+\sqrt{1-\mu+\mu^2}}{2\sqrt{1-\mu+\mu^2}}}\sqrt{\frac{\hbar}{2\omega_{ip,z}m_1}}$	$\eta_2^{ip,z} = \frac{k_z^{(2)}}{\sqrt{\mu}}\sqrt{1-\frac{1-\mu+\sqrt{1-\mu+\mu^2}}{2\sqrt{1-\mu+\mu^2}}}\sqrt{\frac{\hbar}{2\omega_{ip,z}m_2}}$
z-op	$\eta_1^{op,x} = k_z^{(1)}\sqrt{1-\frac{1-\mu+\sqrt{1-\mu+\mu^2}}{2\sqrt{1-\mu+\mu^2}}}\sqrt{\frac{\hbar}{2\omega_{ip,z}m_1}}$	$\eta_2^{op,z} = \frac{k_z^{(2)}}{\sqrt{\mu}}\sqrt{\frac{1-\mu+\sqrt{1-\mu+\mu^2}}{2\sqrt{1-\mu+\mu^2}}}\sqrt{\frac{\hbar}{2\omega_{op,z}m_2}}$
x-ip	$\eta_1^{ip,x} = k_x^{(1)}\sqrt{\frac{\mu-\mu^2+\epsilon_x^2(\mu^2-1)+a_x}{2a_x}}\sqrt{\frac{\hbar}{2\omega_{ip,x}m_1}}$	$\eta_2^{ip,x} = \frac{k_x^{(2)}}{\sqrt{\mu}}\sqrt{1-\frac{\mu-\mu^2+\epsilon_x^2(\mu^2-1)+a_x}{2a_x}}\sqrt{\frac{\hbar}{2\omega_{ip,x}m_2}}$
x-op	$\eta_1^{op,x} = k_x^{(1)}\sqrt{1-\frac{\mu-\mu^2+\epsilon_x^2(\mu^2-1)+a_x}{2a_x}}\sqrt{\frac{\hbar}{2\omega_{op,x}m_1}}$	$\eta_2^{ip,x} = \frac{k_x^{(2)}}{\sqrt{\mu}}\sqrt{\frac{\mu-\mu^2+\epsilon_x^2(\mu^2-1)+a_x}{2a_x}}\sqrt{\frac{\hbar}{2\omega_{op,x}m_2}}$
y-ip	$\eta_1^{ip,y} = k_y^{(1)}\sqrt{\frac{\mu-\mu^2+\epsilon_y^2(\mu^2-1)+a_y}{2a_y}}\sqrt{\frac{\hbar}{2\omega_{ip,y}m_1}}$	$\eta_2^{ip,y} = \frac{k_y^{(2)}}{\sqrt{\mu}}\sqrt{1-\frac{\mu-\mu^2+\epsilon_y^2(\mu^2-1)+a_y}{2a_y}}\sqrt{\frac{\hbar}{2\omega_{ip,y}m_2}}$
y-op	$\eta_1^{op,y} = k_y^{(1)}\sqrt{1-\frac{\mu-\mu^2+\epsilon_y^2(\mu^2-1)+a_y}{2a_y}}\sqrt{\frac{\hbar}{2\omega_{op,y}m_1}}$	$\eta_2^{op,y} = \frac{k_y^{(2)}}{\sqrt{\mu}}\sqrt{\frac{\mu-\mu^2+\epsilon_y^2(\mu^2-1)+a_y}{2a_y}}\sqrt{\frac{\hbar}{2\omega_{op,y}m_2}}$

Table 2.1: **Complete expressions for Lamb-Dicke parameters in a two-ion crystal:** Here $k_i^{(1)}$ and $k_i^{(2)}$ are the k-vectors along a given direction that address particle 1 and 2.

2.3.1 Two Ion Crystal Preparation

From Fig. 2.3a it is clear that when two trapped ions have different masses the normal modes become decoupled. This has a huge implication if only one ion is being actively Doppler cooled. That ion becomes less efficient at sympathetically cooling the second ion [73], [80].

As mentioned in the previous section, and elaborated on in Ch. 6, a mixed-species crystal where $\mu \neq 1$ also has decreased atom-light coupling on certain motional modes of the laser cooled ion. These effects impact daily use of mixed-species ion crystals when the mass ratio deviates from one [73], [81]. When only one ion is laser cooled, the other ion is sympathetically cooled dependent on its eigenvector component (see Fig. 2.3a). This play an important role in loading and operation times [82] and precision of measurements obtainable [52], [73]. This is why experiments with a dark ion (typically the science ion) choose a Doppler cooling ion with a similar mass [65], [83], [84].

Collisions with background gas (which occur on the order of 100s in ultrahigh vacuum (UHV) systems) can cause the ions to reorder. A single collision event can also deposit a significant amount of energy into the ion crystal cause the ions to thermalize (to 20 - 30 K [73]) out of the crystal phase, leading to a random ion orientation. These events result in ion conditions similar to when loading [65], [81]. Dumping and reloading the ions would defeat the principle advantage of ion traps, and so we need a procedure to both crystallize a mixed-species sample.

When either loading or after a collision with background gas has occurred, the ion temperature is orders of magnitude higher than being in a crystal phase from Doppler cooling [85]. Doppler cooling of a single hot ion has been modeled in [86], [87] and for two ions in [73], [80], [84]. In the case of two trapped ions, all of the authors conclude that the conditions

to achieve the lowest temperature ion, having the Doppler laser set to saturation intensity and detuning of half the transition linewidth, are not the same conditions to optimally cool a hot ion crystal. In general, it is found that use of a second, further red-detuned laser with an intensity larger than saturation is extremely beneficial in crystallizing the ions. The authors find that a detuning on the order of 5-6 Γ, where Γ is the linewidth of the cooling transition, is optimal. This second laser enhances the scattering rate of the rapidly moving ion.

In Ref. [73] it is shown that the cooling rate for a hot crystal is comparable to that of a single ion. After crystallization, the normal mode picture indicates which modes are cooled well and which are not, based off strong or weak coupling to the cooling ion. As a result it is also important to set the trap parameters accordingly during these procedures. The authors of [80] find that the cooling time dependents directly on the inverse of the trap frequency cubed. They go onto say that if the hot ion has its initial energy set primarily by the potential energy it gains when loaded, it is thus desirable to operate is a weak trap when loading and/or recrystallizing. If the trap voltages are adjusted near an instability point for an axial crystal (see Fig. 2.3b and 2.2b), the two ions begin to tilt at an angle. In this situation, the six motional modes are projected at an angle to the principle axes, increasing the coupling between them [82].

Another means of crystallizing hot ions is to add additional cooling ions [80], [82]. The experimental challenge is then to eject the extra refrigerant ions, as the goal is typically to work with just a two ion crystal. If the refrigerant ion is heavier than the dark ion, the RF voltage can be switched on/off quickly. Since the heavier ion is less bound in the trap than the lighter one, it is more likely to be ejected. If the refrigerant ion is lighter than the dark ion, the trapping potential can be gradually increased to near instability of the lighter ion. If laser cooling is turn off for brief time, the lighter ions may be ejected.

After crystallization or recrystallization, it is desirable to set the orientation of the ions (i.e. $m_1 - m_2$ vs $m_2 - m_1$). Lasers used to address the ions are typically tightly focused such that the intensity may vary between the two ion positions. Gradients in electric or magnetic fields can also act to increase systematic errors if the ion positions are not controlled [88], [89].

The reordering of ions from $m_2 - m_1$ to $m_1 - m_2$ can be achieved in effectively two ways. Ions will align themselves radially if the RF voltage is decreased, axial voltage increased, or a combination of both. A DC voltage applied to one of the rods can also orient the ions along the radial direction as the heavier mass experiences less of a pondermotive force than the lighter ion. With a radially aligned crystal, a new static field is needed then to push (or pull) one ion more than the other, which will reorient them. A gradient along the axial direction, $E_z = \frac{dE_z}{dx}x$, then turns the ion pair. After relaxing the potentials the ions are now in a desired orientation [88], [90], [91]. This process should be complimented by application of laser cooling to dampen any heating effects as the ions are moved.

CHAPTER 3

Single Ion Apparatus:

The Illusion (and Demonstration) of Control

... he knows he doesn't control it.
He's at the mercy of it.
Michael Crichton
"Jurassic Park"

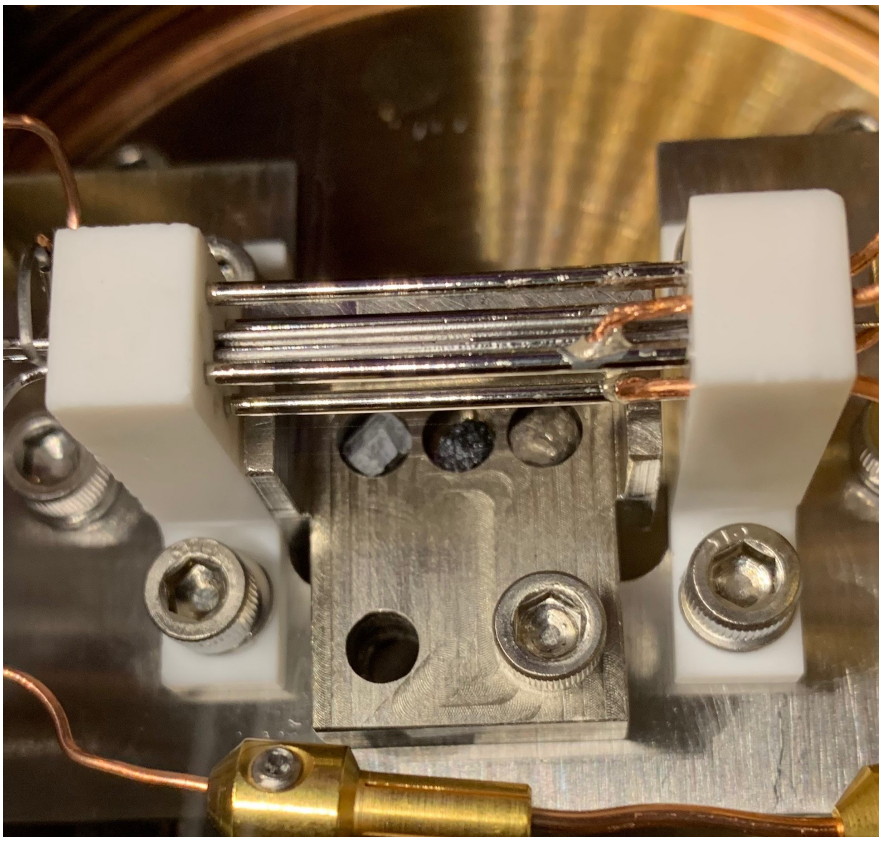

Figure 3.1: **Ion Trap Photo:** A top down view of the single ion trap is shown. The outer compensation rods appear shinier and the inner RF rods can be seen inside those. Below the trap sits the samples which from left to right are: barium, silicon monoxide and calcium.

While most of this apparatus has been described in [74], [92], [93] the experiment has undergone a lab move since [92], [93] and a vacuum system change since [74]. In this section I will briefly go over most of the experimental apparatus sans the laser systems used, those of which are described in the following chapters.

The irony is we call this the single ion experiment yet the goal to trap two ions, one atomic and one molecular ion. We even trap three ions to making it easier to prepare a two ion crystal.

3.1 Single Ion Trap

The main ion trap used to produce results shown in this thesis can be seen in Fig. 3.1. A different ion trap was used regarding some work presented in Ch. 5. The details of that trap can be found in two recently published theses [48], [94]. In the single ion experiment, a four rod Paul trap is used to store single ions and a detailed description of its design can be found in Ref. [93]. The trap is built to produce large trapping potentials such that the resulting motional frequencies are typically >1 MHz. The electrode configuration is shown in Fig. 3.2 and the dimensions of the trap are shown in Fig. 3.3. Not shown is the endcap to endcap spacing ($2z_0$) of 1.9 mm and the ion to electrode distance which is $r_0 = 0.457$ mm.

The RF voltage is generated from an Agilent 33521A Synthesizer whose output first passes through a Mini-Circuits ZYSAW-2-50DR+ TTL switch before seeding an HD Communications HD28326 amplifier. The switch is normally closed, and only opened, breaking the circuit, for $\sim$2 μs pulses when ions are ejected (see Sec. 3.4). The Agilent Synthesizer is amplitude modulated from an analog input voltage, computer controlled, which adjusts the RF power and tunes of the secular frequencies. The output of the amplifier first passes through a bi-directional coupler and then seeds the primary coil of a home-built helical res-

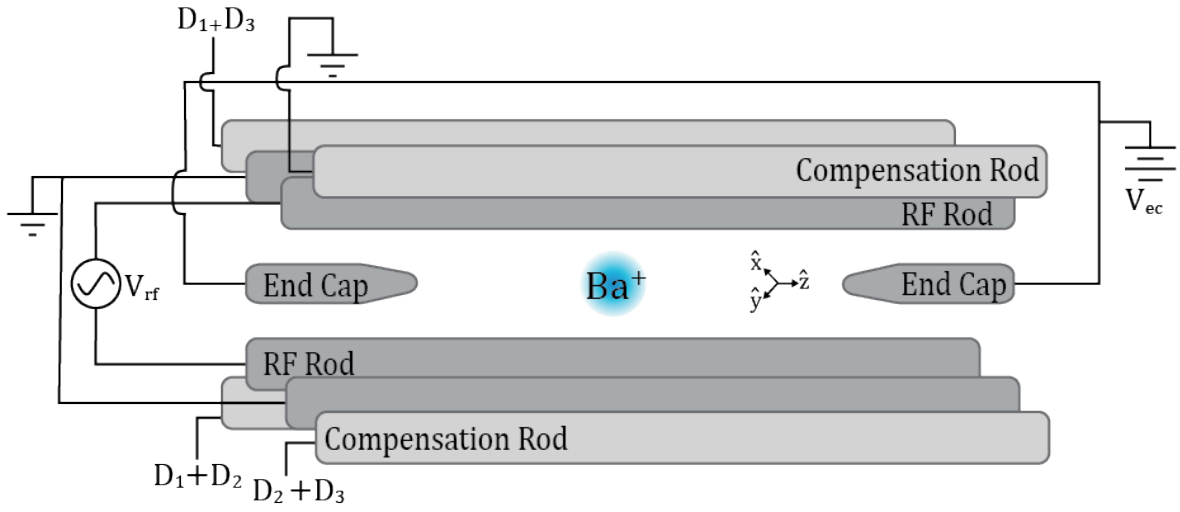

Figure 3.2: **Ion Trap Electrode Configuration:** a) A linear Paul Trap confines ions near the center. An RF voltage is applied to two diagonal rods, while the other two are grounded. Surrounding the RF rods are DC compensation rods to reduce micromotion of the ions. A separate DC voltage is applied to the endcaps. b) Side view

onator [93]. The bi-directional coupler measures both the input power and reflected power from the resonator.

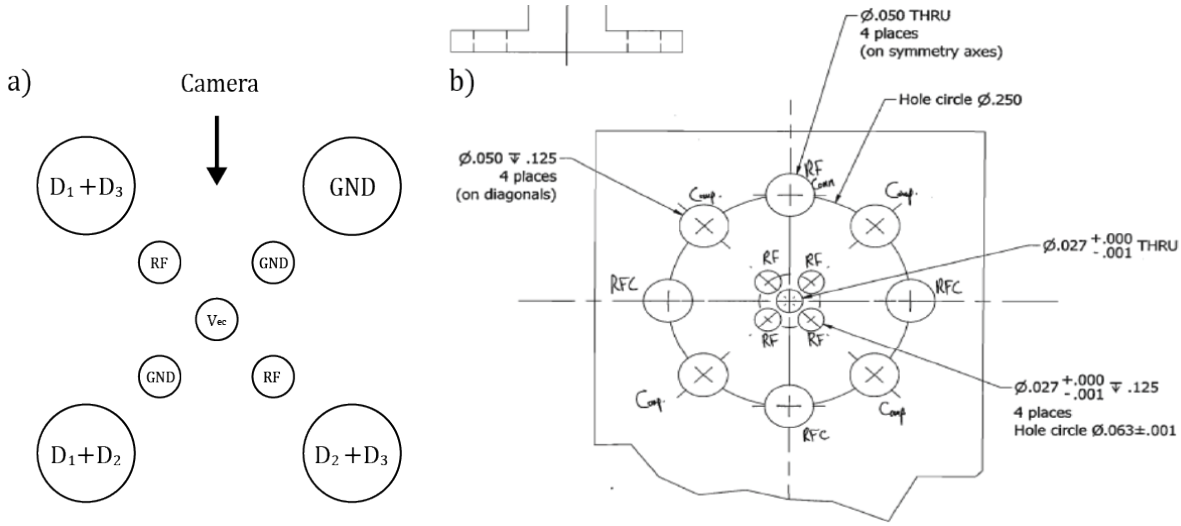

Figure 3.3: **Ion Trap Dimensions:** a) A side view of the trap showing the RF and DC rods, as well as on-axis endcaps. b) Dimensions showing the size and distance from the trap axis of the electrodes.

The helical resonator uses magnetic induction to couple RF energy into the trap resonator. The coupling coils, electrically connected to the trap rods, form an LC circuit with the former acting as the inductor and latter the capacitor. Typically the rods have 5 to 10 pF of capacitance. The resonator was designed to have a resonance at 25 MHz, and has been experimentally found to be $\Omega_T = 2\pi$ x 23.3066 MHz. Since the RF system uses a helical resonator, any DC bias applied to the antenna will not carry to the trap rods. This is the reason the compensation rods are added to the trap.

The bi-directional coupler outputs to Mini-Circuits ZX47-40LN-S+ power detectors which convert the RF power to a DC voltage. The resulting voltages are monitored daily with a digital multimeter to observe power and frequency drifts in the resonator. Resonance of the RF system is found by minimizing the reflected power, which is maximizing the detect voltage along that channel. It has been found that the voltage the trap is left at overnight influences the power coupled into the resonator the following day. The hypothesis is that the total current flowing through the rods heat them and change the impedance of the system. As a result, it is best to keep the trap set to mid-level power in terms of typical use.

The radial on-off was inspired by Ref. [82] and implemented to aid in loading of hot ions. We predominately use the on-off to eject extra refrigerant ions. The RF response, measured by the reflected power back monitor, to the TTL switch off is shown in Fig. 3.4. The voltage decays with a time constant of ≈ 5.1 μs. From this, we can estimate a quality factor of the resonator to be $Q \approx 374$, where $Q \sim \tau\Omega_T/2$. This matches previously found quality factors [92], [93].

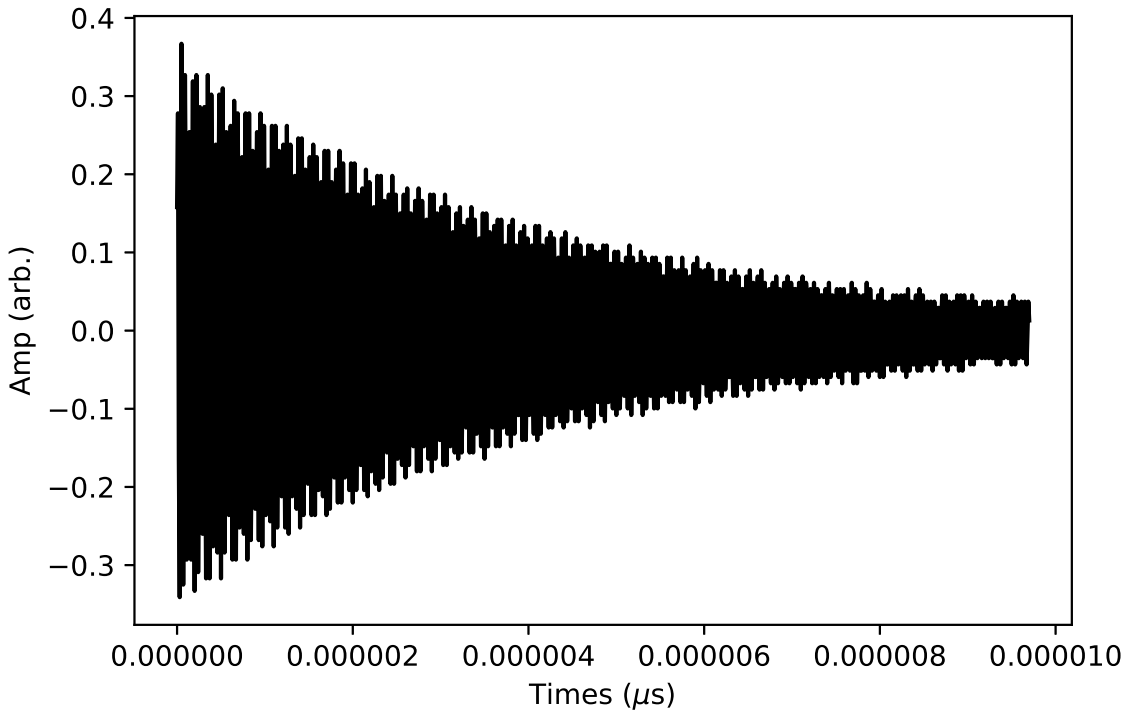

Figure 3.4: **RF on/off Reflected Power** By monitoring the reflected power from the resonator we can observe the effect of the TTL on/off switch. Here a 10 μs pulse was applied, and the power decays with a time constant of ≈ 5.1 μs.

The DC voltages for the endcaps and RF bias voltages are each generated from an NI PXI-6704 card, which is computer controlled. The analog output channels from the NI card control serve as the gate for a two-stage amplifier from which an Acopian DC voltage supply acts as the source. The voltages pass through a low-pass filter with a 3 dB cutoff of 0.14 Hz, reducing any RF noise on ground as well as pickup on the electrodes from the trap rods.

3.1.1 Micromotion Compensation

The compensation rods are used to compensate for stray fields electric fields that would displace the ions from trap center. This is accomplished by changing the voltages D_1, D_2

and $D_1 + 2$, shown in Fig. 3.3. To measure the level of excess micromotion we use the procedure outlined in [95].

First, the ion position is measured using the camera software under tight and weak trapping conditions. Under weak trap conditions (those typically used for loading) a DC offset is applied to the endcaps to move the ion in the axial direction and to D_1 which adjusts the ion position parallel to the focal plane.

At this point ion motion perpendicular to the camera focal plane is uncompensated. Motion in this direction will modulate detected photon counts, which can be measured. A fluorescence measurement is made by correlating detection with the RF drive frequency. Photon counts are measured with an SRS single photon detector, and binned into 5 ns windows. By fitting a sinusoidal function at the RF frequency, the modulation index corresponding to the amplitude of the sine wave is found. By minimizing this modulation index as a function of D_2, excess micromotion is fully compensated to the level of current sensitivity.

A more precise method can be used for very low levels of excess micromotion in three dimensions. This is outlined in Ref. [52] and is used to characterize the excess micromotion in the NIST Al^+ clock.

3.1.2 Trap Calibration

It is important to understand the trap voltages and resulting motional frequencies. This is especially neccesary when attempting to load two ions with different masses and crystal preparation is desirable (Sec. 2.3.1). To measure the radial frequencies, an RF voltage is applied to one of the compensation rods. By trapping a single Ba^+ ion and measuring its fluorescence as function of the 'tickling' frequency, the radial secular frequencies can be measured. While the voltages of D_1, D_2 and $D_1 + D_2$ tackle micromotion compensation (see

$V_{labview}$ (V)	CPL_REV (V)	$\omega_x/2\pi$ (MHz)	$\omega_y/2\pi$ (MHz)
-4.0	1.3124	0.494	0.592
-3.5	1.2280	0.823	0.891
-3.0	1.1660	1.106	1.184
-2.5	1.0992	1.386	1.463

Table 3.1: **Radial Calibration:** For an xy offset voltage of $D_3 = 30$ V applied and $V_{ec} = 20$ V the radial modes were measured. The voltage measuring the reflected power from the trap is also shown. It is useful to monitor this value daily to observer any potential drifts.

Sec. 3.1.1), the other bias voltage D_3 splits the radial degeneracy and makes the trapping potential in the x- and y-directions different. The compensation rods are shielded by the RF rods, and further from the ion, such that an applied voltage of $\mathcal{O}(10)$ V is needed to create a $\mathcal{O}(100)$ kHz splitting. For a fixed $D_3 = 30$ V, the calibration of the RF set point to actual voltage seen by the ion, is shown in Table 3.1.

From this data we a ≈ 80 kHz splitting between the two radial resonances. Using the expressions from Eq. 2.16, can solve for V_{RF} in terms of ω_x and ω_y. From that, a line fit gives the relation that the RF voltage on the rods is:

$$V_{RF} = 219.3(1.7) * V_{labview} + 1112.5(5.6)V. \tag{3.1}$$

Taking the results from the fit, we can then plug in V_{RF} to solve for V_{xy} in either direction and the result is mean value of $V_{xy} = 0.78(9)$ V. Note how different this is from the applied 30 V to D_3 which emphasises the screening effects the trap rods have.

To measure the axial frequencies, we first measure the programmed voltage (computer setting) to actual voltage into the trap. This is shown in Fig. 3.5

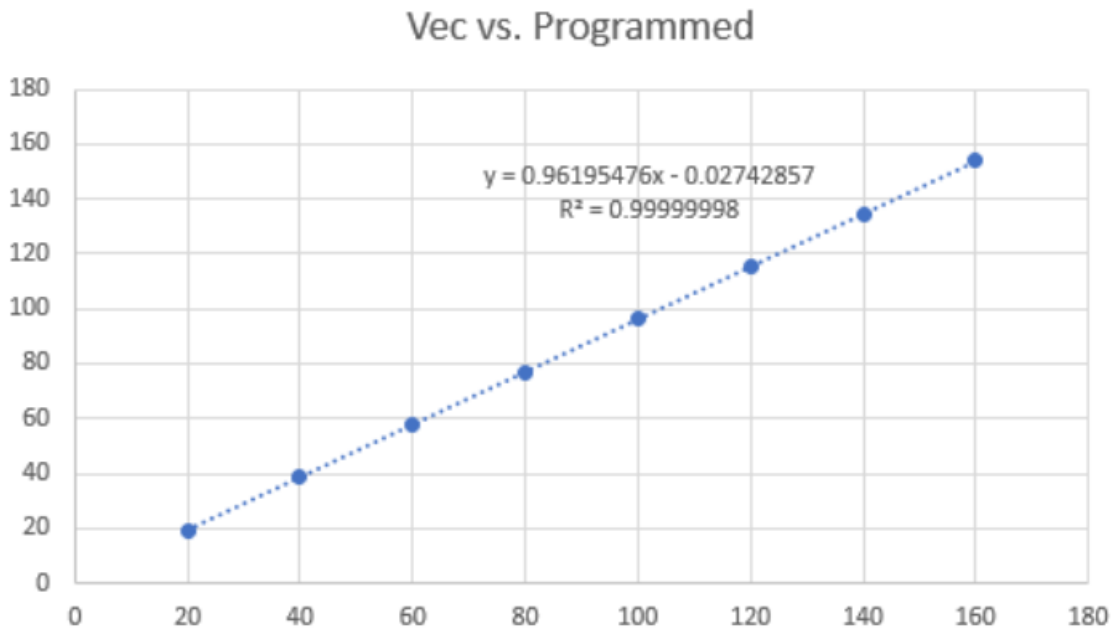

Figure 3.5: **DC Voltage to Endcaps:** It is important to understand the small difference between programmed and actual voltage to the endcaps when kHz to sub-kHz resolution is desired. The fit shows a very linear relationship.

Due to electrical connections, it is not easy to apply an RF voltage to the DC endcaps without also changing the DC value. As a result, the tickling method is not used to calibrate the axial frequencies, which is also a procedure to find κ from second expression of Eq. 2.16. The axial frequencies are instead measured by observing the sideband transitions that dress atomic transitions. This is explained in detail in Ch. 6. By plotting the axial frequency versus V_{ec} we can find κ. This is neccesary when using the motional sidebands for mass spectrometry [75]. The results for our trap are shown in Fig. 3.6.

This experiment was conducted for a single Ba^+ ion. The interesting result is that the radial voltage appears to influence the value of κ. We need to know κ to the level of 0.002, since a change of 0.004 results in a 20 kHz shift, which is 1 amu resolution for a mass 138 - 44 crystal at typical operating values. Note that in Eq. 2.16, the value of ω_z does not

depend on V_{RF} (though $\omega_{x,y}$ does depend on V_{ec}).

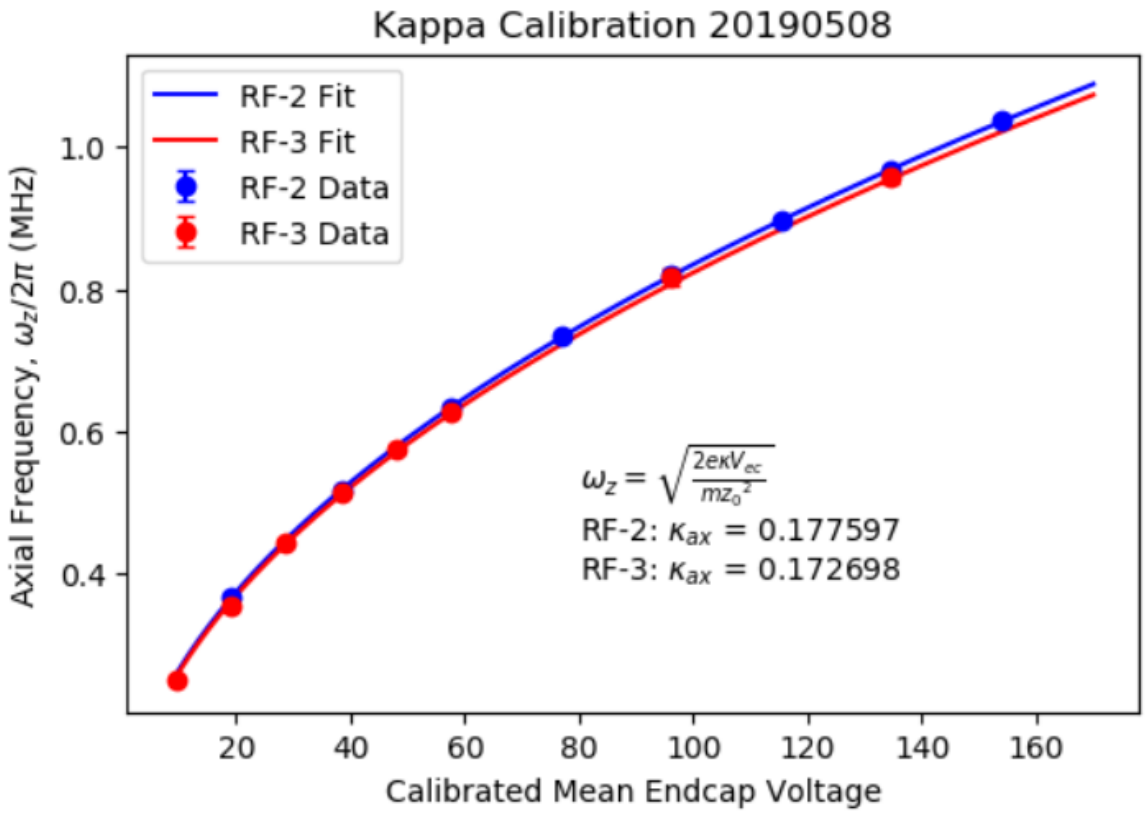

Figure 3.6: **Endcap Voltage Calibration:**

While this coupling is not ideal, it is likely explained by a bend in the endcaps. This can be seen in Fig. 3.7.

Unfortunately this issue has presented itself in several different aspects. The first is shown above. The second is that the values of κ appear to be different for the axial in-phase and out-of-phase modes. This is shown in Fig. 3.8.

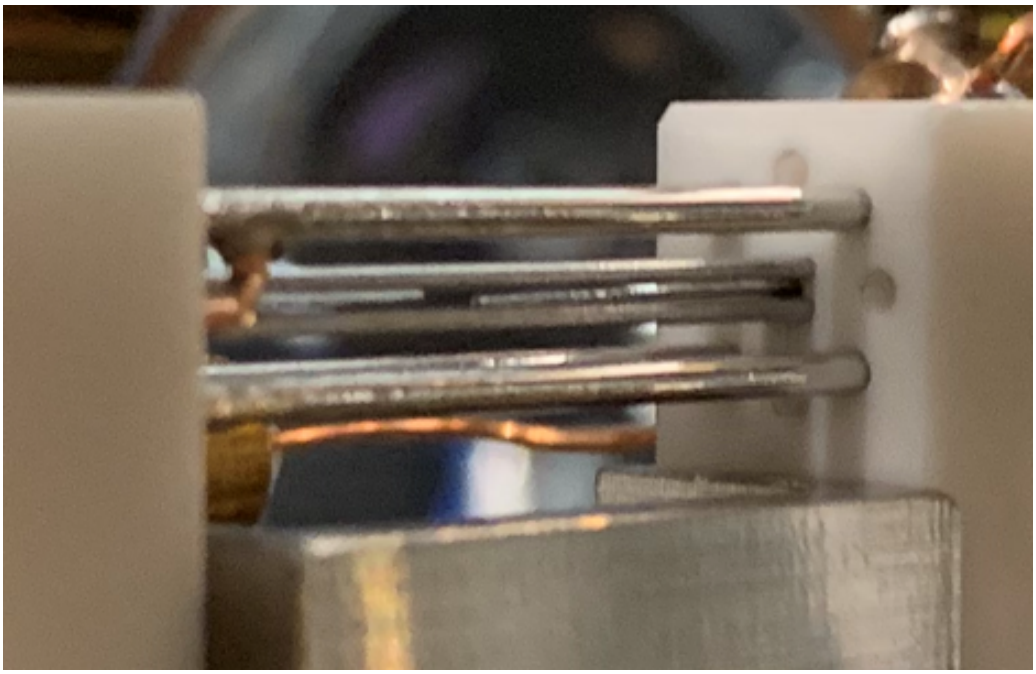

Figure 3.7: **Photo of the bent endcap (left one) in the single ion trap**

From mass spectrometry results, shown in Fig. 3.8, it is not possible for the uncertainty in the dark ion mass to explain the difference. Regardless of what Barium isotope was trapped, a different κ for either mode is needed to fit the resulting axial frequencies.

In Sec. 6.3.1, it is also found that the tilt of the endcap change is present in the wavevectors of light between the x- and y- directions. As a result, it appears that the radial directions are tilted with respect to a line connecting diagonal RF rods. Anharmonicities and cross-couplings in ion traps have been investigated in [89], [96]–[98]. In relation to the effects presented here, the authors find that frequency shifts can occur, though on the low level of 100 Hz. Phonon exchange between axial and radially modes can also occur but that happens only if one mode frequency is at a multiple value of another. These results indicate the need for daily monitoring and calibration, to understand experimental results when working in a two ion crystal and the dark ion of unknown mass.

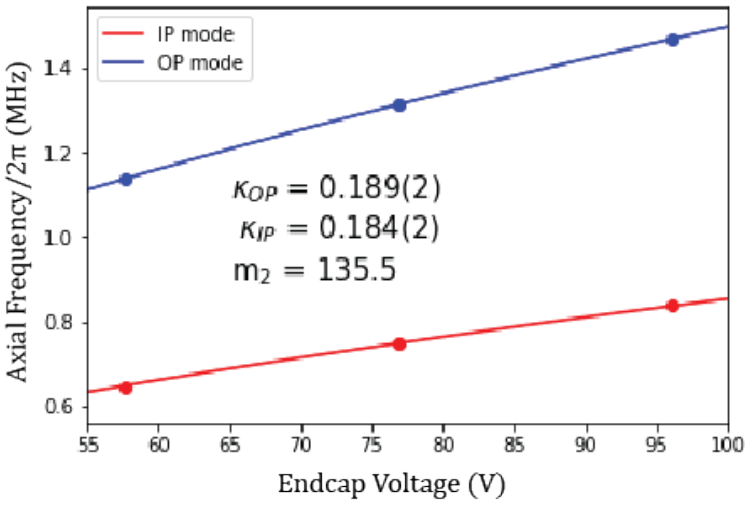

Figure 3.8: **Difference in κ between axial modes:** Here, with one Ba-138 and one Ba-135.5(5). The precision on κ is found by propagating the uncertainties in the endcap voltage and line centers.

3.1.3 Typical Trap Frequencies

With a complete calibration of the ion trap, we can estimate what the couplings and motional modes will be for the one or two ions trapped. For a single Ba^+ we find,

	RF: -4, V_{ec} = 10 V	RF: -3, Vec = 80 V	RF: -2, V_{ec} = 160 V
Mode	$\omega_i/(2\pi)$ (MHz)	$\omega_i/(2\pi)$ (MHz)	$\omega_i/(2\pi)$ (MHz)
$\hat{z}$	0.268	0.756	1.069
$\hat{x}$	0.568	1.035	1.556
$\hat{y}$	0.568	1.108	1.625

Table 3.2: **Single Ba^+ ion Motional Frequencies:** Ion loading is typically accomplished at 'low' trapping voltages of RF: -4, V_{ec} = 10 V. The RF setting here is a computer controlled voltage that adjusts the RF power out from the synthesizer. The 'tight' trap at RF: -2, V_{ec} = 160 V is the highest trapping voltage used with Ba^+ .

For a crystal of Ba^+ - SiO^+ we find:

Table 3.3: **Eigenvector Components and Frequencies for Ba^+ and SiO^+:** For typical trap parameters of operation, we show the normalized mode parameters b_1 and b_2 where $b_1^2 + b_2^2 = 1$. We refer to $\hat{z}_1$ as the in-phase (ip) and $\hat{z}_2$ as the out-of-phase (op) modes. Lamb-Dicke parameters for Raman addressing of Ba using the 493 laser and the X-B transition on 385 nm.

Mode	$\omega/2\pi$ (MHz)	b_1^2 (Ba^+)	b_2^2 (SiO^+)	$\eta^i_{Ba^+}$	$\eta^i_{SiO^+}$
$\hat{x}_1$	3.090	0.002	0.998	0.003	0.127
$\hat{x}_2$	0.813	0.998	0.002	0.116	0.010
$\hat{y}_1$	3.310	0.001	0.999	0.001	0.033
$\hat{y}_2$	0.899	0.999	0.001	0.030	0.002
$\hat{z}_1$	0.760	0.885	0.115	0.118	0.048
$\hat{z}_2$	1.720	0.115	0.885	0.028	0.089

3.2 Vacuum system

The experiment is housed in a 6.0" Spherical Octagon Vacuum Chamber [1]. The primary change from Ref. [74] is that the ante chamber containing a movable sample tray of Ba and LiAlH4 was removed. Additionally to load AlH^+, 213 nm light was needed for Resonant Multi-Photon Ionization (REMPI), and the best viewport to use was not transparent at that wavelength. While SiO also uses 216 nm, its 1:3 mass ratio with Ba^+ , it more efficient for sympathetic cooling and coherent operations. Since solid SiO samples can handle the $\sim$ 100 °C temperatures of baking, the antechamber was no longer needed. By removing the sample tray from Ref. [74], a new sample holder was needed. A small piece of aluminum was machined, degreased, sonicated and prebaked for installation.

[1] Kimball Physics MCF600-SphOct-F2C8

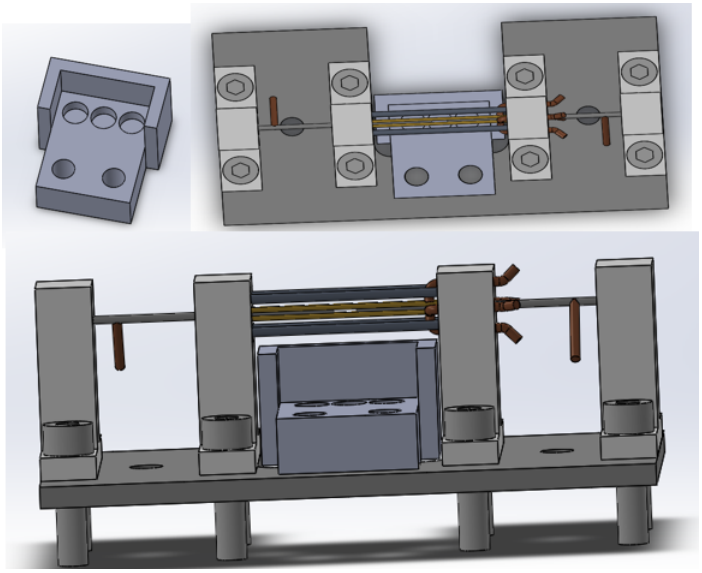

Figure 3.9: **New Sample Tray:** From left to right will sit a solid rock of Ba, SiO, Ca.

Fig. 3.9 shows the design and fit of the new sample tray into the trap design. The samples sit 12.7 mm below the trap z-axis, with the left and right samples 5.08 mm off-center. The holes are 3/16" ($\approx$ 4.763 mm) in diameter. Fig. 3.1 shows the sample tray installed. The samples installed are (from left to right): Barium (99.9% purity) [2], Silicon(II) Oxide (99.9% purity) [3], and Calcium (99% purity) [4].

The vacuum chamber was vented under the flow of nitrogen to limit water accumulation. Installation also included adding new viewports (see below). Since the samples were still exposed to air for roughly 20 minutes during installation and an oxide layer was created but quickly later ablated away. A scroll pump was used to pump the pressure down to 0.1 Torr, after which a leak checker (which has a rough pump as well) was installed and pumped the system down to 2×10^{-2} Torr. At this pressure the turbo pump was turned on. After the

[2]ESPI, 3N, Knc2109, Lot #Q17147, 3-6 mm pieces
[3]Alfa Aesar, Stock # 41711, Lot # J06W020
[4]Sigma Aldrich, 215147-5G Lot # STBH5121

turbo pump was on for 30 minutes the pressure read 2.1×10^{-6} Torr. A Helium leak checker is then used to test leaks.

A first round of baking lead to the only ion gauge installed breaking which was baked too high. As a result, it was necessary to bring the system back to atmosphere and replace the gauge. The same pumping procedure was used, and leaks were again checked for. After baking for a week at temperatures of 50 - 100 °C, the system achieved 4×10^{-10} Torr and quickly got to 1×10^{-10} Torr after closing the right angle value (with a 20.4 Nm torque), removing the turbo pump from the system.

Since the experiment does not generate large gas loads, only passive pumping systems are needed at UHV. A Valcon 20 L/S Starcell Plus[5] maintains the system at UHV. A Titanium Sublimation Pump[6] is also installed to pump 'getterable' gases such a hydrogen and nitrogen. The filaments were replaced to increase the longevity of the TSP during the aforementioned vacuum maintenance. The three filaments were degassed by running 50 A through each for 90 seconds. Pressure at UHV is constantly monitored using a Ganville-Phill 370 Stabil-ion guage and controller. The ion gauge too has to undergo a degas after being exposed to atmosphere.

[5]Model # 919-1145
[6]Gamma Vacuum # 360043

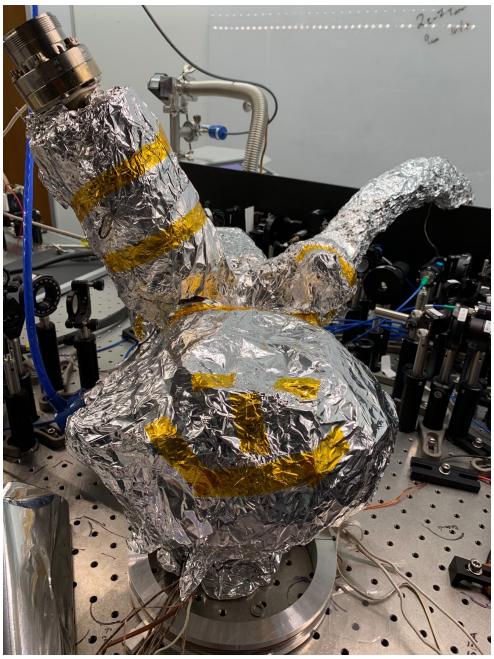

Figure 3.10: **Baking the Vacuum System:** Happy Halloween (taken 10/24/2019). The face here is the science chamber. The left horn the large TSP and the right is the baffle connecting the turbo and rough pump to the system.

The system currently has dropped further and operates at 2.7×10^{-11} Torr. Achieving this level of pressure is vital to making significant progress on the experiment. As noted in Refs. [48], [94] SiO^+ reacts with background H_2 to create $SiOH^+$ on the timescale of 5 - 10 minutes at 2×10^{-10} Torr. When this happens, a new SiO^+ molecule is needed to be loaded. At the pressure reached here, I find an operator has about 30 - 45 minutes to take data before SiO^+ reacts. That is enough time to take data for the experiments presented in this thesis.

Another concern in the rate of collisions with background gas [68]. Langevin rates give an upper limit for the timescale at which background neutral particles to penetrate the angular momentum barrier and undergo a spiraling-type collision into the ion. The electric field from the ion polarizes the neutral particle and creates an attractive like potential. At UHV, the

dominant background gas is H_2, which has a molar mass of 2.015 g/mol and an rms velocity at room temperature of 1933 m/s. This results in a Langevin rate constant of 1.64×10^{-9} cm^3/s^{-1} . At our pressure of 3.86×10^{-9} Pa, we find the number density of H_2 molecules is $\approx 9.3 \times 10^5$ $1/cm^3$, giving a Langevin rate of reaction or charge exchange $\gamma_{Langevin} \approx 0.0015$ s^{-1} or one every ~ 7 minutes.

Another concern is heating from elastic collisions, which we expect to occur at a rate faster than then Langevin rate because not every collision needs to penetrate the angular momentum barrier to heat the ion. We find $\gamma_{elastic} \simeq 0.013$ s^{-1} or about one event every 1.1 minutes. This process deposits enough energy to decrystallize (thermalize) the ion pair [73]. As a result the experimental code needs a scheme to recrystallize the ions. This is discussed in Sec. 3.5.8.

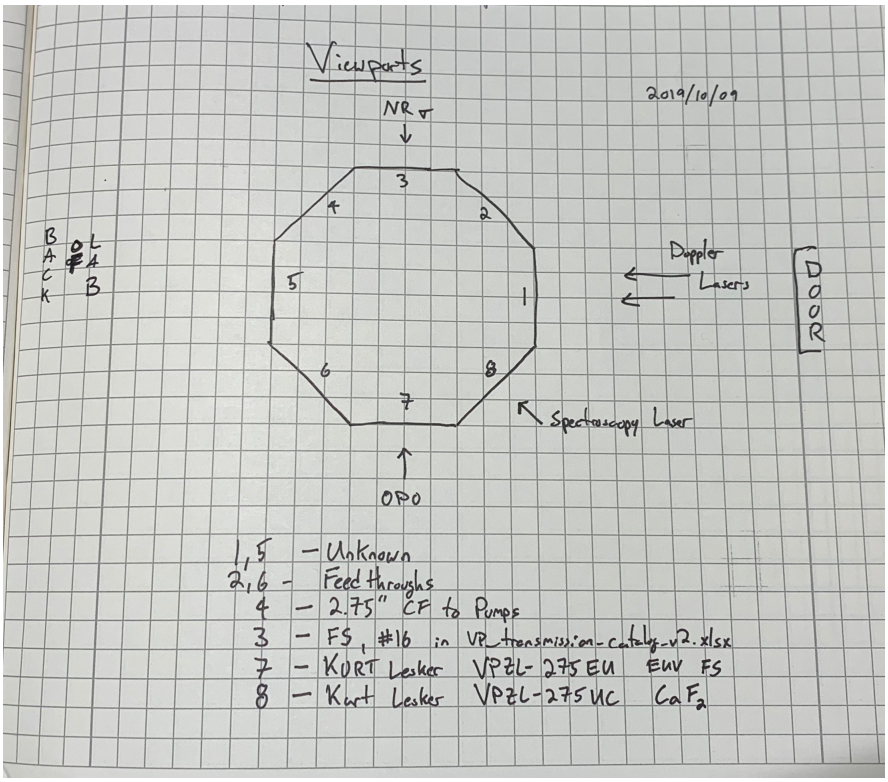

Figure 3.11: **Diagram of Viewports Installed**

The wavelengths involved in the experiment, ranging from 216 nm REMPI loading to 1762 nm addressing a quadrupole transition, the transmission of the vacuum viewports is an important consideration. Originally no usable window permitted 213 nm to attempt AlH^+ loading or 216 nm for loading SiO^+ . As a result, new viewports were purchased and a list of those installed are shown in Fig. 3.11.

3.3 Magnetic Field

One of the main limiting aspects in the original experiment was coherent operation lifetime due to magnetic field fluctuations [99]. This is due to noise on the current that drives Helmholtz coils to create the magnetic field (quantization field). Several remedies were attempted, and for a brief time a feed-forward technique was used [100]. Using a spectrum analyzer, 60 Hz and its higher harmonic's were measured on the ground line of the experiment. By applying 60 Hz tones at a certain amplitudes and phases, the noise could be reduced. Coherence times increased by a factor of 2 - 3. However, the noise characteristics varied day by day and with the RF amplitude, making this method unreliable.

Another method is to generate a well defined magnetic field is from permanent magnets [101]. In this way, no electrical noise is present in the magnetic field, and its magnitude only varies due to thermal fluctuations. If several magnets are installed into an holder of radius R, at a distance z from the center of the trap, then the magnetic field at the location of the ion is,

$$B = 2\frac{\mu_0}{4\pi} \cdot \frac{(3r \cdot \mu(r_i - r)) - \mu(r_i - r)^2}{|r_i - r|^5} \cdot n\frac{z}{r_i} \ , \tag{3.2}$$

where $r_i = \sqrt{z^2 + R^2}$, $r = 0$ (because we are on the z-axis), $\mu = B_r \ \mathrm{V}/\mu_0$ is the magnetic

moment for a single magnet of magnetic remanance B_r and volume V, and n is the number of magnetcs used. The factor of two in front is because two rings of magnets are used, each placed on opposite sides of the trap. The permanent magnets used are Samarium Cobalt 26[7] and each has a ≈1.07 T remanance. In each aluminum ring ten magnets are installed in aluminum rings with a diameter of 2.375" = 6.03 cm = 2R and placed roughly 10.5 cm from the trap center. The resulting field at the trap center, where the ions are, is ∼3.1 G.

A small gradient has been found over 5 μm, between the two lattie sites Ba^+ can occupy when a two ion crystal of Ba^+ and SiO^+ is loaded. A 20 kHz difference was found in the Zeeman splitting depending on whether Ba^+ is on the right or left of SiO^+ . This converts to a 6.77 mG difference between the two locations, or a gradient of 1.3 mG/μm (a 0.2% change). While not ideal, this gradient is mitigated by fixing the ion orientation.

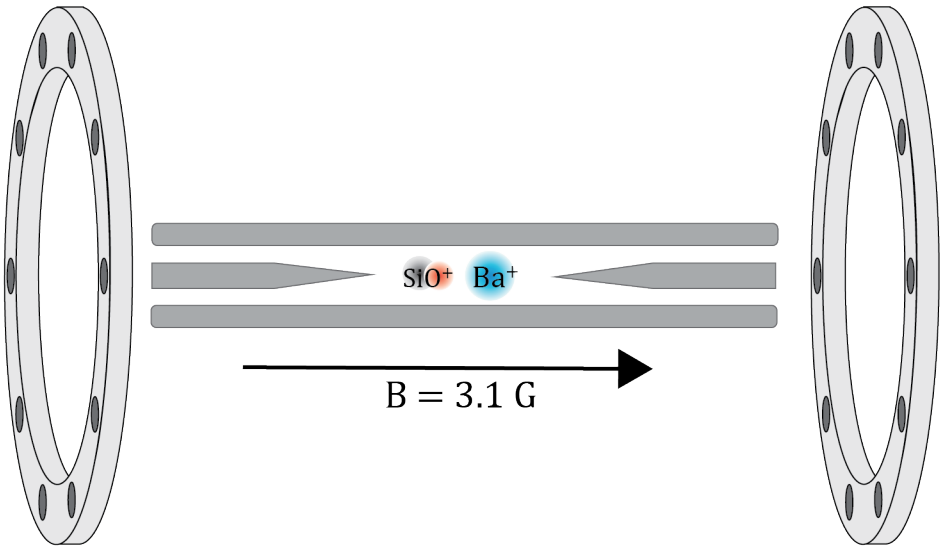

Figure 3.12: **Depiction of the Permanent Magnets in Their Mounting Rings**

[7]DuraMagnets, MGOe magnets of 0.251" Dia and 0.187" Depth

3.4 Ion Loading

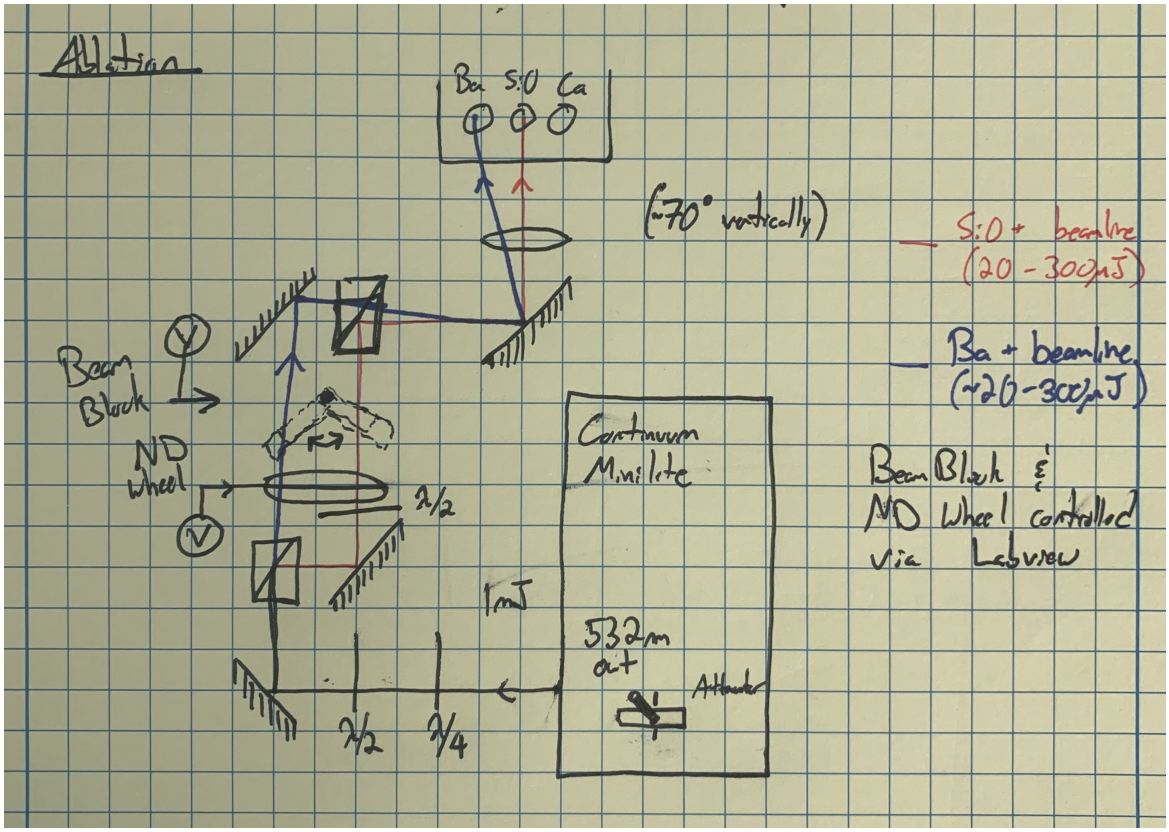

Figure 3.13: **Laser Ablation Optical System**

As seen in Fig. 3.1, solid samples of Barium and Silicon Oxide are placed underneath the ion trap. The method of loading ions into the trap involves ablation of the solid samples. In our experiment, a Continuum Minilite low-power pulsed Nd:YAG laser outputs 3-5 ns pulses at a 10 Hz repetition. Low laser energy (20 - 80 μJ) heats the solid targets and a neutral particle plume is created from sublimation. The short pulse duration results in a very low gas load compared to experiments that use ovens and vapor techniques. In this way, the deposition of the gas on the inside of the vacuum chamber is extremely slow and has not

been noticed over the experiments ten year lifetime. The ablation optical arrangement is shown in Fig. 3.13.

The output from the laser (tuned to 1 mJ energy) is polarized and then split into two beam paths using a polarizing beam splitter, one for loading the atom and other for loading the molecule. A neutral-density (ND) wheel controls the relative energy of each beam path. The ND filter is attached to a servo motor (TowerPro SG92R Micro Servo) that is computer controlled from an analog voltage, which adjusts the angle of the motor. Another servo motor blocks one beam path so that only one target is ablated at a time. The two beam paths are then slightly overlapped again using another polarizing beam splitter and focused onto a specific sample.

The ablation process is fairly controlled at low powers and the dominant products are neutral particles. While ablation can create ions directly, high powers are needed and this process is very inefficient. We generate ions by using a separate laser and photo-ionizing the neutral particles through a REMPI process, which takes place near the trap center. In this way, the ions are 'born' inside the trap and their kinetic energy $\mathcal{O}$(1-10) meV from ablation [94]) is much smaller than the trap depth of a few eV.

The photoionize, an Ekspla NTC342-10-SH/SFG OPO is used due to its wide wavelength tuning range and high energy output. Internally two photons undergo sum-frequency-generation to output a wide range (410 - 2600 nm) of wavelengths. The wavelength of the laser is controlled in software onthe experiment computer through its parallel cable port. The output of the laser is guided through right angle prisms, which have minimal loss in the 400 nm range. The two beam lines (for loading atoms and molecules) are separated using a polarizing beam splitter. Ba^+ is loaded on the 1+1 REMPI channel ($^1S \rightarrow^3 D \rightarrow$ IP) at 413.2 nm. The OPO can directly output this wavelength and its beam path is directed

into the trap and focused using an f = 150 mm lens. SiO^+ is loaded using a 1+1 REMPI channel from $|X, v = 1\rangle \rightarrow |A, v = 6\rangle \rightarrow IP$ at 216 nm [102]. While the Ekspla OPO used in the large SiO^+ trap [48], [94] has an SHG crystal installed, the one used here does not. As a result, the laser cannot reach 216 nm alone and an external SHG crystal is needed. One output port from the PBS (see Fig 3.14) is focused using an f = 300 mm lens onto a 428 nm SHG crystal. The seed and doubled light at 216 nm are separated by a Pellin-Broca prism with the seed light blocked from further propagation. The 216 nm is then directed into the trap on a separate viewport from the Ba^+ loading light using a movable lens. This makes it much easier to ensure alignment of either beamline into the trap and efficient ion production. Similar to the ablation set-up, a half waveplate is used to tune the energy of the beam paths and a beam block switches between blocking one of the two paths when loading. Both are computer controlled using the same kind of TowerPro servo motors.

Since the experiment aims to load only a single atom and a single molecule, low pulse numbers and energies are needed. For the ablation laser, one to a few Barium ions are loaded using 30 μJ. Since SiO is a harder material, it requires about 80 μJ to load a single molecule. Roughly 20 μJ of 216 nm light is used to photoionize SiO while 500 μJ is used to photoionize Ba. Typically only five pulses are needed to load a single SiO^+ ion. With the addition of the RF on/off pulses, a few Ba^+ can be loaded at a time as individual ions can be ejected at low trap voltages for $\sim$ 3-4 μs pulses. A master clock (set by a Labview .vi) establishes the timing for the firing of each loading laser. The OPO is fired 26 μs after the ablation laser to allow for neutral products to reach trap center after sublimation.

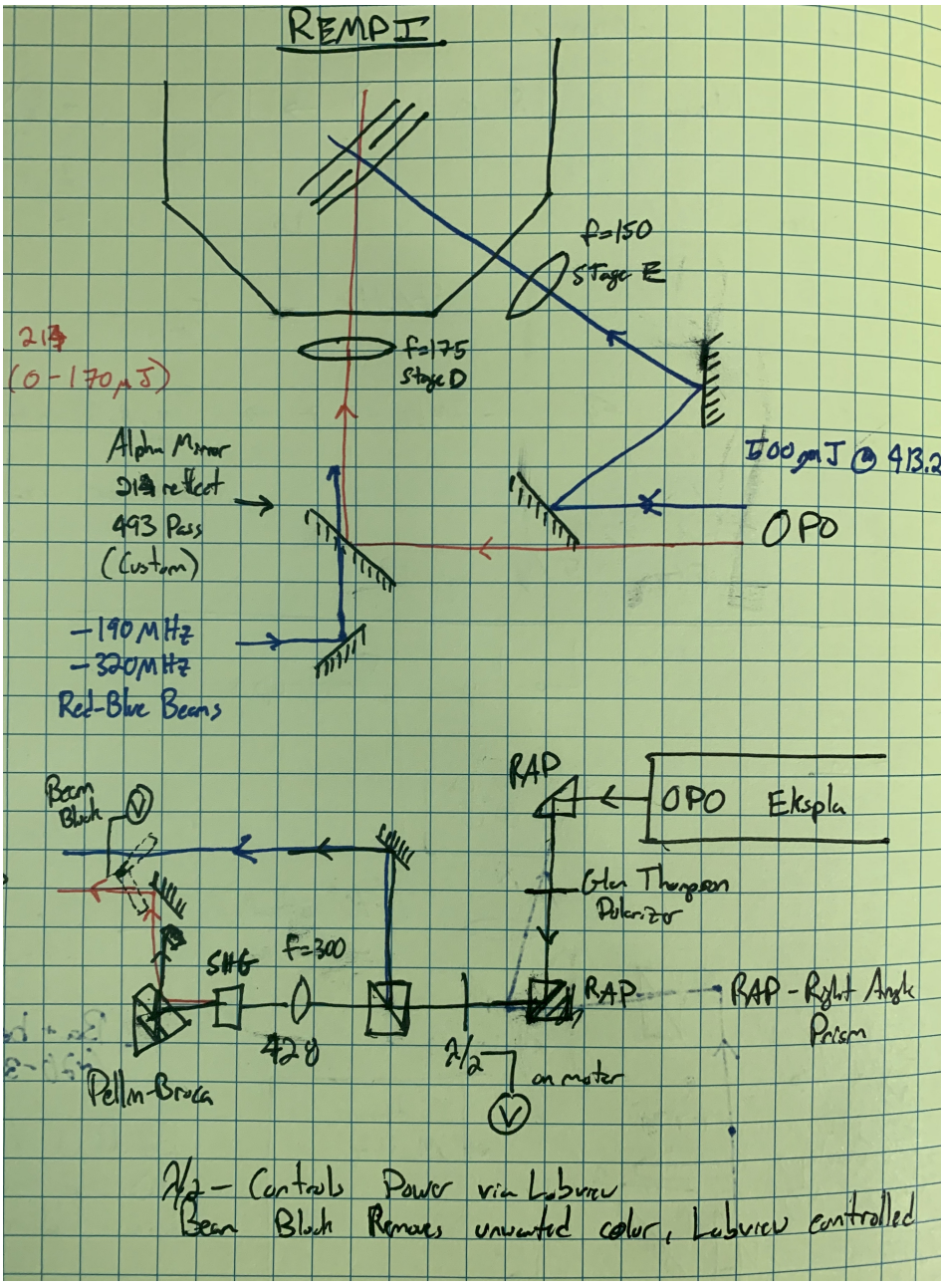

Figure 3.14: **Laser Photoionization Optical System**

Loading of a single SiO^+ takes place using the following process. Two 138-Ba^+ ions are loaded into the trap. At a trap setting of RF: -4.3 and V_{ec} = 20 V the two Ba^+ are tilted

at an angle with respect to the z-axis. This trap setting is close to Ba^+s instability and is chosen because the success of loading a molecule immediately thermalizes the ions and they go dark. When loading Ba^+ or SiO^+ , the RedBlue shutters (see Sec. 2.3.1 and Sec. 4.3.1.3) are open. It has been found that the combination of these red-detuned lasers illuminating the ions and cycling between tight and shallow traps (RF: -4.2, $V_{ec} = 10$ V to RF: -3, $V_{ec} = 60$ V) speeds up the crystallizing time. The trap is set to high voltages for a brief period of time to place a hot SiO^+ ion, at potentially large distances from trap center, closer to the Ba^+ ions, increasing the sympathetic cooling efficiency. In addition, the process of relaxing the trap then causes the crystal orientation to tilt and mix the motional modes, also increasing the cooling efficiency.

Once the three ions have crystallized (typically after 10 - 30 s) a single Ba^+ is ejected using a 3-5 μs RF on/off pulse at low trap settings. The loading of SiO^+ is confirmed with the greatest precision by measuring the axial motional frequencies (Sec. 4.3.2). It is possible to measure the radial frequencies using the tickling method, but this has not been found to be as conclusive as the sideband spectrum is and may also result in the ejection of either ion.

As explained in the next section, much of the experimental procedures were upgraded to be automated. It would be immensely beneficial to eventually automate the loading procedure as well.

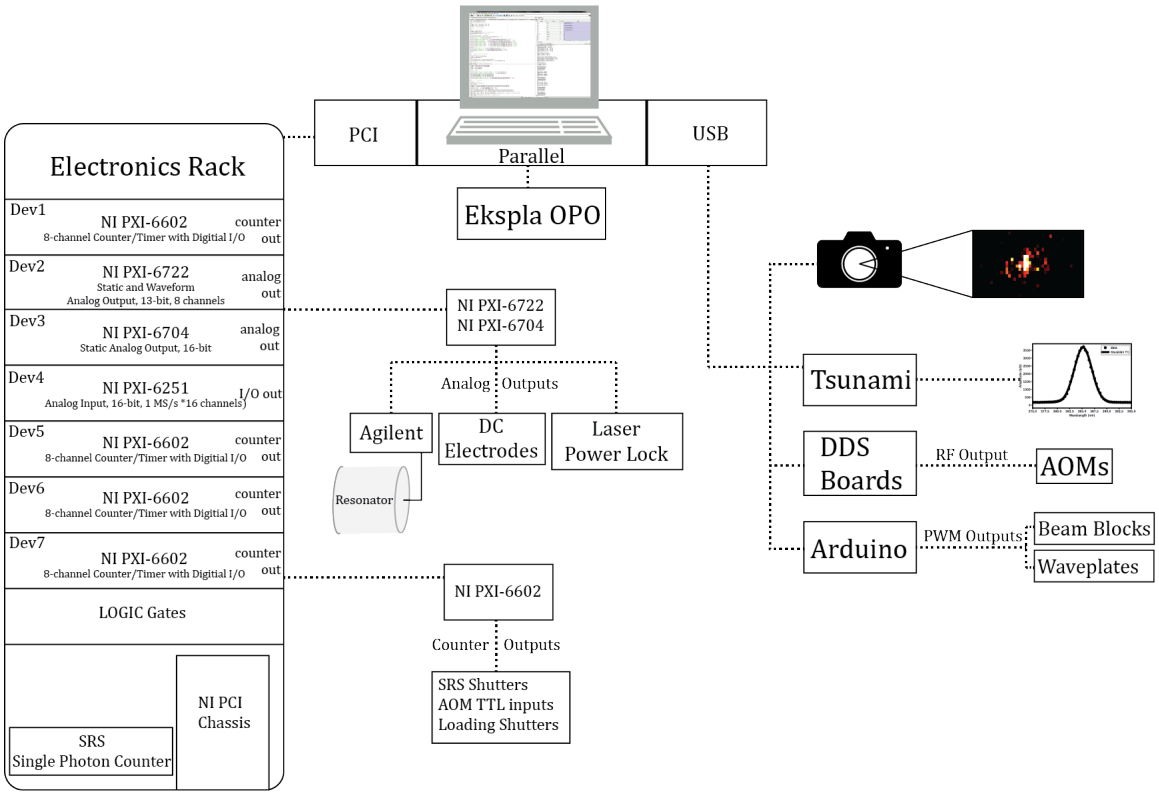

Figure 3.15: **Outline of Experimental Control:** A single PC controls the entire experiment. A majority of the signals are generated from NI PXI cards that output analog voltages, TTL signals and also counts fast TTL pulses generate from the PMT. A web of BNC cables syncs each card based on one master source.

3.5 Experimental Control

At the heart of many experiments is proper and tunable control over the apparatus. This experiment consists of ten lasers, the trap electronics, over twenty modulators and many other subsystems. Typically all of these are controlled under one umbrella computer system that can monitor and adjust settings. An outline of the experimental control, its components and extent are discussed here and shown in Fig. 3.15.

3.5.1 Alignment into Trap

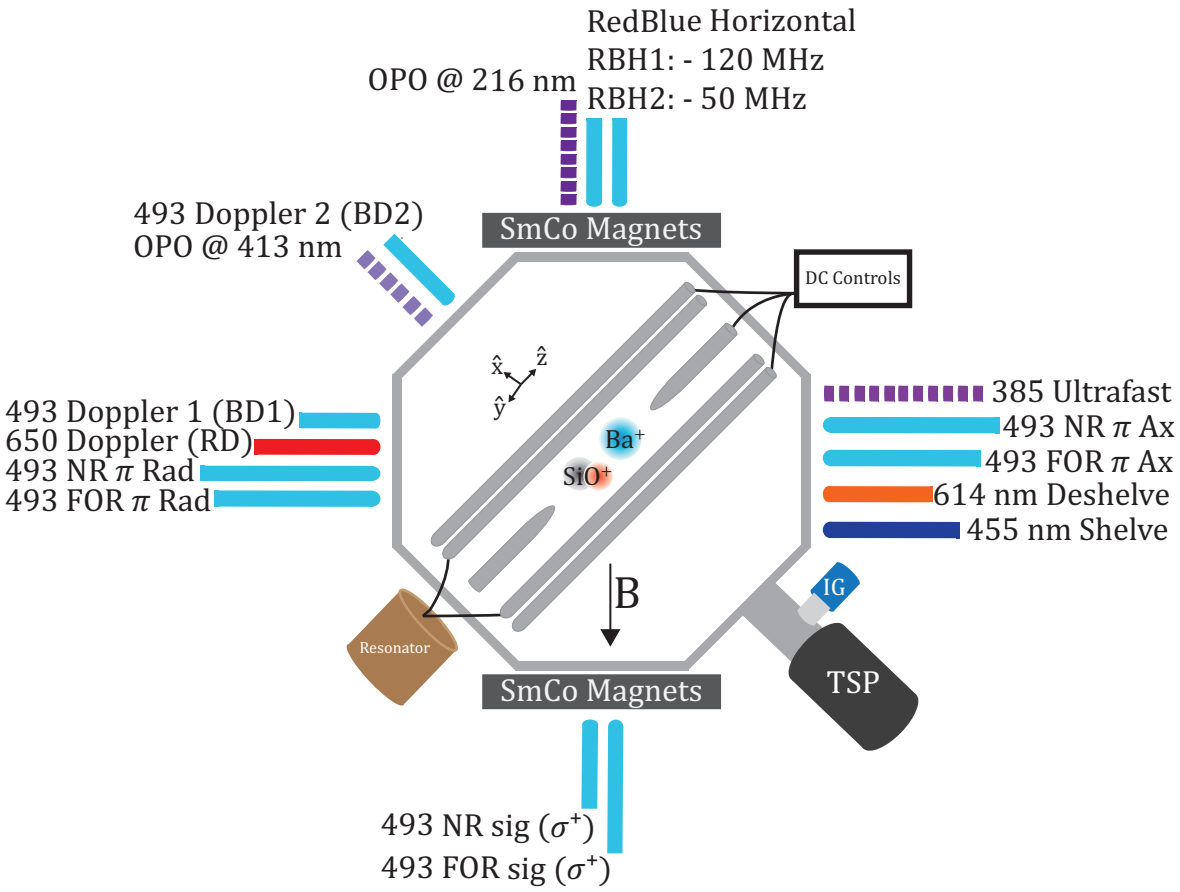

Figure 3.16: **Top Down Diagram of Trap and Lasers**

Since each laser is used to address a single ion it typically needs to be tightly focused and well aligned. To accomplish this, each viewport where lasers are incident (see Fig. 3.16) a (f = 125 or 150 mm) lens is placed in a stage with 3 axis adjustment. In this way, μm control of the lasers position is possible. Since the ion trap sets a well defined geometry, the center can be found. This is accomplished, typically first for the Doppler lasers. The procedure

involves looking at the transmission of the laser beam through the trap and out the other side. When the laser path is in between the two RF rods, then a scan of the micrometer should show the beam blocked at two positions which are separated by 0.444 mm. Finding the center means now the laser is at the same plane as the z-axis. Scanning horizontally, the laser should be blocked by either endcap, at a separation of $\sin(45)$ x 1.9 mm = 1.343 mm. Again, finding the center means the laser is now vertically and horizontally aligned. By loading Ba^+ ions, an increase (or decrease depending on the laser) in fluorescence can be used to adjust the focus of the laser.

Since the trap geometry is well defined, the numbers found by scanning the laser spatially have to make sense. The camera is aligned in a very similar fashion.

3.5.1.1 Laser Polarizations

It is useful to briefly mention the possible laser polarizations accessible given a magnetic field $\vec{B} = B\hat{z}$. The goal is to relate the known polarization of the laser to the ion's reference frame, whose coordinates are set by the magnetic field. We can relate the laser k-vector coordinates $\{\vec{x}', \vec{y}', \vec{z}'\}$ to the atomic coordinates $\{\vec{x}, \vec{y}, \vec{z}\}$ by,

$$\begin{aligned}
\vec{x'} &= \vec{x} \\
\vec{y'} &= cos(\theta)\vec{y} + sin(\theta)\vec{z} \\
\vec{z'} &= -cos(\theta)\vec{y} + sin(\theta)\vec{z}\ ,
\end{aligned}$$

where θ is the angle the k-vector makes with the z-axis. We have imposed the condition that x' // x. Then, recall that in the polarization basis we can relate,

$$\vec{x} = \frac{1}{\sqrt{2}}(\epsilon_+ + \epsilon_-)$$
$$\vec{x} = \frac{1}{\sqrt{2i}}(\epsilon_+ - \epsilon_-)$$
$$\vec{z} = \epsilon_0 \ .$$

Then we can relate $\epsilon' \rightarrow \epsilon$ and we find,

$$\epsilon'_0 = sin(\theta)\boldsymbol{\epsilon_0} - cos(\theta)\frac{1}{2i}(\epsilon_+ - \epsilon_-) \tag{3.3}$$
$$\epsilon'_+ = \frac{1}{2}\Big(1 + cos(\theta)\Big)\epsilon_+ + \frac{1}{2}\Big(1 - cos(\theta)\Big)\epsilon_- + \frac{isin(\theta)}{\sqrt{2}}\epsilon_0 \tag{3.4}$$
$$\epsilon'_- = \frac{1}{2}\Big(1 - cos(\theta)\Big)\epsilon_+ + \frac{1}{2}\Big(1 + cos(\theta)\Big)\epsilon_- - i\frac{isin(\theta)}{\sqrt{2}}\epsilon_0. \tag{3.5}$$

These relations indicate that a given laser polarization ϵ'_i will appear as a certain combination of polarization's to the atom. If $\theta = 0$ and the input polarization is right circular polarization, ϵ'_+ then the atom sees right handed circular polarization ϵ_+. If $\theta = 0$ and the laser is set to linear polarization, the atom sees a combination of circular polarizations, $\frac{1}{\sqrt{2}}(\epsilon_+$ - $\epsilon_-)$. For $\theta = 90°$ and linear polarization input the atom sees linear polarization, ϵ_0.

3.5.2 Python Scripts

Daily operation of the experiment consists of initialization using LabView programs. In this way, manual tuning of laser powers, shutters, trap electronics, loading laser pulses and setting are all controlled easily. To operate experimental sequences and data collection, Python scripts are used. A research assistant in our group, Matthew Dietrich, wrote the

C backend functons to interface our Python control code with the National Instruments NI cards whose analog and digital outputs set the experimental timings, laser powers and trap settings [92]. Many of these functions can be found, with LabView and DAQmx installed, by opening the 'NI-DAQmx C Reference Help' file. Thanks to him, all experimental code is run in Python, data is then easily plotted and analyzed in Python as well.

While these codes control the laser timings (by setting shutter on/off times) and powers, they were not able to adjust the frequency and powers of our Raman lasers. In Ref. [92] a homebuilt acousto-optical modulator (AOM) driver set-up makes use of Analog Devices AD9959 DDS boards to generate the Raman laser powers and frequencies. However, these settings were controlled by their software and needed to be set properly prior to running a specific experiment. A Python friendly package to control the DDS boards was found on the website[8] and implemented. This code was then modified to: obtain amplitude modulation, clock setting, and operation with multiple DDS boards. See Appendix E.1 for the code.

In addition, all the experimental settings are kept in LabView, but when data is collected, Python overwrites these values. As a result, each setting needs to either be reinitialized in Python or appropriately set in LabView prior to running a script. This presents a large window for errors to occur. To improve this, a dictionary file was written. All of the relevant experimental parameters are stored in that file. This also includes calculations for motional frequencies, Lamb-Dicke parameters and other values. Each experimental script then uploads these values to memory and sets the data collection timing and settings appropriately. At the end of each data run all of the relevant values are then saved. In this way, past settings can also be reused to aid in optimization or debugging. Additionally, a single change to the endcap voltage, for example, is accounted for and the proper frequency range to scan over is

[8] https://github.com/Schlabonski/evalcontrol

computed and automatically corrected for in the code. This significantly reduces the chance for error or inconsistencies between experiments. An example of this file, and how it is used can be found in Appendix E.2.

For experiments measuring the time variation of the proton-to-electron mass ratio, or clock measurements, time stamping is also important. In this way both linear and oscillatory behavior in time can be measured [103]. This is also possible now with the implementation of a dictionary file.

3.5.3 Photon Collection

Laser induced fluorescence of an ion on a dipole-allowed transition produces typically $\mathcal{O}(10^6$ - $10^8)$ photons per second. Even with collection efficiencies of ~ 0.001 this leads to $\approx 10^5$ photons per second detected from a bright Ba^+ ion at saturation. The collection efficiency is primarily limited by the solid angle photons are collect from, which is typically set by the geometry of the rods. If background counts are kept to the $\mathcal{O}(10^3)$ level this still is a signal-to-noise ratio of at least 100 which is sufficient for most experiments.

In this experiment, we project all measurements (whether it is internal states of the atom or molecule, or the external motional states) to the Ba^+ ion brightness through the electron shelving technique [71].

Improving on spherical aberration, the initial lens with aspheres that reduce that. The addition of an achromatic doublet (Thorlabs AC508-300-A) brings light into focus at the pinhole. We measure a 50 μm pinhole to be 80 pixels wide. At a 10μm pixel size this gives us a magnification of 16x or 0.645 μm per pixel in the object plane.

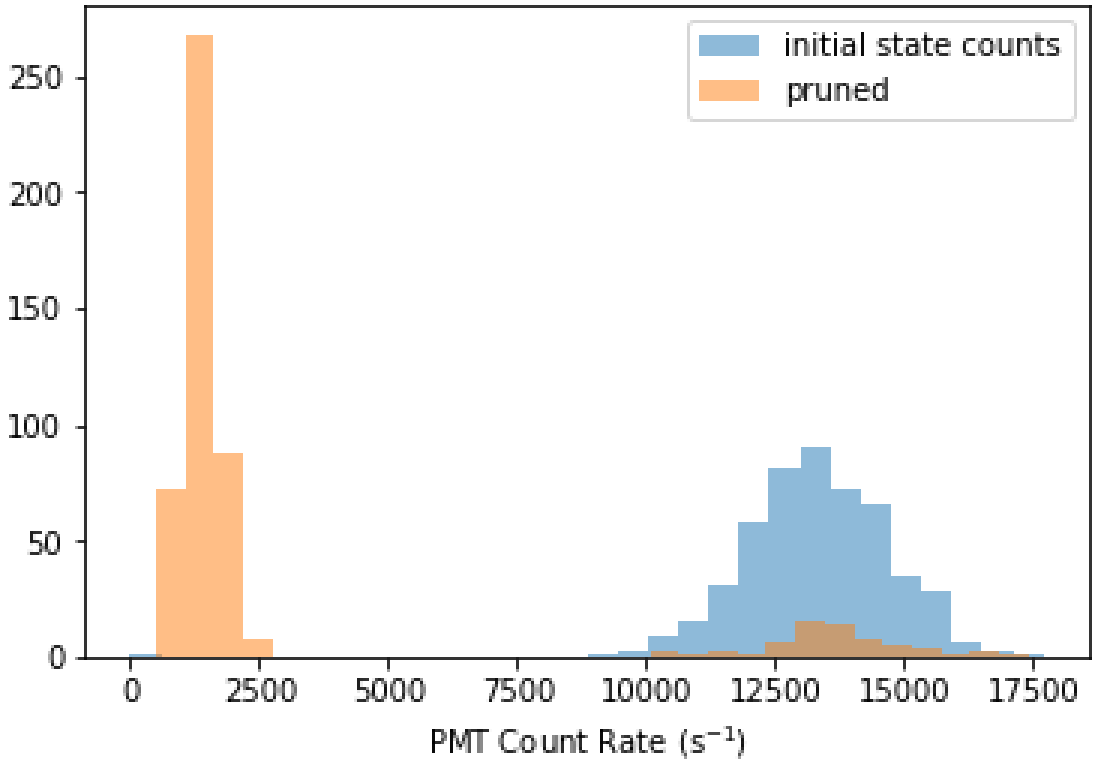

Figure 3.17: **Single Ba^+ Photon Counts:** The PMT is used to measure the total photons collected in a given time window (typically 10 ms). Typically two measurements of the Ba^+ fluorescence counts are made, one during the main experiment and another at the end of each repetition to determine the Ba^+ ion condition. If the repetition measures an 'initial state counts' that do not make sense, that data point is rejected and the resulting data set used is the 'pruned' one. The y-axis here is the number of times 'x' amount of photons were collected per second.

3.5.3.1 Imaging System

The entire imaging system for the single ion trap is shown in Fig. 3.18. This set-up involves improvements made to address spherical aberrations with the addition of asphere lens'. Upon installation we measured an 80 pixel wide 50 μm aperture. For a 10 μm pixel size this gives a magnification of M = 16. This is similar to the previous magnification. After installation we measured a 25% increase in photon counts without an increase in the

background rate.

The imaging system sits above the ion trap and collects light from single ions as they pass through the 6" viewport at the top of the vacuum chamber. The entire imaging system its mounted to a 3 axis micrometer mount that provides precise alignment to the trap center.

3.5.3.2 Camera

The presence of Ba^+ ions in the trap is detected - under the illumination of Doppler lasers (Sec. 4.3.1) - on an EMCCD (Andor Luca S) Camera. Since all measurements are made using fluorescence counts from Ba^+ and no low level light measurements are needed, we send 50% of the light emitted to the camera. The ions are at least ≈ 3 μm apart when crystallized, at a magnification of 16 and pixel size of 10 μm, two ions reside at least ≈ 5 pixels apart on the camera image which is easily resolvable.

Under continuous measurement and 0.1 s averaging, the light level detected on the camera is used to measure the alignment of most lasers. The camera signal is used purely for daily operation of loading and alignment of lasers. No experimental data is taken using the camera software. It does serve as a guide to the ion conditions while the experiment is running and extremely beneficial to have.

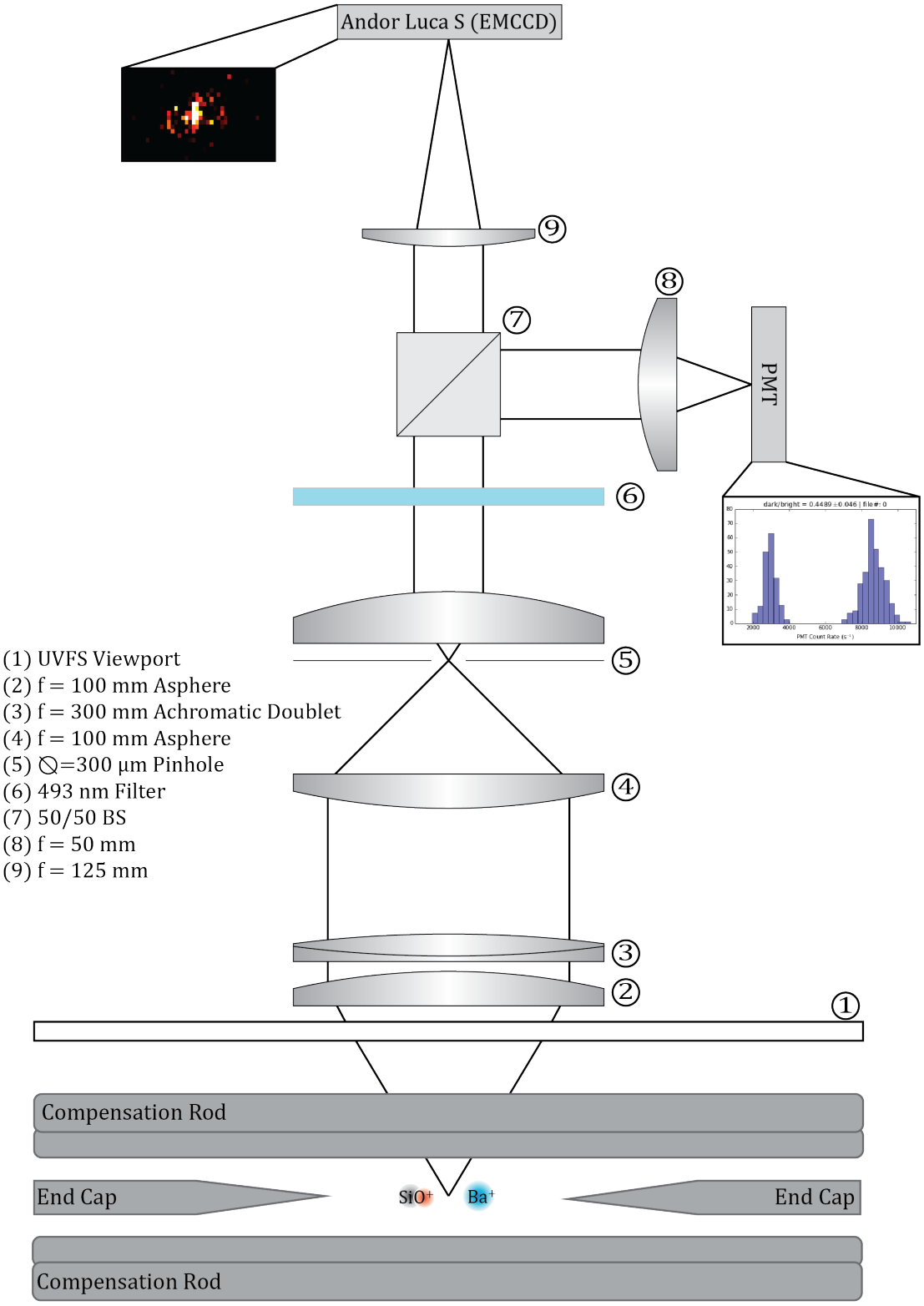

Figure 3.18: **Single Ion Imaging System:** Half of the photons collected go to an Andor camera and half are detected using a PMT.

3.5.3.3 PMT

Half of the photons scattered from Ba^+ are incident on a Hamamatsu H8259-01 PMT. The PMT signal is used in all data collection. The PMT outputs TTL pulses which are read into a digital counter channel in an NI-PXI 6602 card. Typical background counts are $\approx$ 2000 per second while a single Ba^+ provides $\approx$ 15,000 counts per second. Due to this large separation a discriminator is applied during analysis to determine whether the Ba^+ ion was 'bright' or 'dark'. An example photon histogram is shown below.

3.5.4 Laser Control

The wavelength of the laser is the first aspect needed to set daily, since the output power typically varies between laser modes. Most transitions we address in Ba^+ are dipole-allowed, the associated linewidths are typically $\mathcal{O}$(1-10) MHz. This allows us to lock to a HighFinesse Wavemeter WU-10 with 2 MHz accuracy is sufficient. The wavemeter is stabilized and referenced to a HeNe Laser (Newport N-STP-912).

A LabView code was written to take the wavemeter reading as an input and create an error signal. The same code generates digital outputs that switches the individual AOMs shown in Fig. 3.19 in sequence so that only one laser couples into the fiber and read on the wavemeter at a time. The beam paths and AOMs are set-up in such a way that the first order diffraction peak is aligned into the fiber. When no RF signal drives the AOM then the laser is not coupled into the fiber and not detected on the wavemeter. This set-up allows for a wide wavelength range of CW lasers to be locked to the wavemeter and takes only a 4 sq. ft imprint on an optical table.

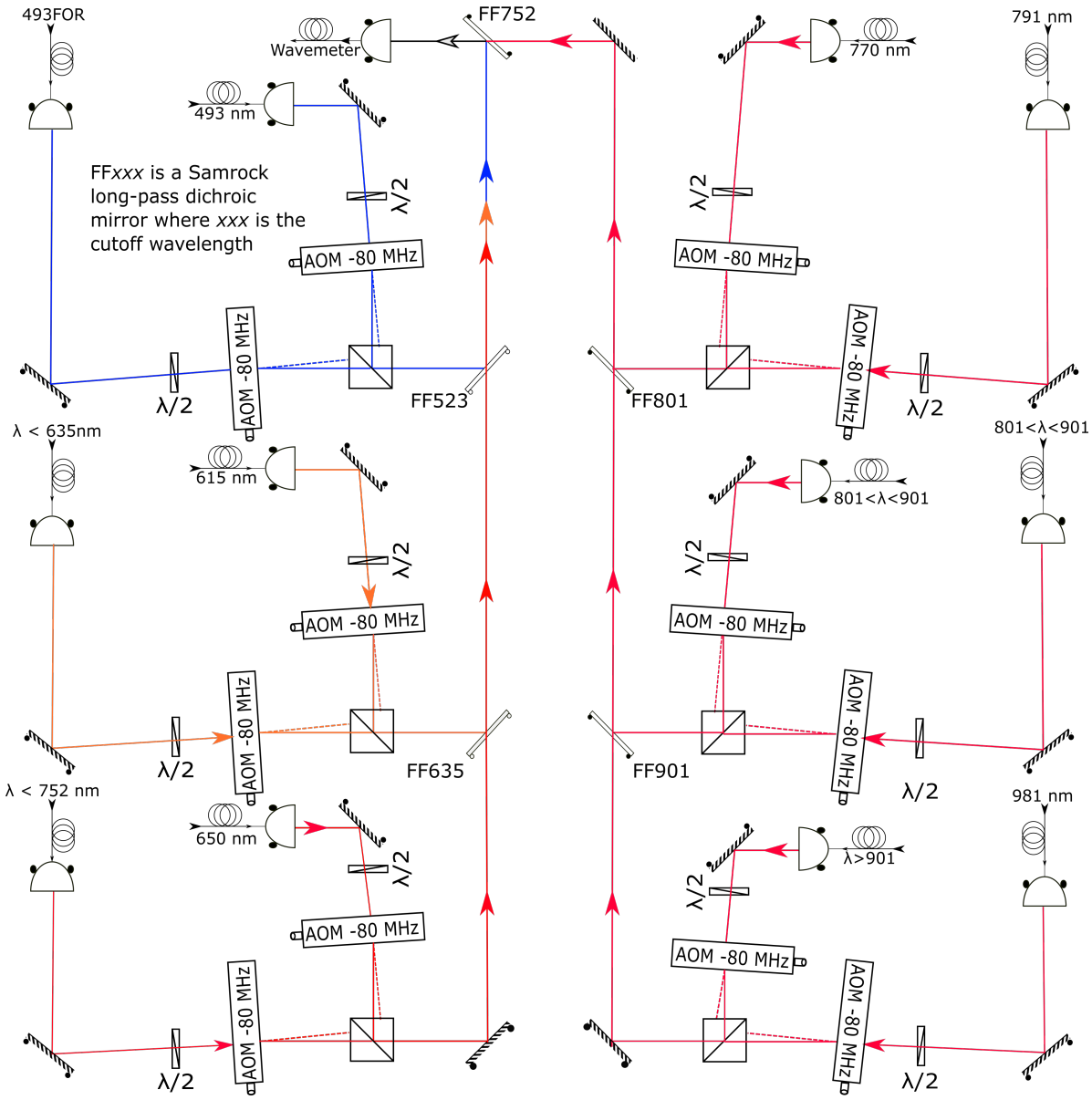

Figure 3.19: **Laser Switching Set-up:** Here, each of these AOMs are switched in sequence so that they are exposed to the wavemeter for 10 ms each.

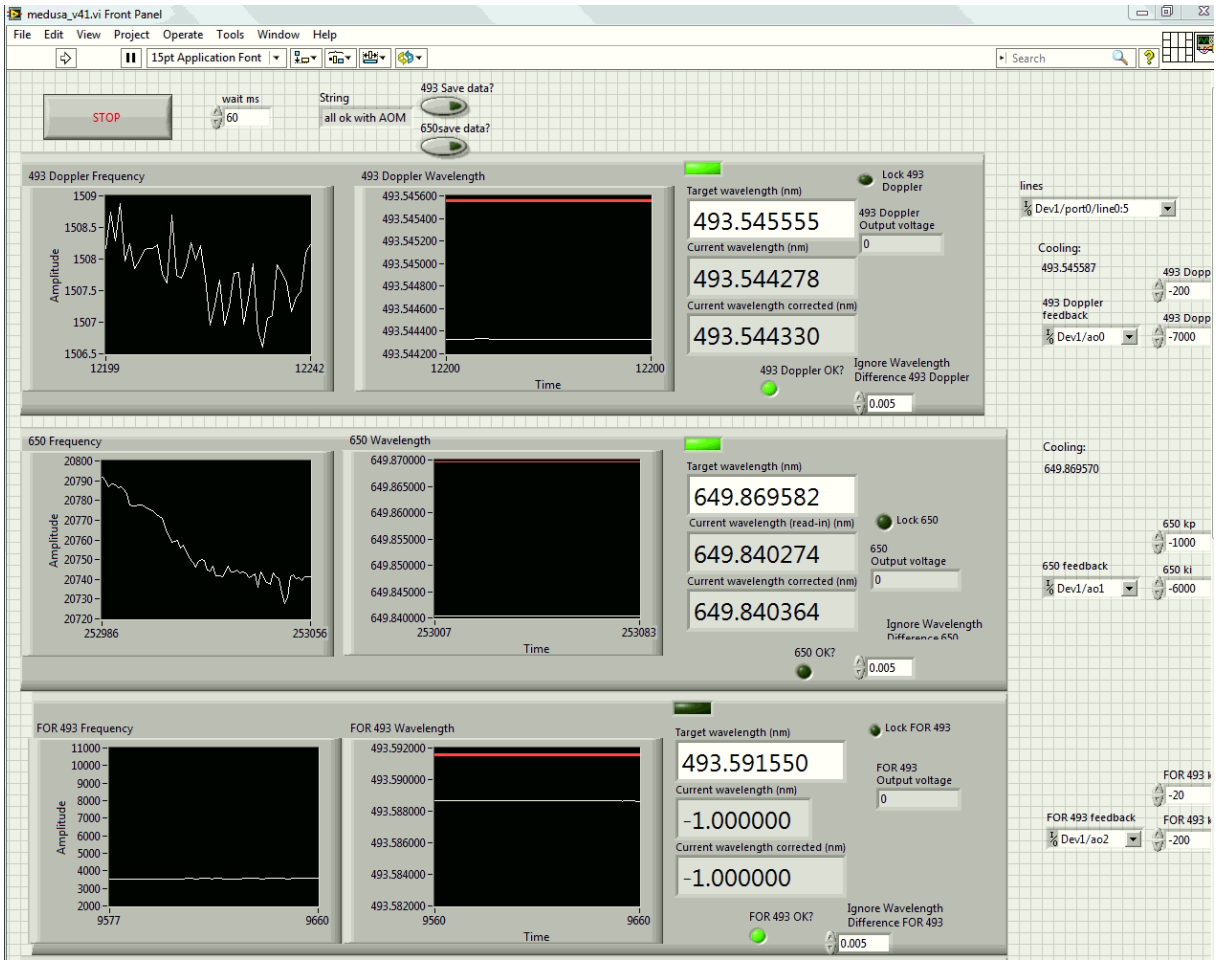

Figure 3.20: **ECDL Laser Locking Program:** Medusa uses her snake hairs to simultaneously lock up to six lasers at once. A error signal is generated and fed back to individual AOMs that frequency steer the laser to resonance.

As discussed in Ch. 4 the main wavelengths used are 455, 493, 614, and 649 nm. Two 493 nm and one 649 nm laser is power locked to the $\sim$ 1 nW level over several seconds [92]. A photodiode measures the laser power close to the trap, and an error signal is generated by setting a specific voltage as the set point. An analog voltage is fed back to the amplitude modulation port of the respective IntraAction AOM drivers in which the light is in a double-pass configuration. The double-pass (used for amplitude and frequency shifting) AOMs

are placed before the single-pass AOMs (used for laser shuttering) so that the power lock electronics do not need to take this dead time into account.

3.5.5 Laser Shutters

A typical experimental run involves a tailored pulse sequence of different lasers exposed to the ions for a specific time. To achieve this, a combination of single-pass AOMS and mechanical shutters[9] are used to deflect or block the laser beams respectively. When no RF signal is driving the AOMs, there is nearly zero laser light in first-order path (<nW) yet stray light is sufficiently strong to cause excitation on the dipole-allowed transitions in Ba^+ . The SRS shutters are used to mitigate this unwanted effects of leakage light from the AOMs which causes measurement errors and reduces signal strength.

The use of mechanical shutters comes at the cost of switching times and minimum 'on' times. It has been found that it takes roughly 1.5 ms for the SRS shutter to fully switch between open and closed positions. In addition, the shutter remains open for a minimum of 5 ms due to the control electronics. This extends experimental time and can potentially limit achievable frequency uncertainties [19]. This switching time is much longer than the $\sim$ 1 μs switching time scale of the AOM drivers.

3.5.6 AOM Drivers

Many of the beam lines use IntraAction Corp. AOMs and their associated AOM drivers, which have frequency and/or amplitude adjustment, to fine tune frequency and laser power in individual beam paths. Some also have the ability for fast switching using an TTL input pulse. As described in Ref. [92], the use of Raman processes involves the need for frequency

[9]Stanford Research System SR470 controller and SR474 shutter

Laser	AOM (rise/fall)		SRS (rise/fall)	
	time (μs)	delay (μs)	time (ms)	delay (ms)
493	2	2	1/1	2.5/3
649	1	3	0.6/0.65	2.75/2
NR σ	0.3	1	1.5/2.0	3/3.5
FOR σ	0.2/0.2	1/1	0.6/0.6	2.5/2.5
NR π	0.14/0.14	1.4/1.2	0.3/0.3	2.6/2.4
FOR π	0.2/0.12	1.55/1.3	0.4/0.35	2.5/2.5
455	0.6/0.5	1.3/1.15	0.65/0.55	2.2/2.6
614	0.5/0.5	0.6/1	0.2/0.26	2.65/2.7

Table 3.4: **Characteristic switching and on/off times:** For both AOMs and SRS shutters for the primary Ba^+ lasers. The delays are measured from the TTL trigger sent to the SRS SR470 control electronics.

adjustment of two lasers, whose frequency source needs to be the same or phase-locked. This prompted the need for homebuilt AOM drivers to be made. As described in Ch. 6, two iterations of CW sideband cooling were used, and each require their own RF source, based on specific needs. The design of each will be described here, and their use and results are described in Sec. 6.2.1 and Sec. 6.3.

In general, every single CW laser in the experiment (493 and 650 Doppler, Near-Resonant (NR) and Far-off-Resonant (FOR), 455 shelve and 614 deshelve) utilizes a two AOM set-up. First, the lasers go through a double-pass AOM which provides $\pm$ 20 MHz bandwidth of frequency tuning range, without changing the beam pointing. Secondly, the lasers pass through a single-pass AOM that provides fast switching.

3.5.6.1 RF IQ Mixing

Designed by Vincent Carrat, one method to cool two motional modes (both axial modes for a two ion crystal) is to drive a single AOM with two RF frequencies. This will impart two tones onto a single laser used for sideband cooling (see Ch. 6). Since the two motional

frequencies are typically separated by $\sim$ 0.5 - 1 MHz, a lower frequency RF signal can be mixed onto the main RF frequency ($\approx$ 80 MHz) that drives an AOM. The issue with conventional mixing is that two sidebands (ω_s) are produced around the carrier (ω_c) and the total spectrum has components at: $\omega_c - \omega_s, \omega_c, \omega_c + \omega_s$. Since the level splittings in a harmonic oscillator are evenly spaced, then tuning ω_c to the axial in-phase red sideband and $\omega_c + \omega_s$ to the axial out-of-phase red sideband (see Sec. 2.3 and Appendix A) would mean that the frequency component at $\omega_c - \omega_s$ would lie near the carrier or even on the blue sideband part of the spectrum, which limits the ability to motionally cool the ion.

To mitigate this, an IQ mixer can be employed to produce a single sideband. This is a common technique in signal/image processing where power saving and low bandwidth are required. An IQ-mixer takes both an in-phase ($\cos \omega_m t$) and corresponding quadrature ($\sin \omega_m t$) signal from a given source and mixes each, independently with the carrier (typically $\omega_{car} = 80$ MHz AOM drive frequency in this case). The appropriate placement of 90° phase shifters (inside the IQ mixer) produces a resulting signal that contains the carrier and a single sideband, $s(t) = \cos \omega_{car} t + \cos(\omega_{car} \pm \omega_m)t$. Higher harmonics can be rejected using a low-pass filter tuned accordingly.

In our set-up a voltage controlled oscillator (VCO)[10] drives two single-ended to differential conversion chips[11] which create the the I,Q and corresponding balanced components (180° out of phase components). These balanced rails are need because the IQ mixer (Linear Technologies LTC5598) used utilizes double-balanced mixers, which reduce conversion gain and higher harmonics in the mixing process.

[10] Analog Devices LTC6902
[11] Analog Devices LT1567

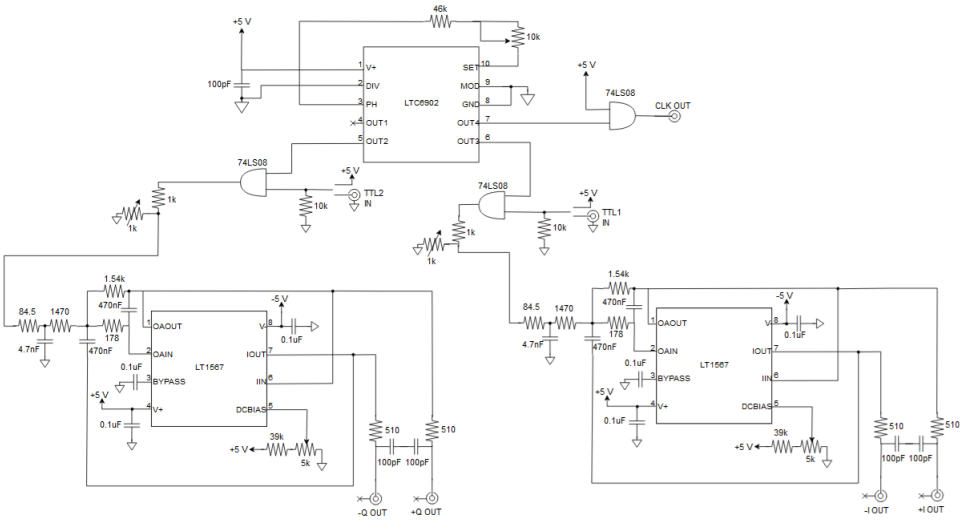

Figure 3.21: **Balanced I and Q frequency generations** The relative amplitudes of each can enhance certain nonlinearities in the mixing process and change the post-mixed spectrum.

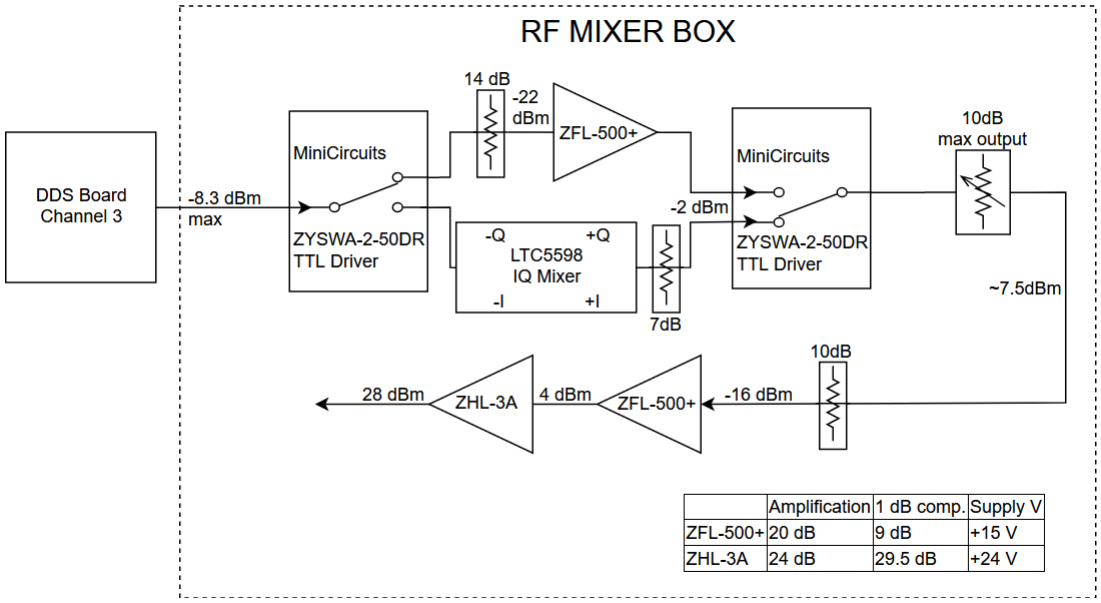

	Amplification	1 dB comp.	Supply V
ZFL-500+	20 dB	9 dB	+15 V
ZHL-3A	24 dB	29.5 dB	+24 V

Figure 3.22: **Raman frequency tuner:** The circuit has the ability to produce one or two sidebands on one of the two Raman beamlines. The top path sends only one frequency to an AOM while the bottom path sends multiple tones. A single digital signal changes between either option. The attenuators and amplifiers are set to balance the power in either line.

From a fit of the measured VCO frequency as a function of input voltage, we determine that the voltage needed to produce a desired frequency (in MHz) is,

$$V_{VCO}(f) = 0.618 * f + 3.8905. \tag{3.6}$$

After construction the RF spectrum from the output of the circuit shown in Fig. 3.22 was measured and is shown in Fig. 3.23a and Fig. 3.23b. We see a 20 dB difference between the '+' or '-' order sidebands. The large C-3*S component when $f_{VCO} = 400$ kHz is due to the low-pass cut off (shown at the input to the LT1567 in Fig. 3.21) set around 1 MHz. I later added a fourth-order low-pass filter to further reduce the higher harmonic components by 20 dB more. After construction and connection to an AOM a beat-note spectrum was observed from the two Raman beams incident on an photodiode, one driven by the IQ source and one without, both set to the same carrier frequency. The resulting signal was measured on a spectrum analyzer. The results are shown in Fig. 3.24.

An AOM itself acts as a mixer with the spectral components diverging in beam path from one another. One a single pass, if the AOM is driven at ω_c and we take the '+' order, then we can observe light now at $\omega_l + \omega_c$. In a double-pass, that beam is retroreflected and again the '+' order is directed further down the optical path with the laser at frequency $\omega_l + 2 * \omega_c$.

When using the IQ AOM driver tuned to single sideband generation, two tones are driving the piezo in the AOM, one at ω and one at $\omega_c + \omega_s$. The single pass produces light at $\omega_l + \omega_c$ and $\omega_l + \omega_c + \omega_s$. The difference between the two set-ups is on the double-pass since we cannot control which tone mixes with which part of the spectrum. As a result we get weight spectrum of: $1/4(\omega_l + 2*\omega_c)$, $1/4(\omega_l + 2*(\omega_c + \omega_s)$, $1/2(\omega_l + 2*\omega_c + \omega_s)$. Since the $\omega_l + 2\omega_c + \omega_s$ is twice as strong as the other components we will use that to component to cool by setting

$\omega_s = 2\pi f_{VCO}$.

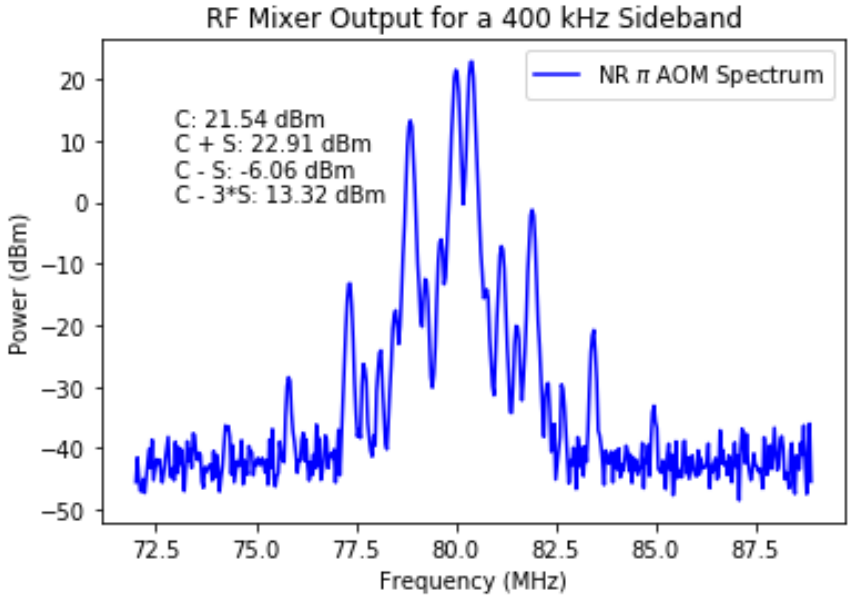

(a) **IQ AOM output for f_{VCO} = 400 kHz**

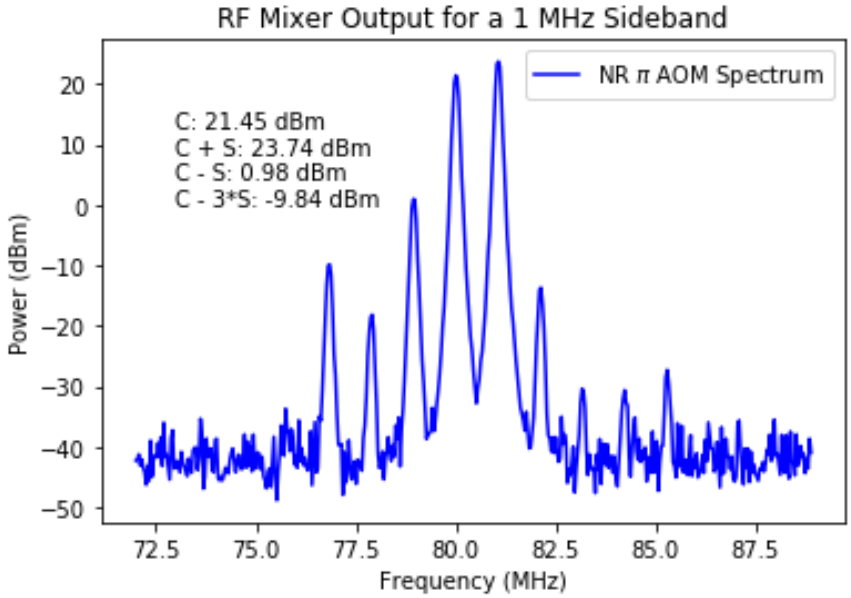

(b) **IQ AOM output for f_{VCO} = 1.0 MHz**

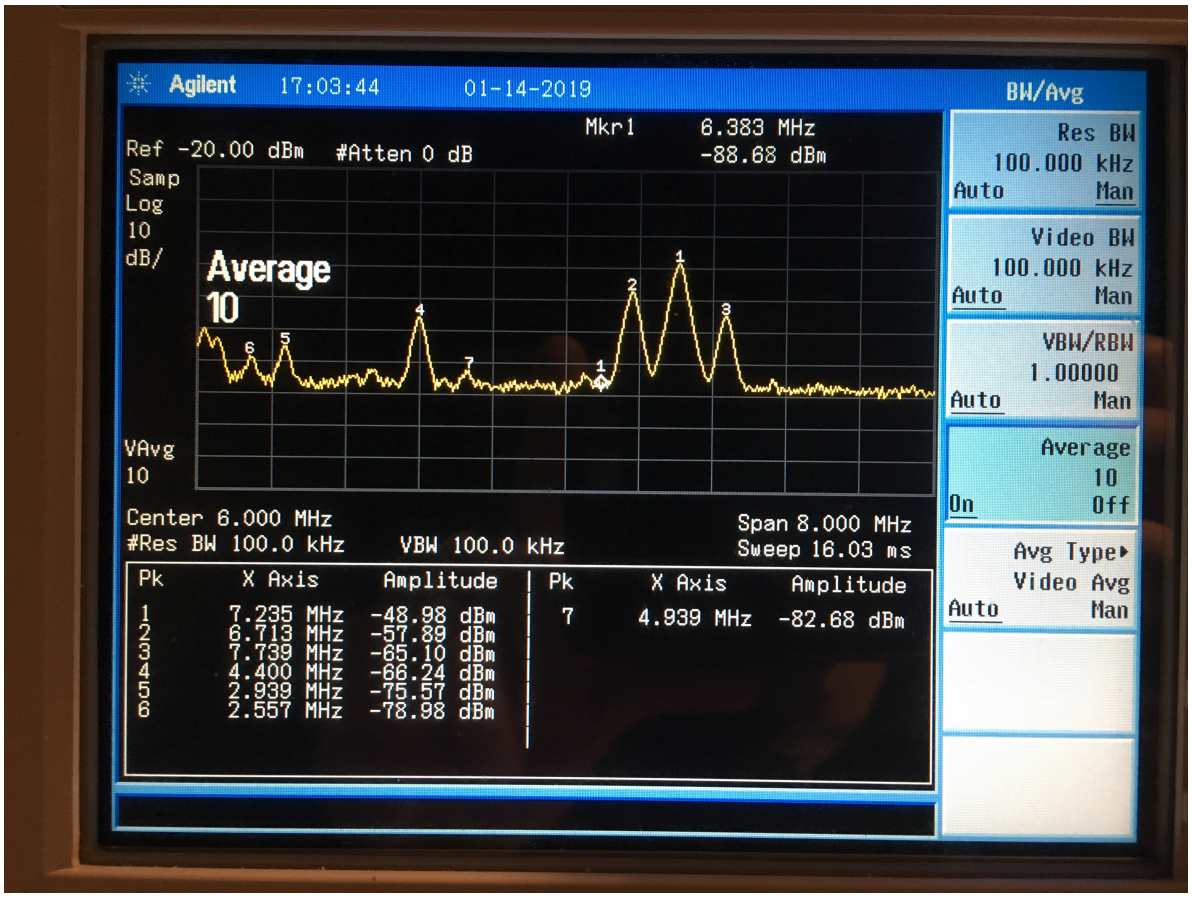

Figure 3.24: **Beat Signal of Two Raman Lasers:** A picture of the spectrum analyzer showing the correct beat signals inidcated in the picture as peak 1 and 2. The two are separated by ~ 500 kHz which is the difference in axial modes for two Ba^+ ions, $\omega_{VCO} = \omega_{z,op} - \omega_{z,ip}$. Peaks at lower frequencies are artifacts the from measurement and any frequency component at higher frequencies will address higher-order red sidebands and are beneficial.

The sideband cooling results when using this AOM driver are shown in Sec. 6.2.1. Note this set-up only involves the change to one AOM driver (NR π) and the remaining home-built drivers used are from the design outlined in [92].

3.5.6.2 EIT Cooling

To implement electromagnetically-induced transparency raman sideband cooling (EIT RSC, [104]) the original home-built drivers from [92] needed to be modified. The original design has both RF generation (from DDS boards) and amplifiers (to achieve 1 W of RF power) in a single box. The following design keeps the amplifiers in place and involves the construction of a separate box for RF generation, which is capable of driving more channels. The set-up also lays the framework to achieve pulsed raman sideband cooling. The only missing piece is a TTL trigger source that would be able to implement a more complicated pulse sequence.

As discussed in Appendix A, two beams are used in a Raman transition and their Δk vector defines which motional sidebands are addressed. From the trap geometry and laser paths, a single Raman laser (the NR-σ) can address all 6 motional modes in conjunction with two counter-propagating π polarized beams (see Fig. 3.16). In this way, at most six channels (for two ions there are six motional modes) is needed to drive a single AOM, with proper isolation so that only one RF signal drives the AOM at a time. Since two radial modes have extremely low eigenvector components in Ba^+ for a Ba^+ - SiO^+ crystal (see Table 3.3) we forgo addressing them for the time being and aim to cool 4/6 motional modes: both axial (z_1 and z_2), one in the x-direction (x_2) and the other in the y-direction (y_2). A potential method to cool these weakly coupled modes (x_1 and y_1) using a pulse sequence is outlined in Ref. [83].

The following system was designed and constructed to achieve this. A schematic of the electrical system is shown in Fig. 3.25.

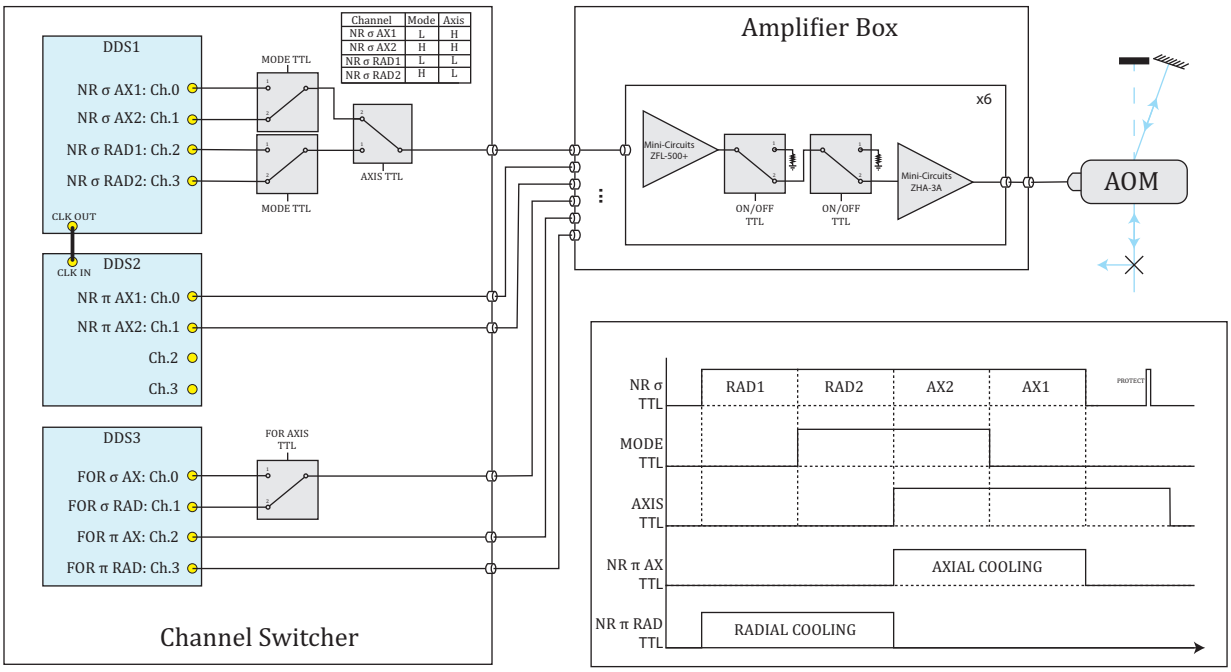

Figure 3.25: **Home-built AOM Drivers for EIT Sideband Cooling:** Modified Version of what was previously used [92]. Two extra DDS boards were added and a slightly more complex switching system was built. Each AOM has two TTL switches to provide $\sim$ 40 dB of isolate when in an off state.

Each DDS board is initialized using the code found in Appendix E.1. The truth table that establishes the order of which motional mode is cooled can be adjusted by simply changing the order and initial state of the 'mode' and 'axis' TTL pulses. This system requires only two TTL pulses to determine the cooling sequence and timings.

3.5.7 Experimental Sequence

An example for the full experimental sequence is shown in Fig. 3.26. Each experiment starts with a ion crystal that is Doppler cooled. If desired, this window can also be used for rotational state preparation of a molecule as well. Then, the ion crystal is cooled to the ground motional state (for 4/6 modes) which achieves $\sim \mu$K equivalent temperatures. Once

cooled, the internal state of the logic ion is optically pumped into a specific qubit state.

At this point, the ion crystal is motionally cold and the internal states are prepared into a specific quantum state. Most of the work presented in this thesis shows how to accomplish this. State preparation of the internal and external modes is the required starting point for spectroscopy using quantum logic [105]. Spectroscopy and state readout can now be attempted (spectroscopy and PRR as shown in Fig. 3.26). The motional state is then mapped to a specific qubit state of the logic ion. Here, this is accomplished using a Far-Off Resonant (FOR) π pulse. The subsequent protect, shelve and detection step measure population in a specific logic ion qubit state.

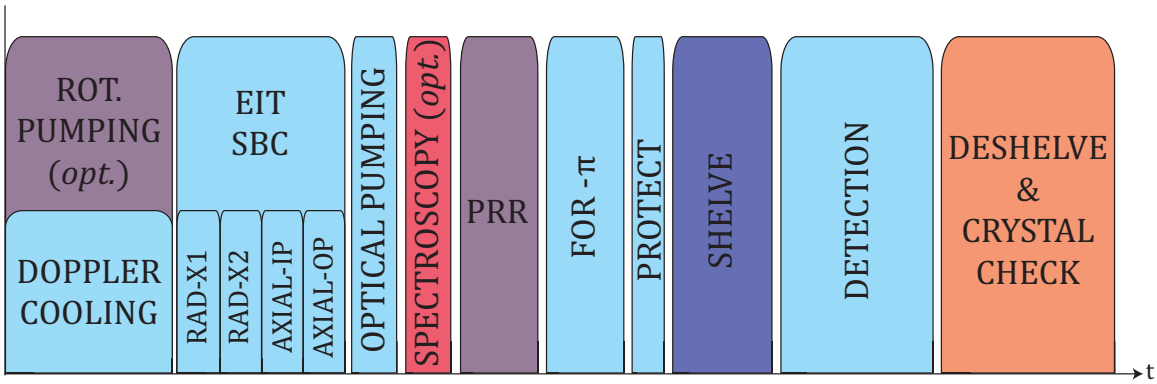

Figure 3.26: **Compiled Experimental Timing Sequence:** pulse widths not to scale

At the end of every experimental repetition the logic ion's electronic state is put back into the Doppler cooling cycle (if it is not there already) and the ions are Doppler cooled and prepared for the next run. The number of scattered photons from the logic ion is measured during this phase to detect if the ion crystal is present and in the correct orientation ($m_1 - m_2$ vs. $m_2 - m_1$). If not, the 'recrystallization' procedure is implemented. Note that the trapping voltages are fixed during the experimental cycle unless recrystallization is needed.

During each experimental sequence, if the ion appears dark at the beginning of a repetition, that is logged. If this happens ten times in a row, the script is automatically aborted and the data is saved. In this way, no post-processing of bad data is needed. Typically this happens if the ions are ejected or the lasers break lock.

3.5.8 Recrystallization and Ion Swapping

As outlined in Sec. 2.3.1, it is necessary to have a procedure where the ion crystal is reprepared. Collisions with background gas can thermalize and decrystallize the ions. In a less energetic event the ions can swap position and reorder themselves (m_1 - m_2 or m_2 - m_1). The ion order is also random after loading. A procedure was implemented to ensure each experimental data point is taken with a cold ion crystal in the proper orientation. This scheme makes use of the mass dependency in the pondermotive potential (Eq. 2.16) and addition of further red-detuned Doppler cooling lasers [73].

At the end of every experimental repetition there window (typically 10 ms) where the Doppler cooling lasers are applied to prepare the crystal for the next repetition. During this window, the PMT counts the total number of photon collected (Sec. 3.5.3.3). If the photons detected are below a determined threshold, a recrystallization procedure is initiated. This is all handled in real time and written into the Python code, see Appendix E.3. There are two main reasons the number of detected photons would be below threshold: the ions have decrystallized or the ions are not in the correct orientation. It has been found that Ba^+ - SiO^+ is the preferred orientation, where Ba^+ typically occupies the left lattice site. This is likely due to some anharmonicity resulting from the bent endcap (see Fig. 3.7).

The ion orientation is determined by tightly focusing the 493 Doppler laser (see Fig. 3.16 and Sec. 4.3.1) and misaligning it to the left (as viewed on the camera), away from

trap center. The level of misalignment is chosen to obtain a good separation of 'bright' and 'dark' ion histograms while retaining a high photon count for a 'bright' ion. The single misaligned 493 Doppler laser is inefficient when loading and recrystallizing so another 493 Doppler beam, Doppler2, was added to the trap (see Fig. 3.16). The photon histograms collected for Ba^+ on the left versus the right lattice site are shown in Fig. 3.27.

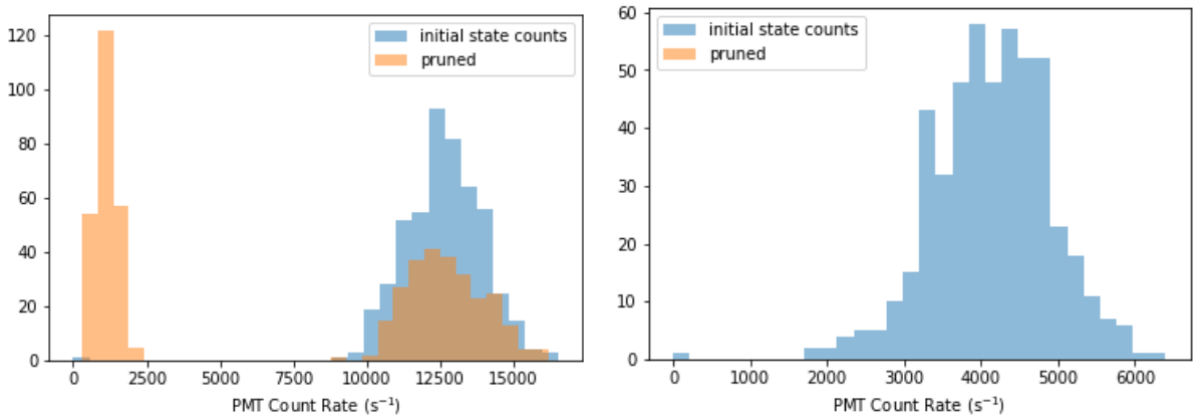

Figure 3.27: **Photon Histogram from Ba^+ in the Left or Right Lattice Site:** The histograms to compare here at the 'initial state counts' which measure the photons scattered under Doppler cooling conditions. A clear difference in mean collected photons exists depending on whether Ba^+ is on the left or right of the spectroscopy ion. From the data, the discriminator set at 7500 counts/s.

If the number of photons detected is below the discriminator (typically $\approx$ 7500 counts per second) then the recrystallization procedure is initiated. The process begins by relaxing the trapping voltages and opening the shutters of the Doppler2 and RedBlue lasers. Lowering the trapping voltage helps to mix the motional modes and coupling between ions as they tilt and experience micromotion. The low trap setting is set such that the resulting ion crystal is tilted from the axial direction. Typically the ions recrystallize before the trap setting fully reaches the low trap settings.

Once recrystallized, the ion orientation needs to be set before another experimental cycle can begins. This is accomplished by ramping the endcap voltage to orient the crystal along

the radial direction. This is preceded by a small increase in the RF voltage, otherwise the endcap voltage increase would eject the Ba^+ ion. By applying an extra 10 V to endcap-1 a gradient in the axial direction is created and the Ba^+ ion is pushed to the left. The trapping voltages are then reset to experimental conditions.

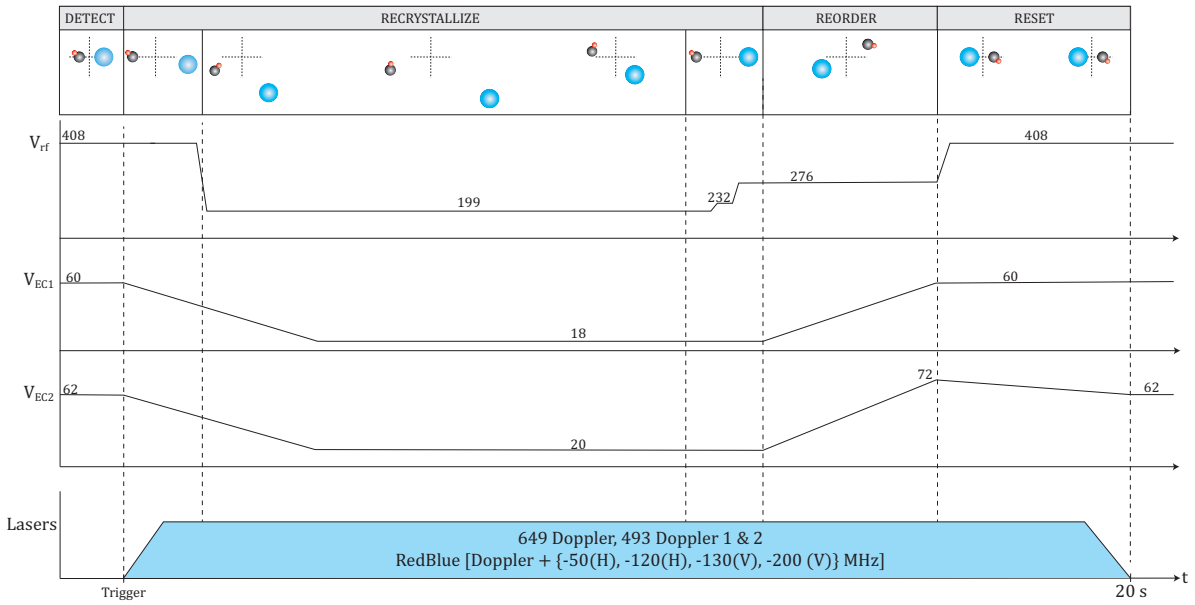

Figure 3.28: **Recrystallization Procedure:** used to successfully and automatically recrystallize or swap the ion position

The recrystallization process takes 20 seconds and is mainly limited by the time-constant of the endcaps, set by the low-pass filters installed (see Sec. 3.1). While no statistics have been taken, from daily operation this procedure is extremely reliable and effective nearly every time.

CHAPTER 4

Ba^+: The Workhorse

The Earth is my body,
my head is in the stars
"Harold & Maude"

Ba^+ has been described as the 'prettiest ion'[1] and the 'future of quantum computing' [2]. Our lab likes Ba^+ because it has transitions in the visible regime which makes alignment of the lasers much easier. While it is possible to achieve isotope-selective ion loading [92], the other isotopes present an opportunity to test two ion crystal manipulation and cooling since their transition energies are well separated from 138-Ba^+ . With the highest naturally occurring abundance (71.7%[3]), we use 138-Ba^+ isotope in all experiments mentioned in this thesis. Ba^+ serves as the logic ion in our experiment and is used for Doppler and sideband cooling, as well as state readout. This chapter aims to describe these procedures, their efficiencies and the lasers used to achieve quantum manipulation of 138-Ba^+ .

[1] Wes Campbell, NACTI Talk 2019
[2] Chris Monroe, Northwestern Physics and Astronomy Colloquium 2022
[3] `https://www.ciaaw.org/barium.htm`

4.1 Level Structure

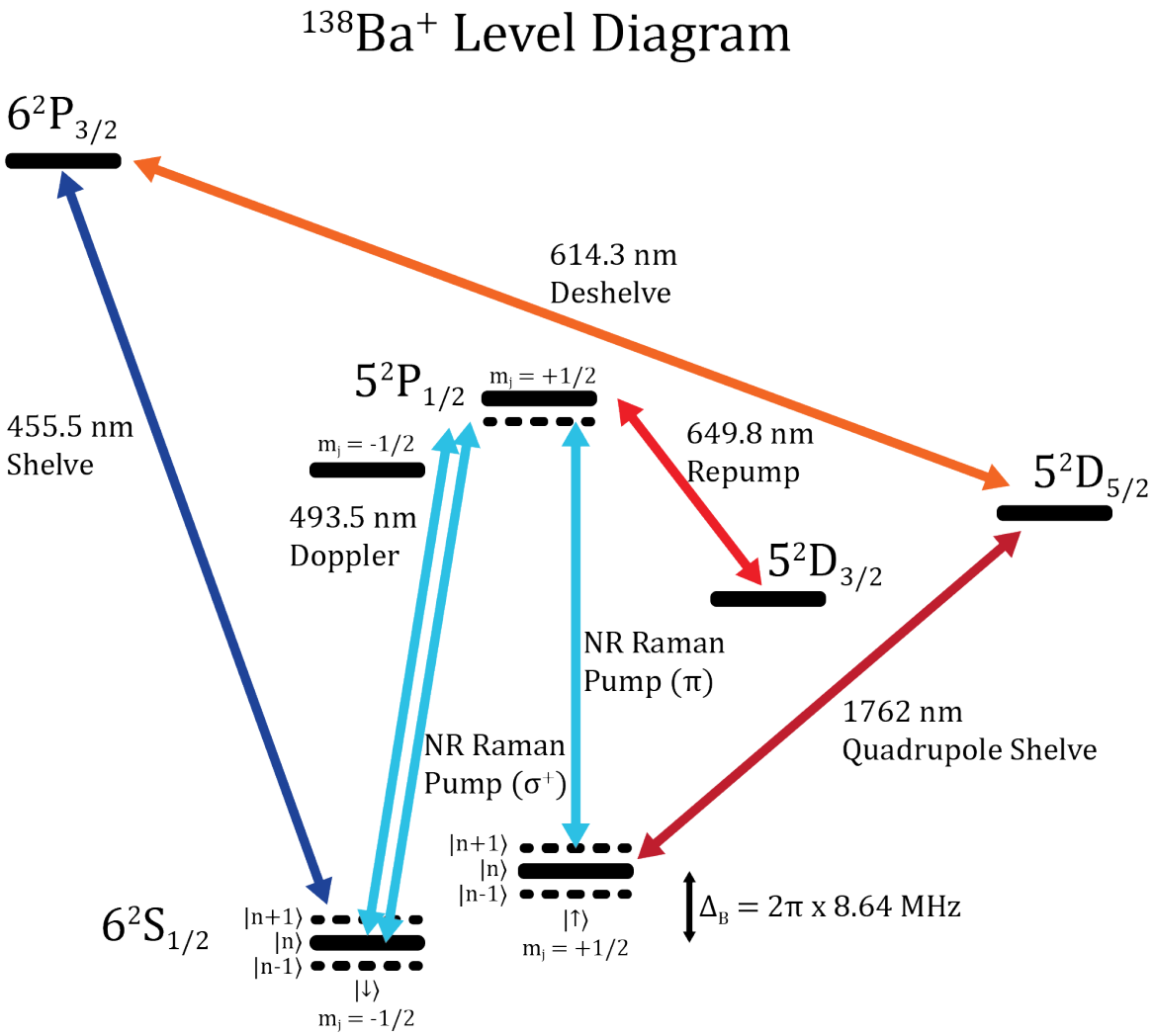

Figure 4.1: **Energy Levels of 138-Ba II**

Fig. 4.1 shows the relevant energy levels of 138-Ba^+ and the lasers used to address them. A more extensive diagram showing transitions to higher energy levels can be found in [94]. With zero nuclear spin ($I = 0$), each electronic state consists of at least two Zeeman

State	Lifetime	g-factor	Reference
$6^2S_{1/2}$	-	2.00249192(3)	[106]
$5^2P_{1/2}$	7.90(1) ns	≈ 0.666	[107]
$5^2P_{3/2}$	6.32(1) ns	≈ 1.334	[108],[109]
$5^2D_{3/2}$	79.8(4.6) s	0.793278(3)	[110],[111]
$5^2D_{5/2}$	31.2(9) s	1.20036739(24)	[112],[113]

Table 4.1: **State lifetimes and Landé g-factors in 138-Ba$^+$**

Transition	Air Wavelength (nm)	D (a.u.)	Branching Fraction	References
$5^2P_{1/2} \rightarrow 6^2S_{1/2}$	493.5454	3.305(14)	0.7293(2)	[114],[107]
$5^2P_{1/2} \rightarrow 5^2D_{3/2}$	649.6898	3.042(16)	0.2707(2)	[114],[107]
$6^2P_{3/2} \rightarrow 6^2S_{1/2}$	455.4033	4.720(40)	0.756(46)	[109]
$6^2P_{3/2} \rightarrow 5^2D_{3/2}$	585.5143	1.349(36)	0.0290(15)	[109]
$6^2P_{3/2} \rightarrow 5^2D_{5/2}$	614.3414	3.945(66)	0.2150(64)	[109]
$5^2D_{5/2} \rightarrow 6^2S_{1/2}$	1762.17448		0.846(25)	[113],[112]

Table 4.2: **Branching Ratios between Relevant 138-Ba$^+$ Transitions** The transition wavelengths were taken from the [115] except for the quadrupole $5^2D_{5/2} \rightarrow 6^2S_{1/2}$ transition which was recently measured with sub-Hz precision [113].

sublevels. In our experiment, the two Zeeman sublevels of the ground $6^2S_{1/2}$ state, $|\uparrow,\downarrow\rangle = |m_j = +1/2, -1/2\rangle$, serve as the qubit states in logic experiments. While progress has been made to utilize an optical qubit between $\left|\uparrow = 6^2S_{1/2}\right\rangle$ and $\left|\downarrow = 5^2D_{5/2}\right\rangle$ (see Sec. 4.5) this has not been fully realized yet.

Table 4.1 and Table 4.2 show the most relevant parameters for the Ba$^+$ electronic transitions addressed in this work. All of these transitions are addressed using CW External Cavity Diode Lasers (ECDLs) with the exception of the 1762 nm quadrupole transition, which is excited using a cavity-locked fiber laser (see Sec. 4.5).

4.2 Loading

Neutral barium has an ionization energy of 5.211 eV [115] which can be addressed using a 237 nm laser. This is the photoionization scheme used in the larger SiO^+ trap [94]. Since the Ekspla OPO in our experiment does not have an internal SHG crystal, we instead use a 1+1 REMPI transition described in Sec. 4.2. The first photon addresses the Ba I $^1S \rightarrow ^3 D$ transition and the second photon ionizates neutral barium with 0.8 eV of extra energy. Typically loading and crystallization of Ba^+ is quick when the Doppler and RedBlue beams are applied.

It should be noted that upon installation of a solid barium target into the ion trap, the barium rock will oxidize fairly quickly. Shining $\sim$ 1 mJ of ablation energy at 532 for several seconds on a particular spot is sufficient to blast away the oxide layer. This is best done shortly after pumping down from a vacuum chamber vent, otherwise it may take several hours to pump down the high gas load emitted when at UHV.

4.3 Ba^+ Cooling

Ba^+ is THE coolest atom in our lab; it is constantly Doopler cooled and also used to sympathetically cool the molecular ions we aim to study. For experiments such as rotational state pumping [43], [46], [47] a Doppler cooled crystal is sufficient and nothing else is needed from Ba^+ . In this experiment, where spectroscopy using quantum logic and precision measurements are the goal, the temperature of Ba^+ must be further reduced. We employ Raman sideband cooling (RSC) to achieve this. The lasers used for Doppler cooling and RSC are discussed here. In Ch. 6 I will detail the results of RSC for a single Ba^+ , two Ba^+ ions and a mixed-species crystal of Ba^+ - SiO^+ . Stay tuned!

4.3.1 Doppler Lasers

The Doppler cooling in Ba^+ is addressed using 493 nm and 649 nm lasers that drive population between the $6^2S_{1/2} \leftrightarrow 5^2P_{1/2} \leftrightarrow 5^2D_{3/2}$ states. The linewidth of the transition is $\Gamma_D = 2\pi$ x 20 MHz. With a collection efficiency of ≈ 0.0013 we measure at most $\approx 25 \times 10^3$ photons per second with the lasers set to saturation. The saturation intensities for the Doppler cooling transitions are 200 and 97 μW/mm^2 for the 493 and 649 transitions respectively. Using an f = 150 mm lens, the 493 and 649 nm beams are focused to a waist of $\omega_0 \approx \{21, 101\}$ μm respectively at the ion. The 493 beam is focused tightly to determine ion orientation, as described in Sec. 3.5.8. At these beam waists, the transitions are easily saturated with only 0.3 and 3 μW for the 493 and 649 nm transitions. The Doppler temperature for Ba^+ , $T_D = \hbar\Gamma/2k_B \cong 480\mu K$. If the trap is set such that $\omega_z/2\pi = 1$ MHz then the mean occupation number is $\bar{n}_z = 10$. Realistically, it likely twice that.

Both the 493 nm and 649 nm lasers, as well as the 614 nm laser (mentioned later in Sec. 4.4) are all located on the lab 'Laser Farm' table. This is a separate optical table whose legs are floating to isolate the lasers and optics from vibrations on the floor. Since at one time, four different experiments used these Ba^+ Doppler lasers, its central location allows for the light to be routed to the different experiments, some in other rooms, via fiber optics that rest on trays running along the ceiling.

The influence of the Doppler lasers on a single ion is routinely checked to measure potential laser power, frequency or alignment drifts. By scanning the 493 nm frequency, while keeping the 650 nm frequency fixed, the red side of the atomic resonance is observed.

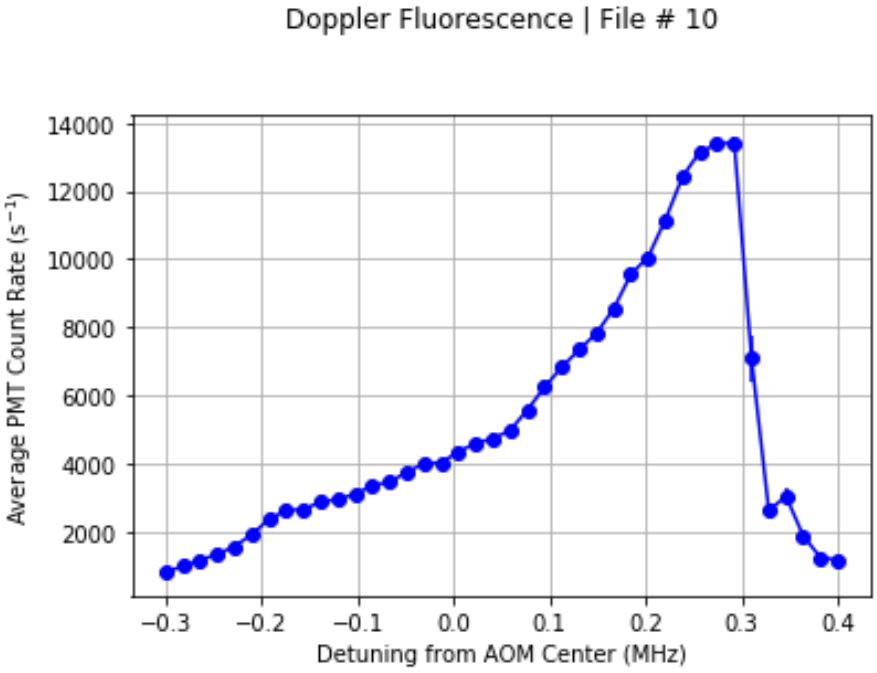

Figure 4.2: **Doppler Scan over the $6^2S_{1/2}$ to $5^2P_{1/2}$ transition:** When the 493 nm laser reaches the positive detunings (the blue side of resonance) the ion is heated up and the scattered photon count drops dramatically. Typically, these scans are taken to set the 493 2x AOM voltage at the -$\Gamma/2$ point of resonance (roughly 0.15 V shown in this plot).

4.3.1.1 493 nm Laser

Light at 493 nm is derived from a Toptica TA-SHG-100[4] laser. A Toptica DL Pro ECDL [5] at 987 nm is amplified using a Toptica BoosTA pro[6] to 3W before passing into a SHG bow-tie that doubles light to 493 nm. The SHG cavity is stabilized by the Pound-Drever-Hall locking technique [116]. A 20 MHz modulation is applied to the current of the 987 nm ECDL, which is used for the modulation-demodulation locking. Typically we obtain about 113 mW of 493 output from the laser, which is then divided among the different experiments.

[4]Serial No. 2V0_00132
[5]Serial No. 11111
[6]Serial No. 07035

The optical arrangement from the output of the 493 nm laser is shown in Fig. 4.3

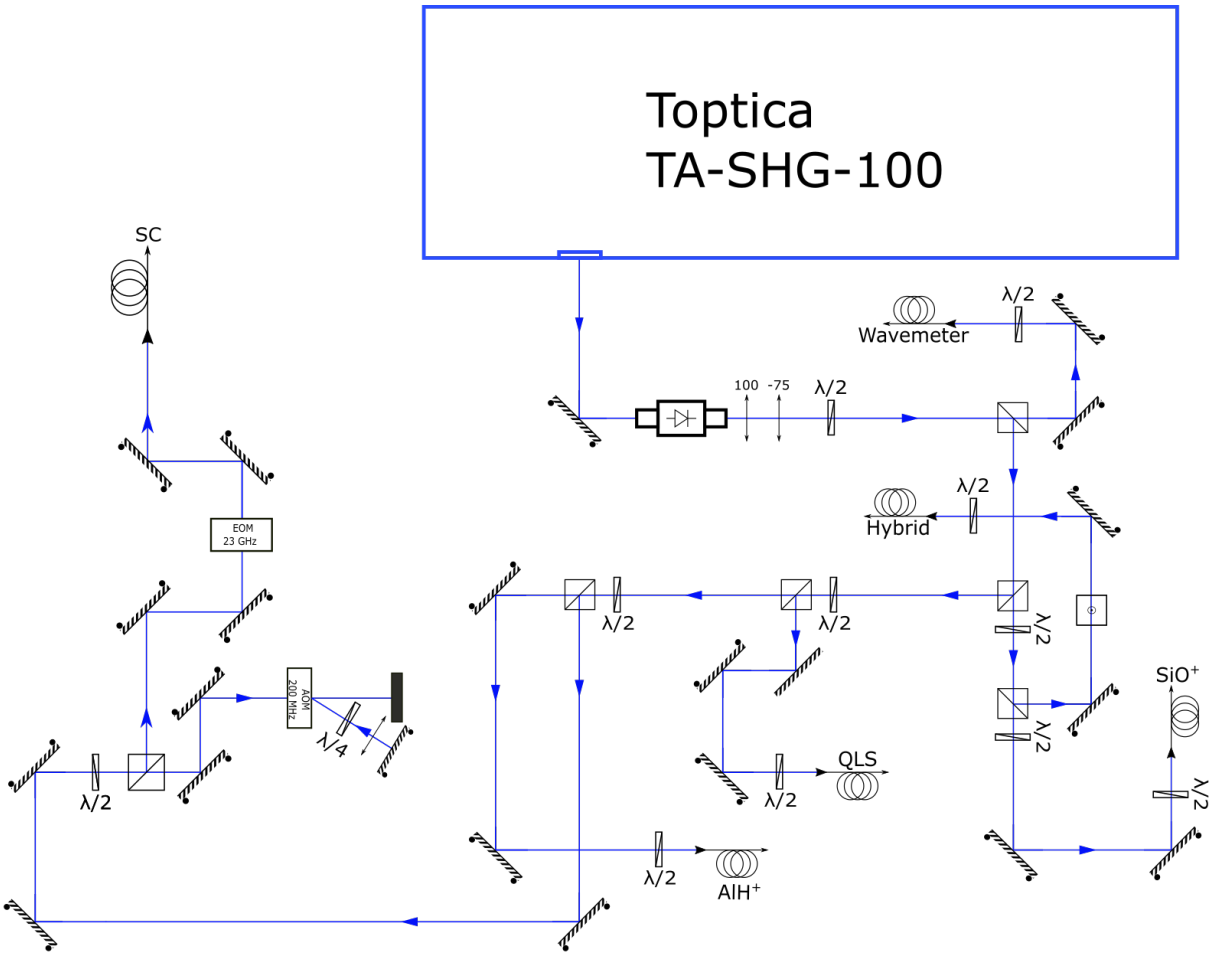

Figure 4.3: **Laser Farm 493 nm Laser Optical System for the Odom Lab**

The most expansive optical system in the single-ion experiment is the 493 laser. That is because the 493 nm light is distributed into two Doppler lasers, four different Raman beam paths and two RedBlue beam lines. As a result, roughly 20 mW is needed from the Laser Farm. A diagram of these beam lines, and their respective frequency shifts are shown in Fig. 4.4.

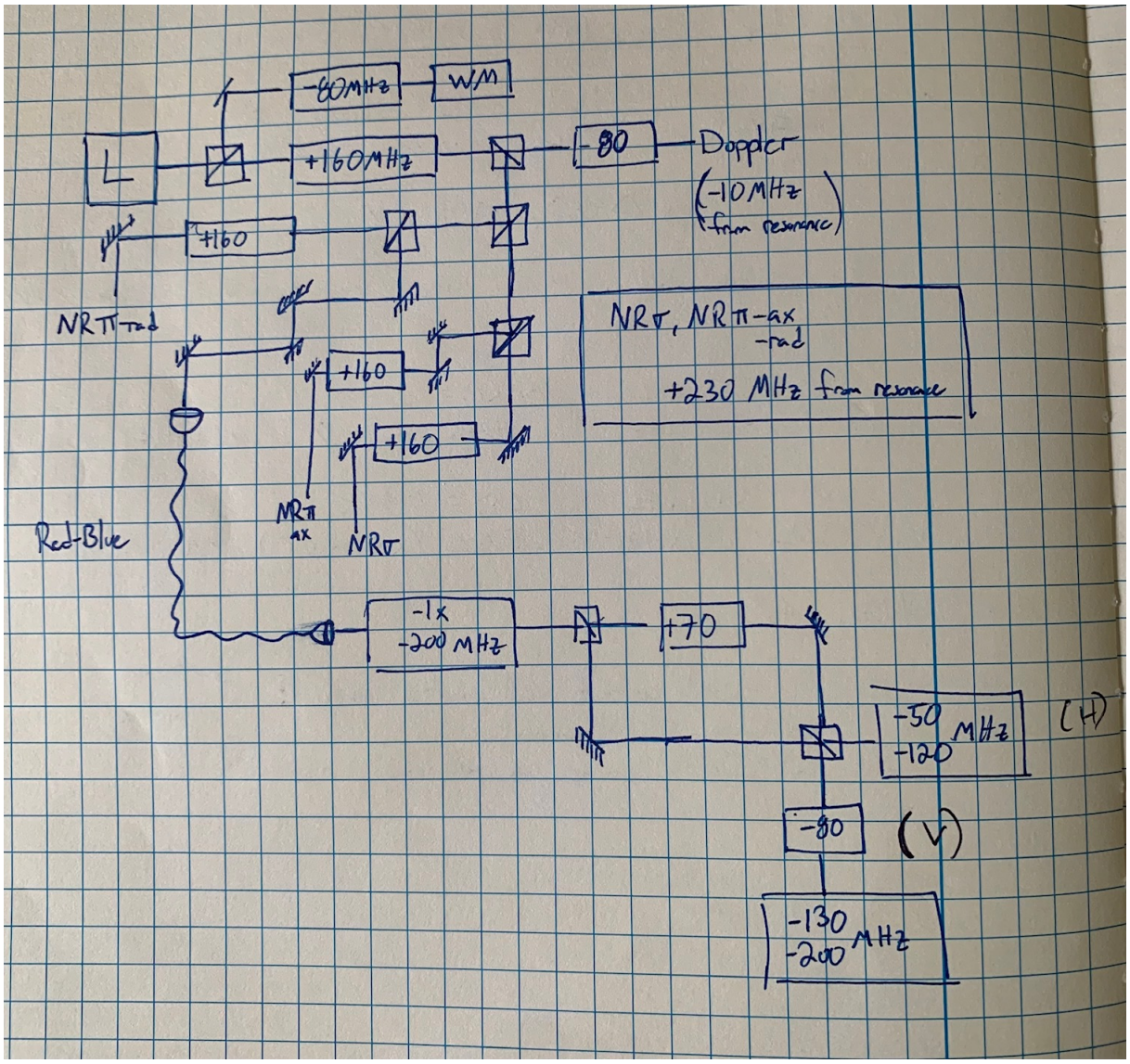

Figure 4.4: **493 nm Optical Beam Path for Single-Ion Experiment**

4.3.1.2 649 nm Laser

The simplest laser system in the single-ion experiment[7], a Toptica DL 100 [8] generates light at 649 nm. Because of the simple and stable ECDL design, daily operation only requires tuning of the PZT to bring the laser on resonance. The distribution of light to the different experiments is shown in Fig. 4.5.

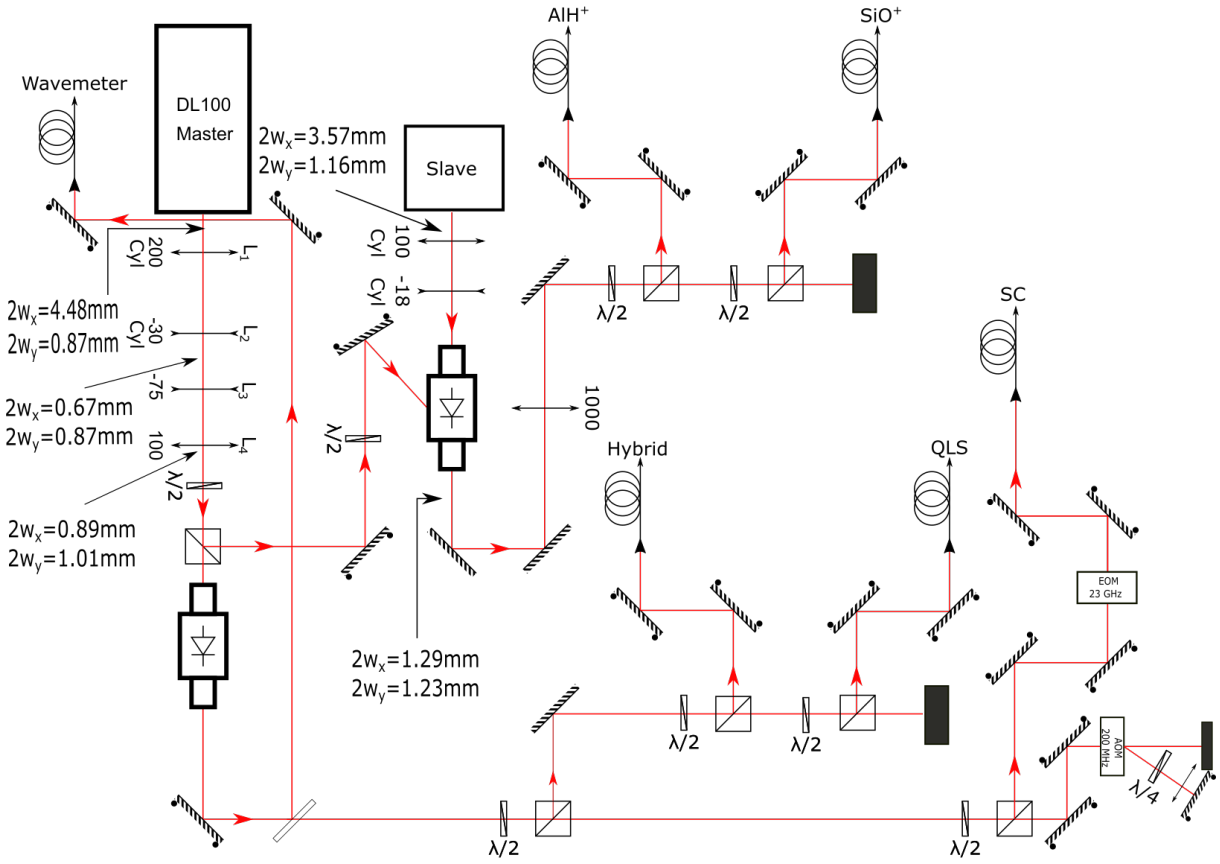

Figure 4.5: **Laser Farm 649 nm Laser Optical System for the Odom Lab**

[7]The irony is that the diode broke in January 2022 and shut down the experiment until July 2022.
[8]SN: 2732

4.3.1.3 RedBlue

As mentioned in Sec. 2.3.1, it can be useful to add several Doppler beams that are set to a detuning larger than $-\Gamma/2$ [73]. Part of the 493 nm light is picked off from the Doppler beam line and sent into a series of AOMs to shift the frequency further from resonance. The optical set-up is shown in Fig. 4.4. Two detunings -50 and -120 MHz, enter the trap parallel to the optical table, with σ_+ and σ_- polarization's. The second pair of detunings, -130 and -200 MHz, are coupled into a fiber and shined into the ion trap at an angle of $\approx 20°$ from the vertical. These were chosen due to convenience and projection onto the trap axes.

4.3.1.4 Destabilization of Dark States

The Doppler cooling transition consists of populating the $6^2S_{1/2}$, $5^2P_{1/2}$ and $5^2D_{3/2}$ states. The $6^2S_{1/2}$ and $5^2P_{1/2}$ states each have J = 1/2 with two magnetic sublevels of $m_J = \pm 1/2$, while the $5^2D_{3/2}$ state has J = 3/2 and four magnetic sublevels. If the $P_{1/2}$ state decays to either $S_{1/2}$ sublevel, 493 nm light with π polarization can address each state. This is easily achievable if the 493 laser has a k-vector perpendicular to the magnetic field, as shown in Fig. 3.16. However if $P_{1/2}$ state decay leads to populating $\left|D_{3/2}, m_j = \pm 3/2\right\rangle$ then 649 nm light with π polarization will not excite all population back to the $P_{1/2}$ state. In this case, the $\left|D_{3/2}, m_j = \pm 3/2\right\rangle$ states are said to be dark states.

This is a well known phenomena in AMO physics, common to the quantum states of ionized alkali-earth metals, and addressed directly Ref. [117]. The authors find the optimal settings for the rabi frequency, polarization and detuning of the 649 laser and also the magnetic field strength to destabilize the D state dark states. The 138-Ba^+ Doppler transition has a linewidth of 2π x 20 MHz. The authors find that the magnetic field should be set to between $0.01 < \omega_B < 0.1$. In this experiment, a magnetic field of 3.1 G splits the zeeman

states by $\sim 0.4\ \gamma$ (see Sec. 3.3) is chosen a compromise between dark state destabilization and separating the Ba^+ Zeeman states so they are well resolved.

The authors also note that that the 649 nm laser should be blue-detuned by $+\gamma/2$ such that the resulting dark resonances are on the blue side of transition, far from the 493 cooling resonance. The 649 polarization is experimentally chosen by rotating a half-wave plate and maximizing the PMT counts from a single ion.

4.3.2 Sideband Cooling Lasers

Aspiring for precision measurements and quantum logic, this experiment requires cooling beyond the Doppler limit. This can be achieved by sideband cooling [53]. From Appendix A we see how the atomic transitions are dressed with motional sidebands. This sidebands are resolvable if the atomic transition addressed has a linewidth smaller than the secular frequency. We see from Table 4.1 that the dipole allowed transitions at 455, 493, 614 and 649 nm are too broad to resolve the motional sidebands, which are typically no smaller than ~ 300 kHz.

We are left then with two options: to address the $S_{1/2} \rightarrow D_{5/2}$ quadrupole transition or use a stimulated Raman transition between the two Zeeman sublevels in the ground $S_{1/2}$ state. The latter is possible because the Zeeman states are long-lived in the absence of external AC fields. Typically their lifetimes are set by fluctuations in the magnetic field source, which is addressed in Sec. 3.3. To address the quadrupole transition at 1762 nm (see Fig. 4.1) requires linewidth narrowing to Hz level and ~ 100 mW of power to achieve sideband Rabi frequencies on a reasonable timescale (order of 100 μs). Despite the challenge, work done to linewidth narrow a 1762 nm fiber laser is discussed in Sec. 4.5.

Using a Raman transition is typically much easier to set-up [53], [68] and so this is the

method we use [92]. Fig. 4.6 shows the relevant states and energy splittings used for Raman Sideband Cooling. The optical path, shown in Fig. 4.4, shows that the near-resonant (NR) Raman lasers are derived from the same 493 laser as the Doppler and RedBlue beams. The Raman system splits the light into three paths: the NR-π-axial, NR-π-radial and NR-σ beam. The NR-σ is typically called the pump beam and the NR-π beam is called the probe because usually the NR-σ power is much larger than the power in the NR-π beam (μW vs. nW respectively).

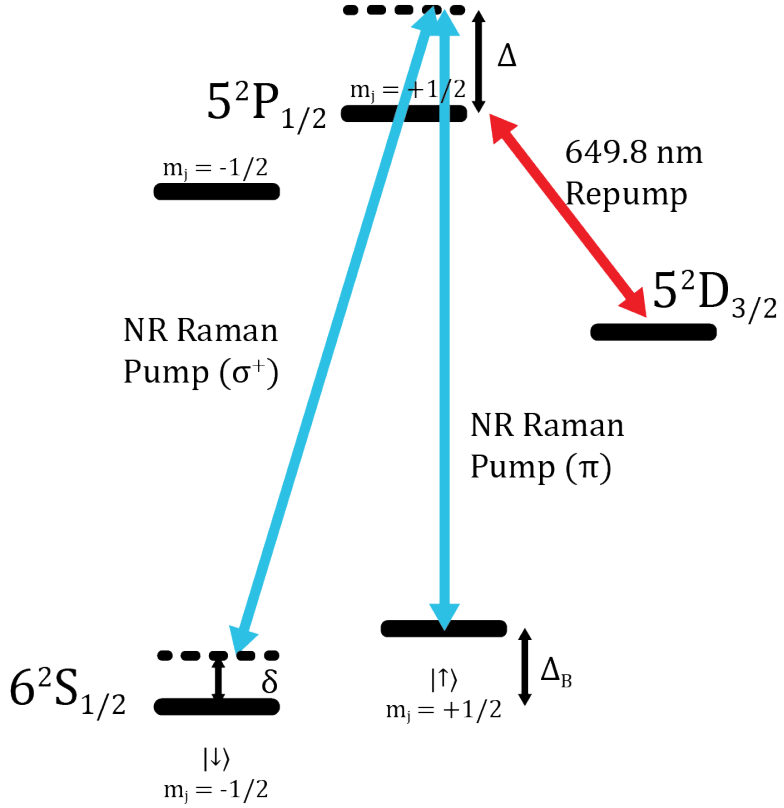

Figure 4.6: **Near-Resonant Raman Scheme for Sideband Cooling in 138-Ba$^+$** The 649.8 nm repump is on to ensure no dark states exist and the cooling process is continuous. Note that this diagram specifically shows the scheme for EIT sideband cooling. CW RSC previously used in Ref. [99] requires red-detuned NR Raman lasers.

Consider the three level system of $|1\rangle = \left|S_{1/2}, m_j = +1/2\right\rangle = |\uparrow\rangle$, $|2\rangle = \left|S_{1/2}, m_j = -1/2\right\rangle = |\downarrow\rangle$ and $|3\rangle = \left|P_{1/2}, m_j = +1/2\right\rangle = |e\rangle$ shown in Fig. 4.6. The system is driven by two lasers, the NR-π with a k-vector of $\mathbf{k}_\pi$ set to π-polarization and a frequency of ω_π drives the $|1\rangle \rightarrow |3\rangle$ transition with a Rabi frequency of Ω_π. The other laser, the NR-σ has a k-vector of $\mathbf{k}_\sigma$, σ^+ polarization and frequency of ω_σ drives the $|2\rangle \rightarrow |3\rangle$ transition with a Rabi frequency of Ω_σ. Their detunings are defined as: $\Delta_\pi = \omega_\pi - \omega_{13}$ and $\Delta_\sigma = \omega_\sigma - \omega_{23}$. The two lasers are in Raman resonance if $\omega_\sigma - \omega_\pi = -\Delta_B - \Delta'$ where Δ_B is the Zeeman splitting of the $|\uparrow\rangle$ and $|\downarrow\rangle$ states due to an applied magnetic field B and Δ' is the total light shift in the system (defined below). Let us define $\delta = -\Delta_B - \Delta'$. If $\Delta \gg \omega_\pi, \omega_\sigma, \Gamma_3, \delta$ then state $|3\rangle$ is said to be adiabatically eliminated [118]. This means that $|3\rangle$ is not populated (which would interrupt the adiabatic evolution of the system from $|1\rangle$ to $|2\rangle$). The effective Rabi Raman frequency (neglecting the phase difference between the two lasers) is,

$$\Omega_{eff} = \frac{\Omega_\sigma \Omega_\pi}{2\Delta}. \tag{4.1}$$

Note that the motional states are not shown in Fig. 4.6 but they are present! For the Raman resonance condition if $\omega_\sigma - \omega_\pi = \delta$, then $\Delta n = 0$, carrier transitions are driven (see Appendix A). For a given motional mode of frequency ω_m, if $\omega_\sigma - \omega_\pi = \delta + \omega_m$ then a blue-sideband (BSB) is driven and $\Delta n_m = +1$ and if $\omega_\sigma - \omega_\pi = \delta - \omega_m$ then a red-sideband (RSB) is driven causing $\Delta n_m = -1$. The subtle point is that instead of the k-vector defining what motional modes are addressed (see the Lamb-Dicke parameters in Ch.2 and Appendix A) in a Raman resonance k is replaced by $\Delta\mathbf{k} = \mathbf{k}_\pi - \mathbf{k}_\sigma$. This follows intuition, that along the direction defining the difference in Raman laser wave vectors a strong optical electric-field gradient is created. It is this gradient that drives the motional transitions. By replacing $\mathbf{k}$

for $\Delta\mathbf{k}$ in the Lamb-Dicke parameters, if $\Delta\mathbf{k}$ has components only along the z-direction for example, then $\eta_x = \eta_y = 0$ and the Rabi frequency for driving radial sidebands is zero; it cannot be done.

It is crucial that the two Raman lasers are phase locked. These terms have been neglected from the above equations for simplicity but can be found in [68], [71]. This is the motivation for building custom AOM drivers as discussed in Sec. 3.5.6. The lasers also have a fundamental coherence length, set by their linewidth, so it is important to keep their path lengths similar and as short as possible before reaching the ion.

It is also important to discuss the light shifts, Δ' associated with the $|\uparrow\rangle$ and $|\downarrow\rangle$ states. The light shifts for the qubit states is given by,

$$\Delta'_{|\uparrow\rangle} = \frac{\Omega^2_{\sigma^-} + \Omega^2_{\pi}}{4\Delta}, \qquad \Delta'_{|\downarrow\rangle} = \frac{\Omega^2_{\sigma^+} + \Omega^2_{\pi}}{4\Delta} \tag{4.2}$$

In our experiment, the σ Raman beam is set to σ^+ polarization with as high extinction as we can such that, $\Omega_{\sigma^-} \approx 0$. This is accomplished by passing the light though a 1000:1 Glan-Thompson polarizer to obtain well defined linear polarization before a quarter-waveplate is used to generate the circular polarization.

The exact relations to achieve RSC for different scheme (CW RSC and EIT sideband cooling) are discussed in Ch. 6. In either of these two methods, the Rabi frequencies of the σ and π beams are imbalanced. In the next section I will discuss a separate pair of readout Raman lasers where the Rabi frequencies are balanced. The same would be true if a pulse sideband cooling method was used.

4.3.2.1 Optical Pumping

The NR-σ^+ laser is also used for optical pumping. By irradiating the Ba^+ ion with NR σ^+ light and 649 nm light, the Ba^+ is pumped in the $|\uparrow\rangle$ spin state, which is a dark state when only these lasers are applied. The NR σ^+ is also used in the 'protect' step of our state readout [99]. In this step, population in $|\downarrow\rangle$ is excited up to the $\left|5^2P_{1/2}, m_j = +1/2\right\rangle$ state. From there it has a 50% probability of decaying to either the $|\uparrow\rangle$ or $5^2D_{3/2}$ state. This is because the Clebsch-Gordon coefficient squared for the $\left|5^2P_{1/2}, m_j = +1/2\right\rangle \rightarrow \left|6^2S_{1/2}, m_j = +1/2\right\rangle$ of 1/3 is equal to the 1/3 branching ratio of $P_{1/2}$ to $D_{3/2}$ decays in Ba^+ . The population pumped in the $D_{3/2}$ state is 'protected' and represents a confirmation signal in our logic scheme.

4.4 State Readout

So far we have discussed the lasers involved in cooling the ions external motion. However, the Doppler lasers alone cannot distinguish between the two qubit states $|\uparrow\rangle$ and $|\downarrow\rangle$ nor can they herald a motionally cooled ion as the scattering process changes the ion temperatures. As mentioned earlier, driving the quadrupole transition can accomplish spin state readout, however experimentally realizing this is challenging and ongoing. These efforts are discussed in Sec. 4.5.

In the meantime, we achieve qubit state readout using the method described in Refs. [92], [99]. A Far-Off Resonant Raman pair transfers population between the two qubit states based on the ion temperature [105] and we implement the electron shelving technique to amplify the signal of one phonon to tens of thousands of photons detected per second. A summary of the entire Ba^+ cooling and readout scheme is given in Sec. 4.4.4. Electron shelving works

by conditionally exciting one qubit state, say $|\uparrow\rangle$, to a long lived metastable electronic state $|m\rangle$ while the $|\downarrow\rangle$ state is untouched. Then any population in $|\uparrow\rangle$ is detected by scattering photons on the dipole transition between $|\uparrow\rangle \leftrightarrow |e\rangle$. If population was transferred to $|m\rangle$ then the ion will appear dark, detection that projects the ion into $|m\rangle$. If the system remained in $|\uparrow\rangle$ then the ion will appear bright and the quantum population of a single state is mapped to $\mathcal{O}$ (10^3) photons detected over a $\sim$ 1 ms interval. If the background counts on a PMT are $\mathcal{O}$ (10^2) over the same 1 ms interval than the two states can be distinguished with high confidence.

Note that if the π-pulse from $|\uparrow\rangle$ to $|m\rangle$ achieves $\geq 50\%$ flopping then the two qubit states can simply be $|\uparrow\rangle$ and $|\downarrow\rangle = |m\rangle$. For Ba^+ this can be accomplished if the 1762 nm transition can be driven directly (see Fig. 4.1 when the Zeeman splitting is larger than the $S_{1/2} \rightarrow P_{3/2}$ linewidth such that $\left|S_{1/2}, m_j = +1/2\right\rangle$ can be resolved from $\left|S_{1/2}, m_j = -1/2\right\rangle$. Currently neither of these options are implemented and we instead use a third option, with less contrast, which is described below. The following section will also describe the photon discriminator and photon histogram analysis used to determine the signal.

4.4.1 Shelve Laser

To distinguish between the two qubit states in Ba^+ , we use the electron shelving method [71]. Here, the $6^2S_{1/2} \rightarrow 5^2P_{3/2}$ transition is driven resonantly by a homemade diode laser [92] at 455 nm. The laser itself is not an ECDL, because there is no grating used in the external arm, which results in a much broader laser linewidth. Typically, a total of 5 mW of 455 nm power is sent to the trap. Since this diode does not include an external cavity, its wavelength is not locked beyond the current and temperature controls of the drive electronics [92]. Typically the laser wavelength may need to be tuned at most once a week.

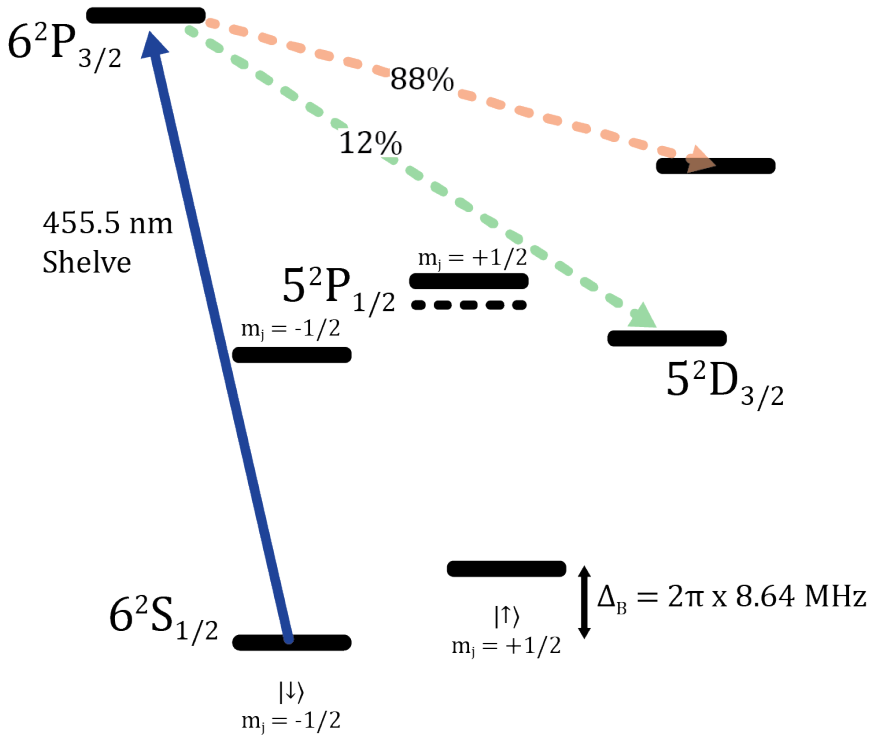

Figure 4.7: **Branching Ratios of the $|5^2P_{3/2}\rangle$ State.** The 455 nm light stimulates the $6S_{1/2} \rightarrow 5P_{3/2}$ transition and shelves the electron to the $5D_{5/2}$ state with 88% probability.

The $|5^2P_{3/2}\rangle$ state branches to the $|5^2D_{5/2}\rangle$ state 88% of the time and to the $|5^2D_{3/2}\rangle$ state 12% of the time. These branching ratios are shown in Fig. 4.7. If both the 455 nm and Doppler lasers are on, all population is eventually pumped into $|5^2D_{5/2}\rangle$, where it remains for $\sim$ 30 seconds. This is how resonance and alignment of the 455 laser are found, since the Ba^+ ion will go dark when pumped into the $|5^2D_{5/2}\rangle$ state.

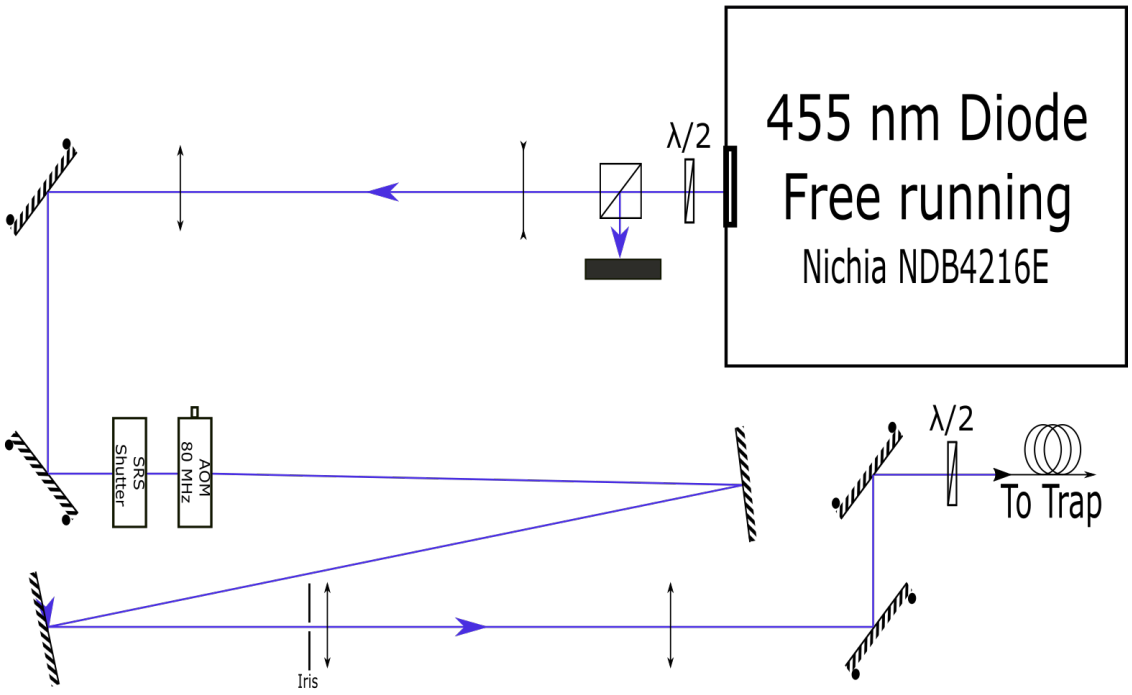

Figure 4.8: **455 nm Optical Path**

Experimentally, we can measure these branching ratios from the following sequence. The Ba^+ ion is pumped into $\left|S_{1/2}\right\rangle$ by turning off the 493 nm laser while keeping the 649 nm laser on for ~ 100 μs. With the Doppler lasers turned off, the 455 nm light is shined on a single Ba^+ ion for 10 ms (set by the lowest 'ion' time of the SRS shutter as mentioned in Sec. 3.5.5). The system is now in the state $|\Psi\rangle = \sqrt{0.88}\left|D_{5/2}\right\rangle + \sqrt{0.12}\left|D_{3/2}\right\rangle$. Then, the Doppler lasers are turn back on (when the 455 nm is fully off) and the PMT counts are read for 10 ms. In a single experimental repetition, the ion will either appear bright (because the electron was in $\left|D_{3/2}\right\rangle$) or dark because it was pumped to $\left|D_{3/2}\right\rangle$. To properly gain statistics, the experiment is repeated 300-500 times and the total photons collected are plotted in a histogram. An example is shown in Fig. 4.9.

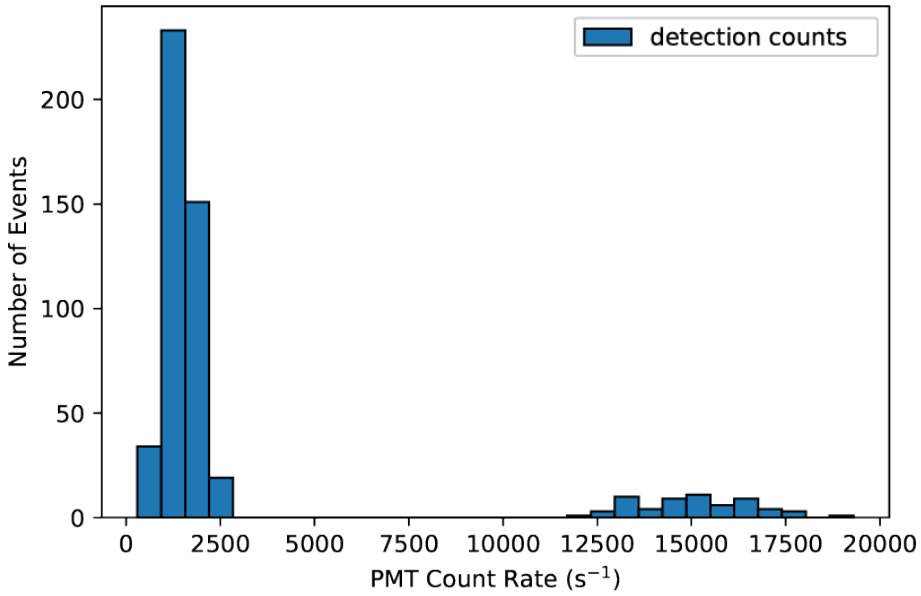

Figure 4.9: **Photon Histogram of Ba^+ from 455 shelving** This experiment ran for 500 trials. The Ba^+ ion appeared dark 87.8 ± 1.5 % of the time which matches the exact branching of 88% well.

Initial analysis of the histogram shown in Fig. 4.9 shows that many more dark counts (PMT count rate <3000 per second) occured than bright counts. The typical bright number of photon counts collected is set by 493 Doppler laser frequency (see Fig. 4.2). The 493 Doppler frequency is set to maximize the counts from a bright ion, while balancing cooling as well. From Fig. 4.9 a clear discriminator at $d_b = 7500$ counts/s can be applied to differentiate the two histograms. A high discriminator of $d_h \sim 25{,}000$ counts/s is also applied to reject unrealistic photon counts. The total number of meaningful photon collection events, called the 'pruned' number, is given by n_0 where n_0 is the number of times the pruned photon count c follows $d_b < c < d_h$. The post-processing, where trial pruning occurs, will be discussed in the next second. Then, the total number of bright counts b_c is found by summing the number of events that obey $d_b < b_c < d_h$. The total number of times the ion appears dark is $d_c = 1 - b_c$. The fraction of total dark events is then $p = d_c/n0$ which is found

to be 0.878 ± 0.015 for the data shown in Fig. 4.9. Since the photon histograms follow Poissonian statistics, the error is given as $\sigma_p = \sqrt{p * (1-p)/n_0}$. As a result, the number of experimental repetitions taken is a compromise between lowering σ_p and duration of the total experiment[9]. The perks of working with a single Ba^+ ion is that all of the branching rates can directly be measured and if the numbers do not follow the theory, the experiment has an error.

Note that the sequence described here does not distinguish between the spin states, both $|\uparrow\rangle$ and $|\downarrow\rangle$ are excited by the 455 nm laser. The ability to distinguish between them will be addressed in Sec. 4.4.4.

4.4.2 Deshelve Laser

When an electron is put into the $5^2D_{5/2}$ metastable state, it will remain there for ≈ 31 s before decaying back to the Doppler cooling cycling. To accomplish anything in a reasonable amount of time, we need to pump it out of this shelf state. As mentioned, the 1762 nm laser is in progress and not used primarily, so we need another way. The $\left|D_{5/2}\right\rangle \rightarrow \left|P_{3/2}\right\rangle$ transition is driven at 614.3 nm to bring the electron out of the shelf state. Since the $\left|P_{3/2}\right\rangle$ state has a short, 6.32 ns, lifetime the electron is quickly pumped back to the ground, $\left|S_{1/2}\right\rangle$ state.

The 614.3 nm light is derived from a 1228 nm ECDL, a wavelength where IR power is plentiful [92]. The light is collimated and fiber coupled into an KTP SHG waveguide[10]. The SHG module is temperature controlled to maintain 614 nm generation. Typically 100 mW of 1228 nm light generates roughly 3 mW of 614 nm light. Part of the 614 nm light is picked-off, measured using the wavemeter (see Sec. 3.5.4) and the feedback signal is sent to the 1228 nm seed laser. After fiber-coupling 614 nm light to the single-ion optical table,

[9] which, among other things, correlates directly with the users patience

[10] AdvR In.c WSH-P13L45AL0-14101701

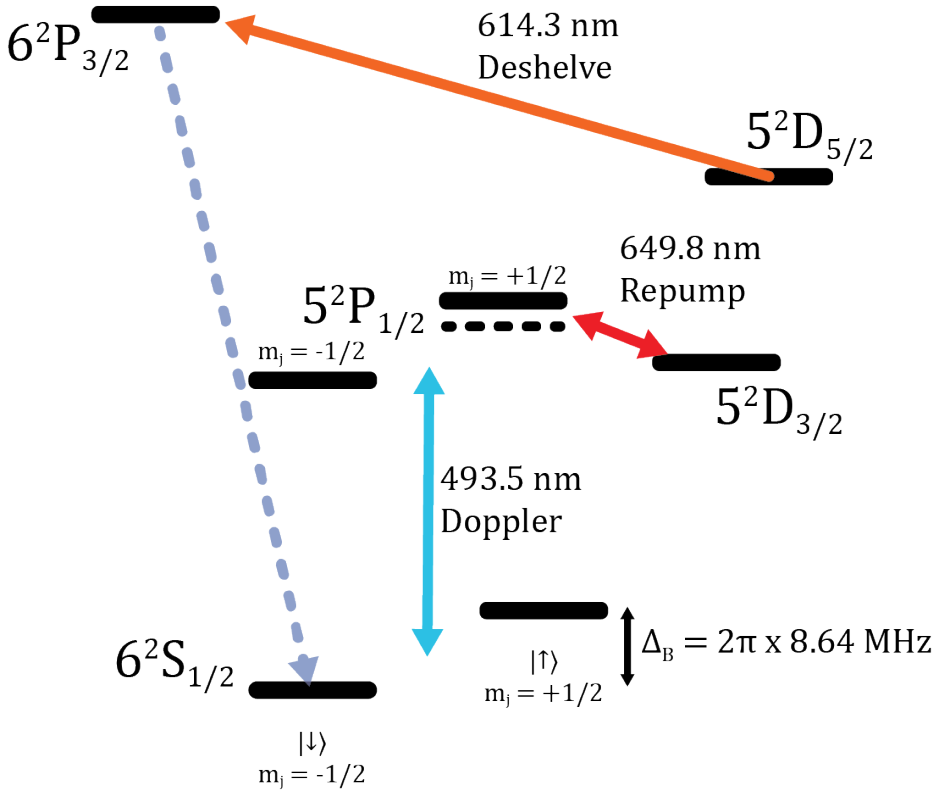

[H]

Figure 4.10: **$5D_{5/2}$ State Deshelving:** Under illumination of the 614 nm laser the electron is pumped back into the Doppler cooling cycle.

switching using a single-pass AOM and on-the-table fiber-coupling leaves roughly 10 μW to the ion, which is enough to saturate the strong electronic transition.

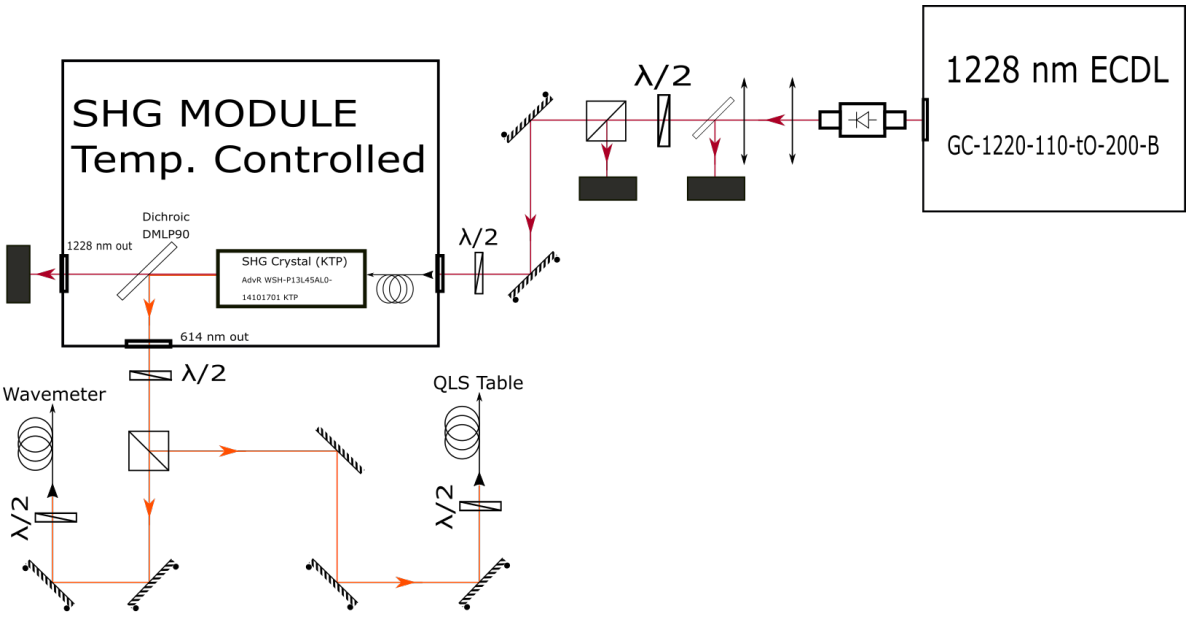

Figure 4.11: **1228 and 614 nm Optical Path**

At the end of every experimental sequence, the 614 nm laser is turned on for 10 ms (due to the minimum SRS on time) and the electron is pumped back into the Doppler cooling cycle. During this time, under illumination from the 493, 614 and 649 nm lasers the PMT is turned on and counts the number of detected photons. These value is logged, named the 'initial state counts', and if a given experimental repetition produces photons below the d_b threshold, that data point is thrown out. The resulting pruned dataset is then analyzed. This may indicate, among other potential issues, that the 614 or Doppler lasers broke lock, the 455 nm laser is still on or the Ba^+ ion is lost. If everything is working, the 614 nm should deshelve the ion 100% of the time. The 'initial state counts' are shown in Fig. 4.12 alongside the pruned data. In this specific run, 2/500 repetitions were culled from the data set.

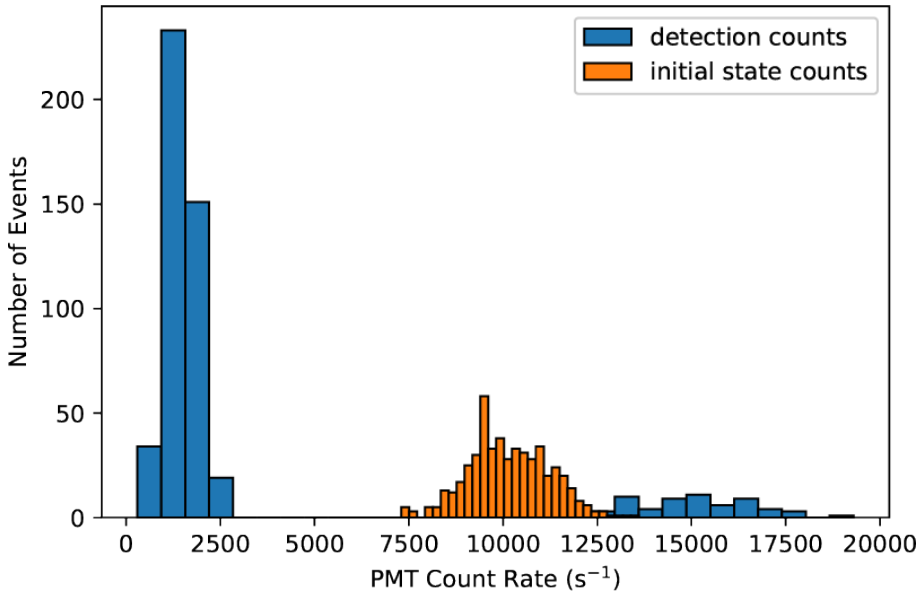

Figure 4.12: **Photon Histogram of Ba^+ from 614 deshelving:** The initial state counts shown here indicate that the ion was bright at the end of 498/500 trials. Leakage of the 455 nm light is likely why the initial state counts have a lower mean count rate than the bright detection counts and highlights one way to debug the experimental timing sequence.

In later versions of the experiment, this 'initial state count' detection time is used to also verify the ion crystal orientation and temperature, as mentioned in Sec. 3.5.8. By purposely engineering the 493 laser and count rate so that Ba^+ only appears bright while crystallized and on left of the SiO^+ , we can, in real time, apply a discriminator to determine if this condition is not met. If not, the recrystallization procedure is initiated.

4.4.3 FOR Laser

The single-ion experiment contains two sets of Raman beams, the near-resonant Raman beams discussed in Sec. 4.3.2, and the Far-Off-Resonant Raman beams use to coherently transfer population from $|\uparrow\rangle$ to $|\downarrow\rangle$. Following the QLS readout scheme, we aim to drive population to $|\downarrow\rangle$ conditionally, if the Ba^+ - SiO^+ pair is motionally heated to $|n = 1\rangle$ or

$|n > 0\rangle$ from a state dependent readout process one step before. The NR lasers cannot accomplish this because their detuning is too close to the 493 resonance and the associated scattering rate for the NR-σ is $\mathcal{O}(10^6)$ for 1 μW power when focused to a waist of 22 μm. While this is ideal for fast RSC and optical pumping, any stimulated Raman transitions would likely decohere due to scattering before any population is transferred.

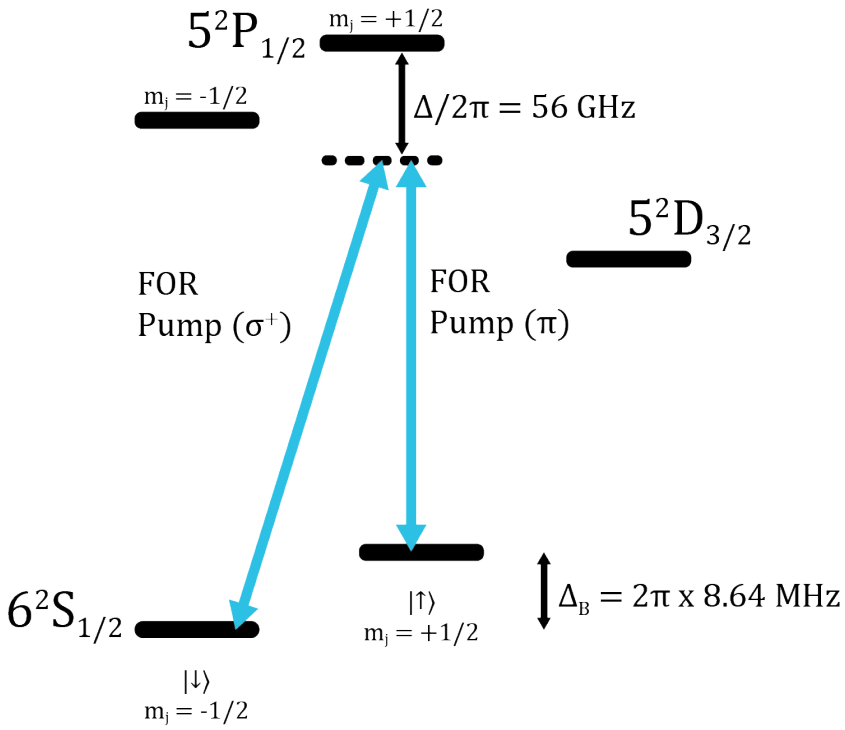

Figure 4.13: **Spin Flips Driven by the Far-Off-Resonant (FOR) Lasers**

To obtain a large enough detuning (ten's of GHz away from the 493 transition) we use a separate 493 nm source named the FOR493 laser. A Nichia NDS1316 laser diode[11] is assembled into a homebuilt ECDL laser. The laser is set to 493.591550 nm, which is -56.6

[11] Serial No. CE0000013 61

GHz detuned from the $S_{1/2}$ to $P_{1/2}$ transition. The output mode of the laser is continually measured on a Fabry-Perot cavity to ensure it remains in a single-mode output. The wavelength is also locked to the wavemeter. The FOR laser light is split into three beam paths, similar to the NR beams, including the FOR π-ax, FOR-π-rad and FOR-σ. Like the NR lasers, we call the FOR-σ light the pump and π light the probe, even though Rabi frequencies balanced for the FOR Raman lasers. Unfortunately there is not enough power to achieve fast Rabi flops in the axial and radial direction simultaneously, so a half-waveplate adjusts the power between the FOR-π-ax and FOR-π-rad paths depending on which state can be read out. An increase in the total FOR power will need to be made if pulse sideband cooling is implemented using the FOR lasers.

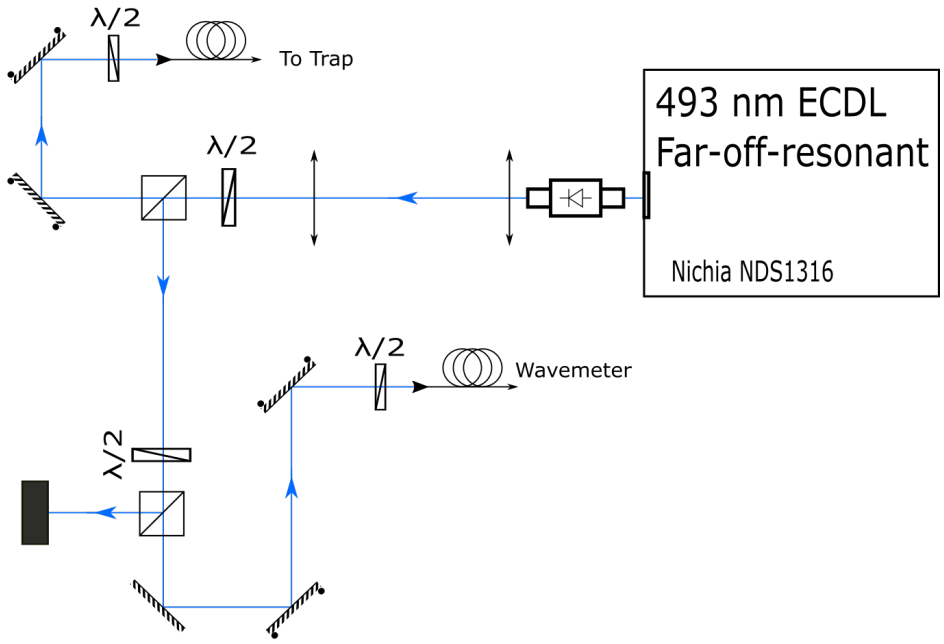

Figure 4.14: **FOR493 nm Optical Path**

For carrier transitions, $\Delta n = 0$, driven by the FOR Raman lasers between $|\uparrow\rangle \rightarrow |\downarrow\rangle$, we can use Eq.4.3.2 to estimate what the FOR powers need to be at this large detuning. If we set $t_\pi = 5$ μs such that $\Omega_{eff} = \pi/t_\pi$ and choose $\Omega_{Raman} = \Omega_\sigma = \Omega_\pi$ then we find that $\Omega_{Raman} \approx 2\pi \times 10^2$ MHz. At a modest 50 μm beam waist then ≈ 82 μW is needed in each Raman beam. The power constraint is relaxed to 30 μW if we focus to a 30 μm beamsize instead. The σ beam waist is experimentally measured by varying the FOR-σ power and measuring the light shift it has on the Raman resonance condition (Eq. 4.3.2). Note that Eq. 4.3.2 indicates a changing FOR-π power imparts the same light shift on both Zeeman states and therefore does not effect the Raman resonance condition. This has been experimentally verified and the small contribution is likely to polarization impurities in the FOR-π light. It is also important to note that for maximal coherence in a stimulated Raman transition, the Rabi frequencies of the two beams should be equal. This minimizes the scattering rate from the excited state [119], which is $|3\rangle = \left|P_{1/2}\right\rangle$ here.

As shown in Fig.3.16, the NR- and FOR-σ beams propagate in the same direction, which is also true for the NR- and FOR-π-ax pair and the NR- and the FOR-π-rad pair. What is not shown in that diagram is that each pair is coupled into the same fiber before an output coupler focuses the light onto the ions. This set-up greatly reduces the number of optics around the vacuum entrance windows. It also has the added benefit that confirming NR alignment also indicates the FOR lasers are aligned to the Ba^+ ion. The NR alignment is much easier to detect by simply detuning the 493 wavemeter lock point to bring the NR detuning closer to resonance. The Ba^+ photon count is then maximized and confirms alignment of the NR and FOR lasers to a single Ba^+ ion.

The FOR lasers would ultimately be used to project the phonon state to atomic internal state in a QLS protocol [105]. Since the shutters used in this experiment are not retriggerable

at the moment, we can only toggle the lasers on once during the experimental sequence. In this way we can use the FOR lasers to perform Rabi Spectroscopy and resolve the motional sidebands. This is also how the endcap calibration, shown in Sec. 3.1.2 is performed. For the carrier transition — which has a Raman resonance of $\delta = \Delta_B + \Delta'$ — the probability to populate $|\downarrow\rangle$, if initialization is in $|\uparrow\rangle$, is given by,

$$P(|\downarrow\rangle) = \frac{\Omega_{eff}^2}{\Omega_{eff}^2 + (\omega_B - \delta)^2} \sin\left(\sqrt{\Omega_{eff}^2 + (\omega_B - \delta)^2}\ \frac{t}{2}\right)^2 \tag{4.3}$$

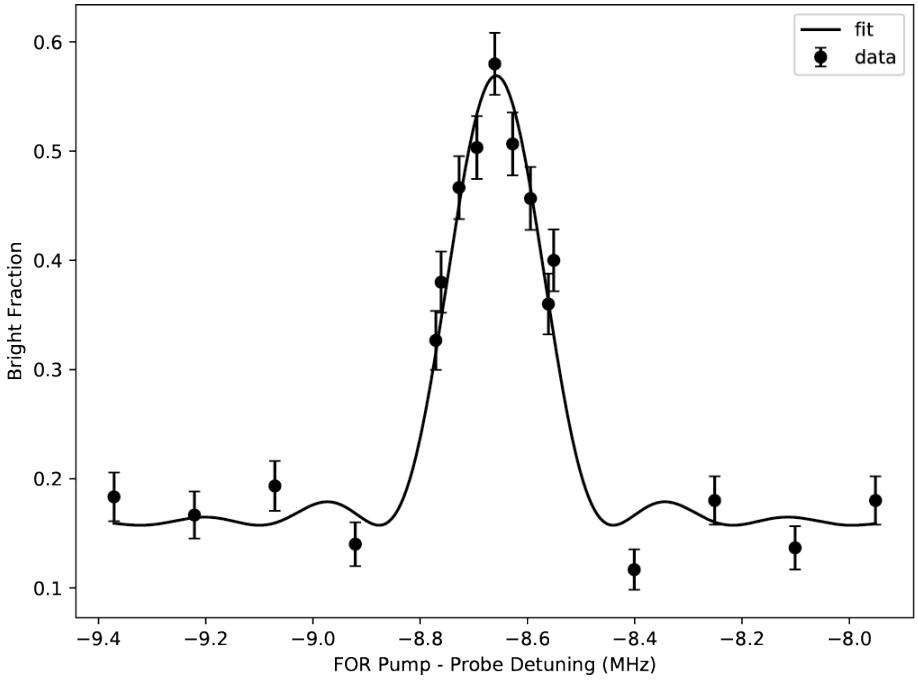

Figure 4.15: **FOR Raman Carrier Frequency Scan:** As the detuning between the FOR-π and FOR-σ beams is scanned, we find the motional carrier resonance. This resonance occurs at $\omega_B + \Delta'$. The data is fit using Eq. 4.4.3. Typically many data points are needed to properly fit the side humps.

The resulting lineshape, for a fixed Ω_{eff} and varying detuning δ has a FWHM of $\approx \pi/t$. If we were to describe driving a blue sideband transition from $|\uparrow, n\rangle$ to $|\downarrow, n+1\rangle$ then Eq.4.4.3

is amended as $\omega_B \rightarrow \omega_B + \omega_m$ and the rabi frequency is $\Omega_{eff} \rightarrow \eta_m\sqrt{n+1}\Omega_{eff}$. For a red-sideband transition from $|\uparrow, n\rangle$ to $|\downarrow, n-1\rangle$ then, $\omega_B \rightarrow \omega_B - \omega_m$ and $\Omega_{eff} \rightarrow \eta_m\sqrt{n}\Omega_{eff}$ where η_m is the Lamb-Dicke Parameter for a given motional mode m (see Appendix A). Experimental observation of these transitions and their use in ion temperature analysis is discussed in Ch. 6.

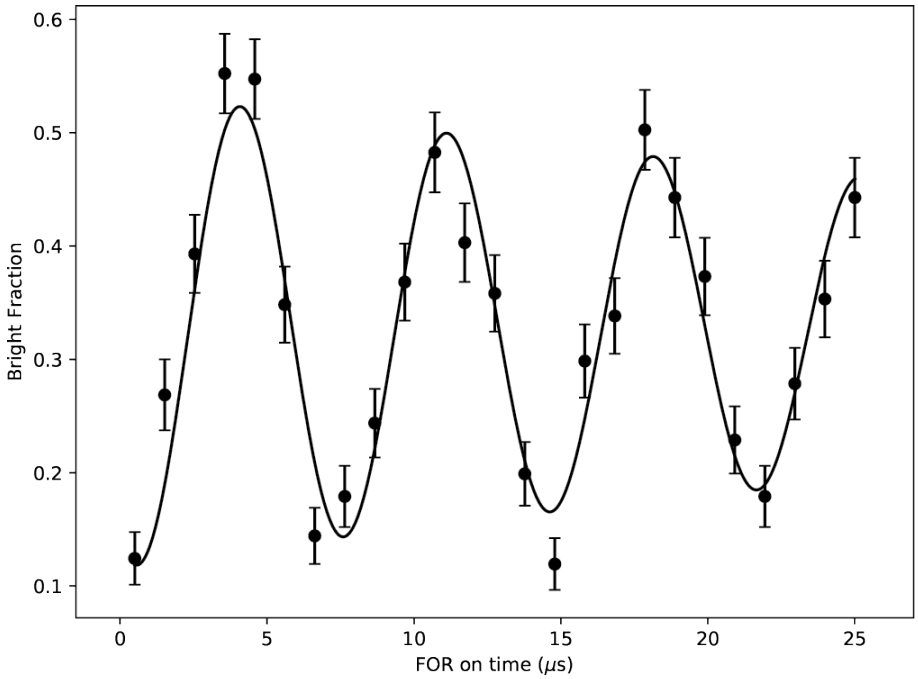

Figure 4.16: **FOR Raman Carrier Time Scan:** At a fixed detuning, the FOR Raman on time is scanned to observe both the π-pulse time necessary to achieve full population transfer and the experimental decoherence time which is indicated by the exponential envelope shrinking the amplitude of the sine wave. From the fit, we find a pi time of 3.5 μs and a decay time of 25 μs

If the FOR Raman lasers detuning is fixed to resonance (usually found first as shown in Fig.4.15) and the exposure time is scanned, we can find the proper π-pulse time. An example of this time scan, for a carrier transition, is shown in Fig. 4.16. This will cause population to continually cycle (Rabi flop) between $|\uparrow, n=0\rangle \leftrightarrow |\downarrow, n=0\rangle$. At a given time t, for this carrier transition, we find,

$$P_{|\downarrow\rangle}(t) = \frac{1}{2}\Big(1 + \exp\{-t/\tau\}\cos\left(2\Omega_{eff}t\right)\Big) \tag{4.4}$$

It is important to note that the coherence time - how long can we flop between the two qubit states - is primarily set by the ion temperature and magnetic field fluctuations. Fig 4.16 shows a single Ba^+ that is not being sideband cooled and it the coherence time is short. This is easily solved by 10 ms of RSC. If RSC is implemented, then the dominant noise source is magnetic field fluctuations, since we are driving Rabi flops between two Zeeman states. If the B field increases (decreases) the Zeeman state energy splitting increases (decreases) and the drift maximally effects the coherence time. Consideration and improvements to the quantization magnetic field are discussed in Sec. 3.3. The results show improved coherence times of up to 2.2 ms and are shown in Ch. 6.

It is important to remember that, while it is desirable to make Ω_{eff} large, so that the associated π pulse time of carrier and sideband transitions are short, a carrier Rabi frequency that is too large will broaden the observed transition and may distort the resolved sideband transitions if they are at comparable frequencies.

4.4.3.1 Raman Beam Characterization

An important experimental parameter that needs to be measured is the beam size of the σ Raman beams at the ion. This beam size, with the laser power, sets the Rabi frequency Ω_σ, which determines a great deal of other parameters including the carrier and sideband π-pulse times and light shift (Δ') setting for EIT sideband cooling. To measure this, FOR carrier scans, as shown in Fig. 4.15, are taken as a function of the FOR-σ power. These peaks occur at the resonance condition of $\delta = \Delta_B + \Delta'$ where $\Delta' = (\Omega_\sigma^2 + \Omega_\pi^2)/(2\Delta)$ and Δ

is the detuning from the transition resonance. This method also measures the base Zeeman splitting, and magnetic field strength, of the system. An example fit is shown in Fig. 4.17

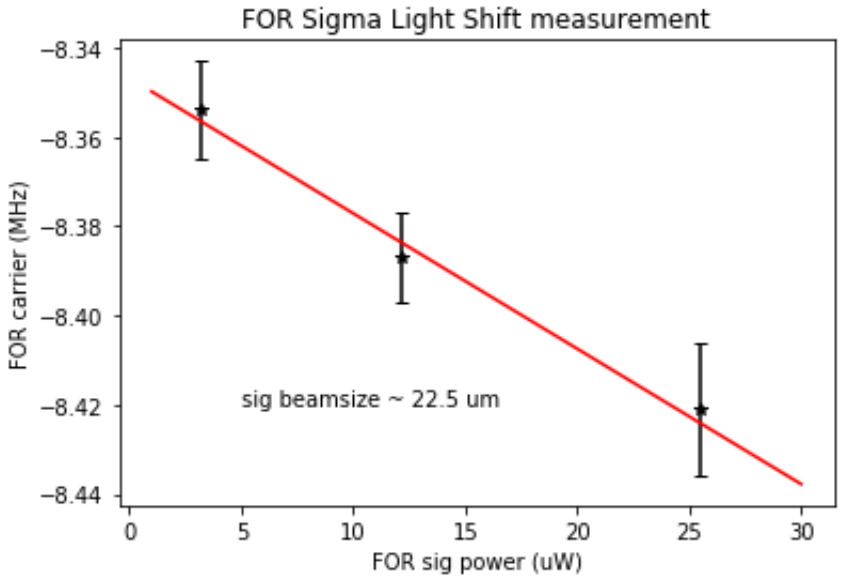

Figure 4.17: σ^+ **Light Shift Measurement:** By increasing the FOR-σ^+ power, a light shift is imparted on the $|S_{1/2}, m_j = -1/2\rangle$ state which increases the detuning needed to achieve a Raman resonance. The above plot gives a resonance of $\delta(P_{FOR_\sigma}) = -(0.00303\text{MHz}/\mu\text{ W})$*P -8.347 MHz.

Note that Ω_π cancels out by finding the slope of the line. From Eq. 4.3.2, we see that

$$\Delta_{|\downarrow\rangle_1'} - \Delta_{|\downarrow\rangle_2'} = \frac{1}{4\Delta}\left(\Omega_{\sigma_1}^2 - \Omega_{\sigma_2}^2\right) \tag{4.5}$$

Since $2\Omega^2/\Gamma^2 = I/I_s$ and $I = P/A$ we can plug in to find write the light shift in terms of the beam power P and area A and find,

$$\frac{\Delta_{|\downarrow\rangle_1'} - \Delta_{|\downarrow\rangle_2'}}{P_1 - P_2} = \frac{\Gamma^2}{8\Delta \cdot A I_s}. \tag{4.6}$$

The first part of the above expression is simply the slope of the light shift with respect to power, and thus we can rearrange and solve for A and ω_0^σ, the beam waist. Finding the

σ^+ beam waist, ω_0^σ, we can plug that into Eq. 4.3.2 for a given light shift Δ', FOR-π and FOR-σ beam power to find the FOR-π beam waist, ω_0^π. Since the NR and FOR beams are coupled into the same fiber they have the same beam waist at the ion. For the data above we find ω_0^σ =22.5 μm and ω_0^π = 37.2 μm. From this measurement we can fully characterize the Raman beams, which is vital in implementing EIT sideband cooling (see Sec. 6.3).

4.4.4 Complete Ba^+ State Readout Procedure

With each of the Ba^+ lasers and their uses outlined, we can now discuss the full Ba^+ readout procedure. We will walk through each step shown in Fig.4.18 and outline the system wavefunction when important.

The cooling and readout procedure for a single Ba^+ ion is:

(1a) Doppler cooling with the 650 nm and 493 Doppler1, Doppler2 and RedBlue lasers for 3 - 10 ms.

(1b) State prepare the molecule if desired during this phase too.

(2) RSC cooling with the NR-σ, NR-π-ax and NR-π-rad, and 649 nm laser for 10 ms

(3) Optical pumping Ba^+ into $|\Psi\rangle = |\uparrow, n = 0\rangle$ using the NR-σ and 649 nm lasers for $\sim$ 100 μs.

(4a) This is where molecular spectroscopy or heating would occur (not shown).

(4b) Conditionally transfer population from $|\uparrow\rangle$ to $|\downarrow\rangle$ using the FOR-σ and FOR-π lasers. For completeness, lets look at the two cases: $|\Psi_1\rangle = |\uparrow\rangle$ (FOR π pulse success) or $|\Psi_2\rangle = |\downarrow\rangle$ (FOR π pulse failed). Rabi π-pulse time ranges from 5 - 120 μs depending on the transition driven.

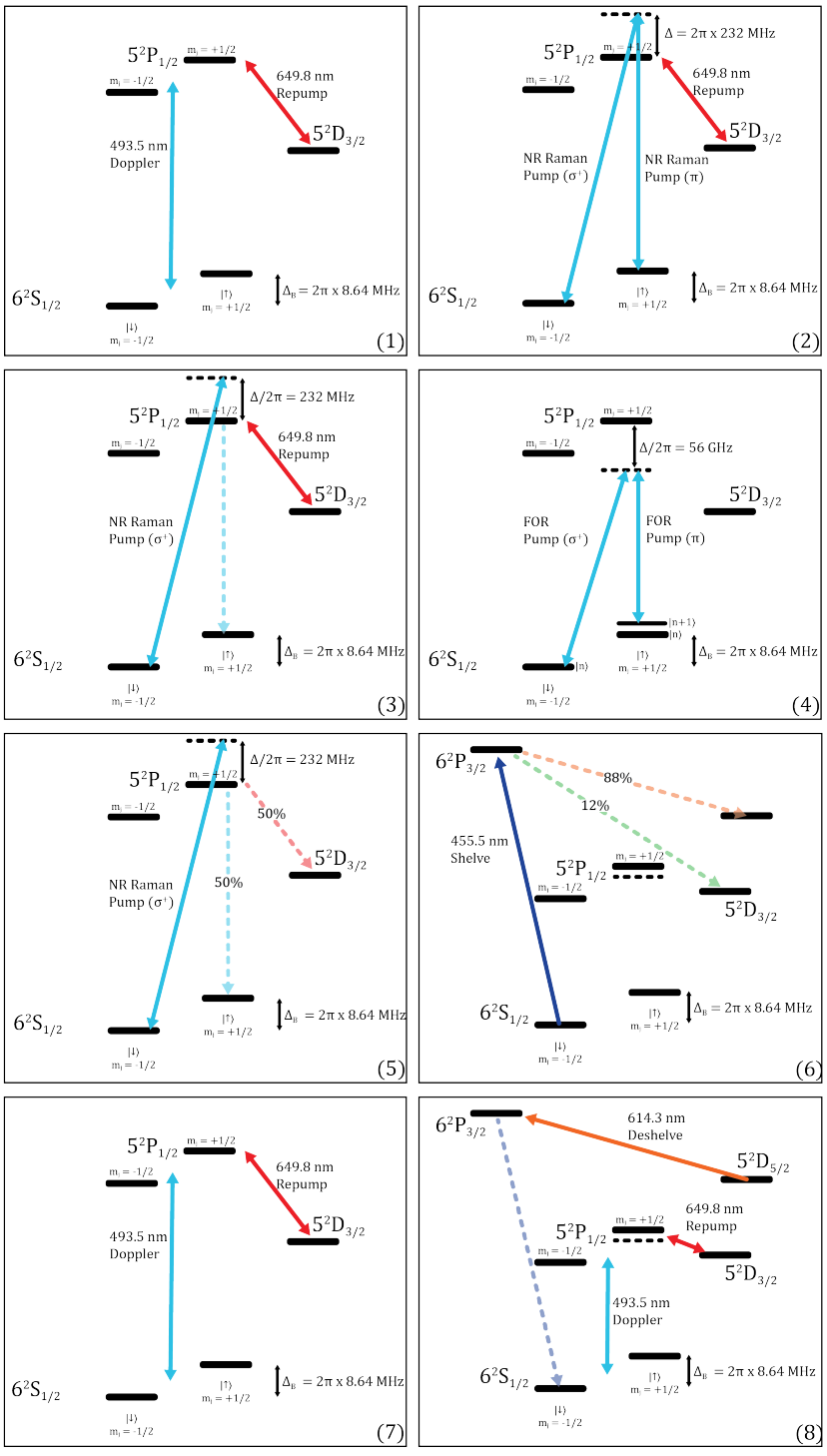

Figure 4.18: **Full 138-Ba$^+$ Readout Procedure:** The following procedure shows the entire Ba$^+$ sequence of (1) Doppler cooling, (2) sideband cooling, (3) optical pumping, (4) FOR state transfer, (5) protect, (6) shelve, (7) readout and (8) deshelve & crystal check. Typically each experimental repetition takes 60 ms which is dominated mostly by minimum shutter times and safely avoiding leakage light.

(5) Protect population that is in $|\downarrow\rangle$ by pumping it to $D_{3/2}$. Here the NR-σ light is turned on for ≈ 5 μs. Then the two conditional systems are at: $|\Psi_1\rangle = |\uparrow\rangle$ and $|\Psi_2\rangle = \sqrt{\frac{1}{2}}|\uparrow\rangle + \sqrt{\frac{1}{2}}\left|D_{3/2}\right\rangle$. The population in $\left|D_{3/2}\right\rangle$ is 'protected' because it got there from $|\downarrow\rangle$ which signified the FOR π-pulse was successful in step (4b).

(6) Shelve any remaining $S_{1/2}$ state population by applying the 455 nm laser for 10 ms. We find, $|\Psi_1\rangle = \sqrt{\frac{88}{100}}\left|D_{5/2}\right\rangle + \sqrt{\frac{12}{100}}\left|D_{3/2}\right\rangle$ and $|\Psi_2\rangle = \sqrt{\frac{88}{100}}\sqrt{\frac{1}{2}}\left|D_{5/2}\right\rangle + \left(\sqrt{\frac{12}{100}} + \sqrt{\frac{1}{2}}\right)\left|D_{3/2}\right\rangle$. Here $\sqrt{\frac{82}{100}}$ and $\sqrt{\frac{12}{100}}$ come from the $\left|P_{3/2}\right\rangle$ branching ratios.

(7) Detect population in $\left|D_{3/2}\right\rangle$ by turning the Doppler lasers back on for 10 ms. For $|\Psi_1\rangle$: $|\left\langle D_{3/2}\middle|\Psi_1\right\rangle|^2 = 0.12$ and for $|\Psi_2\rangle$: $|\left\langle D_{3/2}\middle|\Psi_2\right\rangle|^2 = 0.56$. We call this the 'bright' fraction and find that the maximum contrast obtainable is 0.56-0.12 = 0.44. While it is not a 1:1 correspondence for the population in $|\downarrow\rangle$ from step (4b) it is enough signal to distinguish the two qubit states.

(8) The 493, 649 and 614 nm lasers are applied and the ion is Doppler cooled for 10 ms. Photons collected from the PMT are counted and if they are below a certain threshold the recrystallization procedure is initiated (see Sec. 3.5.8).

The achievable signal from this readout scheme is at max 56% and min of 12% bright ratio with contrast of 44%. Since the photon histograms follow binomial statistics (See Sec. 4.4.1) 100 repetitions provides a max error of 5% which is a minimum signal (for 12%) to noise ratio of only 2.4. This is why typically 300 - 500 and sometimes 1000 repetitions are taken. If we were to improve the total readout contrast this would lower the averaging time. This contrast is shown in Fig. 4.15 and 4.16 where the signal has a baseline of 0.12 and maximal value of 0.56 of bright fraction.

4.5 Future Improvements: Quadrupole Shelving

The two focal points in our group with Ba^+ operations are improving sideband cooling and the readout signal. The former is addressed in Ch. 6. Improving the readout signal has two main components: reducing the overall experimental time and improving the signal contrast. A major review of the experiment would be needed to reduce the experimental time [19]. A much more tangible aspect to improve upon would be our qubit state readout scheme.

The best way to improve our signal is by driving the quadrupole transition from $\left|S_{1/2}, m_j\right\rangle \rightarrow \left|D_{5/2}, m_j\right\rangle$ [113], [120], [121] Since the linewidth of this transition is narrow (2π x 5 mHz) a lot of power, in a narrow linewidth is required to obtain reasonable Rabi frequencies and π-pulse times. Since driving a sideband usually has a $\sim$10 times lower Rabi frequency (set by the Lamb-Dicke parameter) a first step would be to drive carrier transitions and shelve either $|\uparrow\rangle$ or $|\downarrow\rangle$ selectively while still using the FOR lasers to transfer population conditionally between $|\uparrow\rangle$ and $|\downarrow\rangle$. The other advantage of the quadrupole transition is that $\Delta m = 0$ transitions can be driven. If so, the coherence time of qubit operations is still effected by magnetic field fluctuations but to a smaller level. Both transitions move in the same direction in energy, though at a different magnitude due to the different g-factors.

By inheriting a 1762 nm NKT fiber laser (bought almost a decade ago) and a motivated graduate student named Qiming Wu, the hope of driving the $S_{1/2} \rightarrow D_{5/2}$ quadrupole transition became real in 2018. The goal then it to lock the laser to an ultrastable cavity [122] using the Pound-Drever-Hall (PDH) locking technique [116], [123]. These references go into great detail regarding the considerations, noise sources, and how to measure them. I will simply summarize their results: everything is noisy and you need to be worried about every

component, so make everything as stable as possible. The goal of this set-up is to increase the coherence, and narrow the power spectral density of a single laser. I refer the reader to Ref. [122] for a concise list of considerations, design and references for further technical reading.

A 1762 nm NKT fiber laser with an output linewidth of ~ 1 kHz is referenced and locked to an ultrastable cavity. A cavity system was purchased through Stable Laser Systems. The system contains two main components: a vacuum chamber and a ULE (ultra-low expansion) Zerodur cavity. The vacuum chamber is pumped down to 8×10^{-8} Torr from an initial vent to install the ULE cavity and the vacuum is maintained by an ion pump. The lack of air reduces the thermal contact from the outside to the ULE cavity. The vacuum chamber can be maintained at a stable temperature, set to the zero crossing of the ULE cavity though this has not limited operation yet. The cavity consists of two super polished mirrors, one plano and one concentric with a 50 cm radius of curvature. The expected cavity finesse, $\mathcal{F} \sim 3.5 \times 10^5$. The cavity has a free-spectral-range (FSR) of 1.5 GHz which results in mode linewidths of 4.28 kHz. Installation of the cavity is shown in Fig. 4.19.

A diagram of the total 1762 nm optical system is shown in Fig. 4.20. The system is bolted to a Thorlab Nexus breadboard which provide vibration dampening for any vibrations the optics experience. The breadboard is mounted ontop of a stabilized platform to isolate the breadboard from vibrations on the larger optical table and floor. Thick steel posts of a certain height were used when possible to also dampen vibrations.

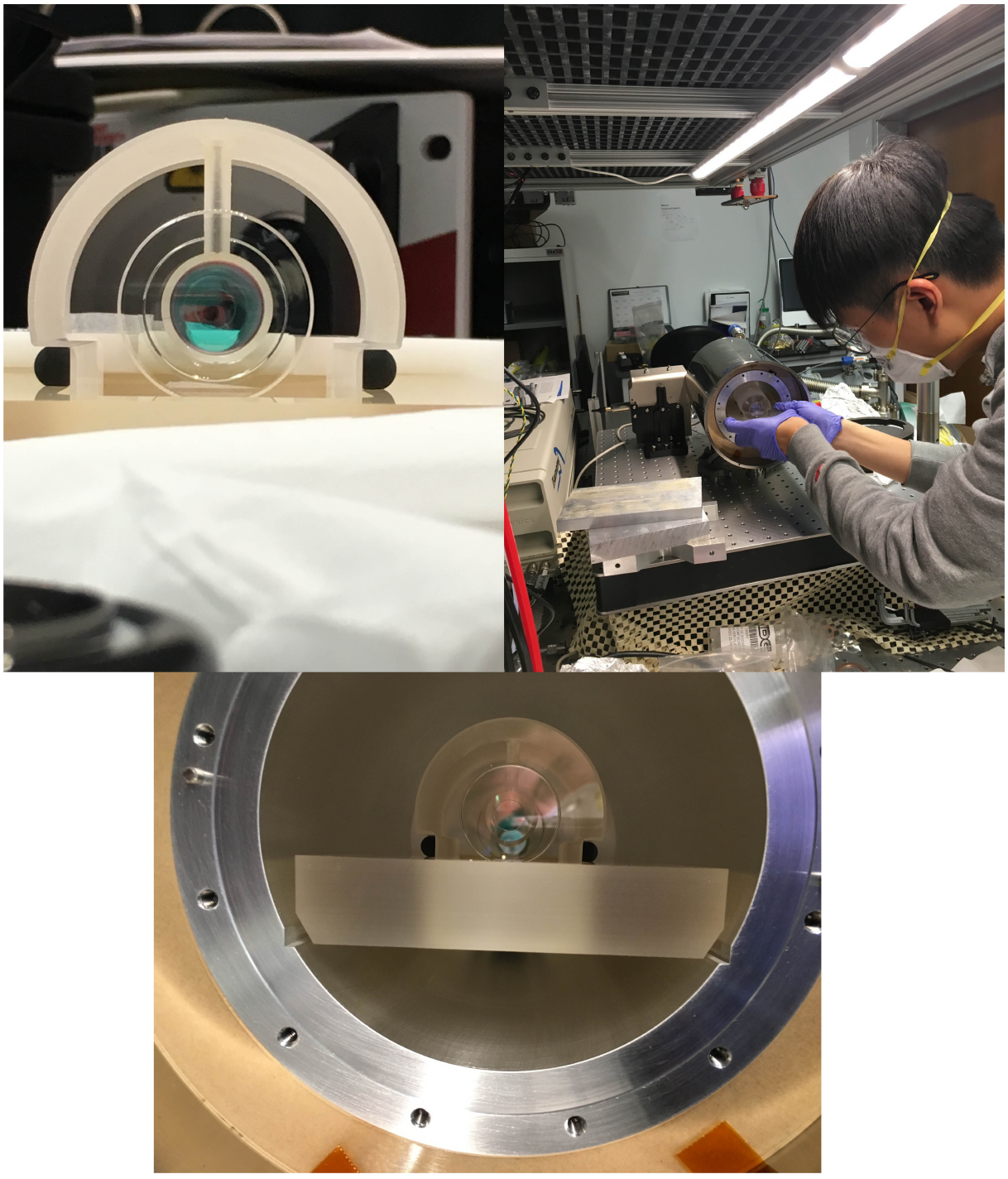

Figure 4.19: **ULE Cavity Install Completed on 10/28/18** The SLS notched cavity design is resting on four Viton balls

The NKT laser has 15 mW of output power at 1762 nm. The beam first passes through several polarization components to obtain linear polarization from its originally circularly polarized light. The light is then passed through a double-pass AOM which acts as a resource for fast-feedback from the PID circuit. This is necessary because the NKT laser is only tunable externally by adjusting the PZT, which responds to low frequencies best (sub-10 kHz). The Brimose AOMs are birefringent and are most efficient with horizontal polarization. As a result, the laser has to be aligned such that the input and output beams are not perfectly overlapped. This is achieved by using a corner cube mirror. When the PDH lock is working an optimized, the output light from this AOM will have a narrow linewidth.

The beam is then split into two paths, one that goes to the ultrastable cavity and the other that is directed towards the experiment. To implement PDH locking, the laser needs to be phase modulated. This is accomplished by passing the laser through a QUBIG EOM[12] driven by a 20 MHz source. The EOM is a LN crystal with a 3x3 mm^2 aperature, R <1% at 1762 nm and to obtain 1 rad modulation 23 dBm of RF drive power is needed[13]. The QUBIG system has a dedicated EOM driver[14] that is also built to demodulate the signal from its own low-noise photodiode [15]. As a result, all of the modulation-demodulation electronics involved in PDH locking are within one system and well engineered [116].

Mode-matching to the cavity is achieved by placing an f = 300 mm lens at a distance d = 200 mm from the front mirror of the cavity. This can be easily modeled to ensure the reflected beam has the same radius of curvature as the input beam. A photodiode and Hammamatsu IR camera are placed at the transmission port to detect the transmitted power and cavity mode. These are extremely helpful tools to aid in alignment and locking. The

[12]Model EO-20L3_IR_T_DC_TXC
[13]Note we later purchased the wedged-face crystal after appearance of RAM
[14]ADU_HP
[15]PD-AC100-SWIR

main principle of PDH locking is that when the laser is on resonance, there is no power reflected back from the cavity. An antisymmetric error signal in the reflected power is due to the phase modulation aspect which then allows the laser to be steered towards resonance. The error signal is generated by the QUBIG driver and sent to a PID module. We have used both a MogLabs FSC module as well as a Toptica FALC module and have found the MogLabs FSC to be easier to operate.

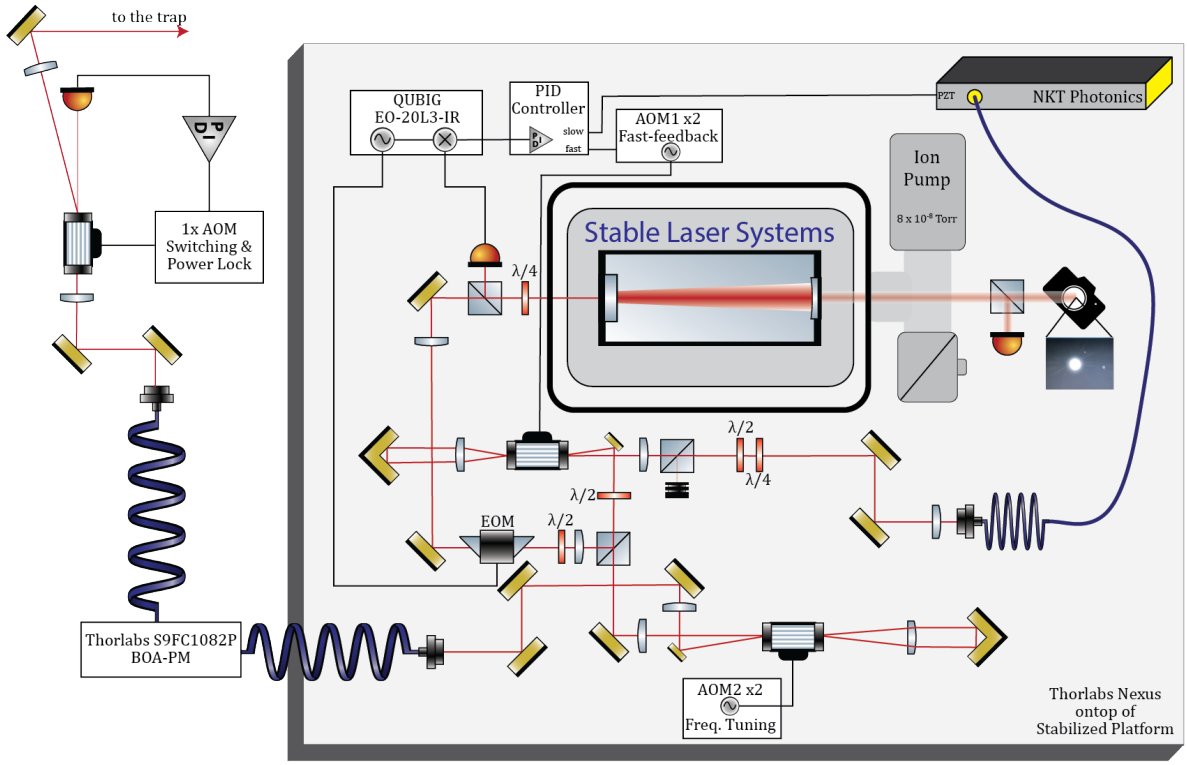

Figure 4.20: **1762 nm Laser System:** Includes all the AOMs for locking, switching and frequency shifting.

When optimized and aligned, the 1762 nm stay locked for hours at a time[16]. To characterize the lock we aspired to first drive the Ba^+ $S_{1/2} \rightarrow D_{5/2}$ quadrupole transition. There is a challenge of finding a laser setting that, when offset by the fast lock double-pass AOM

[16]This was achieved after months of hard work by Qiming Wu

is resonant with a cavity mode and on resonance with the Ba^+ transition. It is too much to wish for the laser frequency plus AOM1 detuning is exactly the Ba^+ resonance, $\omega_L + 2 * \omega_1 = \omega_{quad.}^{Ba^+}$. That is why a second AOM, AOM2 is needed to achieve frequency tuning to reach the atomic resonance. Typically the laser is locked to the TEM_{10} mode to hit both frequency points. A third AOM, AOM3 is installed for fast switching of the 1762 nm laser on and off. AOM3 also serves to lock the power of the 1762 nm light by looking at the carrier power as a function of time, in the same way that the 493, 649 and FOR lasers are power locked. Both AOM1 and AOM2 were chosen for their large, 50 MHz bandwidth and the diffraction orders were carefully chosen to maximize the frequency tuning range. To gain a better understanding of the the laser wavelength and help us to tune the AOM settings, we borrowed a Bristol 521 IR wavemeter with a resolution of 1 GHz[17]. From the recent findings of Ref. [113], we set the initial laser to 1762.174 nm and scanned around.

The 1762 nm laser is aligned to the trap, and copropagates with the NR-π light (see Fig. 3.16). Alignment to the trap was made by overlapping the 1762 nm light with the 650 nm in the near and far field. For a quadrupole transition, with linear polarization and wave vector that is perpendicular to the magnetic field only $\Delta m = \pm 1$ transitions could be driven. If it was desired to drive $\Delta m = 0$ transitions then the 1762 nm light would need to be overlapped with the 413 nm and Doppler2 beams shown in Fig. 3.16.

Upon course scanning of the 1762 nm frequency in 5 MHz steps the resonance was found by observing when the Ba^+ ion would flash dark when also being illuminated by the Doppler lasers and a extremely weak 614 nm laser (which quickly repumps the state). Generally the resonant frequency is going to be found when

[17]Special thank you to the Geraci Group

$$\omega_L = \omega_e + \omega_B^{D_{5/2}} + \omega_B^{S_{1/2}}, \tag{4.7}$$

from which we can rewrite as,

$$\omega_L - \omega_e = \frac{\mu_B B}{\hbar}\Big[g_j^D m_j^D - g_j^S m_j^S\Big]. \tag{4.8}$$

Here, ω_e is the electronic contribution to the transition and $\omega_B^{S,D}$ are the shifts of the Zeeman states in the presence of a magnetic field. Neglecting higher order terms, the g-factors are 6/5 and 2 for the $5D_{5/2}$ and $6S_{1/2}$ states respectively. Since we can only drive $\Delta m = \pm 1$ lets only concern ourselves with the transitions shown in Table 4.3.

Table 4.3: **Magnetic Field Contribution to Different Ba^+ Quadrapole Transitions** Put in order of increasing frequency. While the difference in energy between transition (2) and (1) is the same as (4) and (3), by optical pumping into a given state prior to shelving, we can determine which transition is being driven.

Label	$m_j^S \rightarrow m_j^D$	$\omega_R - \omega_L$	$\omega/2\pi$ (MHz)
(1)	$-\frac{1}{2} \rightarrow +\frac{1}{2}$	$+\frac{8}{5}\frac{\mu_B B}{\hbar}$	18.8
(2)	$+\frac{1}{2} \rightarrow +\frac{3}{2}$	$+\frac{4}{5}\frac{\mu_B B}{\hbar}$	9.4
(3)	$-\frac{1}{2} \rightarrow -\frac{3}{2}$	$-\frac{4}{5}\frac{\mu_B B}{\hbar}$	-9.4
(4)	$+\frac{1}{2} \rightarrow -\frac{1}{2}$	$-\frac{8}{5}\frac{\mu_B B}{\hbar}$	-18.8

In this way, if we find three transitions we can triangulate and determine what each of them is. The AOM used to tune is the '+2 order' meaning that increasing the 'voltage' is also an increase in the frequency. We found the relationship of the Brimrose AOM2 such that the frequency of the laser after the double-pass was ν_{lock} + 32.148*V + 351.99 MHz, where

Table 4.4: **Assignment of $S_{1/2} \rightarrow D_{5/2}$ Lines** Here we set (2) to be at the middle of the two lines observed at (2') = 415.61(5). Without putting a better limit on the lines and magnetic field, we consider this a reasonable agreement to appropriately assign the lines.

Label	Expected Separation $\omega/2\pi$ (MHz)	Measured Separation $\omega/2\pi$ (MHz)
(1)-(2')	9.4	9.3
(2')-(4)	28.2	26.6
(1)-(4)	37.6	35.9

V is the analog voltage applied to AOM2. At the time of taking this data the magnetic field B $\approx$ 8.6 G = 0.00086 T. Estimating frequency separations of (1)-(2) = (3)-(4) = 9.4 MHz, (1)-(3) = (2)-(4) = 28.2 MHz and (1)-(4) = 37.6 MHz.

Line (1) found to be at 424.921(14) MHz which is the frequency shift from stabilized lock. A 20 ms exposure of the 1762 nm light was used here. Line (2) was found to show two repeatable peaks at 415.27(4) and 415.94(4) MHz, a frequency difference of 0.67(6) MHz. This is interesting to observe, at these trap parameters, the axial frequency is 266 MHz, and radial modes at at 569 kHz and 642 kHz. It is possible this is a sideband, however we would expect two sidebands to appear, symmetric about the carrier. Line (3) was not observed surprisingly, even though it was scanned over. Line (4) was found to be at 389.0(1) MHz, using a 10 ms exposure time. Unfortunately only one scan was taken over this line. The results of this analysis and the observed difference between lines are shown in Table 4.4.

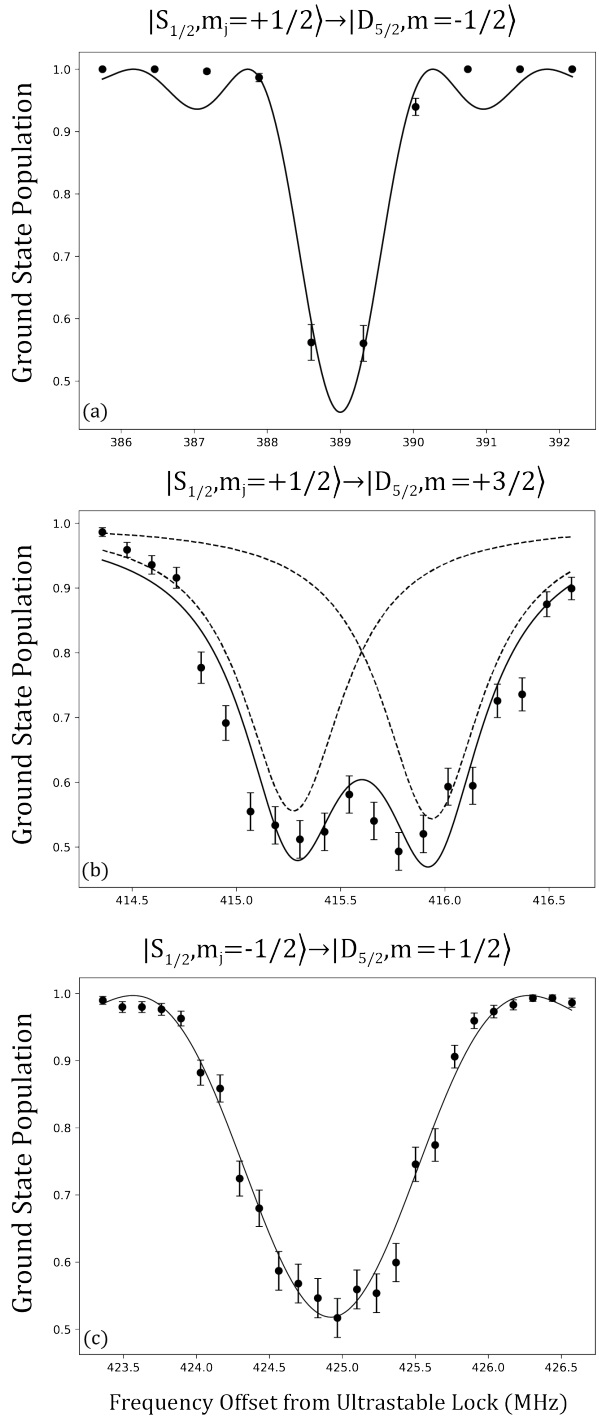

Figure 4.21: **$S_{1/2} \rightarrow D_{5/2}$ Shelving Data:** (a) Shows shelving on line (4), (b) shows shelving on line (2) and interestingly two peaks, (c) shows shelving on line (1) which obtains the largest Zeeman shift because the magnetic sublevels move in opposite directions. Note this not the absolute frequency, there is a +100 MHz after from a +1x switching AOM.

We see good agreement and understanding of what transitions are being driven at the specific AOM frequency settings. All of these lines were taken before acquiring the Thorlabs BOA, such that only 100 μW of 1762 nm was incident on the ion. If we use the BOA then there is 1.6 mW to the ion. After finding a resonance, it is natural to then fix the laser frequency and attempt Rabi flops to determine the Rabi frequency and π-time. From Fig. 4.22 we find that with 1 mW from the BOA we shelve on the 163(14) μs timescale and 50% population exchange at 600 us. Without the BOA we have 100 μW to the trap, a decay time of 1.68(13) ms and 0.50% spin flip at 6 ms. Interestingly, the Rabi frequency (and π-pulse time) scales with $\sqrt{P}$ and we would expect only a ~ 4 times increase in the shelving time. More analysis of the resulting spectrum from the BOA is needed. From Fig. 4.22, it is clear that decoherence is still faster than our π-pulse time. As a result, the laser power, while very helpful to shelve faster, is not the leading issue.

From these initial scans, we can attempt a back of the envelope calculations to the linewidth, using Eq. 3.20 thesis from [124]. Estimating the Rabi frequency as $1/(2^*\tau)$, where τ is the coherence time, then we can estimate a linewidth on the order of 2 π x 300 Hz, depending on the beam size, which is currently unknown. A ratio of transition linewidth to laser linewidth roughly indicates of only 1 μW, 10 nW of the PSD went to the resonance linewidth.

4.5.0.1 Next Steps

While Qiming toiled away for a year setting everything up, all of the experimental data was taken in a week during February 2020. Shortly after COVID shut down our efforts and the progress with the 1762 nm grinded to a complete halt. It would be ideal to repeat the experiments shown above, to find line (3) and understand why two features appear in line

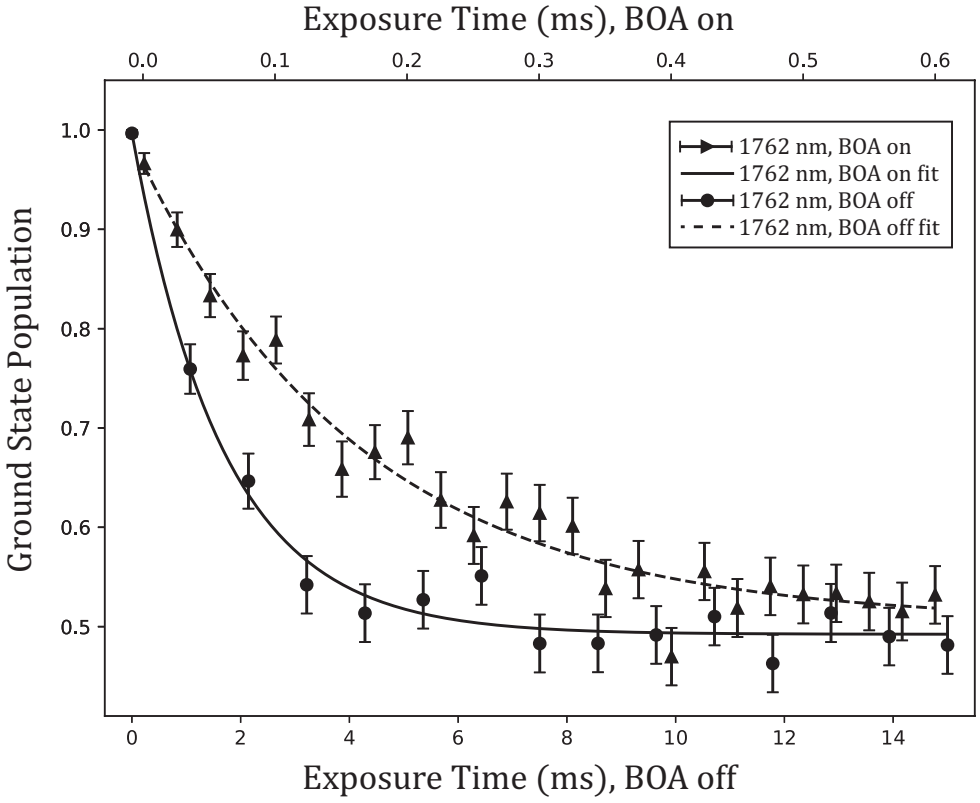

Figure 4.22: **S → D Time Scan:** Here we are flopping on line (2') from $\left|S_{1/2}, m_j = +1/2\right\rangle \rightarrow \left|D_{5/2}, m_j = +3/2\right\rangle$. With the BOA off we have 100 μW to the trap and with it on we have 1.5 mW to the trap.

(2). It would also be important to vary the 1762 nm power and measure the resulting light shift. In this way the beam size can be determined.

Possible experimental upgrades including adding the wedged crystal case option to the EOM. At the time of taking this data residual amplitude modulation (RAM) caused the DC offset of the error signal to drive in time. Etaloning in the crystal is one main contributor to this [122]. We will also increase the EOM resonance to a 45 MHz RF drive. The higher drive frequency creates a tighter lock at the cost of locking window (how large in frequency at the lasers excursions before jumping lock). Other considerations include moving the AOM1 closer to the cavity so that very small beam deflections (caused by the lock) do not couple to the lock. Further work also is needed to improve the error signal amplitude.

CHAPTER 5

SiO^+: The Money Maker

A process cannot be understood by stopping it.
Understanding must move with flow of the process,
must join it and flow with it
Frank Herbert
"Dune"

The molecule silicon monoxide cation, $^{28}Si^{16}O$, was one of the first molecules outlined by our group that may be amenable to Doppler cooling and optical pumping [125]. This is due to its favorable electronic structure, which contains an optical transition at ≈ 385 nm between the $X^2\Sigma^+$ and, short lived ($\tau \approx 70$ ns), $B^2\Sigma^+$ states. While a low lying $A^2\Pi$ state exists, its larger equilibrium bond length means that the $B^2\Sigma^+$ state is unlikely to decay along that channel. The SiO^+ molecule is favorable because the equilibrium bond lengths of the $X^2\Sigma^+$ and $B^2\Sigma^+$ states are similar. This typically occurs when the electron that is excited does not participate in the molecular bonding and is localized to a single atom [94]. In this way, the vibrational state of the molecule is unlikely to change if the molecule cylces between the $X^2\Sigma^+$ and $B^2\Sigma^+$ states.

Motivated by these favorable parameters, our group has worked towards and demonstrated resonant ionization of SiO [102], optical pumping to the ground rovibrational state [46], and optical preparation of higher rotational states [47]. The ability to optically prepare a molecule to a single state or narrow distribution of quantum states opens up several interesting avenues of further scientific pursuit. Here, I discuss some of the applications that are

Constant	Definition	$X^2\Sigma^+$	$A^2\Pi$	$B^2\Sigma^+$
T_e (cm^{-1})	Energy Offset	0	2242.25(28)	26029.0138(16)
ω_e (cm^{-1})	Vibrational Constant	1162.1823(27)	94.28(32)	1136.5802(12)
$\omega_e x_e$ (cm^{-1})	1^{st} Vib. Anharmonic Term	6.9698(15)	7.005(72)	6.92149(45)
B_e (cm^{-1})	Rotational Constant	0.7206159(36)	0.618588(31)	0.7130346(36)
r_e (Å)	Equilibrium Bond Length	1.516	1.636	1.524

Table 5.1: **Depurturbed Values:** For the $X^2\Sigma^+$, $A^2\Pi$, and $B^2\Sigma^+$ state constants reported in [126]. These values are unperturbed and accurate transition energies require rediagonalization of the perturbed Hamiltonian.

possible with state prepared SiO^+ molecules.

Most of this chapter involves work done in the apparatus described in Refs. [48], [94] or modeling from results taken in that set-up. Since the experimental apparatus is described in detail there, I will omit much of that information and refer the reader to those references. The results from rate equation modeling of optical pumping SiO^+ are currently being prepared in a manuscript. Additionally, the experimental results of reaction rate measurements of SiO^+ with background H_2 are also currently being prepared for publication.

5.1 State Structure

The three lowest electronic levels relevant to optical pumping of SiO^+ are the ground $X^2\Sigma^+$ state, and the excited $A^2\Pi$ and $B^2\Sigma^+$ states. The potential energy curves are plotted in Fig. 5.1 and relevant constants are shown in Table 5.1. See [126] for a complete description of the energy levels and their expressions for each state. Among other levels not shown (see Ref. [127]), there is an excited $C^2\Pi$ state that is used for resonant multi-photon dissociation (REMPD) and provide a pathway for quantum state readout [46], [47]. REMPD is a destructive process, and a nondestructive state readout scheme for SiO^+ is proposed in Ch. 7.

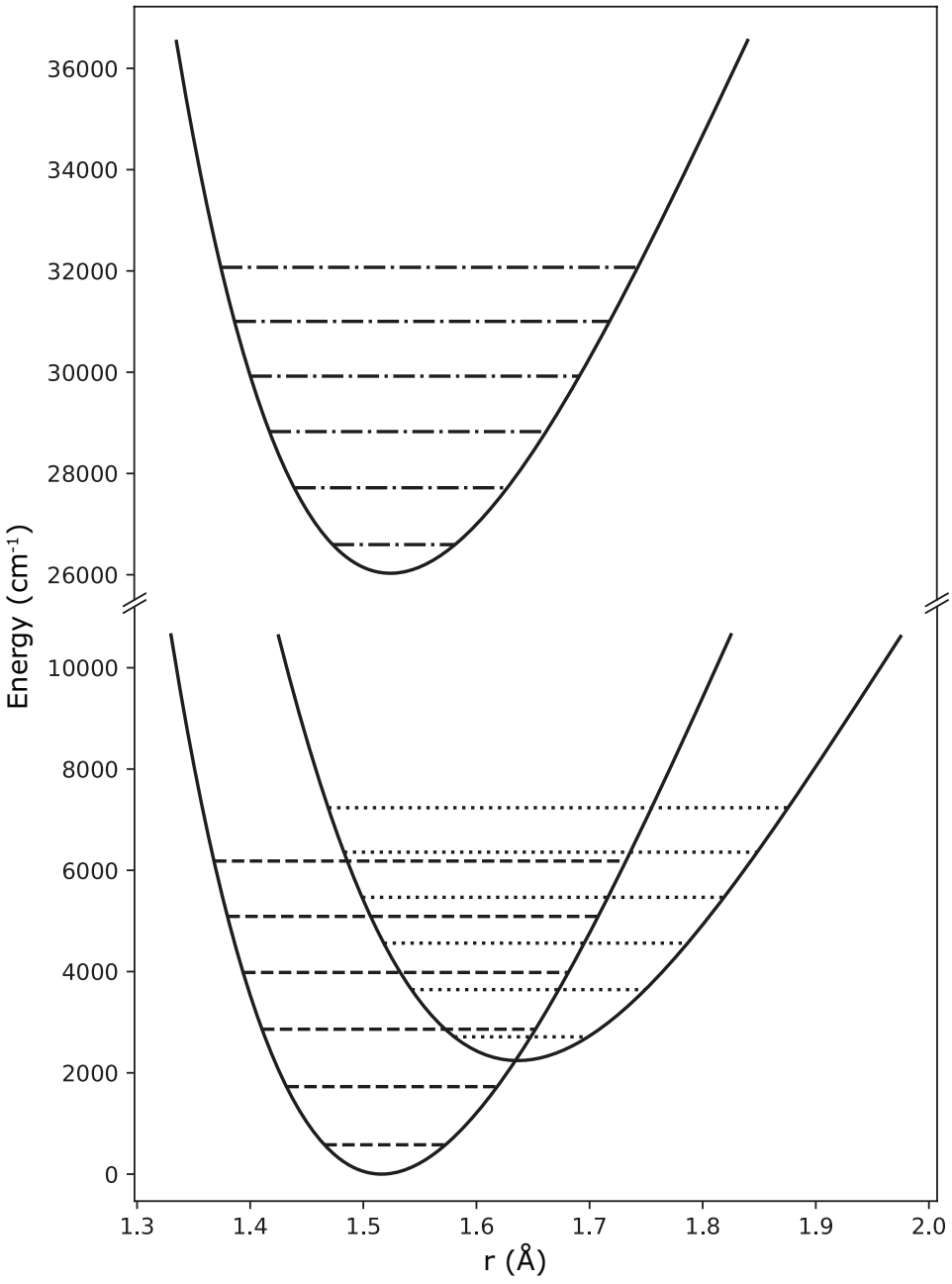

Figure 5.1: **Three Lowest Electronic Levels of SiO^+ :** The ground $X^2\Sigma^+$ (dashed vibrational levels) and the excited $A^2\Pi$ (dotted vibrational levels) and $B^2\Sigma^+$ (dot-dash vibrational levels) states. These curves were obtain by Rydberg-Klein-Rees (RKR) inversion [128] of experimental data [126].

As population is excited on the X→ B transition at 385 nm, several rovibrational states of the X, A, and B levels become populated. Both the X, and B states are described by Hund's case (b) [62] and their wavefunctions can be written (excluding angular momentum sublevels) as $|e, v, N, J, p\rangle$ where e is the electronic state, v is the vibrational quantum number, N is the rotational angular momentum, J is the total angular momentum excluding nuclear spin, and p is the state parity ('+' or '-'). For the X and B state, if N is even then p is even (+) parity and if N is odd, p is odd (-) parity. Additionally, in Hund's case (b) for $S = 1/2$: if N = 0 then J = 1/2 and for $N \geq 1$, $J = N\pm$ 1/2 and every N level is split into a doublet by the spin-rotation interaction [62].

The electronic transition dipole moment (TDM) between two states ($|e, v', J''\rangle$ and $|g, v'', J''\rangle$) is given by,

$$\mu_{i',f''} = \langle\chi_{v',J'}| \langle\psi_e|\hat{\mu}_{el}(r)|\psi_g\rangle|\chi_{v'',J''}\rangle \tag{5.1}$$

The TDMs for transitions that play a role in optical pumping of SiO^+ are shown in Fig. 5.2. It is common to assume that the electric dipole operator, $\hat{\mu}_{el}(r)$, is constant over the vibrational wavefunction and that part can be taken out of the integral. This is known as the Franck-Condon approximaiton and the square of this value is called the Franck-Condon Factor (FCF), defined as,

$$q(v', v'') = |\langle\chi_{v'}|\chi_{v''}\rangle|^2 \tag{5.2}$$

where $\chi_{v'}$ and $\chi_{v''}$ are the vibrational wavefunctions for the upper and lower states. Since the $X^2\Sigma^+$ and $B^2\Sigma^+$ states have similar equilibrium bond lengths, the SiO^+ molecule has "diagonal FCFs" where $q_{v',v''=v'} \approx 1$. As a result, the molecule's vibrational state is unlikely

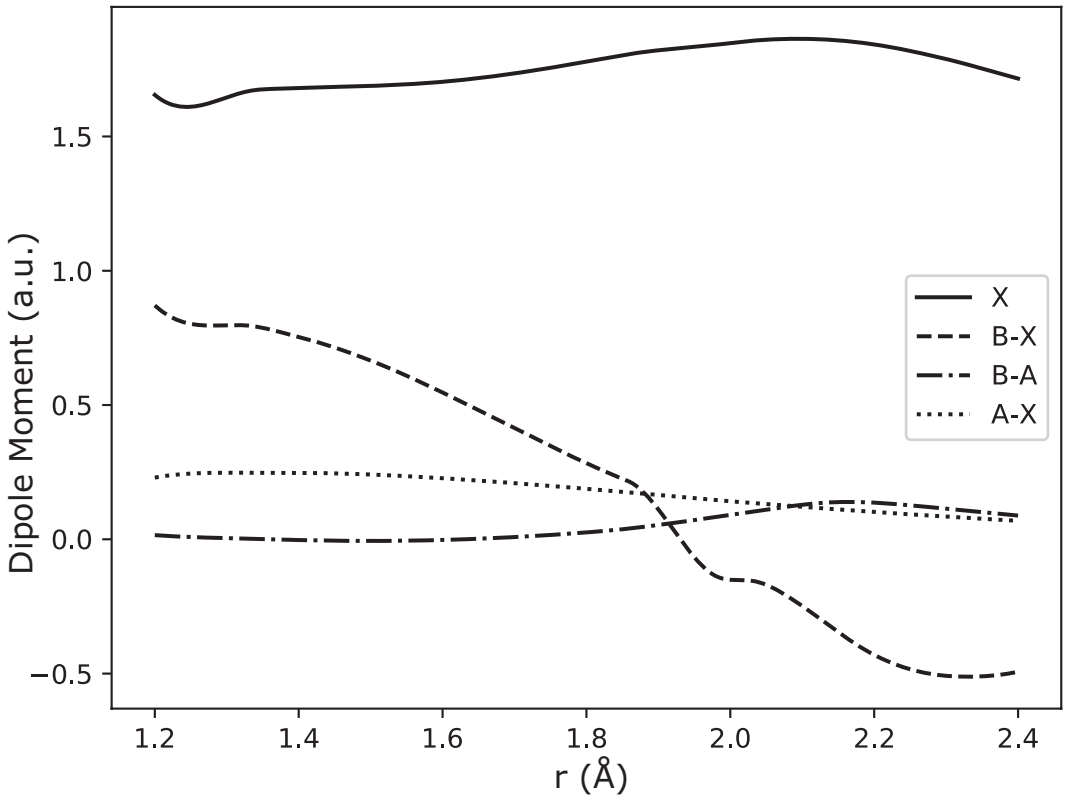

Figure 5.2: **SiO^+ Transition Dipole Moments:** The relevant TDMs between the $X^2\Sigma^+$, $A^2\Pi$, and $B^2\Sigma^+$ States are shown. The permanent dipole moment of the $X^2\Sigma^+$ is shown by the solid line. Note that in the FCF region for the B-X transition ($r \approx 1.52$ Å) the TDM is fairly linear with a comparatively steep slope.

v' \ $v'' - v'$	0	+1	-1
0	98.9 / 0.642	1.1 / 0.024	-
1	96.7 / 0.620	2.2 / 0.031	1.1 / 0.111
2	94.5 / 0.599	3.3 / 0.035	2.2 / 0.154
3	92.3 / 0.578	4.4 / 0.037	3.2 / 0.187
4	90.1 / 0.558	5.5 / 0.038	4.2 / 0.212
5	87.9 / 0.537	6.6 / 0.038	5.2 / 0.234

Table 5.2: **FCFs and TDMs for B-X Decays:** FCFs (%) / $\mu_{v',v''}$ (a.u.) for $\Delta = 0, \pm 1$ transitions of the B-X system. The TDMs in the $v'' - v' =$ -1 column reflect the intensity of vibrational cooling events upon B state decay, whereas $v'' - v' = 1$ represents that of vibrational heating. Note that despite similar FCFs for Δv $= \pm 1$ transitions, the corresponding TDMs, $\mu_{v',v''}$, are quite different.

to change as population cycles between X and B and this drastically reduces the need for additional repump lasers. This is one of the main reasons SiO^+ is an attractive candidate for optical pumping.

The potential energy curves shown in Fig. 5.1 were obtain by Rydberg-Klein-Rees (RKR) inversion [128] of experimental data [126]. Vibrational wavefunctions were then obtained by numerical integration of the potential energy curves and used to calculate FCFs, TDMs between the X, A, and B states as well as perturbation matrix elements between the X and A states. The calculated FCFs and TDMs are shown in Table 5.2. What is interesting is that we find an asymmetry in the TDMs between $\Delta v = \pm$ 1 transitions (so-called 'off-diagonal' transactions), despite the two transitions having similar FCFs. For example, decay from $|B, v = 1\rangle$ to $|X, v = 2\rangle$ has a FCF of 2.2% and TDM of 0.031 a.u. while decay to $|X, v = 0\rangle$ has a FCF of 1.1% and a TDM of 0.111 a.u.. While analysis using only FCFs show that the $\Delta v = +1$ decay is preferred, in fact the TDM is almost four times less than the $\Delta v =$ -1 decay channel.

5.1.1 Harmonic Oscillator Approximation

While direct numerical integration provides the most accurate estimate for TDMs, simplified models can provide insight and rough analysis. Motivated by a further understanding of the asymmetry in the TDMs for off-diagonal decays, one can approximate the molecular potential well as a harmonic oscillator (valid for low v) and use perturbation theory to gain insight. The Hamiltonian for a harmonic oscillator is,

$$H_g = \frac{p^2}{2m} + \frac{1}{2}m\omega^2 x^2 \ , \tag{5.3}$$

or in dimensionless form,

$$\frac{H_g}{E_\mathrm{o}} = \frac{1}{2}\left(\frac{p}{p_\mathrm{o}}\right)^2 + \frac{1}{2}\left(\frac{x}{x_\mathrm{o}}\right)^2 = \frac{1}{2}\tilde{p}^2 + \frac{1}{2}\tilde{x}^2 \ , \tag{5.4}$$

where $E_\mathrm{o} = \hbar\omega$, $p_\mathrm{o} = \sqrt{\hbar m\omega}$, and $x_\mathrm{o} = \sqrt{\hbar/m\omega}$ are the energy, distance and momentum scales and $\tilde{x}$ ($\tilde{p}$) is the dimensionless position (momentum) operator.

Suppose the excited state has a similar potential to the ground state ($\omega = \omega'' \simeq \omega'$) and only differs in equilibrium bond length by $\Delta x = x_e'' - x_e' \ll 1$. Both of these are valid for SiO^+ , see Table 5.1. In dimensionless form we can write $\Delta\tilde{x} = \frac{\Delta x}{x_\mathrm{o}}$. Here, we use the typical convention of molecular emission where parameters of the ground state are denoted by a double prime (x_e''), and those of the excited state by a single prime (x_e'). We then can write down the dimensionless excited state Hamiltonian as,

$$\frac{H_e}{E_\mathrm{o}} = \frac{1}{2}\tilde{p}^2 + \frac{1}{2}\big(\tilde{x} + \Delta\tilde{x}\big)^2 \cong \frac{H_g}{E_\mathrm{o}} + \tilde{x}\cdot\Delta\tilde{x} \ . \tag{5.5}$$

From the above equation, it is clear that the second term is a perturbation, one that

couples adjacent levels of the harmonic oscillator, since $\tilde{x} = \frac{1}{\sqrt{2}}(\hat{a} + \hat{a}^{\dagger})$. In this way, we can write wavefunctions of the excite state (χ'_n) in terms of the ground state wavefunctions ($\chi''_{n,m}$). First order, non-degenerate perturbation theory says that,

$$|\chi'_n\rangle = |\chi''_n\rangle + \sum_{n \neq m} \frac{\langle \chi''_m | H' | \chi''_n \rangle}{(E''_n - E''_m)} |\chi''_m\rangle \,. \tag{5.6}$$

Here, $H' = \tilde{x}\Delta\tilde{x}$. Keeping only terms of the states $v, v+1, v-1$ we find,

$$\chi'_v = \chi''_v + \frac{\langle \chi''_{v+1} | H' | \chi'_v \rangle}{(E''_v - E''_{v+1})} |\chi''_{v+1}\rangle + \frac{\langle \chi''_{v-1} | H' | \chi'_v \rangle}{(E''_v - E''_{v-1})} |\chi''_{v-1}\rangle \,. \tag{5.7}$$

Since the energy levels of the harmonic oscillator are equally spaced, we find that $E''_v - E''_{v-1}$ = - $E''_v - E''_{v+1} = \hbar\omega$. Keeping the signs and reducing the energy dimension (since the operator is dimensionless), we find that in general,

$$|\chi'_v\rangle = |\chi''_v\rangle + \frac{\Delta x}{x_{\mathrm{o}}\sqrt{2}} \Big[\sqrt{v}\, |\chi''_{v-1}\rangle - \sqrt{v+1}\, |\chi''_{v+1}\rangle \Big] \tag{5.8}$$

The transition dipole moment ($\mu_{v',v''}$) for an off-diagonal decay ($v' \neq v''$) is written as,

$$\mu_{v',v''} = \langle \chi_{v''} | \mu_{el} | \chi_{v'} \rangle \tag{5.9}$$

if we expand the electronic dipole moment operator around the equilibrium bond length, to first order in $\tilde{x}$ we can write,

$$\begin{aligned} \mu_{el}(x) &\approx \mu_{\mathrm{o}} + \partial_x \mu \cdot x \\ &= \mu_{\mathrm{o}} + \partial_x \mu \cdot \tilde{x} x_{\mathrm{o}}, \end{aligned} \tag{5.10}$$

where μ_o [a.u.] and $\partial_x\mu$ [a.u./Å] are linear fit coefficients of the dipole moment function given by $\mu_{el}(x-x_e)$, where x_e is the equilibrium bond length of the harmonic potential. Using this expansion, and the excited state wavefunctions, we can write an approximate expression for the TDMs of off-diagonal transitions. From this we find,

$$\mu_{v',v'-1} = \mu_o \left\langle \chi''_{v'-1} \middle| \chi'_{v'} \right\rangle + \partial_x\mu \cdot x_o \left\langle \chi''_{v'-1} \middle| \tilde{x} \middle| \chi'_{v'} \right\rangle \tag{5.11}$$

$$\mu_{v',v'+1} = \mu_o \left\langle \chi''_{v'+1} \middle| \chi'_{v'} \right\rangle + \partial_x\mu \cdot x_o \left\langle \chi''_{v'+1} \middle| \tilde{x} \middle| \chi'_{v'} \right\rangle . \tag{5.12}$$

Plugging in the wavefunctions from Eq. 5.8 we find,

$$\mu_{v',v'-1} = x_o \sqrt{\frac{v'}{2}} \left(\partial_x\mu + \frac{\mu_o \Delta x}{x_o^2} \right) \tag{5.13}$$

$$\mu_{v',v'+1} = x_o \sqrt{\frac{v'+1}{2}} \left(\partial_x\mu - \frac{\mu_o \Delta x}{x_o^2} \right) \tag{5.14}$$

An interesting relation is now evident, as there is the possibility for the two terms in the parenthesis to either add or subtract and thus increase or decrease the magnitude of the TDM. If $\partial_x\mu = \pm\mu_o \frac{\Delta x}{x_o^2}$ then the term in one of the the parentheses is zero. If Δx and $\partial_x\mu$ have the same sign then it is possible for $\mu_{v',v'-1} \gg \mu_{v',v'+1}$. If Δx and $\partial_x\mu$ have different signs then $\mu_{v',v'-1} \ll \mu_{v',v'+1}$ is possible. Additionally, in the case where $\Delta x = 0$, these results follow expectation that the slope of the TDM serves as the primary contribution (when neglecting other anharmonicities) to off-diagonal couplings [63].

The implication is that there may be a fortuitous cancellation of these terms that makes optical pumping of a certain molecule more forgiving. If $\mu_{v',v'-1} \gg \mu_{v',v'+1}$ then the excited

state is likely to decay on a transition that results in relaxation of molecular vibrations. In other words, optical cycling leads to vibrational cooling. Additionally, if this relation were true, the predicted number of scattering events before vibrational heating occurs is higher compared to the prediction from just looking at the FCFs.

Even if an exact cancellation does not occur (we cannot expect nature to be so helpful), the corresponding TDMs can still be reduced. In the case of the X and B states of SiO^+ (see Fig. 5.1 and 5.2), Δx= 0.008 Å, $x_o = 0.053$ Å, $\mu_o \cong 0.6$ a.u. and $\partial_x \mu \cong$ -1 a.u./Å. For $\Delta v = \pm 1$ transitions from $|B, v = 1\rangle$ we find that the two TDMs, $\mu_{12} = 0.037$ a.u. and μ_{10} 0.102, are quite different. Note that these values from the simplified model agree with the results from direct numerical calculation, which are shown in Table 5.2.

While FCFs are typically used to indicate molecules that have favorable branching ratios (less likely to decay on $\Delta v = \pm 1$ transitions), they clearly do not tell the whole story. From this model, we find that the difference in equilibrium bond lengths (Δx) and slope of the TDM $\partial_x \mu$, along with the characteristic vibrational wavefunction length scale x_o are also meaningful parameters that can provide more insight to molecules amenable to optical cycling and pumping.

5.2 Loading

A full description of the loading procedure can be found in Ch. 3.4. Loading a particular molecular ion into a trap can be challenging and slow. This becomes even more challenging when attempting to load a single ion. Even after loading, it may be difficult to understand what molecular species is in the trap since the molecule species is typically not fluorescing enough light to detect. In other words they appear dark. Common methods to understand what is being loaded are to eject them and use time-of-flight analysis, or to measure the

motional sideband spectrum. The former scheme was used to determine the 1+1 REMPI spectrum of SiO^+ [102]. Lacking a channel electron multiplier in the ion trap primarily used in this thesis compared to Ref. [94], the motional sideband spectrum was used to detect proper loading of SiO+.

In all of our group's ion traps, we produce and load ions by ablation of a solid target and ionization through REMPI. A sample of Silicon(II) Oxide was purchased from Alfa Aesar (Stock # 41711, Lot # J06W020) at 99.9% purity. In the larger SiO^+ experiment, the sample is a pressed pellet of SiO powder [94]. Ablation of the solid, neutral sample is a fast and efficient way to produce a jet of particles. A Continuum Minilite II (S/N: 14282) is used to ablate the SiO sample. An Ekspla NTC342C-10SH/SFG OPO laser is used for REMPI laser. Experimentally, it was found that the 216.06 nm transition was most efficient at loading single SiO^+ molecules in the single-ion trap. Here, neutral SiO is excited on the 1+1 REMPI band via the $|A, v = 6\rangle - |X, v = 1\rangle$ transition, where the total 2-photon energy lies 349 cm^{-1} above the SiO ionization energy [102].

5.3 Optical Pumping

As mentioned, the SiO^+ molecule was chosen because of its favorable FCFs, since the $X^2\Sigma^+$ and $B^2\Sigma^+$ states have similar equilibrium bond lengths. This also results in the two states having similar moments of inertia and thus a rotational spectrum that is well resolved between transitions of $\Delta N = -1$ and $\Delta N = +1$. This was experimentally confirmed in [129]. This separation in the spectrum provides the opportunity to spectrally filter broadband laser and address only the $\Delta N = -1$ transitions (see Fig. 5.3). In this way, the SiO^+ molecule can be optically pumped into the ground rovibrational state $|X, v = 0, N = 0, J = 1/2, +\rangle$ [46]. More complicated spectral masks can be used to pump to higher rotational states as

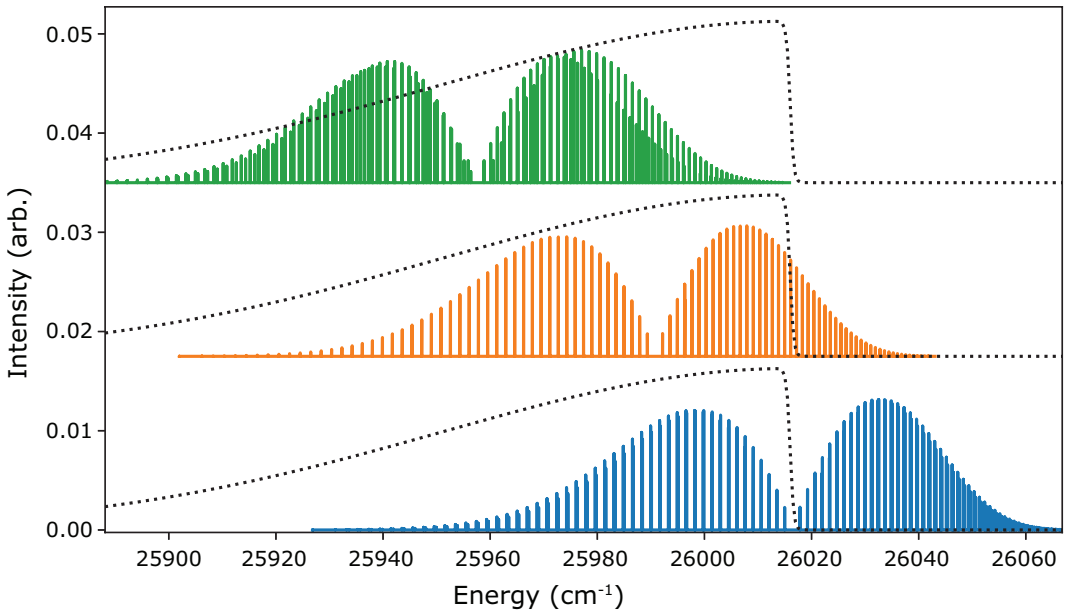

Figure 5.3: **Pulse Shaping Mask:** Shown by the dotted line, the pulse shaping mask is used to prepare the ground rovibrational state covering the B-X 0-0 (blue, bottom trace), 1-1 (orange, middle trace), and 2-2 (green, top trace) bands. The spectral separation of the P-branch ($\Delta N = -1$) and R-branch ($\Delta N = +1$) of SiO^+ is evident. The orange and green bands are offset in intensity for clarity.

well [47].

Interestingly, the B-X 1-1 and 2-2 vibrational bands are in the same spectral region of the laser addressing the 0-0 band. From Table 5.2 we see that the $\Delta v = -1$ transition dominates off-diagonal decays. Thus any population in $|X, v \geq 1\rangle$ will eventually be pumped in to $|X, v = 0\rangle$. The optical set-up to achieve spectral filtering is described in detail in [43], [93], [94]. Rovibrational state preparation of SiO^+ was first demonstrated in 2020 [46]. Plotting the ground state population as a function of time, the authors found two cooling timescales appeared (see Fig. 4 of Ref. [46]).

The apparent conclusion was that the two timescales appear due to state parity. The two-photon process of excitation and decay on the dipole-allowed X$\rightarrow$ B$\rightarrow$ X transitions results in no net parity change between initial and final state. For example, if population

starts in $|X, N = 2, +\rangle$, then after spontaneous emission from the $B^2\Sigma^+$ state, population will either be in $|X, N = 0, +\rangle$ or $|X, N = 2, +\rangle$. As a result, after the fast parity preserving rotational cooling timescale the two lowest rotational states, $N = 0$ and N=1, become equally populated. These two states having opposite parity are not coupled by a two step dipole transition. A one- or three-photon process will result in a parity flip, where population in $N = 1$ can go into $N = 0$ and remain. While Ref. [46] gives a brief explanation into possible parity flip processes, there was not a determination made at the time of publication.

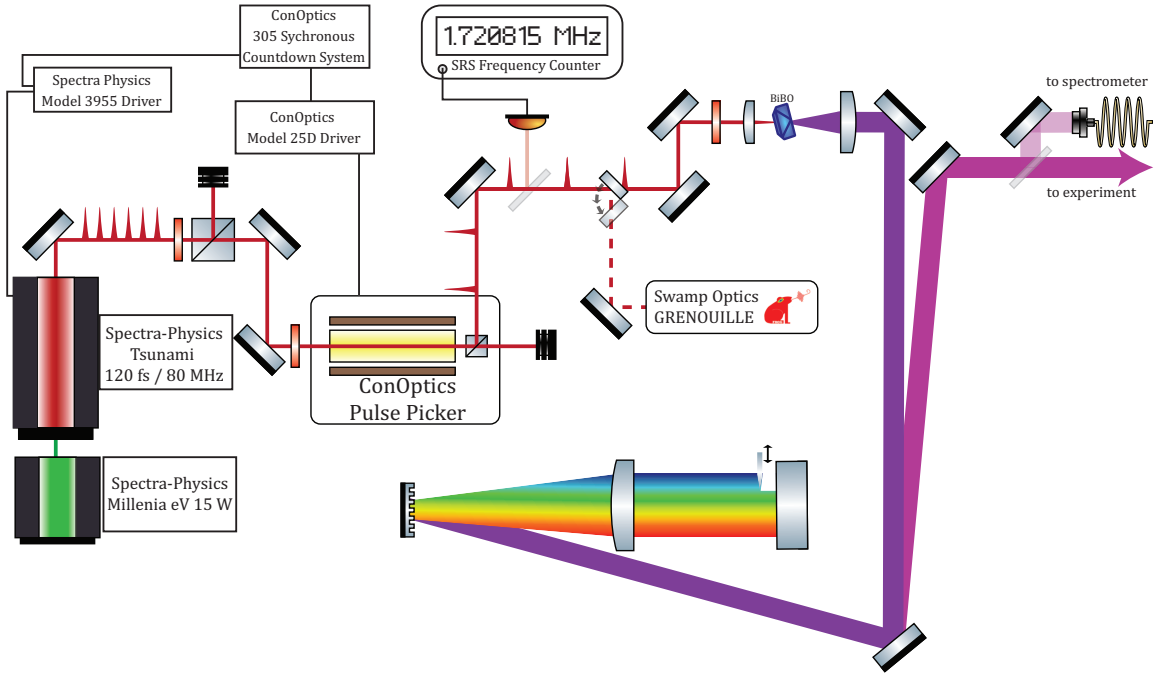

Figure 5.4: **PRR Experimental Set-up:** Here the important lasers, electronics and optics are shown diagramming the laser set-up from ultrafast pulse generation to spectral filtered light that the ion may see.

5.3.1 Pulse Shaping

To achieve rotational cooling and state preparation on the single-ion set-up, we needed to duplicate the pulse shaping and spectrometer set-up from the big SiO^+ trap [94]. Here, I will briefly describe the set-up of the single-ion pulse shaping system which was built following

the design from Ref. [93], [94]. In Fig. 5.4 a diagram containing both the pulse-picking apparatus (see Ch. 7) and pulse shaping set-up are shown.

A Spectra-Physics Tsunami fs laser system is set to 770 nm and focused (Thorlabs f = 35mm B coated lens) onto a type I SHG crystal[1] to generate light at 385 nm. The diverging light is then collimated using an Thorlabs f = 250 mm (D = 50.8 mm)- A coated, achromatic lens. Beamsize measurements in the far field are made to adjust the telescope such that the far field measurements of the beam size match the near field beamwaist of $\omega_x = 4.34$ mm. With a collimated beam, the light is then shined onto a Richardson Grating #53006BK01-530H and the first-order light is used, which is only 50% of input power. The grating acts to spatially separates the different wavelength components of the fs laser. This divergent light is collimated using a homemade doublet lens comprised of an f = 1000 mm lens (Thorlabs LE4822) and f=500 mm lens (Thorlabs LA4337-UV). The light is then retroreflected back $\approx$ 500 mm away and nearly overlapped to the incident path using a 2" mirror. The resulting light is telescoped down to half its original beam size, to make use of 1" OD optics.

In front of the retroreflecting mirror a razer blade acts to block some of the broadband lasers spectrum from propagating further. In this way, light resonant on the $\Delta N = +1$ X-B transition is blocked so that only $\Delta N = -1$ transitions are driven. As a result the $|X, v = 0, N = 0, J = 1/2, +\rangle$ is a dark state (since there is no $\Delta N = -1$ transition to drive) and population is trapped there.

To characterize the spectral filtering, a homemade spectrometer is built. Since the rotational constant of the X state in SiO^+ is only 0.7 cm^{-1} . Again borrowing from the larger SiO^+ experiment [93], [94], the design of the spectrometer is as follows. A portion of the pulse shaped light is picked off and coupled into a multimode fiber (see Fig. 5.4). The

[1]Newlight Photonics BTC 5200 SHG 852/897(I)-UC, 5 x 5 x 2 mm

output collimated light (Thorlabs A110TME-a, f=6.24 mm) from the fiber passes through a Thorlabs UV beam expander (BE10-UVB). The enlarged beam is incident onto a grating (Richardson Grating #53009BK01-170 R, 3600 grooves/mm) to again spatially separate the wavelength components in the laser. The diverging light is collimated using a replica of the homebuilt doublet mentioned above. The resulting light is then detected $\approx$ 500 mm away using a CCD (Mighttex TCN-1304-U S/N: 13-191104-004).

To calibrate the spectrometer, the SHG output of an M-Squared CW Solstis laser is shined into the spectrometer and its pixel location is measured. The output wavelength was measured using a wavemeter (High Finese WS8-2). The results are shown in Fig. 5.5.

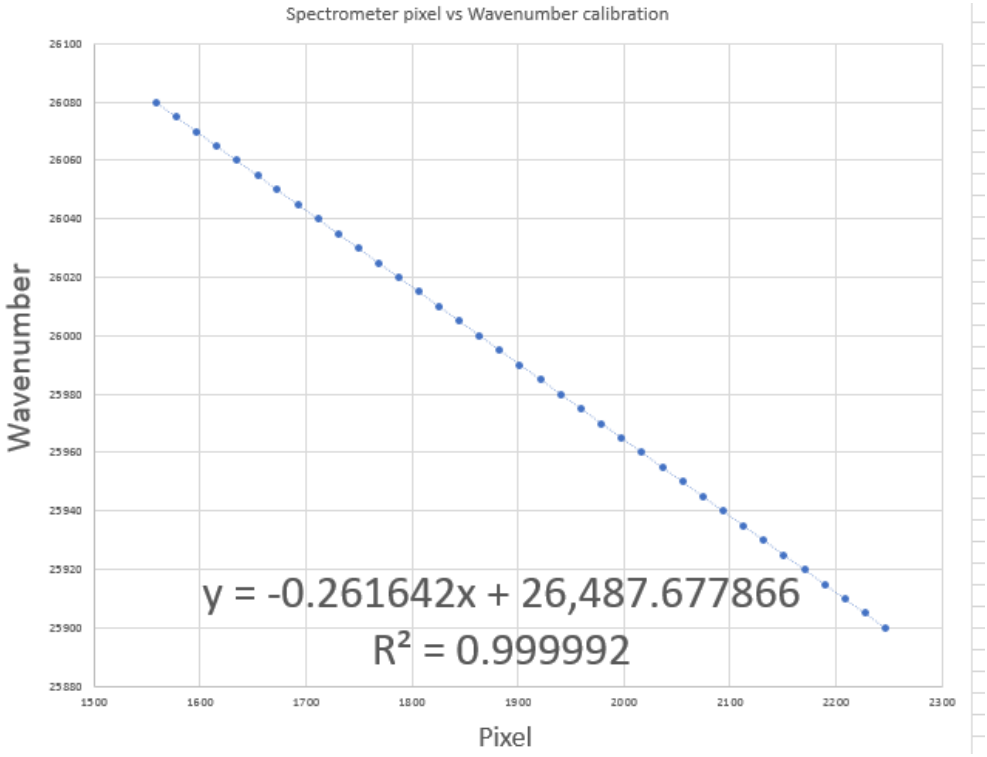

Figure 5.5: **Homebuilt Spectrometer Calibration:** The pixel location for a given CW laser wavelength is shown. From the fit, the slope was found to be 0.26 cm^{-1} /pixel (7.8 GHz/pixel).

From the calibration, the sensitivity was found to be 0.26 cm^{-1} /pixel (7.8 GHz/pixel)

giving an overall resolution of 0.52 cm^{-1} , which is notably smaller than the SiO^+ rotational constant, B_e. As a result, spectral resolving and filtering of single rotational transitions can be performed. Constant detection of the laser spectrum is mad using a LabView script [94] and then the mask can be set accordingly. To optically pump to the ground rovibrational state, the mask, resulting in the laser spectrum seen in Fig. 5.6.

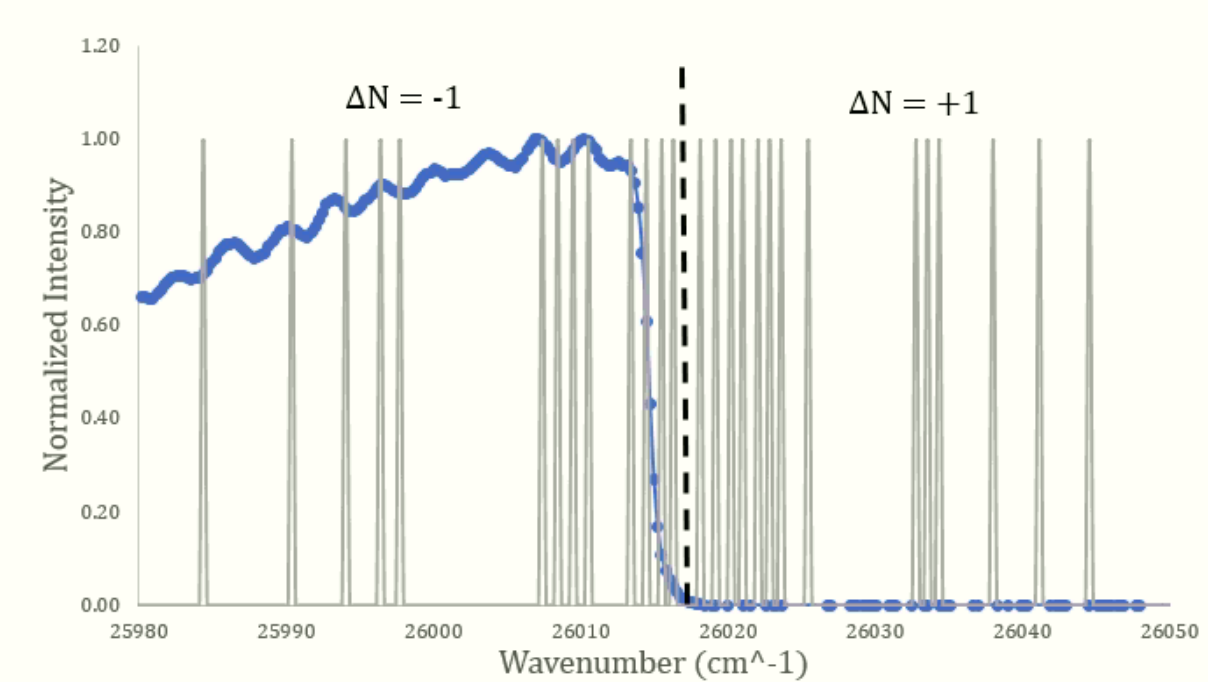

Figure 5.6: **Spectral Filtered Laser:** By setting the mask at an appropriate location, frequency components at the $\Delta N = +1$ transitions can be blocked. The blue line shows the laser intensity measured on the CCD and the gray lines are certain rotational lines plotted for aid. The dotted line shows separation between the ΔN = -1 and $\Delta N = +1$ branches.

5.3.2 Ground State Cooling

By spectral filtering a broadband laser, we can gain exquisite control over the rotational state distribution, which was first demonstrated for SiO^+ in Ref. [47], [130]. In preparation for survey spectroscopy of certain overtone transitions in SiO^+ (discussed later in Sec. 5.6)

ground rotational state preparation was demonstrated in the large SiO^+ trap. This was accomplished using a spectral mask similar to what is shown in Fig. 5.6.

Determination of successful ground state cooling was performed following the relative cooling efficiency described in Ref. [130]. While continually rotational pumping using a Spectra-Physics Mai Tai (described in full in [94]) a dye laser near 226 nm is scanned over the $|X^2\Sigma^+, v = 0\rangle$ to $\left|C^2\Pi_{3/2}, v = 1\right\rangle$ dissociative transition. Using laser cooled fluorescence mass spectrometry (LCFMS), when SiO^+ is dissociated there are less molecules to heat Ba^+ when tickled at the secular frequency, and the Ba^+ fluorescence signal remains high.

The dye laser is fired at 10 Hz, 300 pulses are exposed to the ion trap at a specific frequency f, and the fluence is tuned such that the probability of dissociating a molecule per pulse is less than one. During the 30 s exposure, the LCFMS signal is measured and the decaying signal, at each dye frequency f, is fit. In this way, the steady-state rotational distribution is probed.

As noted in Ref. [130], the $|X^2\Sigma^+, v = 0\rangle$ to $\left|C^2\Pi_{3/2}, v = 1\right\rangle$ transition was chosen for its good separation between lines originating from N=0 or N=1. In this way the relative population between the two states can be found. Population in $|X, v = 0, N = 0, J = 1/2\rangle$ can only be excited to $|C, v = 1, N = 2, J = 3/2\rangle$ (the s(0) lines). Population in the states $|X, v = 0, N = 1, J = 1/2\rangle$ or $|X, v = 0, N = 1, J = 3/2\rangle$ is excited to $|C, v = 1, N = 2, J = 3/2\rangle$ (the s(1) lines) while $|X, v = 0, N = 1, J = 3/2\rangle$ is excited to the $|C, v = 1, N = 3, J = 5/2\rangle$ state on the r(1) line. Using PGopher [128], the relative populations in N=0 and N=1 are found by fitting a Lorentzian contour to the spectrum and floating the state populations. PGopher was used, instead of a simple free Lorentizan fit, to find the line center because the peak amplitudes depend on both the line strength and relative population.

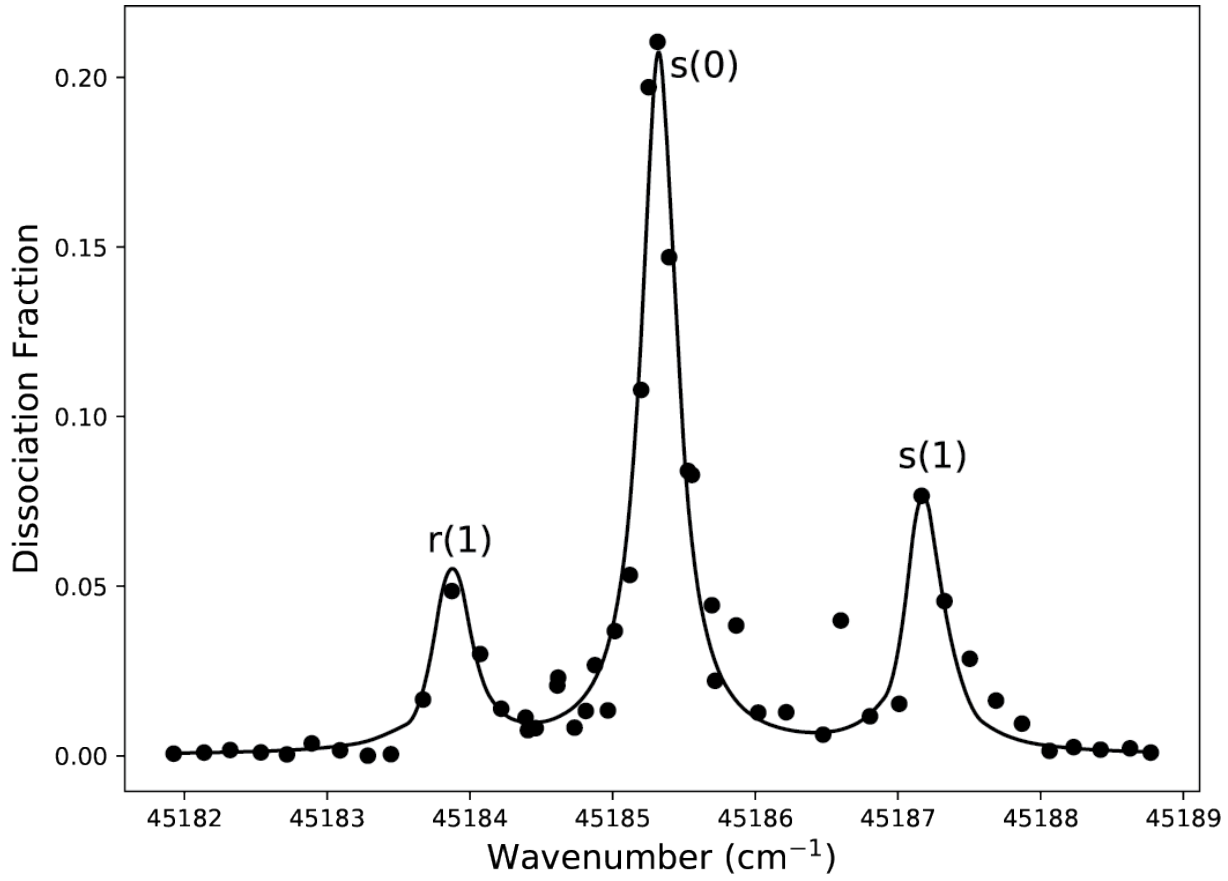

Figure 5.7: **Ground Rotational State Preparation of SiO^+ :** Dissociation from the $|X, v = 0, N = 0, J = 1/2\rangle$ state at 45185.5 cm^{-1} and the $|X, v = 0, N = 1, J\rangle$ states at 445184.14 and 45187.45 cm^{-1} is shown by driving the $\left|X^2\Sigma^+, v = 0\right\rangle$ to $\left|C^2\Pi_{3/2}, v = 1\right\rangle$ transition [130].

From a contour fit of the resulting data, shown in Fig. 5.7, shows successful pumping to the ground rotational state. The fit was optimized until the residuals were at the level of the noise (≈ 0.02). From the fit, the ratio of population in N=1 to N=0 is 32(6)%, so we expect that we have roughly 68(6)% of the molecules in the ground rovibrational state. While this is not quite as good as the pumping to N=0 with 94(3) % efficiency shown in Ref. [130], this still demonstrates the effectiveness of using the spectral mask. This data was not taken with the interest of obtaining the best possible N=0 population, and a simple scan of the mask cut-off position could be made to improve this. Additionally, no spectral features of

dissociation from N≥2 are found, indicating the population is truly being pumped into the two lowest rotational states.

5.4 Optical Pumping Simulations

Motivated by the desire to understand the dominate parity flip mechanism, the optical pumping process of SiO^+ was modelled. Spectra of the X-X, A-X, B-X and B-A systems were simulated with the PGOPHER package [131] using ab initio calculations and experimental data from [126]. Permanent electric dipole and transition dipole curves for the X, A, and B states were obtained from ab initio calculations [47]. Deperturbed vibrational constants of from Ref. [126] were used in RKR inversion to reconstruct the potential energy curves of the X, A, and B states. The number of vibronic levels used in RKR was limited to 10 for the X state, 11 for the A state and 6 for the B state. Vibrational wavefunctions were then obtained by numerical integration of the potential energy curves and used to calculate transition dipole matrix elements between the X, A, and B states as well as perturbation matrix elements between the X and A states. The PGOPHER package was used to predict the transition energies and Einstein A coefficients for transitions between rovibrational levels of the X, A, and B states. The main rates of optical pumping, blackbody radiation (BBR) and spontaneous emissions rates are shown in Table 5.3.

5.4.1 B - X

As discussed in Sec. 5.1, the B-X at ~ 385 nm has the largest TDM. Since the two states have very similar equilibrium bond lengths, this transition is ideal for optical pumping. FCF analysis shows decays leading to vibrational state changes are unlikely, and our calculations of TDMs show that when this does happen, $\Delta v = -1$ transitions are more likely to occur.

Transition	A (s^{-1})	Transition	Bρ (s^{-1})
$\|B, v=0\rangle \rightarrow \|X, v=0\rangle$	1.42×10^7	Optical Pumping	
$\|B, v=2\rangle \rightarrow \|A, v=0\rangle$	1.10×10^6	$\|X, v=0, N>0\rangle \leftrightarrow \|B\rangle \rightarrow \|X, v=0\rangle$	300 - 700
$\|B, v=1\rangle \rightarrow \|X, v=0\rangle$	4.82×10^5	$\|X, v=1\rangle \leftrightarrow \|B\rangle \rightarrow \|X, v=0\rangle$	90
$\|B, v=0\rangle \rightarrow \|X, v=1\rangle$	1.78×10^4	$\|X, v=0, N=0\rangle \leftrightarrow \|B\rangle \rightarrow \|X, v=0\rangle$	10
$\|B, v=0\rangle \rightarrow \|A, v=0-5\rangle$	1.31×10^4	$\|X, v=0, N>0\rangle \leftrightarrow \|B\rangle \rightarrow \|X, v=1\rangle$	1.2 - 1.5
$\|A, v=5\rangle \rightarrow \|X, v=0-5\rangle$	1.16×10^4	$\|X, v=0, N>0\rangle \leftrightarrow \|B\rangle \rightarrow \|A\rangle$	0.9 - 1.3 *
$\|X, v=5\rangle \rightarrow \|A, v=0-3\rangle$	1.56×10^3	$\|X, v=0, N=0\rangle \leftrightarrow \|B\rangle \rightarrow \|X, v=1\rangle$	1.6×10^{-2}
$\|A, v=0\rangle \rightarrow \|X, v=0-1\rangle$	2.79×10^2	$\|X, v=0, N=0\rangle \leftrightarrow \|B\rangle \rightarrow \|A\rangle$	1.2×10^{-2} *
$\|X, v=3\rangle \rightarrow \|A, v=0\rangle$	1.52×10^2	BBR	
$\|X, v=2\rangle \rightarrow \|X, v=0-1\rangle$	32.5	$\|X, v=0, N=20\rangle \rightarrow \|X, v=0\rangle$	0.97
$\|X, v=1\rangle \rightarrow \|X, v=0\rangle$	0.066	$\|X, v=1\rangle \rightarrow \|A, v=0\rangle$	0.91
$\|X, v=0, N=20\rangle \rightarrow \|X, v=0, N=19\rangle$	0.066	$\|X, v=1\rangle \rightarrow \|X, v=2\rangle$	0.03
$\|X, v=0, N=1\rangle \rightarrow \|X, v=0, N=0\rangle$	5.7×10^{-6}	$\|X, v=0\rangle \rightarrow \|A, v=0\rangle$	1.6×10^{-2}
-	-	$\|X, v=0, N=0\rangle \rightarrow \|X, v=0, N=1\rangle$	2.5×10^{-3}
-	-	$\|X, v=0, N=1\rangle \rightarrow \|X, v=0, N=0\rangle$	8.2×10^{-4}
-	-	$\|X, v=0\rangle \rightarrow \|X, v=2\rangle$	4.1×10^{-4}
-	-	$\|X, v=0\rangle \rightarrow \|X, v=1\rangle$	2.8×10^{-4}

Table 5.3: Comparison of spontaneous emission rates and optical pumping rates for SiO^+. Unless noted otherwise, rates are calculated for the lowest rotational state. *Calculated with unmodified B-A TDM value from Qin et. al. [127]

As a result, driving the B-X is optimal for optical cycling.

5.4.2 A - X

The A-X system has the second largest TDM (between X-B, A-X and B-A transitions), with a value of $\mu \approx 0.2$ a.u. near the $A^2\Pi$ equilibrium bond length. While the X and A state have very different equilibrium bond lengths, since the two states are close in energy perturbative terms need to be accounted for. Rotational levels of the X and A state can interact by several terms including spin-orbit interactions and rotational couplings. The matrix elements for these terms can be calculated base on the experimental data from Ref. [126]. For states separated by several hundred cm^{-1} the resulting perturbations are of several tens of cm^{-1} for spin-orbit and **LS** couplings and $\sim$0.01 - 0.1 cm^{-1} per **J** for **L**-uncoupling (**JL** terms). However when certain A and X states are close in energy, strong perturbations can arise. For example, $|X, v = 2\rangle$ is nearly degenerate with $|A, v = 0\rangle$ (see Fig. 5.1) and produces a large energy shift in the $|X, v = 2\rangle \leftrightarrow |B, v = 2\rangle$ spectrum. As a result, the probability of decay from $|B, v = 2\rangle$ to $|A, v = 2\rangle$ is increased to 15%. The intensity of certain transitions is also increased use to these perturbations. For example, the $|X, v = 2\rangle$ wavefunction borrows $\sim$16% of the $|A, v = 0\rangle$ wavefunction and vice versa. Therefore transitions that are normally weak ($|B, v = 2\rangle \rightarrow |A, v = 0\rangle$ and $|X, v = 2\rangle \rightarrow |X, v = 0\rangle$) become orders of magnitude stronger [125].

5.4.3 B - A

The smallest TDM present is between the B and A states (Fig. 5.2). The most recent MRCI calculations [127] predict an electronic TDM of <0.05 a.u. near the equilibrium bond length of the A state. This results in a $\approx 10^{-3}$ probability of $|B, v = 0\rangle \rightarrow |A, v\rangle$ decay.

It is worth noting that the calculated TDM is not fully converged, with the largest basis set/highest level theory calculation predicting significantly higher TDMs [127] compared to the previous lower level works [132]–[134].

5.4.4 X - X

We also need to account for rovibrational transitions in the X state. Due to the $\sim$1.7 a.u. dipole moment, the X state rotational levels can strongly interact with blackbody radiation (BBR). However, the spectral density of the blackbody spectrum at room temperature, where the transitions between low-lying rotational states (N < 20) are, is low. Subsequently, the rates for interaction with BBR are small (see Table. 5.4). Spontaneous emission rates, shown in the same table, are another 1-2 orders of magnitude slower. Compared to the B-X optical pumping rates, which in our experiment [46] can exceed $\sim 10^3$ s^{-1}, these processes can be neglected.

The flatness of the X-X dipole moment curve results in weak vibrational transitions. The radiative decay lifetimes of the $|X, v > 0\rangle$ states, via vibrational ladder transitions, are on the order of seconds (see Fig. 2 in [125]). However, due to the near degeneracy and perturbative coupling with the state $|A, v = 0\rangle$, the decay rate from $|X, v = 2\rangle$ to $|X, v = 0\rangle$ is two orders of magnitude stronger than from $|X, v = 1\rangle$. Rates of spontaneous emission, optical pumping by BBR and the broadband laser used in our experiments are compared in Table. 5.3.

5.4.5 Simulation Details

With the TDMs, transition energies and Einstein A coefficients calculated, a full model of population dynamics in the X, A, and B states can be made. If $\mathbf{N}$ is a state vector the

J"	J'	E (cm^{-1})	A (s^{-1})	B ρ_{BBR} (s^{-1})
0.5	1.5	1.425	5.70×10^{-6}	8.25×10^{-4}
1.5	2.5	2.870	5.50×10^{-5}	3.97×10^{-3}
2.5	3.5	4.305	2.00×10^{-4}	9.58×10^{-3}
3.5	4.5	5.740	4.90×10^{-4}	1.75×10^{-2}
4.5	5.5	7.175	9.70×10^{-4}	2.77×10^{-2}
5.5	6.5	8.609	1.71×10^{-3}	4.05×10^{-2}
6.5	7.5	10.044	2.74×10^{-3}	5.55×10^{-2}
7.5	8.5	11.478	4.12×10^{-3}	7.28×10^{-2}
8.5	9.5	12.912	5.91×10^{-3}	9.25×10^{-2}
9.5	10.5	14.346	8.14×10^{-3}	0.114
10.5	11.5	15.779	1.09×10^{-2}	0.138
11.5	12.5	17.213	1.42×10^{-2}	0.165
12.5	13.5	18.646	1.81×10^{-2}	0.193
13.5	14.5	20.078	2.26×10^{-2}	0.224
14.5	15.5	21.510	2.79×10^{-2}	0.257
15.5	16.5	22.942	3.39×10^{-2}	0.291
16.5	17.5	24.373	4.07×10^{-2}	0.328
17.5	18.5	25.804	4.84×10^{-2}	0.367
18.5	19.5	27.235	5.70×10^{-2}	0.408

Table 5.4: **X-X Transitions for Low Rotational States:** Transition Energies (cm^{-1}), Einstein A coefficients (s^{-1}), and rates of BBR pumping (s^{-1}) for $|X, v = 0, J', e\rangle \rightarrow |X, v = 0, J'', e\rangle$ transitions of SiO^+ .

population statistics, then the steady state population distribution can be found by solving,

$$\frac{d\mathbf{N}}{dt} = \mathbf{MN}, \tag{5.15}$$

where the rate coefficient matrix $\mathbf{M}$ is defined as $\mathbf{M} = \mathbf{A} + \mathbf{B} + \mathbf{L}$. Here, $\mathbf{A}_{ij}$ is the Einstein A coefficient connecting states i and j where $E_i < E_j$, $\mathbf{B}_{ij}$ ($\mathbf{B}_{ji}$) and $\mathbf{L}_{ij}$ ($\mathbf{L}_{ji}$) are products of the Einstein B coefficients with the blackbody and laser spectral density respectively. The room temperature blackbody energy density was calculated using Planck's law. The laser spectral energy density, ρ_L in $J/m^3/Hz$, was calculated using the expression

v_f \ v_i	0	1	2	3	4	5
0	-	*0.141*	*34.639*	*2.331*	*0.413*	*65.534*
1	$\mathbf{5.55 \times 10^{-4}}$	-	*10.185*	*0.680*	*0.514*	*25.667*
2	$\mathbf{5.97 \times 10^{-4}}$	**0.044**	-	*7.226*	*21.276*	*18.315*
3	$\mathbf{1.98 \times 10^{-7}}$	$\mathbf{1.39 \times 10^{-5}}$	**0.035**	-	*0.971*	*3.268*
4	$\mathbf{1.93 \times 10^{-10}}$	$\mathbf{5.42 \times 10^{-8}}$	$\mathbf{4.99 \times 10^{-4}}$	$\mathbf{5.02 \times 10^{-3}}$	-	*1.505*
5	$\mathbf{1.65 \times 10^{-10}}$	$\mathbf{1.42 \times 10^{-8}}$	$\mathbf{2.28 \times 10^{-6}}$	$\mathbf{8.61 \times 10^{-5}}$	$\mathbf{8.03 \times 10^{-3}}$	-

Table 5.5: **X-X Vibrational Transitions:** Upper right triangle, italic - Einstein A coefficients (s^{-1}); lower left triangle, bold - BBR pumping rates (B ρ_{BBR},s^{-1}) for transitions $|X, v_i\rangle \rightarrow |X, v_f\rangle$. Rates are averaged over the upper state's rotational levels populated at T = 300 K.

$$\rho_L = \frac{F}{100\sigma c^2 2\pi^{3/2}} \times \exp\left[-\frac{(E-E_0)^2}{2\sigma^2}\right] \frac{1}{1+e^{s(E-E_c)}}. \quad (5.16)$$

In Eq. 5.16, F is the laser flux, σ is the laser's spectral bandwidth, E_0 is the center wavelength, E_c is the pulse shaped cut-off position [46] and s is the cut-off steepness (see Fig. 5.6). Typical experimental parameters are: F = 0.6 MW/m^2 (42 mW focused to a waist of $\sim$ 150 μm), σ = 65 cm^{-1} , E_0 = 26016 cm^{-1} and s = 3 cm. Fig. 5.3 shows the simulated laser spectral curve (see experimental curve in Fig. 5.6) that was used to model ground rovibrational state preparation. The cut-off, E_c, was set at 26016 cm^{-1} so that the $|X, v = 0, N = 0, J = 1/2\rangle$ state is dark.

The state vector $\mathbf{N}$ is comprised of rovibrational levels of the X, A, and B states where $v \leq 5$ and $J \leq 49.5$ typically. The result is that $\mathbf{M}$ is a 2400 x 2400 matrix. The initial state vector $\mathbf{N}_0$ was set such that at time $t = 0$, all population was equally distributed between $|N = 14, J = 13.5\rangle$, $|N = 14, J = 14.5\rangle$, $|N = 15, J = 14.5\rangle$ and $|N = 15, J = 15.5\rangle$ rotational levels of $|X, v = 0\rangle$ which is consistent with the photoionization scheme used to load SiO^+ at 213.96 nm [102].

The simulation integrated Eq. 5.15 for a desired time range and the esults are shown in Fig. 5.8. At different times the simulation was stopped and the population in $|X, v = 0, N = 0, J = 1/2\rangle$ was recorded and plotted as open circles in in Fig. 5.8. We find that the simulation reflects the time cooling timescales that was experimentally measured in Ref. [46]. The population in the ground state was fit using,

$$n_0(t) = A_{even}\left(1 - e^{-\lambda t}\sum_{i=0}^{M-1}\frac{(\lambda t)^i}{i!}\right) + A_{odd}\left[1 - e^{-\lambda t}\left(\sum_{i=0}^{M}\frac{(\lambda t)^i}{i!} + \sum_{i=M+1}^{\infty}\frac{(\lambda-\kappa)^i t^i}{i!(1-\kappa/\lambda)^M}\right)\right], \tag{5.17}$$

Here, A_{even}, A_{odd}, λ and κ are parameters determined from the fit. The value M is equal to the number of excitation steps before reaching the lowest rotational state of a given parity. For population in state $|N\rangle$, there are $M = N/2$ steps for even parity states, and $M = (N-1)/2$ steps for odd parity states to reach $N = 0$. In the model, λ is the effective rate of rotational cooling without changing parity, when N is reduced by 2. The rate of parity cooling is given by κ, where N changes by 1. Modeling the ground state population in this way allows us to separate the two parity cooling processes and understand their rates individually.

From Fig 5.8 it is clear that the simulation results and fit are in excellent agreement. At short times (t <20 ms), the population between even (blue line) and odd (red line) parity states remains equal, despite $\langle J\rangle$ (dot-dash line) falling. This follows the hypothesis that rotational population is pumped into an equal distribution among $|N = 0\rangle$ and $|N = 1\rangle$ on a fast, $\lambda \approx 700$ s^{-1} timescale.

After the fast parity preserving process, population in odd parity state are pumped into even parity at a rate of $\kappa \approx 1$ s^{-1} . Cooling is complete after 5 s with the state $|X, v = 0, N = 0, J = 1/2\rangle$ containing 96% of the total population and $\langle J\rangle = 0.56$. The remaining 4% of the population is likely continually cycled between X - B due to the steepness and location of the cut-off. This remaining population in states outside the ground state reflects why the blue line (total population in even parity states) is higher than the data at long cooling timescales.

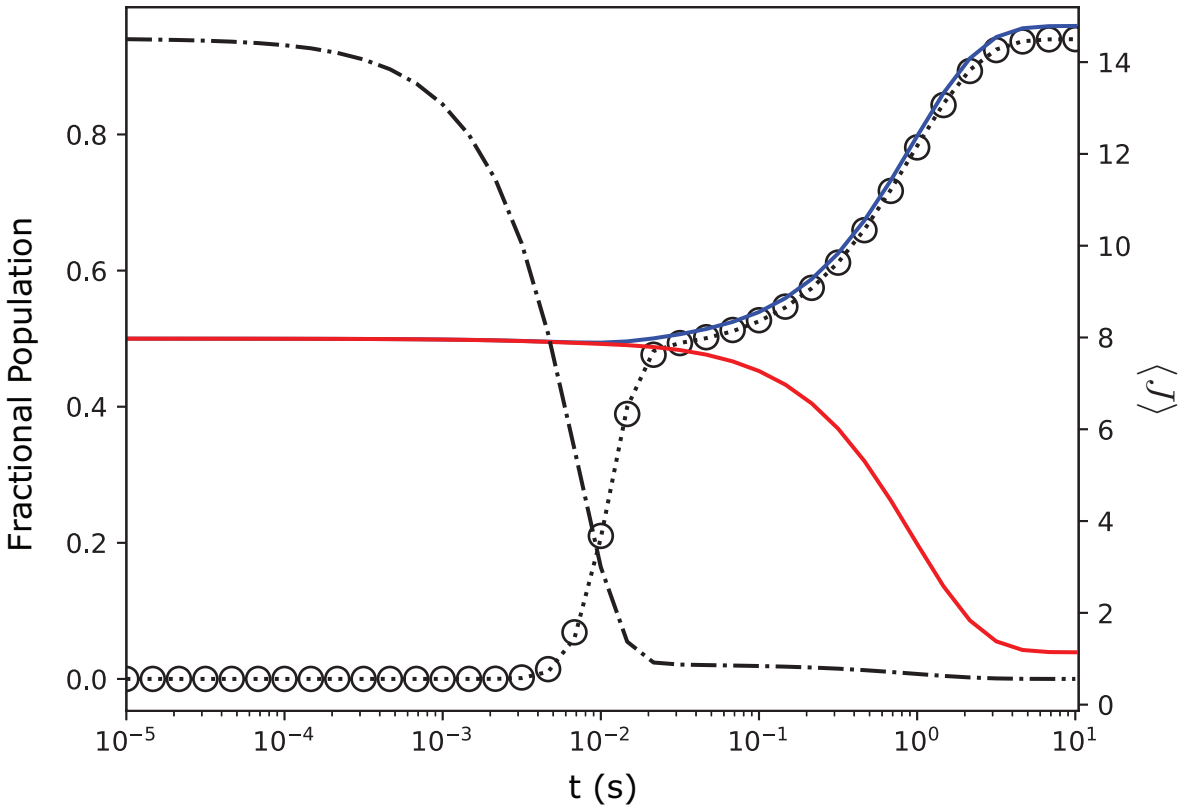

Figure 5.8: **Ground State Cooling As a Function of Time:** Open circles - time dependence of the simulated population in the $|N = 0, J = 0.5\rangle$ state, dashed line - fit with Eq. 5.17, dash-dot line - average rotational level, and the red and blue solid lines show the total population in all the odd and even total parity states respectively.

Of the two cooling rates, $\lambda \approx 700$ s^{-1} is in good agreement with the experimentally determined value of 650(90) s^{-1} from [46], while $\kappa \approx 1$ s^{-1} is an order of magnitude lower than the measured value of 9(4) s^{-1} . Evident from Fig. 5.8, κ reflects the rate at which an absorption and emission event results in $\Delta N = -1$, and the state parity is flipped.

Parity conversion requires an odd number of state changes. For population in $|N = 1\rangle$ to reach $|X, v = 0, N = 0\rangle$ it can either go there directly from a one photon process or by a three photon process of $|X, v = 0\rangle \leftrightarrow |B, v = 0\rangle \rightarrow |I\rangle \rightarrow |X, v = 0\rangle$. Here, $|I\rangle$ is some intermediate parity flip state which could either be a vibrationally $|X, v > 0\rangle$ or the electronically $|A, v\rangle$

excited states.

A one photon process would involve either interaction with blackbody radiation or collisions with background gas. The experiment was conducted in UHV conditions such that collisions take place on the order of a minute, which is much slower than a $kappa \approx 1$ s^{-1} . From Table 5.3, it is clear the $|X, v = 0, N = 1\rangle \rightarrow |X, v = 0, N = 0\rangle$ BBR rate of 8.2×10^{-4} is also too slow. However, the same table shows that decays from the B state to $|X, v > 0\rangle$ or $|A, v\rangle \rightarrow X, v = 0$ are fast enough to explain the observed parity flip rate κ.

5.4.6 Parity Flips

The simulation was repeated for varying B-A branching ratios, which is set relative to the B-X branching ratio. Here, $A_{B\rightarrow A}/A_{B\rightarrow X}$ was varied from 0 to 4.6%. The result from each simulation was fit using Eq. 5.17 and λ and κ were recorded. Since the theory is not converged on the B-A transition dipole (see Sec. 5.4.3) it is possible the original simulation ran included an inaccurate B-A branching fraction.

The results of the simulation are plotted in Fig. 5.9 which shows that κ has a strong dependency on the B-A branching fraction, while λ only minimally depends on it. The lowest rate of κ is 0.0683 s^{-1} corresponding to zero B-A branching while the highest rate of 26.1 s^{-1} is found for 4.6% branching. The B-A branching predicted in [127] is shown in the dotted line and is clearly too small to match the results from the experiment, shown in the dot-dash line [46]. Fig. 5.9 shows that a B-A branching of 0.146% matches the experimental results. This value of 0.146% also agrees with the upper bound set in [129].

If the parity flip rate was set solely by decay from B $\rightarrow |X, v > 0\rangle$, κ would be expected to be much larger than its value for zero B-A branching. When using the mask shown Fig. 5.4, it is likely that any population in $|X, v \geq 1\rangle$ cycles to $|B, v \geq 1\rangle$ and back, eventually

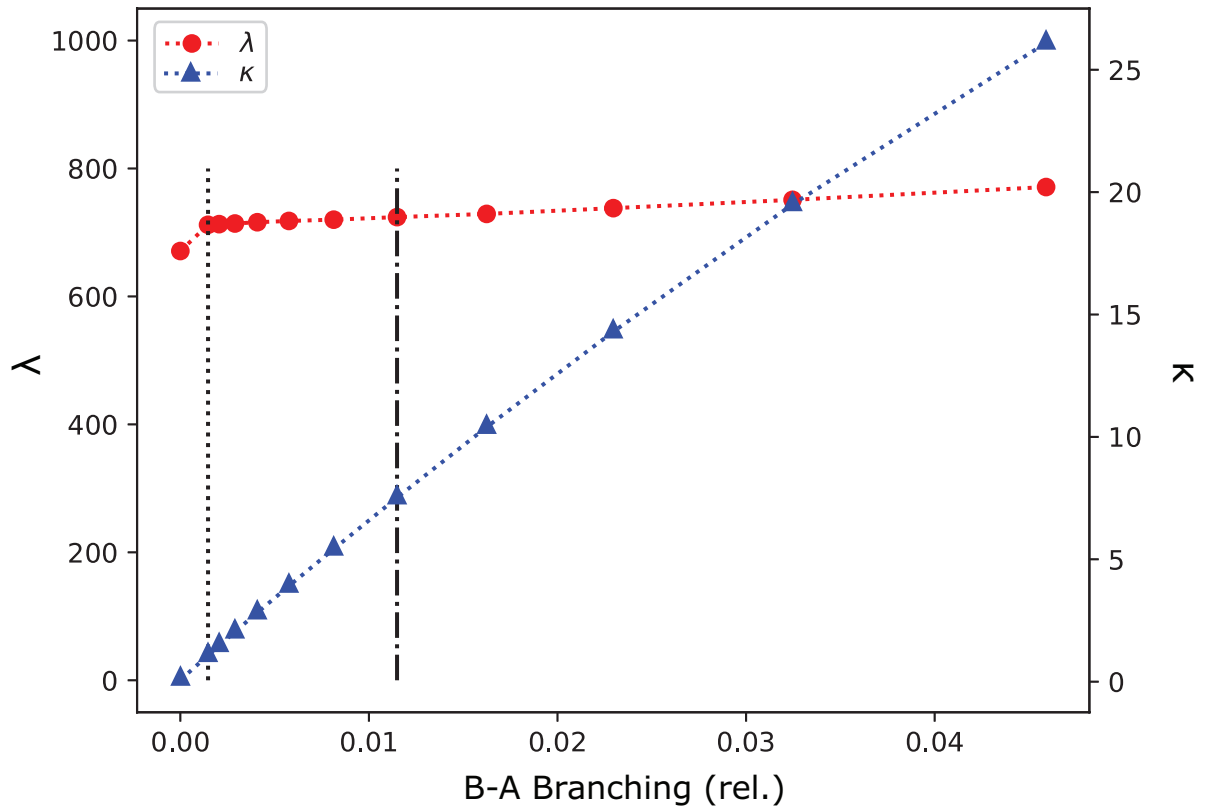

Figure 5.9: **Parity Cooling Dependency on B-A Branching:** Rates for single parity cooling λ and parity flip κ rates as function of the B-A transition rate. Vertical lines: dashed - cooling rates from B-A branching of 0.147% using [127], dot-dashed - cooling rates needed to fit experimental data [46] with a B-A branching of 1.15%. The first red point is an artifact of the fit.

decaying into $|X, v = 0\rangle$ following the conclusions from Sec. 5.1.1 and Table 5.2. If this two step pathway dominates, compared to direct decay from $|X, v > 0\rangle \rightarrow |X, v = 0\rangle$, then parity is likely to remain the same.

The discrepancy between the theoretical B-A branching fraction and experimentally estimated value is a factor of ≈ 10.2. These results show that the B-A dipole moment is likely 3.2 times larger than predicted, a value of $\mu_{B\rightarrow A} \sim 0.064$ a.u., which agrees with previous experimental bounds [129]. It is likely that the TDM from [127] is underestimated in the Franck-Condon region (r $\sim (r_e^A + r_e^B)/2$) where the TDM is at it's minimum value of $\mu < 0.02$ a.u. (see Fig. 5.2).

5.4.7 Conclusions

Initial calculations and measurements of the SiO^+ molecule [125], [129] showed that it is a favorable candidate for optical pumping. As outlined here, there is more insight to be gained and ground rovibrational state preparation is even more fortuitous. The SiO^+ molecule is found to have an asymmetry in the TDMs for $\Delta v = \pm 1$ decay channels from $|B, v\rangle$. The asymmetry is beneficial to the optical cycling process because it leads to vibrational cooling. This also results in more possible scatters between B to X before a vibrational heating event occurs. While direct calculations find more accurate values, the model presented in Sec. 5.1.1 shows that three simple molecular parameters, the difference in equilibrium bond length Δx, spatial wavefunction extent x_o, and TDM slope $\partial_x \mu$, also provide insight. This analysis is akin to FCF analysis and indicates which molecules are amenable to optical pumping and cycling.

Additionally, a third electronic state is found to benefit the optical pumping cycle. Due to the state parity set by the rotational quantum number, rovibrational state preparation

is dependent on two timescales. Since the parity flip rate is found to be much slower than parity-preserving transitions, couplings to extra states and additional decay pathways can be beneficial. In SiO^+ , B state decay through the A state is found to be the dominant channel for parity to flip, namely from $|X, v = 0, N = 1, -\rangle \rightarrow |X, v = 0, N = 0, +\rangle$. This goes against conventional wisdom that predicts extra decay pathways to be undesirable. Since the A state is able to provide a pathway for parity to flip, no extra lasers or microwaves are needed. However, directly driving the $|X, v = 0, N = 1, -\rangle \rightarrow |X, v = 0, N = 0, +\rangle$ transition using a microwave can result in faster parity flip rates.

The presence of the extra decay channels and their benefit can possibly be extended to non-diagonal molecules. CaO^+ was recently proposed for quantum computing applications [11], [12], [135], and has an $A^2\Sigma^+$ state that lies only ~ 600 cm^{-1} above the ground $X^2\Pi$ state [136]. It may be possible to pump on the $X^2\Pi$ - $B^2\Pi$ transition, if the B state is non-dissociative. While X-B pumping may populate vibrationally excited states of X from spontaneous emission, their decay to ground vibrational state may be sped up by the presence of the A state. As in SiO^+ , rovibrational state preparation of $|X, v = 0\rangle$ in CaO^+ may be possible on a $\mathcal{O}(100)$ ms time scale.

Similar logic can be extended to polyatomic molecules. Recently work highlights the feasability of optical cycling in linear triatomics [37]–[39], [137], symmetric and asymmetric top molecules [40], [138], and other polyatomics with increasing complexity [42], [139]. Intervening states – electronic or vibrational — with strong dipole allowed transitions to the ground state may permit optical pumping and state preparation.

Understanding the usefulness of intervening electronic states, and potential TDM asymmetries for off-diagonal vibrational decays, widens the view of molecules that may accommodate optical pumping.

5.5 Reaction Rates

While ground rovibrational state preparation is possible, more complicated masks than shown in Fig. 5.6 can state prepare SiO^+ molecules in higher rotational states [47], [48]. As a result, it is possible to measure chemical reactions under highly non-equilibrium conditions. It is common for SiO^+ to react with background H_2 gas in a vacuum chamber, and at pressures of $\times 10^{-10}$ Torr this occurs on the order of a few minutes [48]. At this timescale, it is possible to continually measure the number of SiO^+ ion trapped and see the reaction slowly occur as $SiO^+ + H_2 \rightarrow SiOH^+ + H$.

In this way, the reaction timescale can be measured as a function of SiO^+ rotational state. The body of this work is currently being prepared in a manuscript [7] and is also a major part of Ref. [48]. I will quickly outline the experiment and its results here.

The amount of SiO^+ loaded into an ion trap can be measured by tickling (see Ch. 2.2) at the SiO^+ secular frequency. When an applied frequency (to the end caps or trap rods) matches the SiO^+ motional resonance, the molecules motion will be excited and that will in turn heat up the co-trapped Ba^+ ions. The total fluorescence from Ba^+ will drop because of Doppler broadening, and this lower photon count indicates the presence of SiO^+ in the ion trap. Since SiO^+ and $SiOH^+$ have different secular frequencies, the amount of reacted molecules is measured by a change in the dominant frequency which causes the fluorescence to drop. Continual measurement over time indicates the rate of reaction.

These reaction rate measurements have been made as a function of SiO^+ internal state including rovibrationally cooled, no pumping (rotational distribution after loading), and super rotors ([47]. The results, reproduced from Ref. [48], are shown in Fig. 5.10.

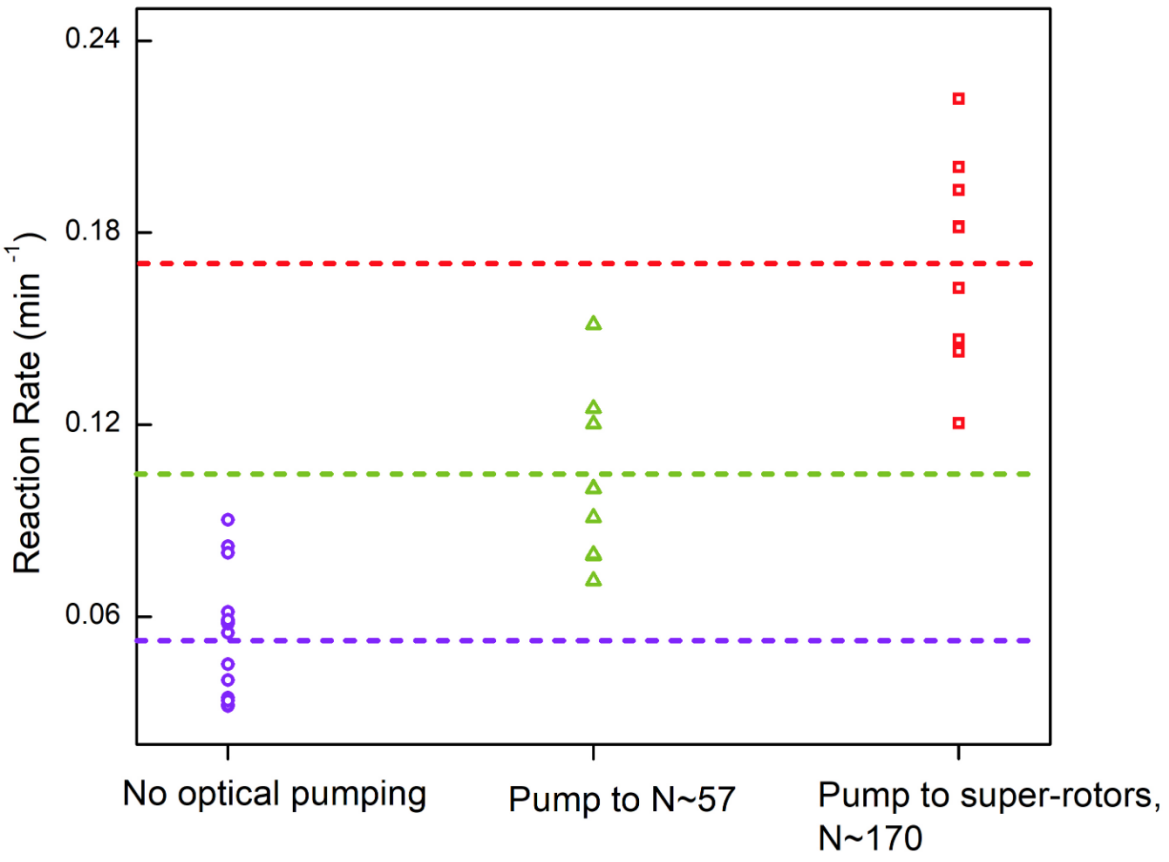

Figure 5.10: **Reaction Rates of SiO^+ with H_2** The dotted lines indicate the average for each distribution. There was not a residual gas analyzer and so the absolute concentration of H_2 could not be determined. Otherwise the absolute reaction rates could be measured.

From Fig. 5.10 we see that there is a clear difference in the mean reaction rate for various rotational distributions of SiO^+ . Collaboration with Hua Guo and Prof. Anyang Li is ongoing to understand the underlying physics and a manuscript is being prepared [7].

5.6 Probe for Fundamental Physics

The role of molecules in measurements for fundamental physics is broadly seen as a promising avenue [14], [15], [17], [23]. Measuring fundamental constants of nature using precision spectroscopy can set both an absolute standard and an upper bound to any potential temporal or spatial variations. The former provides insight to the Standard Model of Physics and theoretical models, while both give insight to potential physics beyond the Standard Model.

Our lab is motivated by the idea that certain fundamental constants — the proton-to-electron mass ratio $\mu = m_p/m_e$ or the fine structure constant α — may not be constant in time. Since no current theory predicts their present values, it is acceptable to reason they may actually change over time. The vibrational energies of molecules depend directly of μ and allow for model independent measurements to be made [19], [26], [36]. A search for an ideal molecular species led by Mark Kokish [19], [74] found that TeH^+ is a suitable candidate to probe and measurements can lead to a 10^{-18} precision on $d\mu/dt$. His work also showed that systematic effects in polar molecules can be managed. The main challenge with TeH^+ is that it has never been experimentally produced [74].

While TeH^+ has never been trapped in our lab, loading, trapping and control of SiO^+ is now routine. Since full state preparation including rovibrational cooling to the ground state has been demonstrated, it is useful to consider the precision that is possible to achieve using SiO^+ as a probe of $d\mu/dt$.

5.6.1 Time Variation of m_p/m_e

The best limit set on the time variation of μ was held for awhile by astrophysical observations of emission lines from methanol emitted 7.5 billion years ago and sets $(\mathrm{d}\mu/\mathrm{dt})/\mu < 2(2) \times 10^{-17}$ / yr [140]. With the precision of atomic clocks reaching the 10^{-19} level [65] it is desirable to match these astrophysical observations with probes of molecules in a laboratory setting. Only very recently has an atomic measurement surpassed the limit set from methanol and the new results constrain the temporal drift to be $(\mathrm{d}\mu/\mathrm{dt})/\mu < 8(36) \times 10^{-18}$ / yr [50]. It took time for atomic measurements in a lab to catch up because the atomic sensitivity to μ is determined by changes to the nuclear spin and hyperfine energies, both of which scale less than the coupling in molecules. While the sensitivity is lower, atoms still beat the best measurement made using a molecular sample simply due to the high level of state preparation, control and coherence. The best measurement made probing molecules employed a near degenerate transition in KrB to achieve a precision of $(\mathrm{d}\mu/\mathrm{dt})/\mu < 0.3(1.0) \times 10^{-14}$ / yr [51]. As indicated, we believe measurements at the 10^{-18} level can be made using molecular samples.

The promise of using molecules is in their direct sensitivity to μ. One can relate a fractional change in μ to a fractional change in the energy of some transition — $\hbar\nu = (E_e - E_g)$ — by,

$$\frac{\Delta\nu}{\nu} = K_\mu \frac{\Delta\mu}{\mu}. \tag{5.18}$$

The sensitivity coefficient K_μ is,

$$K_\mu = \frac{\mu}{\nu}\left(\frac{dE_e}{d\mu} - \frac{dE_g}{d\mu}\right). \tag{5.19}$$

Here, we see the sensitivity coefficent depends directly on $\mathrm{dE}_i/\mathrm{d}\mu$. Ideally, the state energies change in opposite ways, or one state is much more affected by a change in μ than the other. Combing the above two equations we find,

$$\Delta\mu = \Delta\nu\Big(\frac{dE_e}{d\mu} - \frac{dE_g}{d\mu}\Big)^{-1}. \tag{5.20}$$

We can estimate $\mathrm{dE}_i/\mathrm{d}\mu$ by expressing the rovibrational energy levels in terms of the Dunham parameters [63]. In this way,

$$E(v,J) = \sum_{k,l} Y_{k,l}\Big(v+\frac{1}{2}\Big)^k [J(J+1)-\Omega^2]^l \ , \tag{5.21}$$

where $\mathrm{Y}_{k,l}$ refer to the different rotational and vibrational constants of the molecule, v is the vibrational quantum number, J is the total angular momentum not including nuclear spin and Ω is the projection of the total angular momentum onto the internuclear axis. Taking the derivative of Eq. 5.21 with respect to μ,

$$\begin{aligned}\frac{E(v,J)}{d\mu} &= \sum_{k,l} \frac{dY_{k,l}}{d\mu}\Big(v+\frac{1}{2}\Big)^k [J(J+1)-\Omega^2]^l \\ &\approx \sum_{k,l} \frac{-Y_{k,l}}{\mu}\Big(l+\frac{k}{2}\Big)\Big(v+\frac{1}{2}\Big)^k [J(J+1)-\Omega^2]^l \end{aligned} \tag{5.22}$$

In SiO^+ , a transition driven has an energy set predominantly by the the first-order vibrational constant and so we can approximate the sensitivity purely in terms of vibrational constants and quantum numbers. Expanding to the first two orders of vibrational constants (ω_e and $\omega_e x_e$), see Table 5.1,

$$K_\mu \nu = \frac{1}{2}(v_g - v_e)[\omega_e - 2(1 + v_g + v_e)\omega_e x_e]. \tag{5.23}$$

Eq. 5.23 describes the absolute sensitivity that a given transition between vibrational states v_g and v_e at frequency ν has, in terms of μ. From this equation, we gain insight into the most desirable molecular parameters. The highest sensitivity can be achieved by driving a high energy transition to large v_e in a harmonic well (where $\omega_e x_e$ is small).

5.6.2 Candidate Transitions in SiO^+

Since we can prepare SiO^+ in its ground state, $|X, v = 0, N = 0, J = 1/2\rangle$ lets focus on the sensitivity and prospective precision obtain from this ground state. The deep well of the X state supports many vibrational transitions, however their lifetimes are strongly affected by the presence of the A state and tend to be sub-ms for $v > 5$. From the calculations of the TDMs and vibrational state energies using PGopher , including A state perturbations, mentioned in Sec. 5.4 we outline the SiO^+ X-X overtone transitions, shown in Table 5.6. The 0-2 and 0-1 overtone transition were omitted for their low transition energy and the fact that the 0-2 is nearly degenerate with the $|A, v = 0\rangle$ state, where perturbations and couplings would likely complicate systematic effects.

Note that the short lifetime of these states is predominately due to the A state. For example, due to the small dipole moment that couples the 0 - 12 overtone, the associated Einstein A coefficient would be ~ 0.22 s^{-1} , while from the total linewidth we can only resolve from that state to $\sim 1/\tau = 1/0.06$ ms $= 166$ s^{-1} . Despite the lowered state lifetime, resolving molecular transitions to the $\mathcal{O}(100)$ Hz level is promising and would still advance the level of precision molecular spectroscopy.

From these values, we can estimate the sensitivities of the overtone transitions as the

Overtone	Wavelength (nm)	Uncertainty (GHz)	Dipole Moment (a.u.)	$A_{v',0}$ (s^{-1})	Total Lifetime (ms)
0 - 3	2936.77	1.4	6.94×10^{-4}	0.333	4.65
0 - 4	2216.31	2.3	6.26×10^{-4}	0.270	1.23
0 - 5	1783.99	3.7	5.65×10^{-4}	0.220	0.55
0 - 6	1495.80	5.4	2.12×10^{-4}	0.031	0.31
0 - 7	1290.01	7.6	5.67×10^{-4}	0.221	0.20
0 - 8	1135.73	10.0	4.32×10^{-4}	0.128	0.14
0 - 9	1015.78	14.1	5.66×10^{-4}	0.221	0.11
0 - 10	919.89	18.3	8.42×10^{-4}	0.490	0.09
0 - 11	841.43	23.4	1.53×10^{-4}	0.016	0.07
0 - 12	776.11	29.4	2.17×10^{-4}	0.033	0.06
0 - 13	720.88	36.4	2.08×10^{-4}	0.030	0.05
0 - 14	673.56	44.5	2.71×10^{-4}	0.051	0.05

Table 5.6: **Estimation of SiO^+ X-X Overtone Transitions:** Details for the overtone transition $|X, v = 0, N = 0, J = 1.5\rangle \rightarrow |X, v', N = 1, J = 0.5\rangle$ are presented. The estimated transition wavelengths, twice their uncertainty, direct dipole moments, corresponding Einstein A coefficients and total state lifetimes are shown. Note that the dipole moments and Einstein A coefficients are purely from the coupling of $v'' = 0 \rightarrow v'$. The total state lifetime is much lower due to $A^2\Pi$ state coupling. These are found from numerical integration and the use of the PGopher package [131], which includes perturbations from the A state.

associated precision obtainable. The challenge is that as the transition energy increases with v, the state lifetime decreases, which sets the fundamental limit on how well a transition can be resolved with typical spectroscopic methods. Plugging in the transition energies from Table 5.6 and constants from Table 5.1 into Eq. 5.23 we obtain very similar values for K_μ regardless of overtone driven, where $K_\mu \approx$ -0.46.

Following the treatment from [19], the uncertainties that can be reached are not solely dependent on K_μ and also depend on the signal contrast and probe time - which has an upper bound given by the state lifetime. We can define $\sigma_y(T) = \delta\nu(\mathrm{T})/\nu$ as the Allan deviation from an overall measurement time T. Here, $\delta\nu$ is the frequency uncertainty of the measurement. We can then write the statistical sensitivity of the measurement as $\xi(T) = |K_\mu|/\sigma_y(T)$. We can then relate the frequency shift $\Delta\nu$ and frequency uncertainty $\delta\nu(T)$ to a fractional change in μ as,

$$\frac{\Delta\nu}{\delta\nu(T)} = \xi(T)\frac{\Delta\mu}{\mu} \tag{5.24}$$

If we make a projection-noise limited Ramsey-style measurement on a single molecular ion, then the root-mean-squared error is,

$$\delta\nu(T) = \frac{1}{T_R C}\sqrt{\frac{T_c}{2T}} \tag{5.25}$$

where T_R is the Ramsey wait time, T_c is the cycle time, T is the measurement time (total integration time), and C is the fringe contrast. Note that for a frequency line measurement, both sides of the fringe need to be measured. Typically $C = 0.6$ if $T_R = \tau$ where τ is the total state lifetime of the excited state being probed. In the limit of zero experimental dead time then $T_c = 2\ T_R = 2\ \tau$ such that $\delta\nu(T) = \frac{1}{C}(\tau T)^{-1/2}$. From this, we can estimate the

sensitivities achievable by driving overtones in SiO^+ , which is shown in Table 5.7.

From Table 5.7 we see that the sensitivities and achievable precision does not vary by more than an order of magnitude for overtones. This is due to the relative short lifetime of the $|X, v\rangle$ states, from coupling to the $A^2\Pi$ state. While no measurements of $\dot{\mu}$ made using SiO^+ can out perform the most stringent limits set by Ref. [50], the 0-3 can potentially beat the best limits set by molecules [51]. The challenge here is achieving an ultra-narrow linewidth laser at 2.9 μm. These overtones can possibly achieve similar precision to Ref. [51] if the systematic errors reside at the $(\mathcal{O})10^{-15}$ level.

5.6.3 Survey Spectroscopy

The predicted sensitivity of SiO^+ to a time variation in μ in Table. 5.7, show that the 0-3 overtone can achieve the highest level of precision, for the transitions shown. However, finding accessible lasers to address these NIR transitions is a challenge. Without a major difference in transitions that are best to probe for $\dot{\mu}$ measurements it would be ideal to have large wavelength scanning that can address multiple. The only known CW laser to achieve this is a Toptica TOPO which provides high power output (Watt level) from 1.45 - 4 μm. The large accessible wavelength range comes at a large price tag. Some diode lasers can be widely tunable (80 - 100 nm)[2] and achieve moderate powers ($\sim$ 20 mW) and linewidths (<200 kHz). However one laser would only be able to address one transition.

Motivated by the relative flatness of the achievable precision versus driven overtone, a good starting point to work with lasers one has on hand. A recently purchased M Squared Solstis CW Ti:Sapphire laser is capable of outputting $\sim$ 2 W in the Ti:Sapph fundamental region of 700 - 1000 nm. That range provides access to the 0 - {10,11,12,13} overtones.

[2]Spectra-Physics TLB-67326, for example

	T = 1 s				T = 1 day			
Overtone	$\delta\nu(T)$ (Hz)	$\delta\nu(T)/\nu$	$\xi(T)$	$\sigma_y^\mu(T)$	$\delta\nu(T)$ (Hz)	$\delta\nu(T)/\nu$	$\xi(T)$	$\sigma_y^\mu(T)$
0 - 3	24	2.1×10^{-12}	-2.0×10^{12}	-5×10^{-13}	0.08	7.2×10^{-15}	-6.0×10^{14}	-1.7×10^{-15}
0 - 4	47	6.0×10^{-12}	-1.4×10^{12}	-7.3×10^{-13}	0.16	2.0×10^{-14}	-4.1×10^{14}	-2.5×10^{-15}
0 - 5	71	1.1×10^{-11}	-1.1×10^{12}	-8.8×10^{-13}	0.24	3.7×10^{-14}	-3.3×10^{14}	-3.0×10^{-15}
0 - 6	95	1.6×10^{-11}	-1.0×10^{12}	-9.9×10^{-13}	0.32	5.5×10^{-14}	-3.0×10^{14}	-3.4×10^{-15}
0 - 7	117	2.1×10^{-11}	-9.4×10^{11}	-1.1×10^{-12}	0.40	7.2×10^{-14}	-2.8×10^{14}	-3.6×10^{-15}
0 - 8	139	2.6×10^{-11}	-9.0×10^{11}	-1.1×10^{-12}	0.47	9.0×10^{-14}	-2.6×10^{14}	-3.8×10^{-15}
0 - 9	160	3.1×10^{-11}	-8.6×10^{11}	-1.2×10^{-12}	0.54	1.1×10^{-13}	-2.5×10^{14}	-3.9×10^{-15}
0 - 10	179	3.5×10^{-11}	-8.5×10^{11}	-1.2×10^{-12}	0.61	1.2×10^{-13}	-2.5×10^{14}	-4.0×10^{-15}
0 - 11	198	4.0×10^{-11}	-8.3×10^{11}	-1.2×10^{-12}	0.67	1.3×10^{-13}	-2.4×10^{14}	-4.1×10^{-15}
0 - 12	217	4.4×10^{-11}	-8.1×10^{11}	-1.2×10^{-12}	0.74	1.5×10^{-13}	-2.4×10^{14}	-4.2×10^{-15}
0 - 13	233	4.7×10^{-11}	-8.1×10^{11}	-1.2×10^{-12}	0.79	1.6×10^{-13}	-2.4×10^{14}	-4.2×10^{-15}
0 - 14	243	4.8×10^{-11}	-8.2×10^{11}	-1.2×10^{-12}	0.83	1.6×10^{-13}	-2.4×10^{14}	-4.1×10^{-15}

Table 5.7: **Lifetime Limited Measurements in SiO^+ :**. Not shown here are the corresponding sensitivity coefficients K_μ, which has a max value of -0.49 for the 0-3 overtone and at minimum of -0.45 for the 0-14 overtone. These values were computed using the lifetimes and transition energies from Table 5.6 and relevant equations from [19].

Unfortunately these transitions have never been observed experimentally, and the uncertainty on the line centers which is at the ($\mathcal{O}$) 10 GHz level challenges the search for these $\Gamma \sim 2\pi$ x 10 kHz wide transitions. These uncertainties were calculated by propagating the errors on the molecular constants from Ref. [126] into the transition energies [3].

Interestingly, the 0-5 transition at 1783 nm is close to the $6^2S_{1/2} \rightarrow 5^2D_{5/2}$ quadrupole transition at 1776 nm in Ba^+. By linewidth narrowing a 1776 nm laser to address Ba^+ , that spectral purity can be transferred to another laser at 1783 nm through a frequency comb. As the use of Ba^+ in quantum computing applications grows [141], [142] high power 1776 nm lasers are becoming more available from vendors such as Menlo Systems, NKT and Toptica.

Despite the large uncertainty on the line centers, it may be possibly to conduct survey spectroscopy in a way similar to Ref. [143]. There, a single CaH^+ molecule was dissociated in a state dependent way, if overtone excitation occured. Since the rotational states are thermally populated and not precooled, a broadband mode-locked laser is used to address this distribution. However, the large laser bandwidth limits the precision to 3 nm. The authors benefit from the simple level of structure of Ca^+, such that resonant dissociation is immediately followed with an increase in fluorescence as the Ca^+ product is in resonance with applied laser cooling light.

Motivated by the possibility of observing the overtone transitions in a similar fashion, we set the M Squared laser to the 0 - 12 overtone transition. The major difference is that we will use a CW laser here, while the authors of [143] used a broadband laser for spectroscopy. The 0 -12 overtone was chosen since it is near the peak output power of the laser. From our modeling of population dynamics, we find that the total decay rate from $|X, v = 12\rangle$ to $|A, v\rangle$ is $\sim 1.65 \times 10^4$ s^{-1} , with $\sim 50\%$ branching to $|A, v = 6\rangle$. From $|A, v = 6\rangle$ the total

[3] See Table 3 of [126]

decay rate to $|X, v\rangle$ states is $\sim 1.62 \times 10^4$ s^{-1} with $\sim 50\%$ to $|X, v = 1\rangle$. By summing over all pathways, the total two-step decay probability from $|X, v = 12\rangle$ to $|X, v = 1\rangle$ is $\sim 48\%$ after 500 μs. Following the eventual decay of $|X, v = 12\rangle$ to $|X, v = 1\rangle$ we can dissociate the molecule through the $|C, v = 2\rangle$ state at 44795.2 cm^{-1} . A dye laser with Coumarin-450 can produce light at this wavelength[4]. This process has an advantage over direct dissociation from $|X, v = 12\rangle \rightarrow |C\rangle$ since the X-C,1-2 transition has already been observed [48], [94] while the other has not. The depletion of SiO^+ molecules in the trap are measured by radial tickling [94].

Due to the narrow linewidth of the 0 - 12 overtone transition ($\approx 2\pi$ x 3 kHz) one has to be careful that either the wavelength tuning step-size is smaller than then this linewidth or that the transition is broadened to much higher levels. The challenge of the latter choice is that the $|X, v = 12\rangle$ state has its lifetime shortened due purely due to $A^2\Pi$ coupling, and the dipole moment for the $|X, v = 0\rangle \rightarrow |x, v = 12\rangle$ (see. Table 5.6) provides a much weaker coupling. As a result, at 1 W input power focused to a waist of $w_0 = 2$ mm the observed overtone is only broadened to 2π x 400 Hz, which is less than its natural linewidth. At a waist of 200 μm and 1.5 W of power we can modestly broaden the linewidth to 2π x 10 kHz. Unfortunately this would still require 300 steps to cover the $\sim$ 30 GHz uncertainty on the line center.

Being limited by the power of a reasonably high power CW laser, we were motivated to drive the overtone using a Spectra-Physics Mai-tai fs pulsed laser, similar to the scheme from Ref. [143]. This is the same laser system used to accomplish rotational cooling. Instead of doubling the output to address the X-B transition at 385 nm, the fundamental output can be tuned to 776 nm with $\sim$ 1.3 W to the ions. Unfortunately at the time a second Mai-Tai

[4]See Sectoin 5.4.1 of [94]

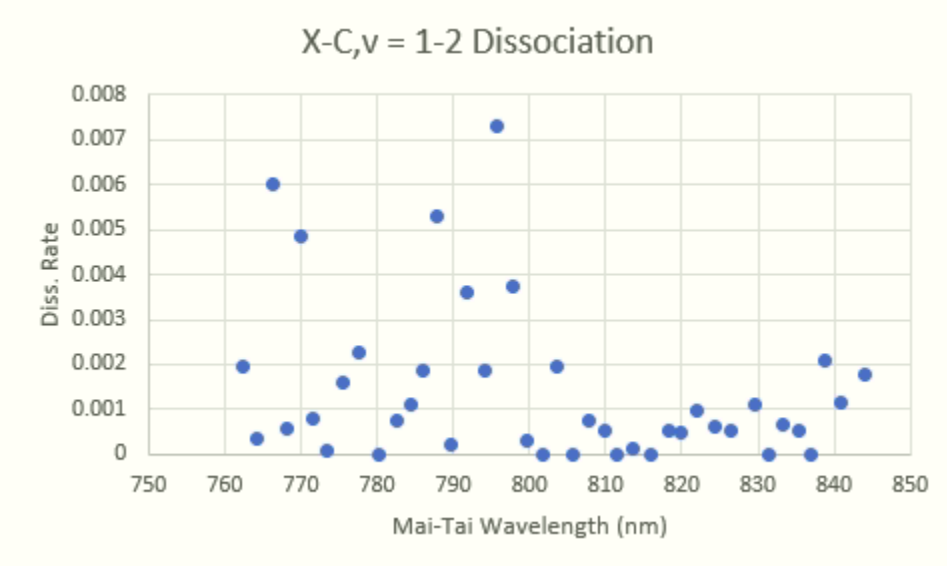

Figure 5.11: **Preliminary Scans of 0 - 12 Overtone:** Dissociation rate of SiO^+ molecules are a 10 ms exposure of the spectroscopy laser. The data shown is likely just noise and no conclusions can be drawn. Typical credible dissociate rates range from 0.01 - 0.1 s^{-1} [130]. The fitting script from LabView does not provide an uncertainty on the fit, but that can be estimated to be on the order of the data shown here.

laser was not available. If both were operational, then one laser could be used to rotationally cool the molecules and the second used to probe the overtone transition. As a result, the rotational distribution of the SiO^+ molecules was thermally populated from REMPI [129] when conducting the measurements.

It is likely that the data in Fig. 5.11 missed the line center by taking 2 nm steps, or by misalignment of the laser. As the output wavelength of the Mai-Tai is tuned, the beam moves laterally causing it to potentially miss the SiO^+ ion core. The experiment may benefit from rovibrational cooling to $N = 0$ first which results in less diffusion of the rotational population as it decays down to $|X, v = 1\rangle$ from $|X, v = 12\rangle$. It may also be useful to perform this experiment in the single-ion set-up where dissociation of a single SiO^+ will result in the product Si^+ ion to be ejected from the high trapping potential. The Ba^+ cooling

laser can be misaligned, producing less photons/s at the center of the trap than if offset by a co-trapped SiO^+ molecule. This decrease in photons can potentially provide a clearer signal and also the resulting dissociation rate gives insight to the transition strength, similar to Ref. [143].

5.6.4 Future Directions

While SiO^+ may not achieve record breaking precision in measurements of $\dot{\mu}$ from those made in atoms, it may be able to compete withe the measurements made in molecules. A more rigorous analysis of the systematics, similar to the work done for TeH^+ [19], [74], would provide insight to the viability of precision measurements in SiO^+ . Our ability to rovibrationally prepare SiO^+ samples can also serve as a platform to make test measurements and demonstrate new readout techniques. Outlined in Ch. 7, optical cycling between $X^2\Sigma^+$ and $B^2\Sigma^+$ with a pulsed laser can serve as a nondestructive readout method akin to, and potentially easier, than QLS. After state preparation to the ground rovibrational state, a microwave pulse can prepare SiO^+ into $|X, v = 0, N = 1, J = 1/2\rangle$, where then a CW laser tuned to the $|X, v = 0, N = 1, J = 1/2\rangle \rightarrow |X, v = 0, N = 0, J = 1/2\rangle$ transition can scatter $\mathcal{O}(10^3)$ photons/s before population diffuses to the A or $|X, v\,0\rangle$ states [48].

CHAPTER 6

Sideband Cooling: How Low Can You Go?

You've applied the pressure
to have me crystalised
The xx
"Crystalised"

6.1 Introduction

The demonstration of spectroscopy using quantum logic (QLS) [105] showed that the internal state of one ion can be mapped to the internal state of another, through a shared motional mode. QLS and other nondestructive spectroscopy methods (see Ch. 7) provide a method to efficiently measure narrow transitions without destroying the molecule, utilizing the long storage times that ion traps afford. The prerequisite for these experiments is that the ion pair must be cooled to the ground motional state of a given mode. Ideally all the modes in three dimension are cooled due to the influence of Debye-Waller Factors (see Ref. [68] and Appendix A) and second-order Doppler effects [52], [65].

The requirement of ground state cooling is at the heart of the QLS scheme: one phonon of energy is added to a ion pair conditional on the spectroscopy ion excitation. If the phonon is added, a RSB transition can be driven. Otherwise a RSB transition cannot be driven because there is no energy state lower than the zero-point energy state ($|n = 0\rangle$ for harmonic oscillator motional states. Preparation of the $|n = 0\rangle$ state is achieved by sideband cooling where $\Delta n = -1$ transitions are resonantly driven until the ground state is reached. Detection

of sideband cooling (detailed in Appendix A) provides a measure of $\bar{n}$, the mean occupation number. In our trap, after Doppler cooling $\bar{n} \sim 20$ and after sideband cooling $\bar{n} \to 0.05$ which indicates 95% of population is in the ground state, $|n = 0\rangle$, for a given mode.

There are several ways to implement sideband cooling including continuous methods [119] (where the RSC lasers are constantly on) to pulsed methods that repeatedly drive RSB π-pulses [53]. Pulsed RSC techniques typically reaches a lower $\bar{n}$ and is faster, but requires specifically tailored pulse sequences [52] and modeling if the ion has a high $\bar{n}$ after Doppler cooling, due to certain $|n\rangle$ states where the Rabi frequency is zero (see Eq. A.6).

In this thesis, I will only discuss CW RSC methods as these were the only type used. This is primarily due to the limitations of our experimental control, see Sec. 3.5, where the TTL channels used to toggle the lasers on and off are not retriggerable. There are commercial systems now available, including Artiq[1], to upgrade and implement a more versatile control scheme. That work is for another day and another thesis.

In general, resolved sideband cooling works by tuning a laser system (single photon or two-photon Raman) to the red-sideband (RSB) such that the $|\uparrow, n\rangle \to |\downarrow, n-1\rangle$ transition is driven. Optical pumping from $|\downarrow\rangle \to |e\rangle \to |\uparrow\rangle$ can put the system into $|\uparrow, n-1\rangle$, so that $|n\rangle$ can be lowered again. Since the sideband transitions are suppressed by the Lamb-Dicke parameter $\eta \sim 0.1$, the motional state, on average, is unchanged from the optical pumping process. The process is then repeated until the $|n = 0\rangle$ state is reached, since there is no lower energy state to drive a RSB on. While the theoretical limit on $\bar{n} < \mathcal{O}(10^{-3})$, heating due to trap fluctuations will limit the minimum $\bar{n}$.

In this chapter, I will briefly review the previous sideband cooling scheme, CW RSC [99] before going into the upgrades made to that system and further improvement by imple-

[1] https://m-labs.hk/experiment-control/artiq/

menting EIT sideband cooling. Cooling of a single Ba^+ , two Ba^+ ions and a mixed-species crystal of Ba^+ -SiO^+ is demonstrated and the results are shown. The main challenge in this experiment, as discussed in Ch. 2, is the mass imbalance between the Ba^+ and SiO^+ ions which makes cooling schemes inefficient and readout take longer. The relevant level structure and detunings for each of the three schemes used are shown in Fig. 6.1.

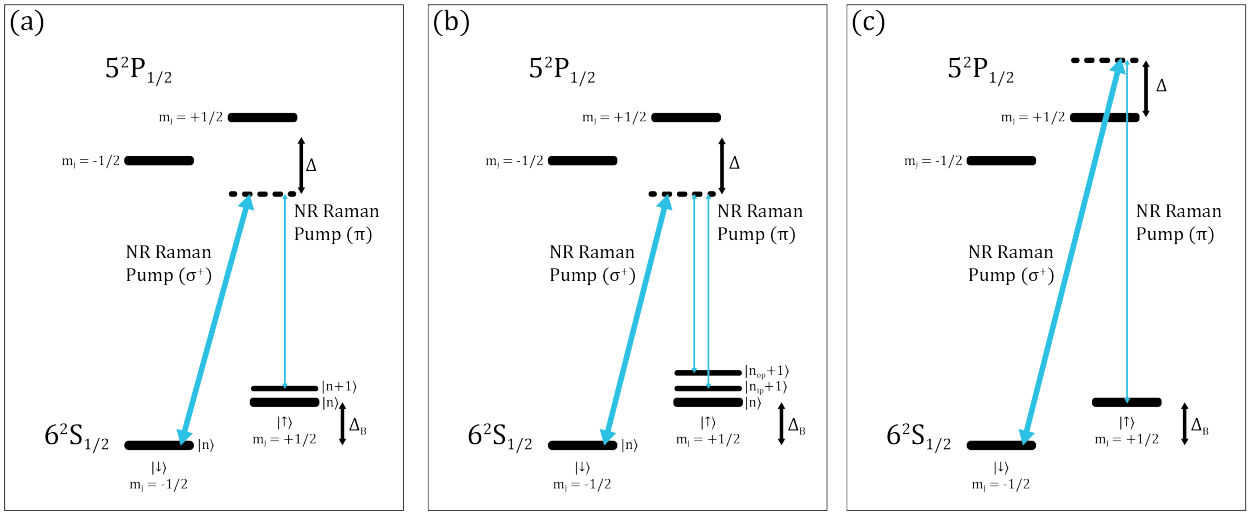

Figure 6.1: **Types of RSC Schemes Used:** a) CW RSC on a single mode, Δ = -2π x 90 MHz here. b) CW RSC using the IQ mixer: the NR-π has two frequency components and Δ = -2π x 90 MHz here. c) EIT sideband cooling: The NR beams are necessarily blue-detuned and set to Δ = +2π x 230 MHz. In each three case $\Omega_\sigma \gg \Omega_\pi$, which ensures the cooling direction and enables fast pumping back to $|\uparrow\rangle$. The NR-σ light is also denoted as the pump beam while the NR-π light is the probe beam. Not shown is the 649 nm light which is continually on during the RSC schemes, pumping population out of $\left|5^2D_{3/2}\right\rangle$

6.2 CW Raman Sideband Cooling (RSC)

In 2016 our group demonstrated CW RSC of a single Ba^+ ion to an $\bar{n} = 0.15$ [99]. Here, the NR-σ and NR-π beams are detuned to Δ = -90 MHz from the $S_{1/2} \rightarrow P_{1/2}$ resonance and their Rabi frequencies are set accordingly, $\Omega_\sigma \gg \Omega_\pi$. Typically, $\Omega_\sigma \approx 2\pi$ x 15 MHz, $\Omega_\pi \approx 2\pi$ x 1 MHz and $\Omega_{eff} \approx 2\pi$ x 100 kHz. RSC is achieved when the relative detuning of

the NR beams is set to $\delta = \Delta_\sigma - \Delta_\pi = \Delta_B + \Delta' - \omega_m$, where Δ_B is the Zeeman splitting, Δ' is the light shift, and ω_m is the motional frequency. Since the NR-σ Rabi frequency is much larger than Ω_{eff}, the population in $|\downarrow\rangle$ is more likely to be pumped back into $|\uparrow\rangle$ by a one photon transition (that typically preserves $|n\rangle$) than by the two-photon stimulated Raman transition which would return the state to $|\uparrow, n+1\rangle$. This ensures that RSC leads to $|n\rangle \rightarrow 0$. For all discussion in this section we will focus on cooling the axial mode of motion, ω_z and $|n_z\rangle$.

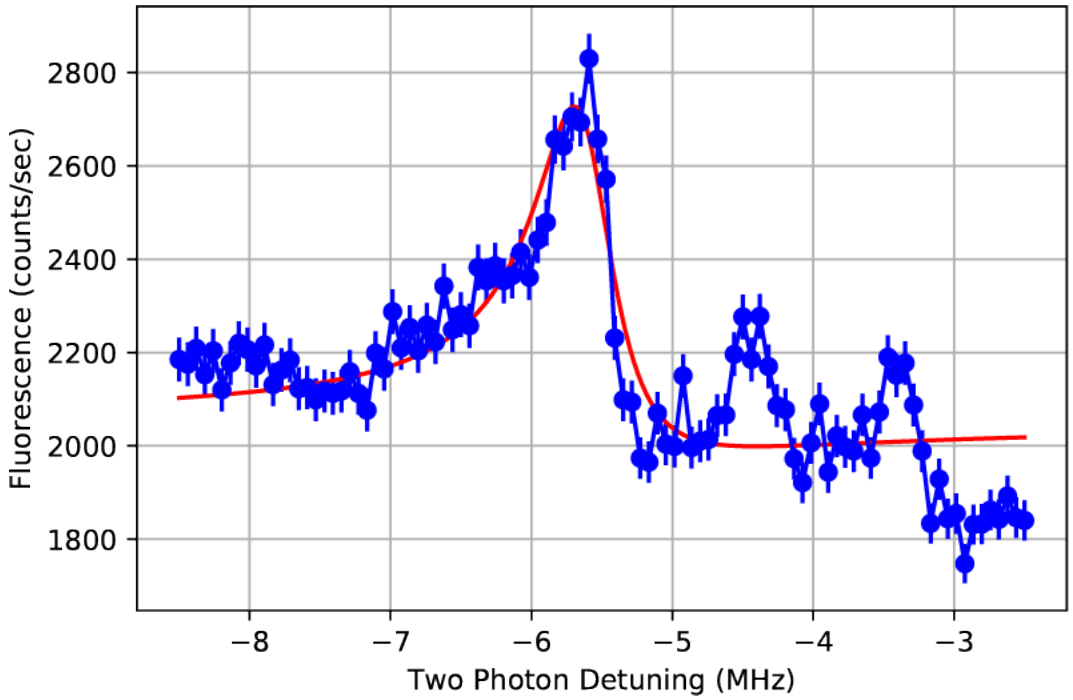

Figure 6.2: **CW RSC Fluorescence Spectrum:** As the NR-π resonance is scanned over the Raman resonance, RSC is verified by the lack of a RSB, since this transition cannot be driven if the motional population is in $|n = 0\rangle$. We clearly see the first- and second-order BSBs to the right of the main carrier transition. The resulting spectrum is fit using Eq. 5.17 from Ref. [119] to estimate the spectrum FWHM, Ω_{eff} and $\bar{n}$. Mainly the scan is taken to find the carrier resonance (which is at $\Delta_B + \Delta'$). Note that by varying the NR-σ power and measuring the carrier resonance we can also measurement of the NR-σ beam waist, ω_0^σ, though with less precision than the technique mentioned in Sec. 4.4.3

.

The NR Raman resonances can be found by scanning the weak, NR-π detuning while keeping the NR-σ detuning fixed. When the detuning matches a Raman resonance condition (carrier or sideband) population is pumped into $|\downarrow\rangle$ and then repumped by the strong pump (NR-σ) beam. The light scattered from the optical pumping step is detected and a typical scan is shown in Fig. 6.2

The resulting spectrum is known as a Fano profile and is due to the interference between the two paths to populate $|e\rangle = \left|P_{1/2}, m_j = 1/2\right\rangle$, which appears as a continuum if the $|\uparrow\rangle \rightarrow |e\rangle$ transition is not saturated [144]. The first path is directly from $|\uparrow\rangle$ to $|e\rangle$ and the second path is the three-photon process of first the stimulated Raman transition to $|\downarrow\rangle$ then the one photon absorption exciting $|\downarrow\rangle$ to $|e\rangle$. Since the second path passes through the the narrow, discrete state $|\downarrow\rangle$ it interferes with the one-photon $|\uparrow\rangle \rightarrow |e\rangle$ process to the 'continuum'.

To understand the efficacy of RSC, we measure the red and blue sidebands using a FOR frequency scan. Fitting each peak and comparing the ratio of the amplitudes gives a direct measurement of $\bar{n}$. For a mathematical description of this see Appendix A. An example plot, showing CW RSC of a single Ba^+ ion along z-axis is shown in Fig. 6.3

The small RSB amplitude in Fig. 6.3 heralds the success of RSC along the axial direction. At this time, there was not an additional NR-π-rad beam path that could achieve RSC in the radial directions, nor was there a FOR-π-rad to readout motional sidebands in the radial direction. Recall that it is the $\mathbf{\Delta k}$ vector that sets the direction of the electric field gradient, and from the geometry shown in Fig. 3.16, the $\mathbf{\Delta k}$ vector between the NR-σ and NR-π-ax is purely along the z-axis.

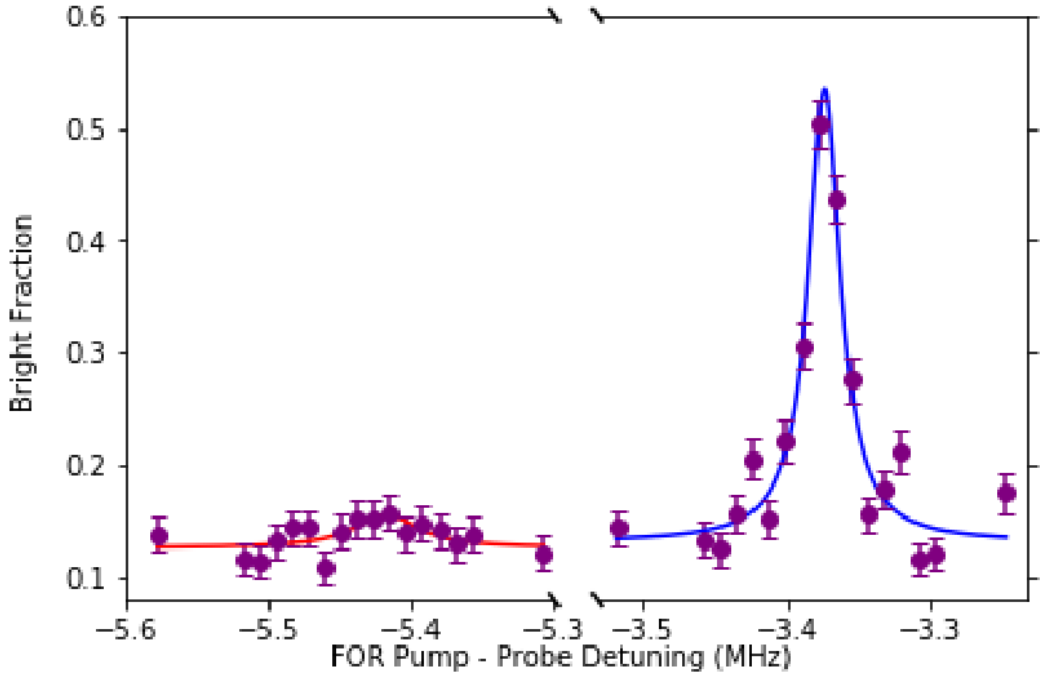

Figure 6.3: **CW RSC of a Single Barium-138 Ion:** From a fit of the amplitudes we find that $\bar{n}_z = 0.08(3)$ is achieved after 10 ms of cooling.

6.2.1 Dual Mode CW RSC

As an extension to the CW RSC scheme mentioned in the last section, we aim to simultaneously cool both axial modes in a two ion crystal (see Fig. 6.1). As discussed in Ch. 2, the normal mode structure now has an in-phase and out-of-phase axial mode along the z-direction, when $\omega_z < \omega_{(x,y)}$. Conceived and originally designed by Vincent Carrat, a way to accomplish this, with minimal change in the experimental apparatus, is to impart two frequency components into the NR-π light using an IQ mixer. The circuit and details regarding the set-up are described in Sec. 3.5.6.1. After careful design and reduction of unwanted frequency components, the NR-π beam contains two frequency tones:

$$\omega_{\pi_1} = \omega_\sigma - \Delta_B - \omega_{ip,z} \tag{6.1}$$

$$\omega_{\pi_2} = \omega_\sigma - \Delta_B - \omega_{op,z} \ , \tag{6.2}$$

which are tuned to the RSBs of the in-phase and out-of-phase modes. This is accomplished by setting the VCO that drives the IQ mixer to $\omega_{VCO} = (\omega_{op,z} - \omega_{ip,z})/2$ where the factor of two accounts for the double-pass AOM adding the frequency twice.

When two Ba^+ ions are loaded into the trap, where one ion is 138-Ba^+ and the other is an isotope which appears dark, we find the CW Raman fluorescence shows the presence of two axial motional modes, shown in Fig. 6.4.

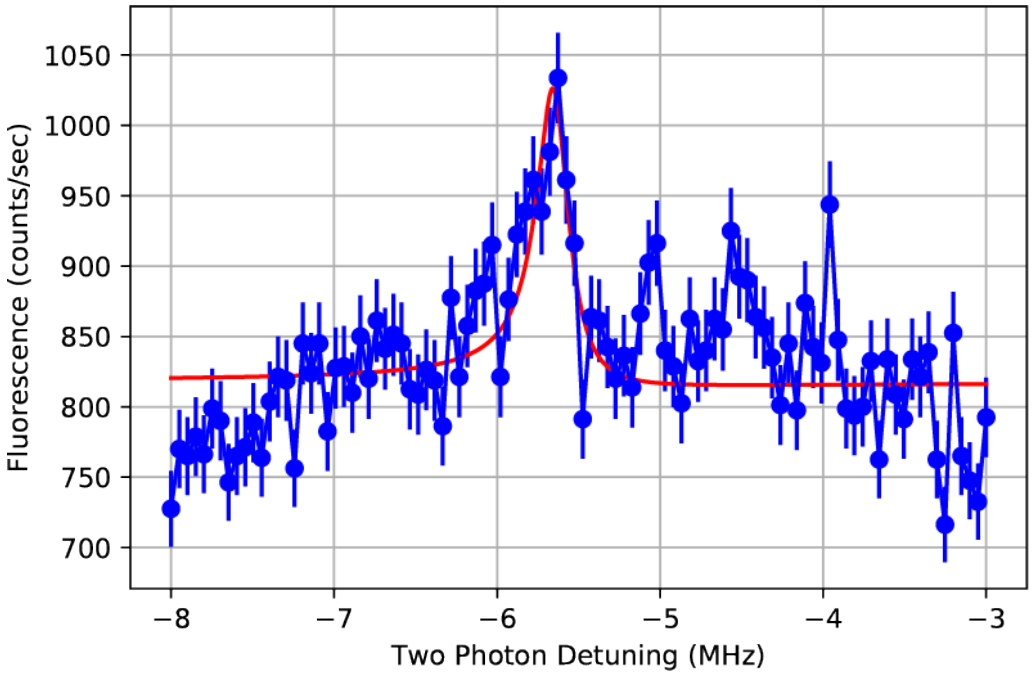

Figure 6.4: **CW RSC Fluorescence Spectrum for $^{138}Ba^+$ and $^{x}Ba^+$** Here, the dark ion, of mass $x \neq 138$, is an unknown Ba^+ isotope. at trap settings of V_{ec} = 40 V and RF: -2, $\omega_{ip,z} \approx 2\pi$ x 0.511 MHz and $\omega_{op,z} \approx 2\pi$ x 0.887 MHz

Again we can characterize the efficiency by observing the FOR red and blue sideband transitions to find $\bar{n}$. The results are shown in Fig. 6.5.

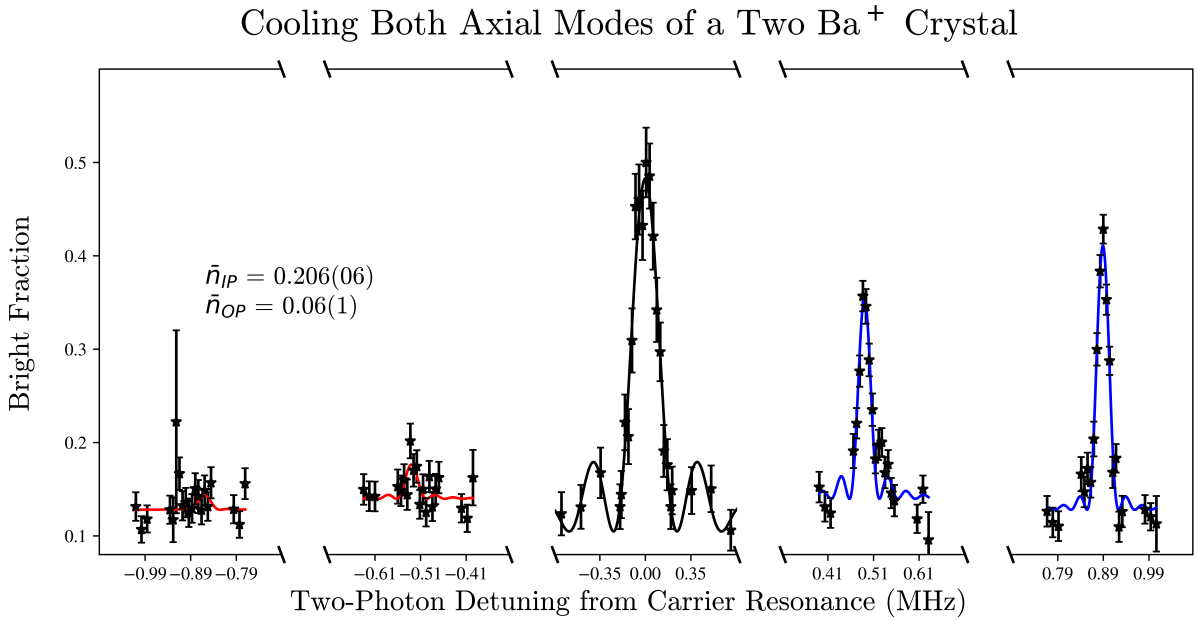

Figure 6.5: **Dual Axial Mode CW RSC:** Two Ba^+ ions, $^{138}Ba^+$ and $^{x}Ba^+$, are trapped at $V_{ec} = 40$ V and RF: -2 and cooled to the ground state for 20 ms.

The reliability of the cooling scheme is robust and Fig. 6.2.1 shows that even lower $\bar{n}$ can be reached. This method can likely be extended to ion crystals of different masses. The drawback of this implementation is that it is slow. Even though we are simultaneously cooling both modes, the entire scheme still takes twice as long, because only Raman transition can happen at once.

The success of this RSC cooling method was soon overshadowed by the challenge of loading and sympathetic cooling a mixed-species crystal of Ba^+ - AlH^+. It took roughly a year to work out proper loading of SiO^+ , after venting and baking the chamber. By that time it became more advantageous to move to a different cooling scheme altogether.

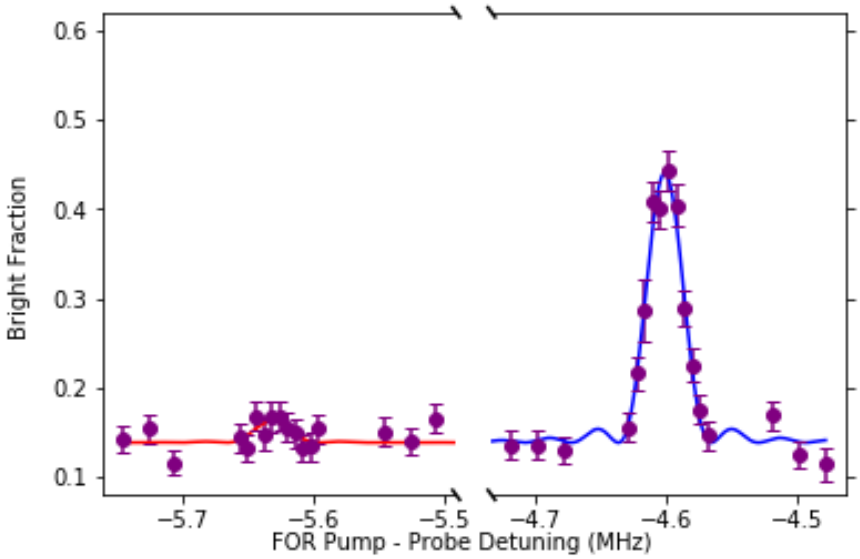

(a) **Cooling on the IP Mode of Two Ba:** Using the IQ mixer driven NR-π AOM we achieve $\bar{n}_{ip} = 0.08(1)$ for one bright and one dark Ba^+ .

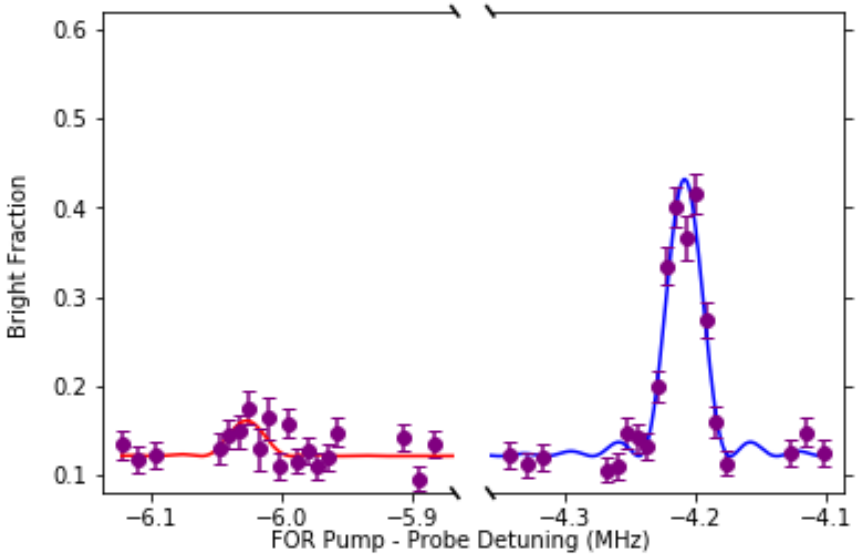

(b) **Cooling on the OP Mode of Two Ba:** Using the IQ mixer driven NR-π AOM we achieve $\bar{n}_{op} = 0.14(2)$ for one bright and one dark Ba^+ .

6.3 EIT Sideband Cooling

Another CW RSC method is electromagnetically-induced transparency sideband cooling. First proposed in Ref. [145] and quickly demonstrated in Ref. [104] with a Ca^+ ion, EIT sideband cooling has proven to be a versatile technique as it has found to be faster than red-detuned CW RSC, reach colder temperatures and it is easier to implement in three dimensions. To cool in 3D, the NR-π-rad and FOR-π-rad beam lines were added at the time of constructing the new Raman AOM drivers, which is described in Sec. 3.5.6.2. EIT sideband cooling is similar to CW RSC, with the main difference is that with EIT the Raman detuning must be blue-detuned from resonance. Additionally, the laser frequencies are set slightly differently.

The main principle behind EIT sideband cooling is the use of, well, an induced transparency in the absorption profile due to an applied laser. Consider the three-level system in Fig. 6.1(c) where the aforementioned Raman transitions are between $|\uparrow\rangle$ and $|\downarrow\rangle$ with weak coupling to $|e\rangle = \left|P_{1/2}, m_j = 1/2\right\rangle$. We already know from experimental results, shown in Fig. 6.2, that the absorption profile of the probe NR-π beam is described by a Fano profile. If the detunings of the pump and probe beams, $\Delta_\pi = \Delta_\sigma$, are equal there is a 'dark resonance' because in the dressed state picture the atomic level has been shifted in energy given by the light shift, Δ' [146]. At the new eigenenergy is where the 'bright' resonance occurs, shown in Fig. 6.7. Recall that $\Delta_\pi = \omega_\pi - \omega_{13}$ and $\Delta_\sigma = \omega_\sigma - \omega_{23}$. These dressed states lie at energies $+\Delta'$ and $-\Delta_\sigma - \Delta'$ from Δ_σ. The dressed states are created by the strong pump beam coupling $|\downarrow\rangle$ and $|e\rangle$. Here (as written in Sec. 4.3.2),

$$\delta_{d.s.} = \left(\frac{\sqrt{\Delta_\sigma^2 + \Omega_\sigma^2} - |\Delta_\sigma|}{2}\right) \cong \frac{\Omega_\sigma^2}{4\Delta_\sigma}. \tag{6.3}$$

The absorption profile of the NR-π is shown in Fig. 6.7 using Eq. 1.4 from [144].

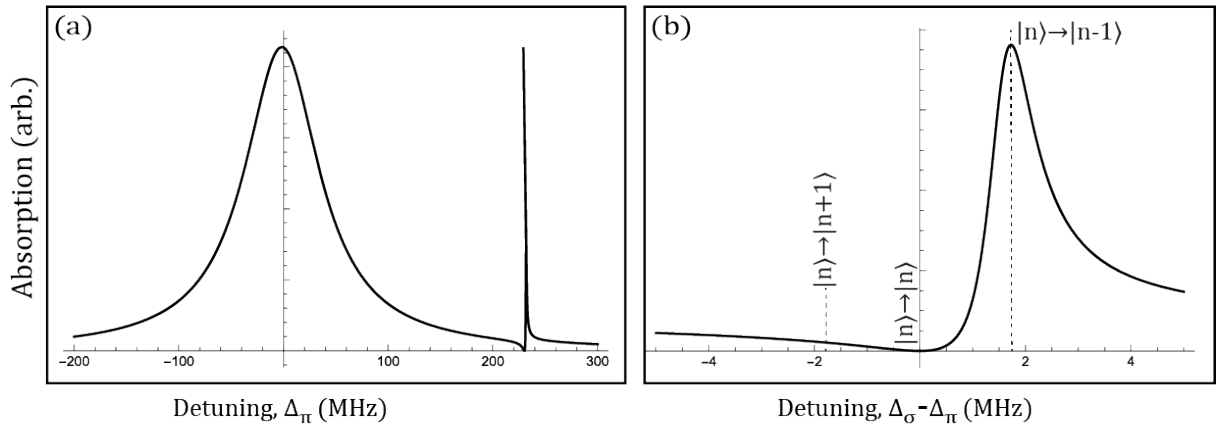

Figure 6.7: **Absorption Profile of the NR-π Beam:** a) When the three-level system is irradiated with a pump beam at a blue-detuning the absorption spectrum contains two resonances: a broad resonance at the bare state and a narrow Fano resonance at $\Delta_\sigma + \Delta'$. b) When $\Delta' = \omega_m$, the bright resonance lies on the RSB and the carrier and BSB are suppressed. Here, $\omega_m = 1.72$ MHz

The splitting of the excited state and dark resonance at $\Delta_\sigma = \Delta_\pi$ is the EIT condition, where the transparency exists. If we now consider the motional states, recall that $\Delta_\sigma = \Delta_\pi$ corresponds to the carrier transition. At this frequency the π light cannot drive carrier transitions. Then, for $\Delta_\sigma > 0$ we can set $\Delta' = \omega_m$ such that one of the dressed state lies on the RSB transition of mode m. This is plotted in Fig. 6.7. Note that while there is zero absorption on the carrier transition, absorption on the BSB is also suppressed. Absorption on these transitions contribute a heating term to the cooling cycle and reduce both the limit of $\bar{n}$ and cooling rate. In EIT sideband cooling these terms are minimized.

With the cooling condition set by Eq. 6.3, we see that the pump detuning and pump laser power set what motional modes are cooled. Interestingly from Fig. 6.7 we see that the 'narrow' resonance has a given width (set primarily by Ω_π and Δ_σ) allowing for absorption on the RSB transition for multiple modes. This is another advantage of EIT sideband cooling

and why it can be applied to two ion crystals [104], [145] and long ion chains [147], [148]

Single ion results: radx - nbar of 0.16(3) heats to nbar of 2.86, rady nbar of 0.19(1) heats to nbar of 1.9, axial nbar of 0.058

two ion results: radx2 nbar of 0.27(3), rady nbar thermal, nbar op - 0.08(3), nbar ip of 0.06(3)heats to nbar of 1.14 by measurement time

6.3.1 Single Ion Results

Since the CW RSC scheme mentioned in Sec. 6.2 utilizes red-detuned (-90 MHz) lasers and EIT requires blue detuning, a simple experimental fix was to flip the AOMs 180 degrees around. In this way, the '+' order is nearly aligned and only a short optimization of alignment was needed. The resulting NR Raman beams are +230 MHz. With a NR-σ beam waist of $\omega_0^\sigma \approx 23$ μm, from Eq. 6.3 we can estimate the power needed to obtain $\Delta'/2\pi = 0.75$ - 1.72 MHz. For that frequency range, the required NR-σ power is found to be 0.97 - 2.3 μW which is extremely reasonable to obtain. Within a day of making the change, a single Ba^+ ion was being EIT sideband cooled in the axial direction. With the AOM upgrade made and radial beams added, three dimension sideband cooling was achieved shortly after.

For each of these modes, a time delay can be added between sideband cooling and readout. In this way the heating rate of each mode can be measured. They have been found to be: $d\bar{n}_i/dt = \{0.30(2), 0.10(3), 0.043(7)\}$ quanta/ms. These are a bit high, though more rigorous analysis is needed to understand the heating sources and dependency on trapping voltages.

With a cold Ba^+ ion, we can also demonstrate coherent BSB flopping between the two qubit states along each direction. In this situation, population is continually driven from $|\uparrow, 0\rangle \leftrightarrow |\downarrow, n_i = 1\rangle$ along a given direction $i = \{x, y, z\}$.

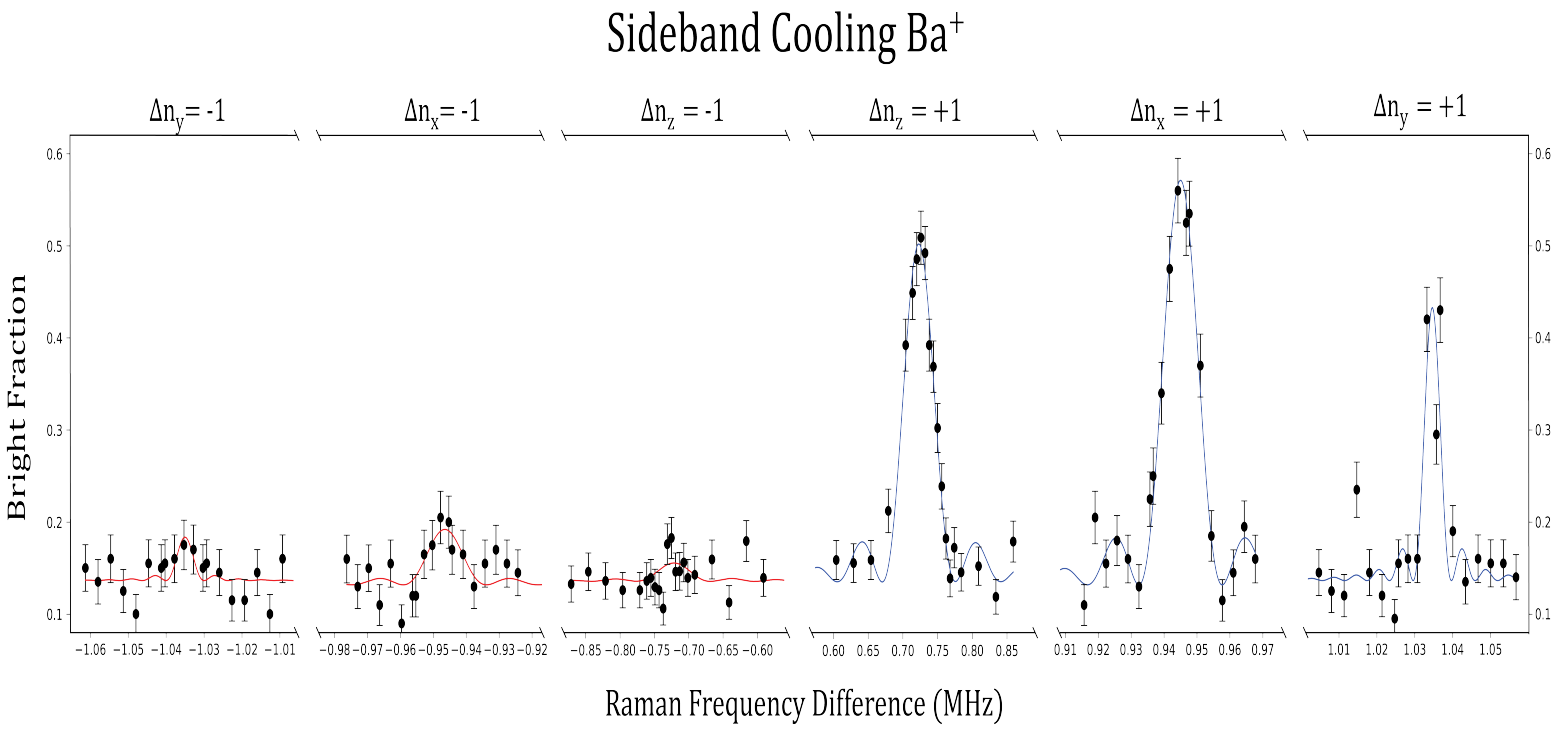

Figure 6.8: **EIT Sideband Cooling of Ba^+ in Three Dimensions:** A single Ba^+ ion cooled to the ground state along each motional axis for 10 ms total. The resulting mean occupation numbers are $\bar{n}_{(x,y,z)} = \{0.16(3), 0.19(1), 0.06(1)\}$.

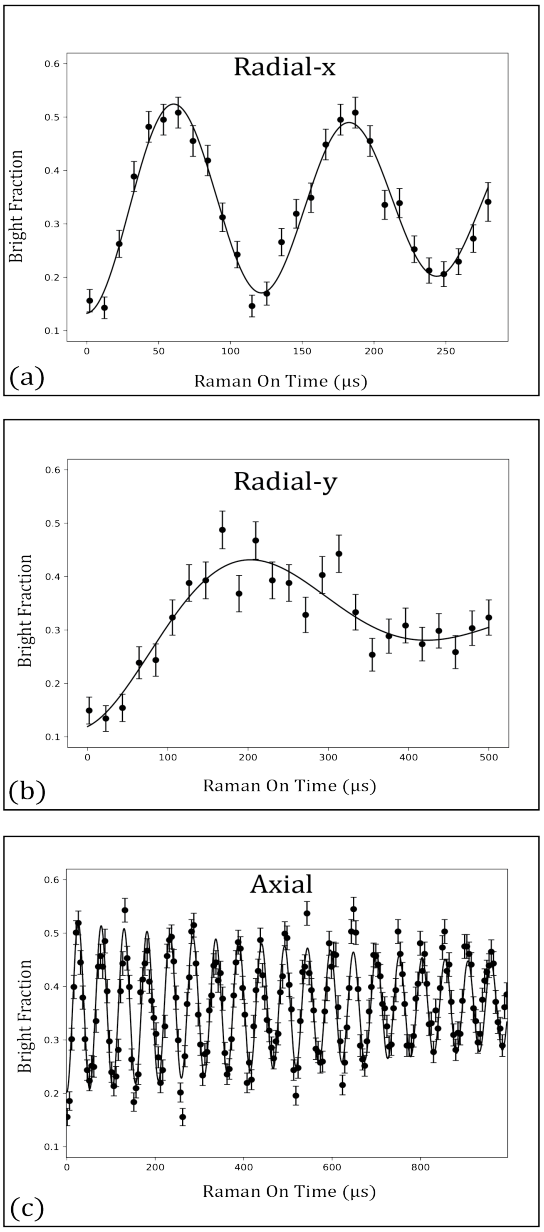

Figure 6.9: **Rabi Flopping on Ba^+ in 3D:** Coherent flopping on the blue sidebands are shown for a) x-bsb, b) y-bsb and c) z-bsb. From sideband cooling, and improvements to the magnetic field, the coherence time in c) is measured to be 2.3(2) ms, a record in this lab. Scan (c) gives an example to find $\bar{n}$ from a time scan, here $\bar{n}_z = 0.21(4)$. For a given FOR pair powers, we find BSB flopping times of $\pi_x = 61(1)\mu$s, $\pi_y = 219(10)\mu$s, $\pi_z = 25.9(0)\mu$s. Ω_{eff} is lower in the FOR-radial pair (due to power constraints), which is why the π pulse times are longer in the radial direction. Note that in a symmetric trap, the π pulse times in the x- and y-directions should be equal.

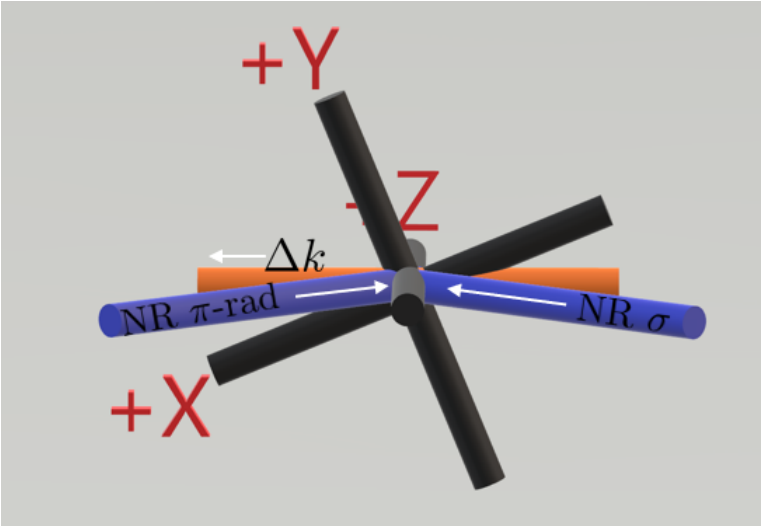

Mode	ω	η	Δk/k	Angle
Axial	0.727	0.128	1.417	Θ ~ 44.9
Rad-x	0.944	0.113	1.36	Φ ~ 15(5)
Rad-y	1.03	0.031	0.408	Φ ~ 16(5)

Figure 6.10: **Δk Vectors of Raman Beams:** The solution of **Δk** allows us to measure the project of **Δk** onto the three Cartesian coordinates. Here, Θ is the angle of **Δk** with the z-axis and makes exactly what we would expect. Φ is the angle **Δk** makes with the x axis.

Dubbed the radial surprise, the first ever Rabi flops on the radial modes showed a surprising result: the π-pulse times were unequal. With the same FOR powers driving the two modes, these results show that potentially the Lamb-Dicke parameters are different along the two radial directions. Since the mode frequencies of ω_x and ω_y only differ by 80 kHz this is not reason why. Then, the Lamb-Dicke parameters would only differ if **Δk** was different. For a symmetric Paul trap and our Raman configuration, **Δk** is expected to intersect each axis at a 45 degree angle. Recall that for a given mode, the BSB Rabi frequency $\Omega_{n,n+1}$ is given by,

$$\Omega_{n,n+1} = \sqrt{\frac{\hbar(\Delta k)^2}{2m\omega_m}}\Omega_{n,n} \tag{6.4}$$

Using the π times found from the fits in Fig. 6.9, we can solve for $\Delta\mathbf{k}$ which in turn allows use to solve for the angle $\Delta\mathbf{k}$ makes with a given axis. These results are shown in Fig. 6.10. The analysis suggests that there is a strong asymmetric in the trapping potential.

The main hypothesis is that the trapping potential is asymmetric due to the bend endcap, see Fig. 3.7. The surprising result is that this does not really influence the axial modes for two ions or the axial Lamb-Dicke parameters. Since we operate the trap under the condition $\omega_z < \omega_x$ it may be likely that the stronger radial confinement shows this behavior. It would be interesting to measure under the opposite condition where the radial confinement is weaker than the axial. The asymmetry of the radial potential may also influence cross-mode coupling [97], [149] and be the reason for the larger heating rates observed in this experiment compared to an identical ion trap [82]

6.3.2 Mixed-Species Results

Once SiO^+ has been successfully loaded, we can demonstrate EIT cooling in a Ba^+ -SiO^+ crystal in three dimensions. Note that within 45 minutes SiO^+ reacts with background H_2 gas to form $SiOH^+$. While we cannot accomplish any spectroscopy, the 1 amu change does not do anything to the EIT cooling efficiency and the change in motional modes (about 20 kHz for the $\omega_{op,z}$ mode) is easily detected. As a result, it is much easier to take preliminary data with a Ba^+ - $SiOH^+$ crystal because it will not further react and thus is stable in the trap. All of the data shown in this section is from a Ba^+ - $SiOH^+$ crystal.

Since there are two radial modes ($\hat{x}_1$ and $\hat{y}_1$) that Ba^+ has extremely weak coupling to Ba^+ (see Table 3.3) we do not bother trying to sideband cool or readout those state. The π times are on the order of ten ms, much longer than our current coherence time. Recently, a novel approach was implemented to deterministically cool on these weakly coupled modes

[83]. In this experiment, we focus on cooling 4/6 motional modes for a two ion crystal. This was built into the design of the AOM system shown in Fig. 3.25. Typically, the focus is on cooling the $\omega_{op,z}$ mode because it has a low heating rate and modest SiO^+ Lamb-Dicke parameter. The cooling order can be set by adjusting the mode and axis TTL initial settings (see Fig.3.25).

Recall that CW RSC on two modes took 20 ms, while Fig. 6.11 shows cooling of four motional modes in 10 ms total. This reflects the power of EIT sideband cooling. For a Ba^+ - $SiOH^+$ crystal the heating rates were measured in the axial directions and found to be $d\bar{n}_{ip,z}/dt = 0.36(2)$ quanta/ms and $d\bar{n}_{op,z}/dt = 0.042(3)$ quanta/ms. These rates follow the expectation that the in-phase mode has a higher heating rate, as homogenous field fluctuations couple only to the center of mass mode.

Of the most importance, BSB Rabi flops on the $\omega_{op,z}$ mode are measured and shown in Fig. 6.12. The ability to Rabi flop and observe a coherent signal indicates proper cooling of the mode and indicates the advance the experiment towards demonstrating quantum logic spectroscopy techniques.

Hindsight is 20/20 and no more data was taken in the radial direction. The y-2 scan would be the first scan repeated. The real challenge is that there is not enough FOR power to obtain fast π-pulse times in the axial and radial direction simultaneously. If so, no experimental adjustments would need to be made and everything can be measured in the same scan. It would be interesting to take cooling rate measurements of the individual modes. It would also be interesting to vary the light shift Δ' and understand how $\bar{n}$ is affect, similar to [104].

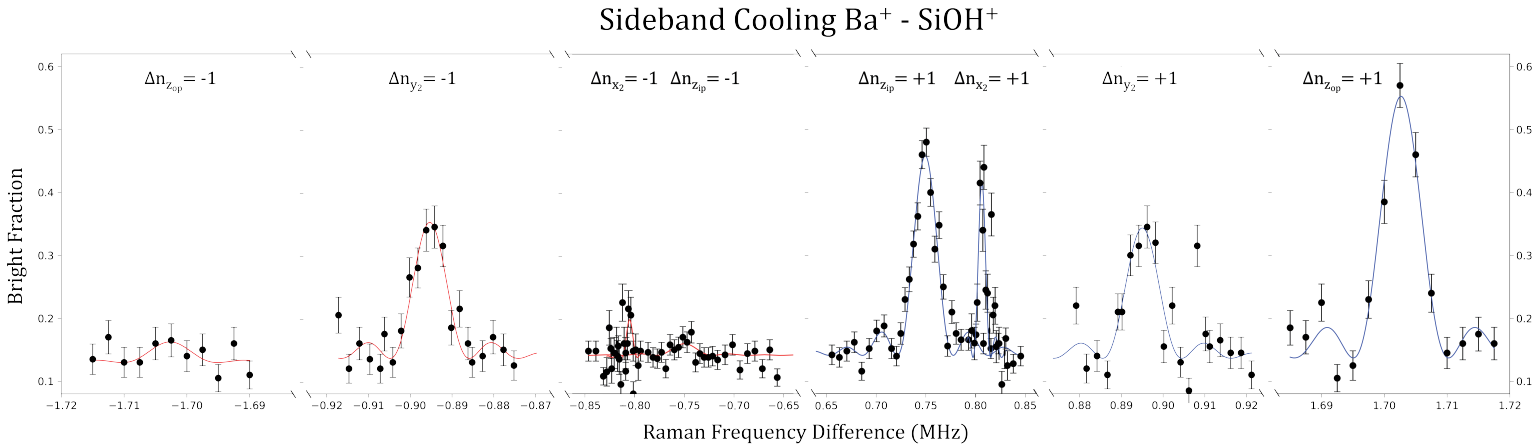

Figure 6.11: **EIT Sideband Cooling of Ba^+ -SiO^+ in Three Dimensions:** Typically each mode is cooled on for 2.5 ms each with a 10 ms total cooling time. The cooling order shown here is: 1) ω_{y_2}, 2) ω_{x_2}, 3) ω_{z_1}, and 4) ω_{z_2}. As a result, the ω_{y_2} mode has 7.5 ms to heat, while there is minimal time for the axial out-of-phase mode to heat. The cooling results in $\{\bar{n_{x2}}, \bar{n_{y2}}, \bar{n_{z1}}, \bar{n_{z2}}\} = \{0.27(2), 3(2), 0.06(3), 0.08(3)\}$

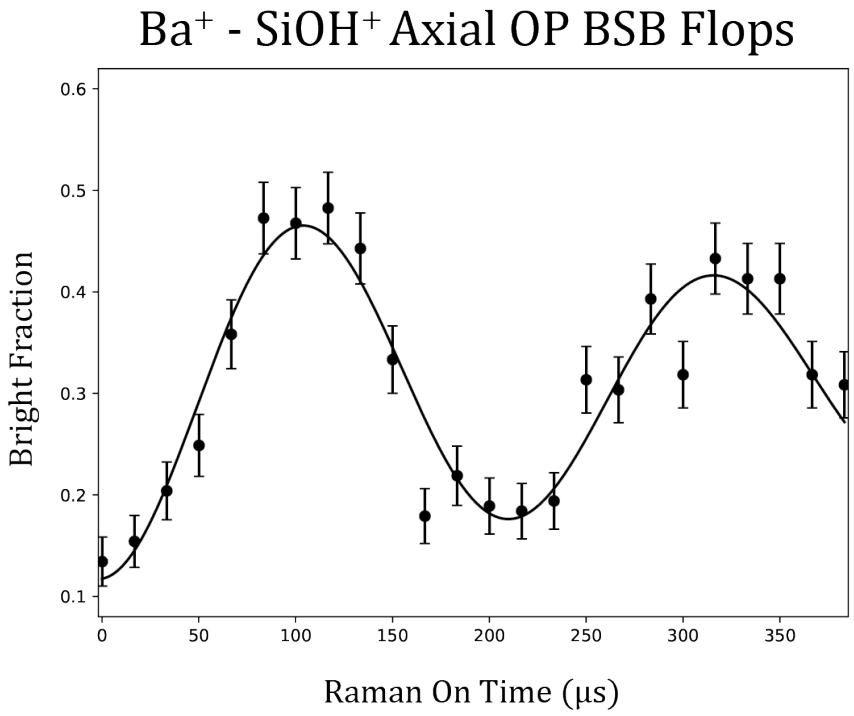

Figure 6.12: **Rabi Flopping the Out-Of-Phase BSB for a Ba^+ - $SiOH^+$ Crystal:** Here, we find measure a π pulse time of 106 μs and a 526 μs coherence time. The reduced coherence is likely due to others modes that may not have been sideband cooled.

6.4 Conclusion

At this point, both internal (for Ba^+ : see Ch.4, for SiO^+ : see Ch.5) and external state preparation (discussed here) has been demonstrated on a mixed-species crystal of Ba^+ - SiO^+ . The experiment can now fully prepare and automatically reprepare the ion crystal allowing us to proceed with developing and demonstrating nondestructive readout methods for single molecule spectroscopy.

CHAPTER 7

Photon Recoil Readout: Kicking a Molecule When it's Down a Potential Well

Then as it was, then again it will be
And though the course may change sometimes
Rivers always reach the sea
Led Zeppelin
"Ten Years Gone"

7.1 Trading Phonons for Photons

When matter is confined in an ion trap, coupling between the internal and external states offers a variety of ways to conduct experiments. One example is in laser cooled fluorescence mass spectromety (LCFMS) which uses an applied AC voltage that can resonantly excite motion of dark ions and heat co-trapped laser cooled ions [46], [150]. The resonance condition is defined by the dark ion mass and trapping conditions, as described in Ch. 2. LCFMS works by raising $\bar{n}$ considerably enough that the laser cooling transition is Doppler broadened and the fluorescence signal lowers.

The internal-external state coupling of ions trapped also makes possible the implementation of nondestructive spectroscopy techniques. One such method already mentioned is spectroscopy using quantum logic. In QLS [105], a single phonon is added to the system if a narrow resonant transition was driven in the spectroscopy ion. The single photon excitation (on the spectroscopy transition) is converted into a single phonon added to a normal

mode. The signal is then converted into thousands of photons using electron shelving. Spectroscopy also be accomplished by applying a state dependent optical dipole force [56], [57], [151]. In this case, the ions motion is resonantly driven when the dipole force is modulated at a frequency equal to a normal mode.

Another form of nondestructive readout is Photon Recoil Spectroscopy (PRS) [152], [153]. In PRS, both readout and spectroscopy are accomplished on the same internal transition, which is necessarily broad. The spectroscopy ion feels a recoil from stimulated absorption, which occurs at a rate equal to one of the motional modes. Kicking the molecule at the same phase of motion as is oscillates increases the ions momentum and a coherent state of motion is created. By scanning the detuning of the spectroscopy laser, which is also the readout laser, momentum is only added at or near resonance. The motional excitation is then readout by the logic ion using the electron shelving technique (see Ch. 4.4.1 and [68]). An extension of this scheme is described in Ref. [154]

These schemes are extremely powerful techniques because they do not rely on the spectroscopy ion to contain a closed-loop cycling transition. This is often the case with molecular structure and where other methods of state readout are typically required. Utilizing nondestructive spectroscopy techniques preserves the molecular sample and allows for short experimental sequences. In this chapter, I will introduce a novel readout scheme called Photon Recoil Readout (PRR). PRR is based on the principle of PRS and works as a readout method for spectroscopy of transitions with intermediate linewidths.

7.2 Photon Recoil Readout

In our experiment, we aim to separate the steps of spectroscopy and readout (state dependent motional excitation). In both QLS and PRS the same laser used for spectroscopy

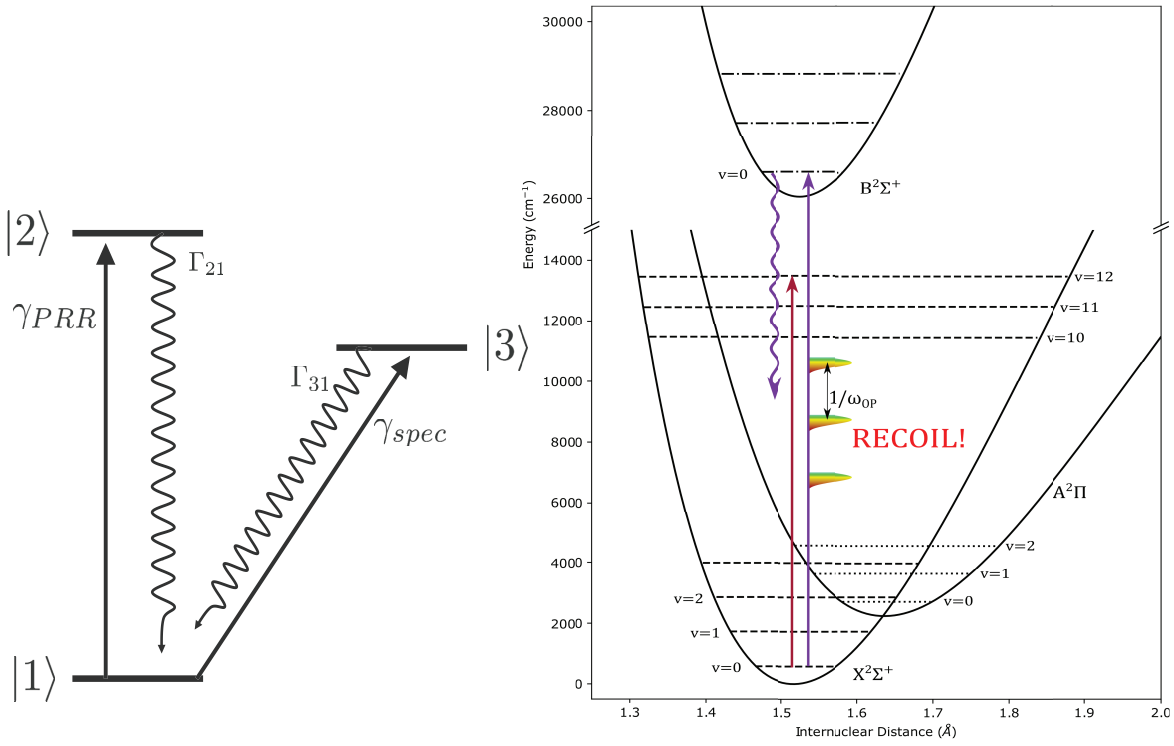

Figure 7.1: **Diagram of Photon Recoil Readout for a Three-Level System and SiO^+:** Dependent on the population in $|3\rangle$, motional excitation may or may not occur by attempting to drive the $|1\rangle \rightarrow |2\rangle$ transition. In SiO^+ : $|1\rangle = \left|X^2\Sigma^+, v=0\right\rangle$, $|2\rangle = \left|B^2\Sigma^+, v=0\right\rangle$ and $|3\rangle = \left|X^2\Sigma^+, v\right\rangle$ where we aim to address $v = 12$. The $\left|X^2\Sigma^+, v=12\right\rangle$ state has a 66 μs lifetime, greater than the anticipated PRR kicking time of ≈ 20 μs (see Sec. 7.3.3).

in the ion also handles motional excitation. When searching for an unknown or narrow line this couples potential challenges — did the readout not work because the laser is off resonant, short exposure time, etc. PRS is most effective when the transition linewidth is larger than the motional frequency ensuring the ion returns to its internal ground state before the next laser pulse arrives, limiting the technique to probing mostly broad transitions ($\Gamma_{spec.} > \omega_m$).

Our method, called Photon Recoil Readout (PRR) separates the spectroscopy and readout step, using two different lasers. This allows the spectroscopy transition to be either broad or narrow. The only limitation, when used for spectroscopy, is that that excited state

lifetime must be longer than the time it takes for the motional excitation to occur ($\Gamma_{spec.} < \gamma_{scatter}$). As in PRS, PRR motionally heats the ion by using short laser pulses (compared to the ion motional period) that are incident on the ion at a frequency equal to one of the normal modes of motion. Motional excitation occurs by driving a transition whose lifetime is less than the pulse to pulse time, so that the initial state is reprepared, by spontaenous decay, between pulses.

PRR works by utilizing a three state, inverted lambda, system. Spectroscopy is conducted on a broad or narrow $|1\rangle \rightarrow |3\rangle$ transition, while state dependent heating is performed by exciting the $|1\rangle \leftrightarrow |2\rangle$ transition. Heating is performed similar to PRS, the laser driving the $|1\rangle \leftrightarrow |2\rangle$ is pulsed at a rate equal to a normal mode of motion and the resulting excited motional distribution is represented by a coherent state. If states $|2\rangle$ and $|3\rangle$ have lifetimes $\tau_2 = 1/\Gamma_2$ and $\tau_3 = 1/\Gamma_3$ respectively, then we require $\tau_2 < \tau_3$. PRR works by driving the $|1\rangle \leftrightarrow |2\rangle$ transition at a rate γ_{PRR}, N times, after excitation on the $|1\rangle \rightarrow |3\rangle$ transition is attempted. We aspire to achieve a scattering rate of $N\gamma_{PRR} \gg \Gamma_3$.

The logical scheme is as follows: if the laser addressing the $|1\rangle \rightarrow |3\rangle$ transition is resonant and population is excited to state $|3\rangle$, then there is no population to excite from $|1\rangle \rightarrow |2\rangle$ and no motional excitation will occur. The ion is motionally heated in the event that state $|3\rangle$ is not populated. The following sections will describe in more detail the theory behind the motional excitation, the estimated rates of these processes, and experimental results will be discussed.

7.2.1 Model

Inspired by PRS and the work performed on Ca^+ [79], [152], [153], PRR aims to excite motion out of the ground state by pulsing a laser at a rate equal to an axial motional mode,

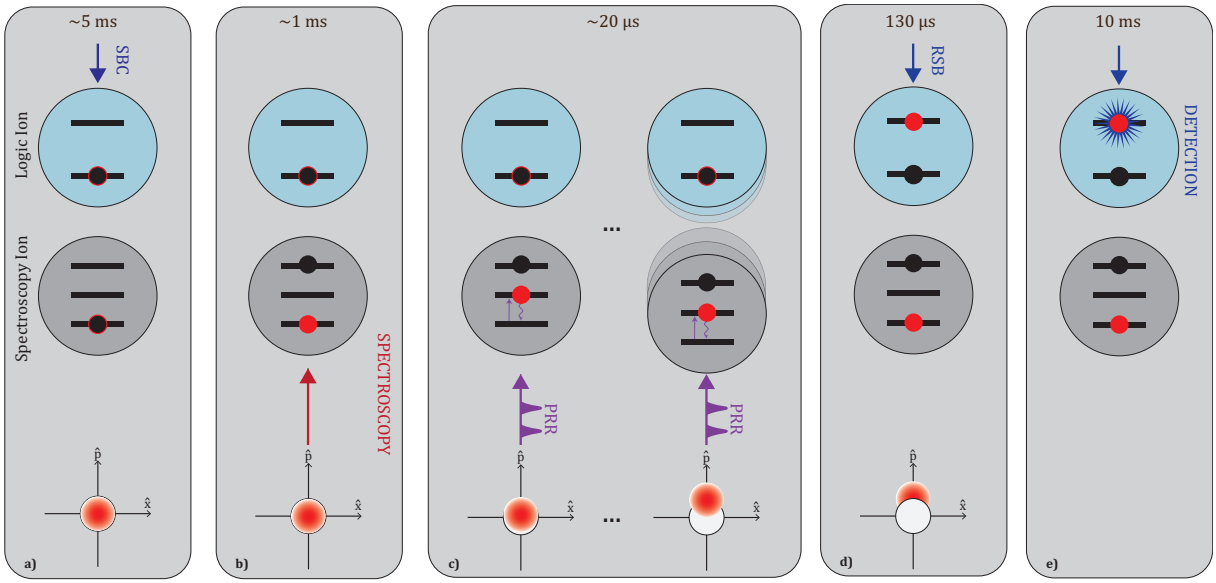

Figure 7.2: **Block Diagram of PRR Logic:** The individual steps for PRR and the associated timescales are shown. a) The two-ion crystal is state prepared and sideband cooled to the ground state. b) Spectroscopy is attempted on the spectroscopy ion (black dot). c) PRR is performed on the spectroscopy ion (red dot), the wavefunction is displaced in momentum space, exciting the motional state only if spectroscopy was unsuccessful. d) A RSB is driven on the logic ion if the molecular ion recoiled from photon absorptions in the previous step. e) The logic is bright and scatters $\sim \times 10^5$ photons conditional on the transfer of population after the RSB in d). If spectroscopy was successful, the logic ion appears dark. To demonstrate PRR, prior to spectroscopy, simply skip step b) and proceed. The ions should gain momentum from photon recoils, in the spectroscopy ion, which is measured by a loss of ground motional state population.

of the two-ion pair. This process ensures the recoil from each photon absorption event is additive along the same direction phase space. In this section I will outline the process of motional excitation and the expected signal.

To begin, lets first consider the effects of a single photon absorption followed by spontaneous emission. We will treat these as sequential events and break up the timescales: laser excitation without considering spontaneous emission and second the times after decay. In our experiment, we will use a mode-locked laser with a $\tau_{fs} = 300$ femtosecond pulse duration for PRR, so the separation of these timescales is justified, with the $|B, v = 0\rangle$ state having a lifetime of $\tau_{XB} \approx 66$ ns.

Start with an ion in the absolute ground state $|\psi_0\rangle = |g, n = 0\rangle$ at time $t = 0$. When exposed to a pulse of duration $\tau \ll \tau_{XB}$, the system evolves under the following Hamiltonian,

$$\hat{H}_{eff} = \hat{H}_m - \frac{\hbar\delta}{2}\hat{\sigma}_z + \left[\frac{\hbar\Omega_0}{2}\hat{\sigma}_+\hat{D}(i\eta) + \text{ h.c.}\right], \tag{7.1}$$

which is the Hamiltonian from Eq. A.22, rewritten in terms of the displacement operator $\hat{D}(i\eta)$. Upon photon absorption both electronic and motional excitation will occur putting the atom in the state $|e, \alpha = i\eta\rangle$. After spontaneous emission, at time t_a, if we assume decay occurs on the dominant carrier transition (no motional change), then the wavefunction will be in state $|\psi(t_a)\rangle = |g, \alpha = i\eta\rangle$.

We find that a single absorption and emission cycle leads to a displacement of the ion's motion in phase space by $i\eta$. Recall from Appendix B.2 that the coherent state of amplitude $|\alpha = i\eta\rangle$ has $\langle p\rangle = \hbar k$, $\langle x\rangle = 0$, and $\langle E\rangle = \hbar^2k^2/2m$ (above the zero-point energy). Thus after a single recoil momentum and kinetic energy of the ion have increased.

The displacement operator has the property that the effect of subsequent displacements are mathematically equivalent to one displacement with the sum of individual strengths, up to a phase factor, such that $\hat{D}(\alpha)\hat{D}(\beta) \approx \hat{D}(\alpha+\beta)$ (see proof in Appendix B.2). As a result, the momentum expectation value after N displacements of strength $\hat{D}(i\eta)$ is $\langle p\rangle = N\hbar k$. By synchronizing the laser pulse repetition rate with the ion's motional frequency we ensure that all displacements are along the same direction in phase space, creating a coherent addition of momentum. The corresponding distribution of population in Fock states ($|n\rangle$ states) describes a motionally excited ion with less and less population in $|n = 0\rangle$ as α grows.

In a two-ion crystal, the Lamb-Dicke parameters are modified, as each of the two ions have separate Lamb-Dicke parameters, $\eta_i^\gamma = \beta_i^\gamma \cdot k\{x_0, y_0, z_0\}^\gamma$, for each mode in each direction (see Table 2.1). Here, i refers to which ion, and γ refers to which normal mode along axis

$\{x, y, z\}$. As outlined in Sec. 2.3 we find that the Lamb-Dicke parameters for each ion grow in difference with increasing mass mismatch between the two trapped ions. While momentum kicks occur on one ion, they influence a normal mode of the system, and thus the motional excitation is found in both ions. Since we synchronize the recoils with one specific motional mode, we do not expect sufficient excitation on the other modes. Those displacements will be randomly distributed of which the mean accumulation of momentum should average to 0.

In our experiment, photon absorption in the SiO^+ molecule, while synchronizing to the OP mode, puts the molecule in the state $|X, v = 0, N\rangle \left|\alpha = iN\eta^{op}_{SiO^+}\right\rangle$ with $\langle p^{op}\rangle = \beta^{op}_{SiO^+} \cdot N\hbar k$. In the PRS experiment [152], motional excitation is measured by using STIRAP (Stimulated Rapid Adiabatic Passage) which transfers any population in $|n^{ip} > 0\rangle$ from one qubit state to another. However, lacking the power and frequency ramping capabilities, we will only measure population in the $|n^{op} = 1\rangle$ mode along the axial direction.

While measuring $P_{|n^{op}=1\rangle}$, instead of $P_{|n^{op}>0\rangle}$, reduces the overall signal strength, less photon recoils are needed to maximally populate that $|n^{op} = 1\rangle$ state. From Appendix B.2 we see that the population in Fock state $|n = 1\rangle$ of the coherent state $|\alpha = iN\eta\rangle$ is,

$$P_{n=1} = |\langle n = 1|\alpha\rangle|^2 = |iN\eta|^2 e^{-|iN\eta|^2} = (N\eta)^2 e^{-N^2\eta^2}. \tag{7.2}$$

Thus we can set $\partial P_{|n=1\rangle}/\partial N = 0$ and solve for N to find the number of scatters needed to maximally populate $|n = 1\rangle$. The result is $N(P^{max}_{|n=1\rangle}) = 1/\eta$. For typical trap parameters (Sec. 2.3) we have $\eta^{op}_{SiO^+} = 0.0885$ which leads to $N \approx 11$.

If we are able to detect all population in motionally excited states, as in the PRS experiment [152], then that signal can be found, first by finding the population left in the ground state,

$$P_{n=0} = |\langle n = 0|\alpha = iN\eta\rangle|^2 = e^{-N^2\eta^2}. \tag{7.3}$$

As a result, the population in states $|n > 0\rangle$ is then,

$$P_{n>0} = 1 - \exp\{-N^2\eta^2\}. \tag{7.4}$$

7.2.1.1 Phase Allowance

One aspect that requires a consideration is how different the ion's motional frequency ($\omega_{op,z}$ for example) can be from the pulsed lasers repetition rate (f_{pp}). The ion's phase of motion when first excited by the laser sets the initial time frame. The two oscillations are written as,

$$f_{pp} = sin(\omega_{pp}t + \phi_{pp}) \text{ and } f_z = sin(\omega_z t + \phi_z). \tag{7.5}$$

We can easily set $\phi_{pp} = \phi_z = 0$ since this is not relevant In other words, when the ion first absorbs a photon it is at some phase ϕ_z of its motion, which we can just define as our reference point and equate to 0. It is the phase difference of the next pulse, and those in succession that we care about. We can relate the two phases, by counting time t in terms of the number N of pulses exposed afterwards which is given by $t = 2\pi N/\omega_{pp}$. The phase of a wave at any time $t = 2\pi N/\omega_{pp} = N/f_{pp}$ is given by,

$$\Phi_{pp} = 2\pi\frac{t}{\tau_{pp}} = 2\pi t f_{pp} = 2\pi N$$
$$\Phi_z = 2\pi\frac{t}{\tau_z} = 2\pi t f_z = 2\pi N\frac{f_z}{f_{pp}}$$

We can then define the phase difference as $\Delta_\Phi = (\Phi_z - \Phi_{pp}) = 2\pi N\left(\frac{f_z}{f_{pp}} - 1\right)$. The worst case scenario is when the phase difference $\Delta_\Phi = \pi$ because now the momentum gained from a photon recoil is in the opposite direction from the beginning of the process. However lets be more stringent and consider when $\Delta_\Phi = \pi/2$. At this phase difference, the momentum gained is equal in either direction and so we expect the motional excitation to substantially slow down. Solving for the number of pulses it would take for the phase difference to be $\pi/2$, in terms of the ratio of the relevant frequencies, we find

$$N = \frac{1}{4\left(\frac{f_z}{f_{pp}} - 1\right)} \ . \tag{7.6}$$

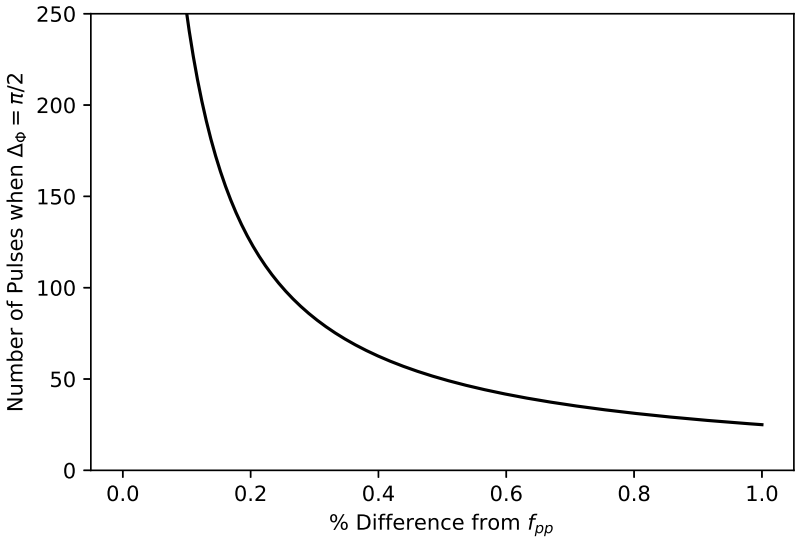

Figure 7.3: **Phase difference between ion motion and pulsed laser:** At a given percentage change of f_z from f_{pp}, it will take N pulses to accumulate a phase difference of $\pi/2$. We can see the two must be very close.

The quantity in the parenthesis is just the percent change that f_z is from f_{pp}. As estimated

in Sec. 7.3.3, we may need to expose as many as 100 pulses so it is important to match these frequencies as best as possible. From Fig. 7.3 it is clear these numbers must match to less than 3.4 kHz for a 1.72 MHz mode — which is a 0.2 % change — to mitigate any unwanted effects. This is just at the level of our frequency resolution for ω_z when conducting sideband spectroscopy using the FOR lasers.

7.2.2 Photon Scattering Statistics

Lets us also outline the photon absorption statistics, which will help us understand the expected signal strength and required excitation time. Here, we consider the total probability of scattering N photons for both Poisson and Geometric distributions.

Photon emission statistics in a two-level atom following a Poisson distribution are given by,

$$\mathcal{P}_p(N, \bar{N}) = \frac{\bar{N}^N e^{-\bar{N}}}{N!} \ , \tag{7.7}$$

for a mean number $\bar{N}$ of scattered photons. This describes the photon statistics when cycling on the 0-0 band of the X-B transition in SiO^+ and no decay has occurred to states outside of the cycling transition. Any decay that leads to vibrational excitation to the $|X, v = 1, 2\rangle$ state will still be in the bandwidth of the laser and thus excited (see Fig. 5.3). The low-lying A state is outside of the X-B cooling cycle and can interrupt the process.

As described in Sec 5.1, we expect about 100 scattering events on the X-B transition before decay to the A state. If the molecular ion decays to the A state then it is taken out of the cycling transition and the experimental routine. The statistics for emitted photons in this case is given by a geometric distribution,

$$\mathcal{P}_g = (1-\chi)^{N-1}\chi, \tag{7.8}$$

where 1-χ and χ is the probability of decay from the B to X state, and from the X to A state respectively. Here, the average number of scattered photons is given by $\bar{N} = 1/\chi$ which is then 100 for the X-B transition.

For either of these distributions to be properly normalized, one needs to sum over at least twice the mean number of scattered photons. This means that if $\bar{N}$ photon recoils achieve a good signal, we want to expose the ion to at least $2\bar{N}$ pulses, assuming less than one absorption and emission per pulse (below saturation), for our expected signal to match the theory.

Since PRR relies on individual absorption and emission events which are probabilistic, the total signal is obtained by combining both the probability of motional excitation and averaging over the photon statistics,

$$S_{PRR}(\bar{N}) = \sum_{N=0}^{\infty} P_{recoil}(N)\mathcal{P}(N,\bar{N}). \tag{7.9}$$

Plotting the expected signals for P_{recoil} given by either Eq. 7.3 or Eq. 7.4 is shown in in Fig. 7.4. These plots provide important insight into the number of photon scatters needed to obtain an adequate signal. If we were able to set-up a STIRAP pulse scheme, as with the work in PRS [152], then 20 - 25 pulses would be needed to obtain the maximum signal in either case of Poisson or geometric photon statistics. For $\bar{N} = 20$, we reach a signal of 0.92 and 0.64 respectively. As expected, only measuring the population in $|n=1\rangle$ gives a lower signal. Since we are only driving $|n=1\rangle \rightarrow |n=0\rangle$, it is only useful to measure at what point the mean number of scatters maximally populate $|n=1\rangle$. From the right side of

Fig. 7.4 we find that value is $\bar{N} = 11$ photons, in either case. By measuring population in $|n = 1\rangle$ only, we reach a signal S_{PRR} of 0.31 and 0.17 for the Poisson and geometric photon distributions respectively.

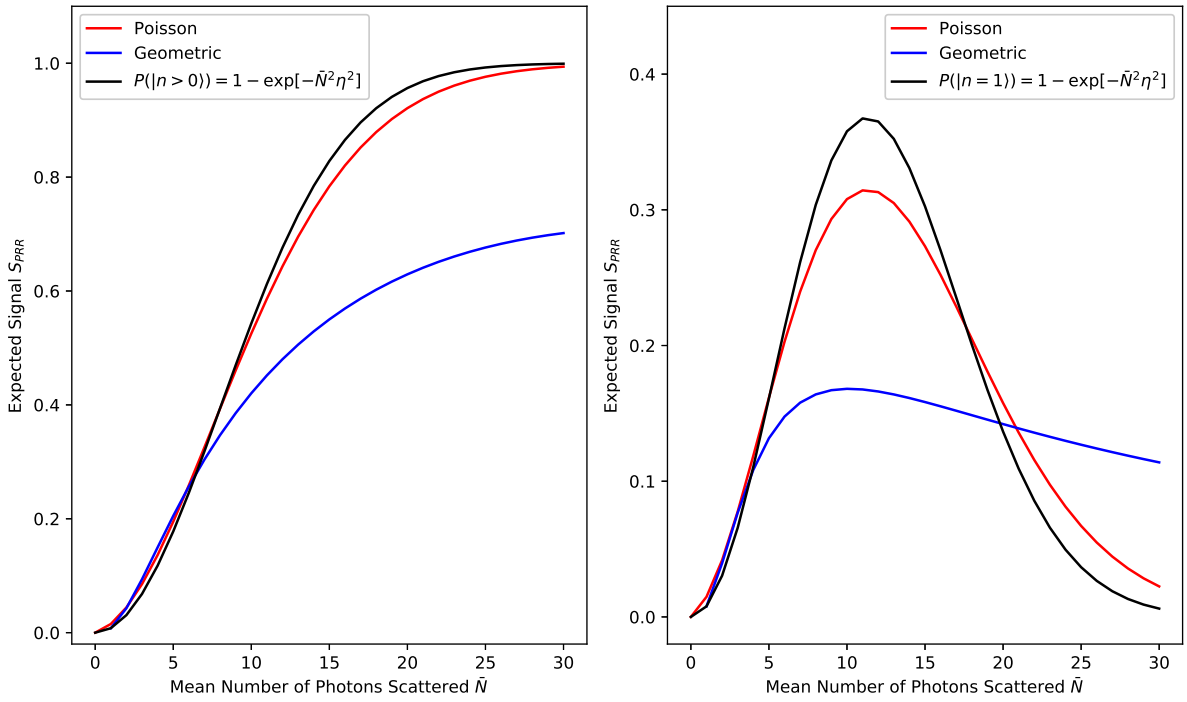

Figure 7.4: **PRR Expected Signal:** **Left:** S_{PRR} is plotted showing the total population in states $|n > 0\rangle$ for either photon distribution. **Right:** S_{PRR} is plotted showing the population in $|n = 1\rangle$, which is what our initial measurement will be. Both photon distributions are shown. The black line in either plot shows the signal if we neglect the photon statistics and the signal is just the motionally excited population. Here, $\eta = 0.0885$ in either case.

As mentioned earlier, we expect about 100 photon scatters before decay to the A state occurs. The results of Fig. 7.4 show that only at most and average of 11 or 20 photon recoils are needed to achieve maximal signal (depending on the measurement scheme). Since these values are less then the B-A branching, it is likely the photon statistics will follow a Poisson distribution in this regime, and we need not worry about decay to states outside of the cycling transitions covered by the broadband laser used (described later in Sec. 7.3.1).

This would not be the case if a CW laser is used (true for the Ca^+ PRS experiments [152]) to specifically kick the molecule. For SiO^+ this would occur by cycling on the $|X, v = 0, N = 1\rangle \leftrightarrow |B, v = 0, N = 0\rangle$ transition. Use of a CW laser would require a more careful estimate of the number of possible photons scattered, before population decays to a higher vibrational state or the A state. Even though 20 photon recoils can result in a strong signal, the number of applied pulses must be larger than this since scattering is probabilistic.

It is also important to note that the expected S_{PRS} signal is not the full signal that is measured in our experiment. If we were able to shelve 100% of the population from our qubit state then it would be. This would be possible if the 1.76 μm laser was in use to address the $S_{1/2}$ to $D_{5/2}$ quadrupole transition. However, the current shelving scheme, as described in Sec. 4.4, leads to a lower contrast. Since our maximum detection efficiency is 44%, then for a signal of $S_{PRR} = 0.31$ when looking at only the $|n = 1\rangle$ population our signal will be 0.136, above a baseline of 0.12 (see Ch. 4.4.4). If we are able to set up a STIRAP scheme, then the total signal improves to nearly full contrast (at our limited detection) at a signal 0.4 above the baseline.

7.3 Experiment

The demonstration of EIT sideband cooling a two ion Ba^+ and SiO^+ crystal to the ground motional state, shown in Ch. 6, allows us to work towards demonstration of PRR. Since ground state cooling is the foundation of the experiment, all that is needed is the addition of a new, pulsed laser to kick the molecule and a device to match the repetition rate to a motional mode frequency.

7.3.1 Equipment

In our experiment instead of pulsing a CW laser with an AOM, as in PRS [152], we will use a femtosecond laser, typically pulsed at 80 MHz, and adjust that repetition rate to match that of the out-of-phase axial mode, $\omega_{z,op}$. The out-of-phase mode is used because of its larger Lamb-Dicke parameter, as well as the low heating rate. A femtosecond laser is beneficial to work with due to the multilevel system of SiO^+ . Without optical pumping of the rotational states, the large bandwidth of the femtosecond laser can address all rotational transitions of the X-B system. Even if we apply rotational pumping to $|X, v = 0, N = 0\rangle$, we still gain by using the femtosecond laser if population diffuses to $|X, v = 0, N > 0\rangle$ after repeated cycles on the X-B transition, there are spectral components to address those transitions.

7.3.1.1 Tsunami

The femtosecond laser used is a Spectra-Physics Tsunami[1] pumped by a Spectra-Physics 15 W Millenia eV15[2]. Both lasers are chilled by a KMC-100 with distilled water set to 18°C. With 14 W of pumping power, we can typically achieve 3 W of average output power at 770 nm, at a repetition rate of 80.84 MHz. Higher pumping power is not used due to the appearance of CW breakthrough in the resulting mode-locked spectrum. We can easily observe the presence of mode-locking and the lasers spectral bandwidth using an Ocean Optics USB2000 spectrometer. Fig. 7.6 shows a fit of the output spectrum from the laser using a $sech^2$ function.

The Tsunami is tunable from 675 - 1100 nm, and is seeded from 532 nm pumping light, which in turn is from a 1064 nm diode that frequency is doubled. The 532nm and 1064 nm

[1]Model #: 3941-M1bb, SN: 2472)
[2]SN: 10415

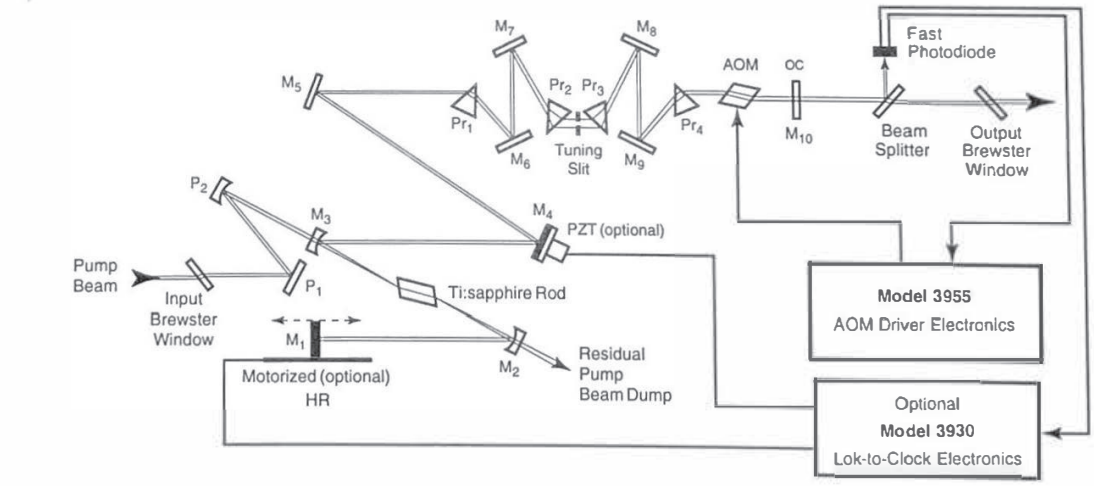

Figure 3-3: Beam Path for *Tsunami Models 3960* and *3941* Femtosecond Configurations

Figure 7.5: **Tsunami Folded Cavity:** Internal laser cavity of the Spectra-Physics Tsunami. Note the tuning slit and prism pair (Pr_2 and Pr_3) positions are adjusted with a individual knobs. These are used for changing the bandwidth and center wavelength of the laser. Image taken from the Spectra-Physics Tsunami Manual.

light are generated inside the Millenia eV. For stable performance, the system is optimized to operate in the 'Standard' range of 720 - 850 nm. Water flow from the chiller is necessary during operation and a flow sensor is connected to an interlock of the Millenia control ensuring this. Chiller water should be drained and refilled every 6 months. Since there is $\approx 1\%$ absorption from water and oxygen at 770 nm, the laser cavity is put under flow of nitrogen when in use. Flow of nitrogen also eliminates problems associated with dust and contamination. Is anyone reading this?

Tuning of the wavelength is achieved by adjusting the prism sequence and the slit position (see Fig. 7.5). The variable slit width acts to block parts of the dispersed beam and change the bandwidth (and also the temporal width). The bandwidth is adjusted by tuning the prism pairs, shown in Fig. 7.5, which introduce negative intracavity group velocity dispersion

(GVD). The position of the center slit changes the center wavelength. When tuning the center wavelength it is best to move both of these knobs together, in the same direction.

The system operates under an active mode-lock configuration by an AOM which is controlled by the Model 3955 Driver Electronics. The AOM introduces a time dependent loss to the cavity by switching the light on and off, modulating the the frequency of light that passes through. If the modulation frequency is chosen to be equal to to c/(4L) where L is the length of the cavity then it matches the repetition rate of the output pulses. In this way the AOM adjusts the phase between the longitudinal modes of the laser cavity. The laser repetition rate is continually measured by picking off a portion of the beam, which is then incident on a photodiode. The AOM drive frequency is then continually adjusted to match this repetition rate which creates regenerative modelocking in the laser. This results in continual mode-locking even if the cavity length fluctuates.

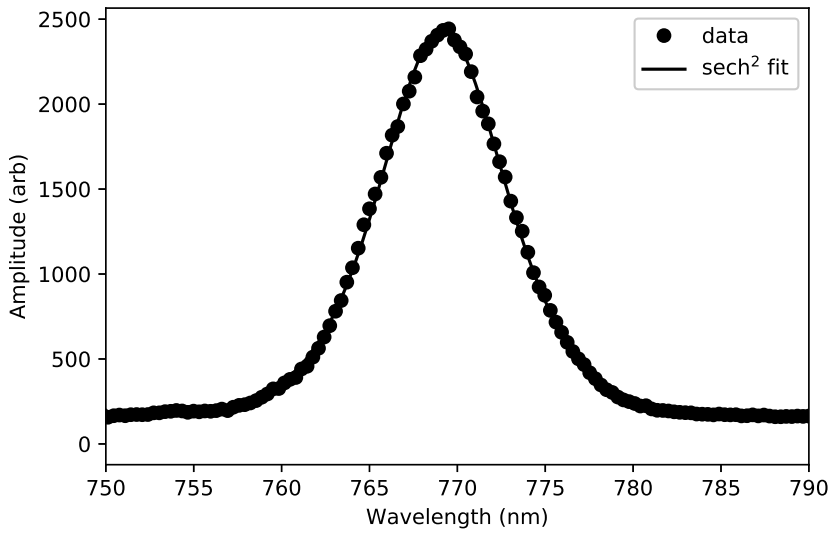

Figure 7.6: **Tsunami Mode-Locked Output:** Typical spectral bandwidth out of a Spectra-Physics Tsunami. Here we determine center wavelength to be 769.16 $\pm$ + 0.01 nm and the the bandwidth to be 9.58 $\pm$ 0.04 nm.

Typically after 1-1.5 hours after turning on and operation at a fixed pump power (14 W here) the laser will mode-lock automatically and the output will remain stable over hours.

7.3.1.2 GRENOUILLE

To make a more precise measurement of the spectral and temporal bandwidth we use a Swamp Optics GRENOUILLE 8-50-329-USB. French for 'frog', the GRENOUILLE (Grating-Eliminated No-nonsense Observation of Ultrafast Light Incident Laser Light E-fields) is a simplified and more robust version of Frequency Resolved Optical Gating (FROG) devices, which are employed to measure pulsed lasers on the femtosecond timescale. The device is extremely beautiful, by replacing a whole optical set-up of a FROG that requires very careful alignment, with three optics, one SHG crystal and a camera. A diagram is shown in Fig. 7.7

In the time domain, the Fresnel biprism causes the laser to interfere with itself inside the SHG crystal, mapping the relative beam delay onto the horizontal position at the crystal. As a result, there is the most amount of light when the two sides are overlapped in time at the center of the crystal, and less at the edges. This essentially converts the time of the pulse to the spatial extent of laser intensity measured on the camera. In the spectral domain, by focusing the laser light onto the thick SHG crystal, the output doubled light is spectrally separated thus producing a linear spectrum of wavelengths detected on the camera. These two processes provide both temporal and spectral measurements of a femtosecond pulse.

Operating of the device is simple. First, one must move the SHG out of the beam path, by turning the knob to 'Space Mode'. Then alignment is accomplished, at low laser power, by centering the laser beam both on the center of the input iris and on the camera. This is seen by operating the QuickFrog software in 'space mode' and centering the laser beam using the cross hairs. While this alignment procedure is at the core of every AMO physicists

skills, it is important to be as precise as possible here since the device's algorithm is based off of symmetric alignment through the lens, biprisim, crystal and camera. It is also important not to saturate the camera. When aligned, put the SHG crystal back in the beam path by turning knob to 'Time Mode' and increase the laser power to just below camera saturation. Higher power here is needed because the device operates off of frequency doubled signal. Under proper operation, we can measure the full output characteristics of the Tsunami.

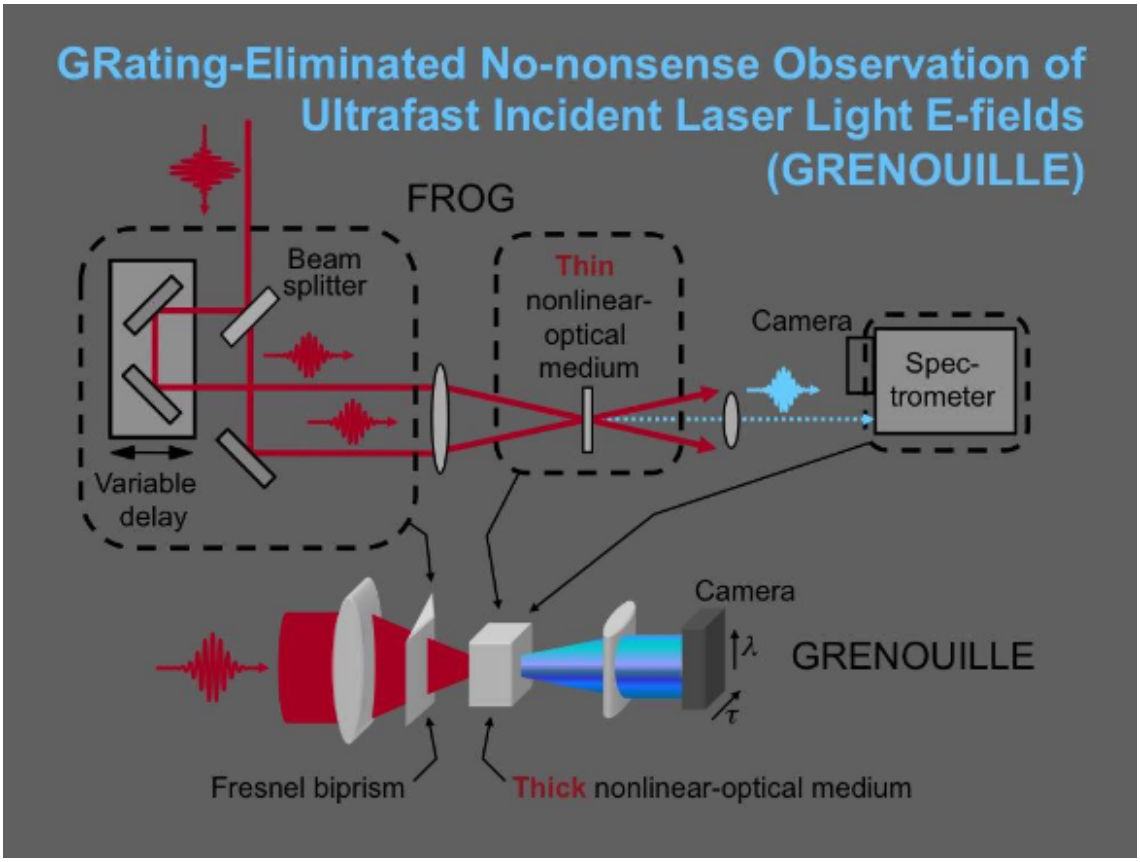

Figure 7.7: **GRENOUILLE:** Diagram set-up of the device and comparison to a typical FROG. Credit: Swamp Optics Website

As shown in Fig. 7.8, we find the temporal FWHM is 120.8 fs and the spectral FWHM: 8.79 nm. The spectral FWHM compares well to the data taken with the spectrometer in

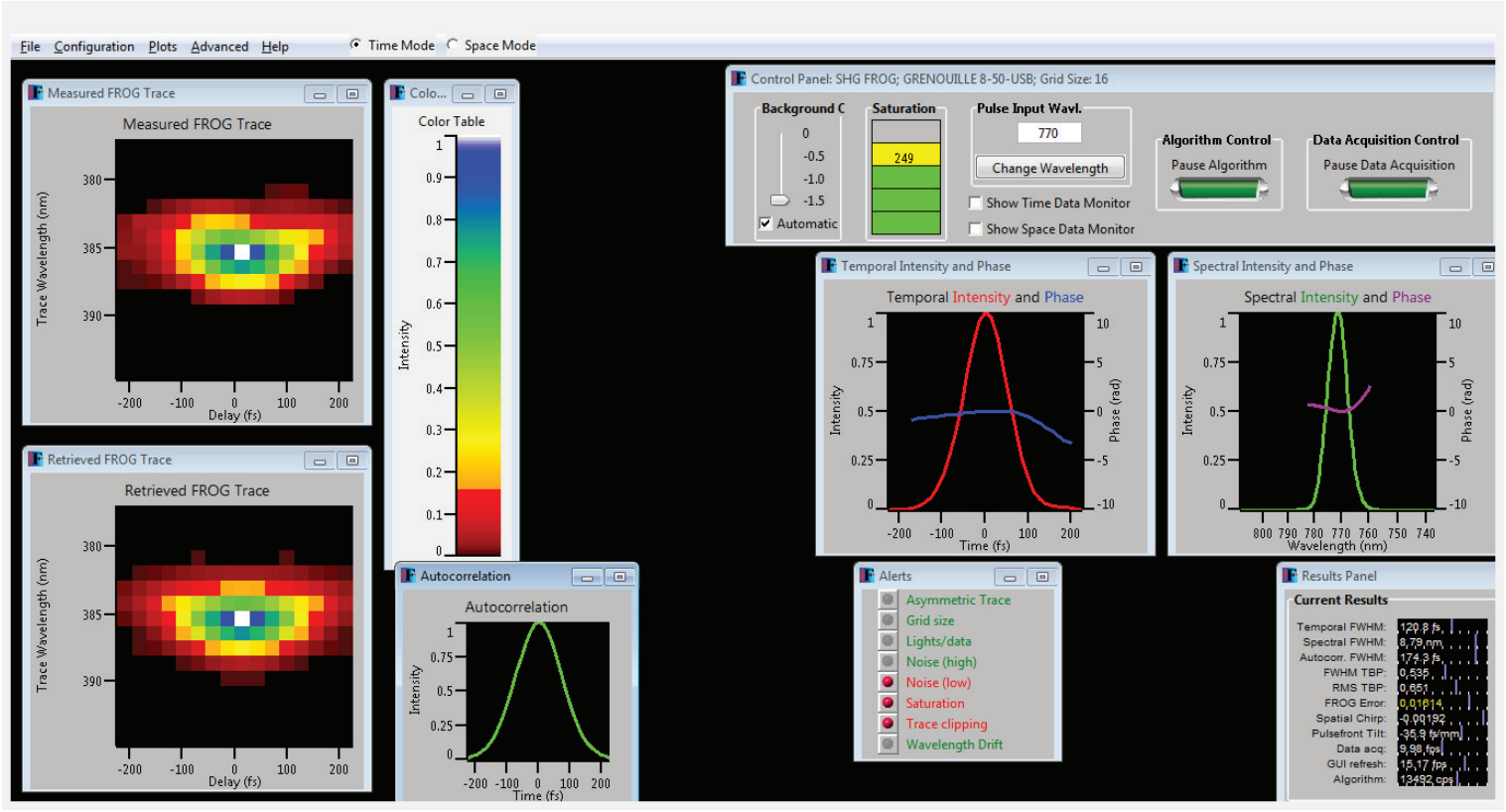

Figure 7.8: **GRENOUILLE Trace:** A single shot measurement of the temporal and spectral qualities of the Tsunami output. This shows a screenshot of the QuickFrog Software that measures the beam parameters in real time. The bottom left shows a measured Temporal FWHM: 120.8 fs and a Spectral FWHM: 8.79 nm.

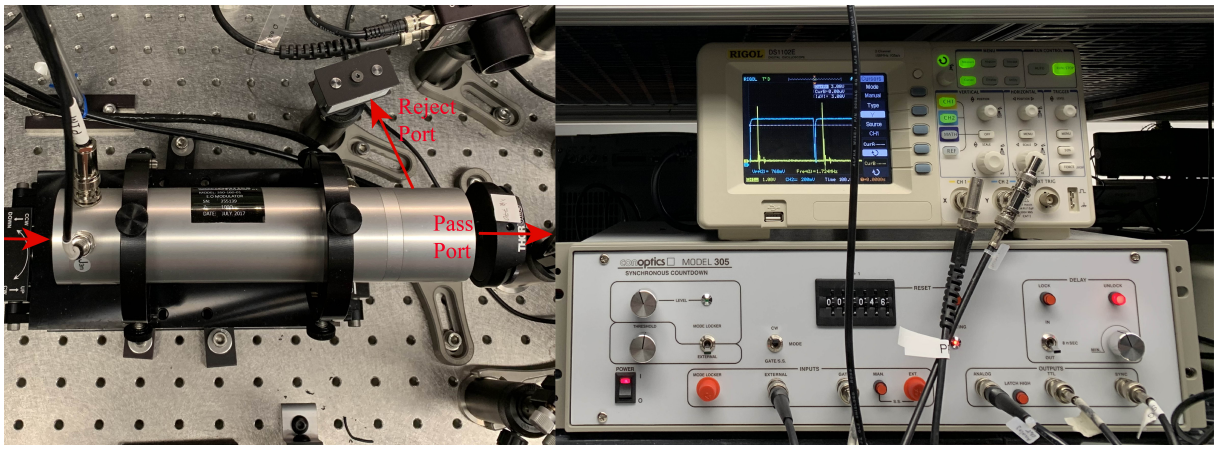

Figure 7.9: **ConOptics E-O Modulator: Right:** Is the electro-optical (EO) modulator housing. Laser light is incident on the left and the bias voltage determines whether the pulse-picked light exits the Pass or Reject port. **Left:** The 305 Synchronous Countdown System is shown. The resulting pulse rate, shown on the oscilloscope, of 1.72 MHz is detected by pick-off irradiation of a photodiode. Here the 305 system is operated in CW mode, typical for alignment and testing purposes.

Fig. 7.6. These measurements will be important to our understanding of the amount of laser power that goes into driving the X-B 0-0 band in SiO^+ .

7.3.1.3 Pulse Picker

One of the most important components of the system is the Pulse Picker (PP) which allows us to reduce the repetition rate of the Tsunami to a frequency that matches a motional mode of the two-ion crystal. In the experiment, we use an ConOptics Model 350-160-01 KD*P Series E-O Modulator, driven by a ConOptics Model 25D Driver. The pulses are gated by a ConOptics Model 305 Synchronous Countdown System.

The ConOptic E-O modulator acts as a transverse field type Pockels Cell. This means the electric field applied is transverse to the optical beam, which reduces the required amount of applied voltage. To modulate the amplitude of the output beam (switch it on and off), the input polarizer is aligned 45° to the crystal axis, with the input laser polarization set

by an external $\lambda/2$ zero-order polarizer. The output polarizer is parallel to the input and such that zero bias voltage results in maximum transmission. If a bias voltage is applied, the resulting birefringence in the crystal will rotate the laser polarization and reduce the output amplitude. It is important to maintain a low DC bias voltage, for the longevity of the modulator.

The E-O Modulator is driven by the ConOptics Model 25D Driver which is set to Analog input mode because it is driven by the Model 305 Synchronous Countdown System. The 25D driver has a 175 V_{pp} maximum output whose output is triggered from a +1 V, high speed analog pulse from the Model 305. The resulting high voltage output has a pulse width fixed at 18 ns. The bias voltage range is approximately ± 400 VDC though we operate between 0 - 190 V which produces a full 90° polarization rotation to maximize or minimize the output.

The Model 305 Synchronous Countdown System, which gates the 25D driver, is a high speed divider that generates a trigger pulse locked in time with an input stimulus. The output trigger rate is an integer multiple of the input clock rate, $f_{pp} = f_{clock}/d$ where d is the divisor plus one, set by a six decade thumbwheel on the front panel. The 305 system is clocked, to the 'Mode Locker' input, by a low voltage sine-wave output from the Tsunami control system. While there is a 'CW' mode, we operate in the 'Gated' mode, where a separate TTL pulse (generated from an NI 6602 counter card) triggers the operation of the 305 box, and thus 25D output, for the duration of the pulse. In this way we can switch the exposure of the PRR laser on and off for a desired time during the experimental sequence. The 'sync' output of the 305 system at frequency f_{pp} is measured, using a SRS frequency counter which gives sub-kHz resolution, allowing us to match f_{pp} to $\omega_z^{op}/2\pi$. There is also a manual delay adjust knob that ensures the PP gating does not clip any of the input laser pulse.

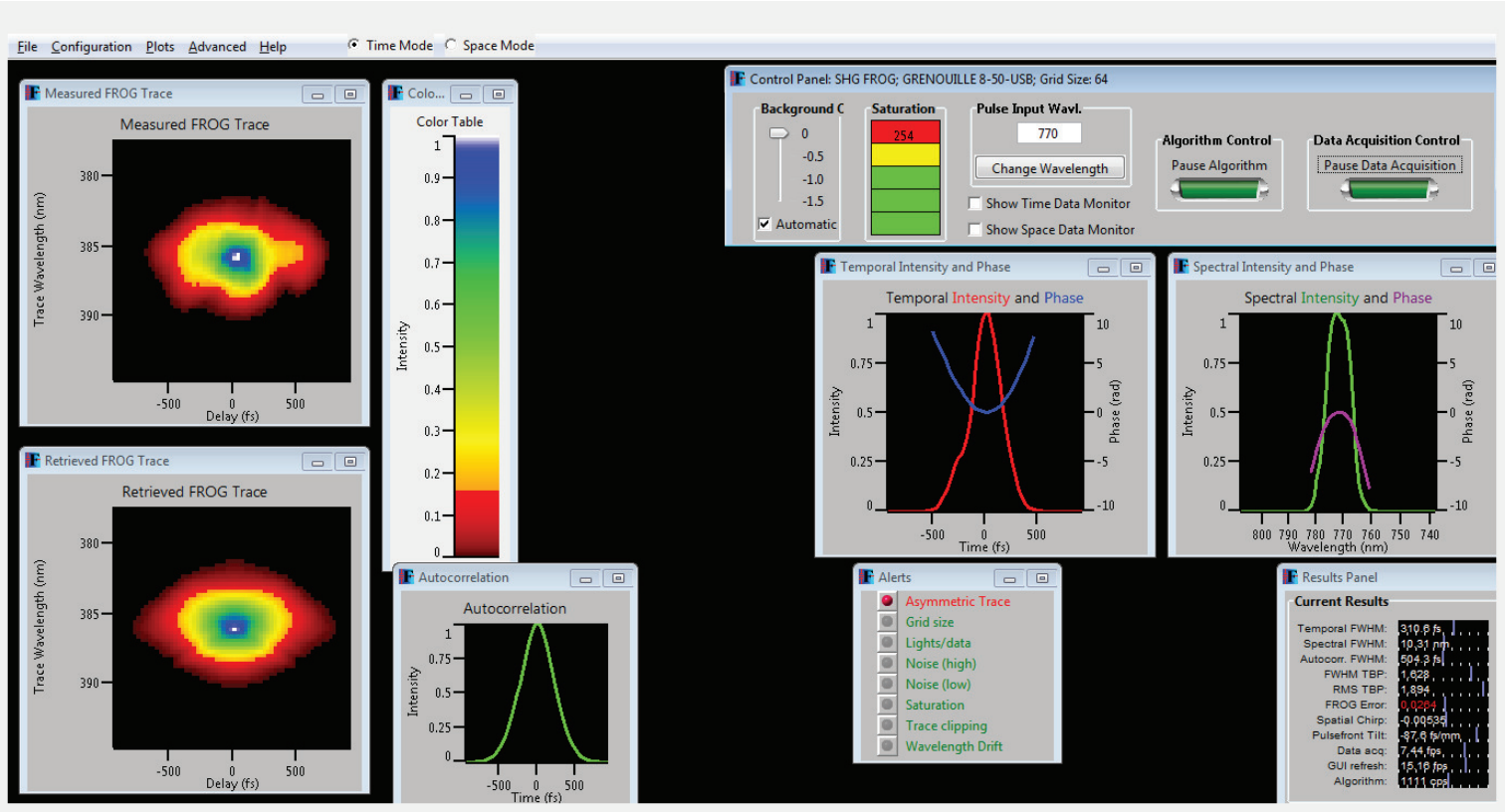

Figure 7.10: **GRENOUILLE Trace after PP:** A single shot measurement of the temporal and spectral qualities of the Tsunami output after passing through the pulse-picker with $d = 7$ so $f_{pp} = 1.72$ MHz. We measure a temporal FWHM of 310 fs and a spectral FWHM of 10.31 nm.

In our application, we wish to use the PP as a fast optical switch, blocking the light and letting only one pulse pass at a rate equal to f_{rep}/d where f_{rep} is typically 80.64 MHz. A full mathematical treatment of the PP and its effect on the resulting frequency spectrum is described in Appendix C. Since our desire is to match f_{pp} to the out-of-phase axial mode of a Ba^+ - SiO^+ crystal, which we measure to be 1.72 MHz, we set $d = 47$. I find that adjusting the spectral bandwidth of the Tsunami, but turning the slit width knob, adjusts f_{rep} slightly.

As indicated in the user manual, by adjusting the input polarization and V_{bias} in the PP, we can minimize the output power. Typically we have 2.88 W into the PP and 2.599 W through giving a transmission efficiency of 88%. To maximize this and the extinction ratio, the Tsunami was telescoped down by $\approx$ 4:1 using an f= 100 and f=25.4 B-coated Thorlabs lens pair. By adjusting V_{bias} we can measure the extinction ratio (ER), which measures the ability of the PP to block the unwanted pulses. Typical values are 2.559 W through at V_{bias} = 8 V and 11 mW transmitted at V_{bias} = 189 V, giving an ER $\approx$ 232. These unwanted pulses will be further reduced after frequency doubling, which depends nonlinearly on input power.

By allowing only one out of every d pulses through, we are also lowering the average power, thus reducing the overall doubled light at 385 nm. The power through is measured to be roughly the input power times the transmission coefficient, divided by the factor d. We find this linear relationship from the plot shown in Fig 7.11 .

Since the PP requires the laser to pass through inches of glass, the ultrafast laser will undergo a great deal of dispersion. This lengthening of the pulse duration will reduce the doubling efficiency. Originally a Swamp Optics BOA-800-106 pulse compressor was installed to pre-compress the pulse, mitigating any dispersion added from the PP. However, due to the 63% transmission efficiency, any improvement in doubling efficiency was washed out by this

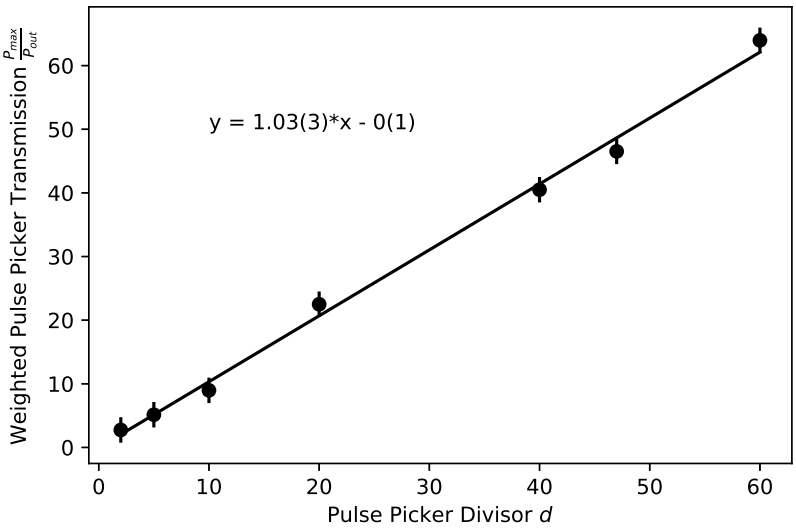

Figure 7.11: **Average Power Through Pulse Picker:** Taking the total transmitted power of 2.559 W and dividing by the power through at a divisor setting d we find a linear relationship.

lower power and resulted in less 385 nm light than without compression and just doubling the light out of the PP.

Using the GRENOUILLE, we can measure the resulting dispersion added from the PP. We see in Fig. 7.10 that the pulse duration is increased to 310 fs up from 120 fs (from Fig. 7.8). Also important to note is the Time-Bandwidth Product (TBP) measures to be 1.628.

7.3.1.4 SHG

Lastly, to address the $|X^2\Sigma, v = 0\rangle \rightarrow |B^2\Sigma, v = 0\rangle$ transition whose band head is at $\approx$ 26016.5 cm $^{-1}$ or 384.37 nm [130] we need to frequency double the Tsunami output wavelength. We achieve this by passing the light through a Newlight Photonics 5x5x2 mm BiBO crystal. With the PP on, V_{bias} = 189V, increasing the Tsunami pulse to pulse separation to 581.4 ns (f_{pp} = 1.72 MHz) and 54.4 mW in, we can obtain 15 mW of 385 nm

doubled light out. Recall the PP has an ER of ≈ 236, meaning the unwanted pulses are reduced in power by $236^2 = 55696$ after doubling, ensuring they have little to no effect of exciting the ion at unwanted phases of it's oscillation.

While the GRENOUILLE cannot measure the characteristics of a femtosecond pulse at 385 nm, we can measure its spectral qualities using a spectrometer (home-built or commercial). Using an Ocean Optics USB2000 we can measure its bandwidth, results which are shown in Fig. 7.12. These spectral properties are important in our understanding of the laser power that contributes to driving the X $\rightarrow$ B transition.

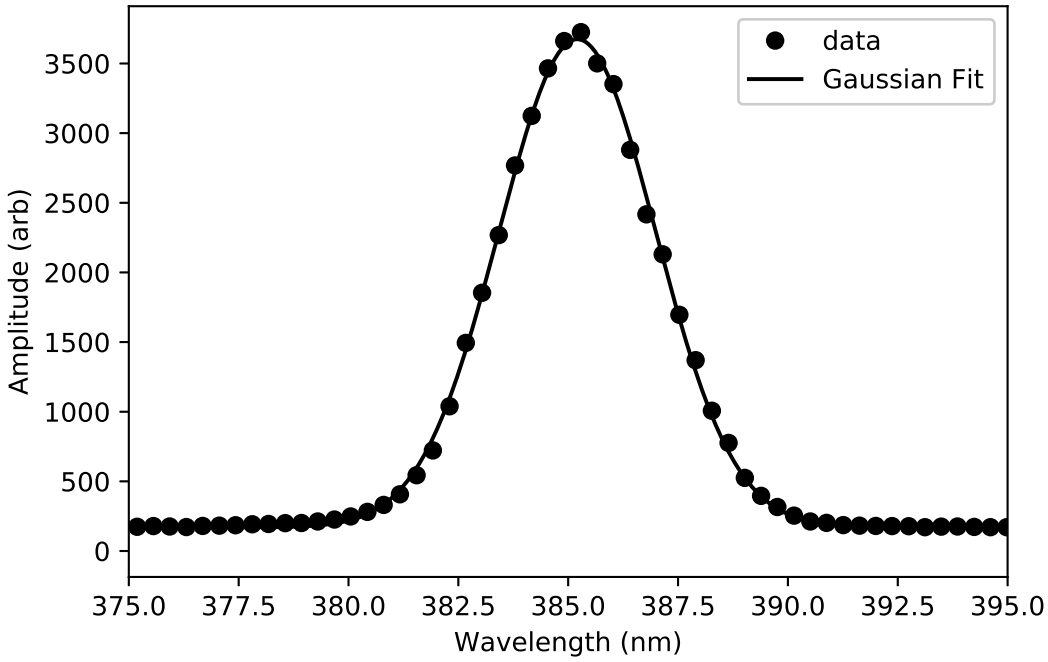

Figure 7.12: **Spectrum at 385 nm:** The resulting 385 nm spectrum after frequency doubling the output of a Spectra-Physics Tsunami at 769 nm. A Gaussian function is used to fit this spectrum because it fit the wings better than a sech^2 function. This is probably due to either the dispersion from the PP or the response of the SHG crystal. The fit gives a center wavelength of 385.21(1) nm and a FWHM of 3.57(2) nm

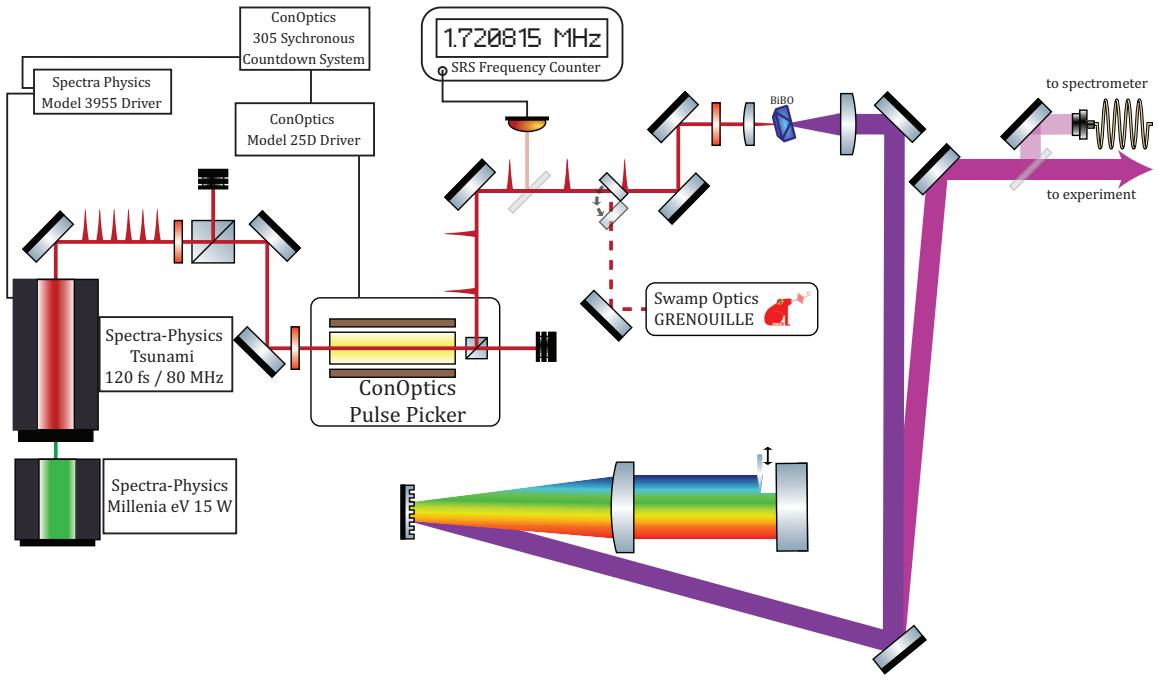

Figure 7.13: **PRR Experimental Set-up:** Here the important lasers, electronics and optics are shown diagramming the laser set-up from ultrafast pulse generation to spectral filtered light that the ion may see.

7.3.2 Summary of PRR Optical System

Light out of a pulsed laser is sent through an EOM that acts as a fast switch that allows one pulse to pass for every $d-1$ pulses, where d is the dial set on the counter. To obtain a finer adjustment of the repetition rate, to that of the ion crystal motional mode the trapping voltages can be changed accordingly. To match the resonance of the X-B transition, we frequency double using a BiBO crystal to obtain 385 nm light. If desired, that light can be spectrally filtered for appropriate rotational pumping. The output is then directed to the ion trap and focused on the ion.

7.3.3 Estimation of Rates

Before beginning any experiment, it is important to understand the timescale at which excitation will occur. This also have implications on future work regarding spectroscopy; the timescale of PRR is needed to be faster than the excited state lifetime of a transition being probed. If not, population falls back to the ground state, enters the PRR excitation cycle and the molecule will be kicked in a state independent way, confusing results. Using a femtosecond laser requires consideration regarding the portion of the laser power that contributes to excitation. Here, I show three approaches that each give similar estimations.

Using the Spectra-Physics Tsunami described in Sec. 7.3.1.1 with an output wavelength set to the SiO^+ X-B 0-0 transition at 769.46 nm, we typically measure a spectral bandwidth of 10 nm. When frequency doubled to 384.73 nm, we find the resulting spectral bandwidth in units of frequency is $\sim$ 7.21 THz. Recall from Sec. 5.1 that the X-B transition has a natural linewidth of 2π x 2.41 MHz. Taking the ratio of these bandwidths, we find $r_b = \frac{2.41 \text{ MHz}}{7.17 \text{ THz}} = 3.3 \times 10^{-7}$ so approximately only 3×10^{-5} % of the laser power is resonant. With 10 mW of average Tsunami power going into the trap, only 3.3 nW addresses the transition.

A second method involves estimating the number of comb teeth in the spectrum of the laser since those finite amount of teeth comprise individual contributions to the average power measured by a typical Thorlabs power meter. For a mode-locked laser that has N modes separated by $\Delta\nu$ the minimum pulse duration of the laser is,

$$\Delta t = \frac{TBP}{N\Delta\nu} \ , \tag{7.10}$$

where TBP is the time-bandwidth product. It can be calculated by taking δt x $\delta\nu = TBP$.

Here, $\delta\nu$ is the FWHM frequency bandwidth of the pulse. Both of these quantities can be measured by Swamp Optics GRENOUILLE and were found to be $\Delta t = 120.8$ fs and $\delta\nu = 4.44$ THz, giving $TBW = 0.535$ (see Fig. 7.8). This measurements were taken right on the output of the laser, and give an estimation of $N \approx 54785$ comb teeth contributing to the Tsunami output.

These measurements were taken before the pulse-picker, where the mode spacing is changed (see Sec. 7.3.1.3 and Appendix C). Here, the output repetition rate was set to $\Delta\nu = 1.72$ MHz, to match the out-of-phase mode of a two-ion Ba^+ and SiO^+ crystal at typical trap conditions (see Ch. 2). We can estimate the number of teeth contributing that would produce a femtosecond pulse, at this repetition rate, which is what the ion will see. We set the repetition rate to $\Delta\nu = \nu_{pp} = 1.72$ MHz and assume the 385 nm temporal bandwidth of 310 fs matches that of the 770 nm seed light after the PP (see Fig. 7.10). These values, with the 7.2 THz spectral FWHM (see Fig. 7.12) of the 385 nm light gives a TBP = 2.232. Plugging these factors into Eq. 7.3.3 we find $N_{385} \approx 4.18 \times 10^6$. Again this is an approximation of how many modes would be contribute to make a 310 fs pulse at 385 nm, at the measured bandwidth. For a 10 mW average pulse power, assuming a flat top distribution of power, this leads to approximately 2.3 nW per comb tooth.

Lastly, we may have to consider the finite spectrum of a single laser pulse, since as described in Sec. 7.2.1, we need about 20 pulses to excite sufficient motion out of the ground state for detection. With femtosecond lasers and pulse trains, the frequency comb structure is found when integrating over a large number of pulses. However, if only $\mathcal{O}(20)$ pulses are needed for excitation, we must ask: what is the frequency spectrum seen by the ion? This does not impact our understanding of whether PRR will work, since the pulse picker still switches the laser on to excite the ion at the same phase in its quantum motional oscillation.

This discussion is only related to the amount of resonant laser power seen by the ion and the frequency components in those pulses.

The pulse picker acts as a fast optical switch, to allow one pulse to pass at a rate determined by $\Delta f_{rep}/d$ where d is the divisor set on the control system of the pulse picker. On the femtosecond timescale, we theorized that the single pulse that passes through still contains the N comb teeth out from the laser, estimated by Eq. 7.3.3, separated in frequency by f_{rep}. For our Spectra-Physics Tsunami output with $\Delta t = 120$ fs and $f_{rep} = 80.64$ MHz, then the number of comb teeth is estimated to be $N \approx 54{,}785$.

However, if we are going to treat one individual pulse, it is more appropriate to use that one pulse's power. With a typical power meter, we measure the average power of a femtosecond laser, which takes the time average. Thus we must discuss the peak power $P_{peak} = P_{avg}/(\Delta\tau\ \nu_{pp})$ which is 18.75 kW for typical parameters. Taking even half this power and putting it in terms of the power per comb tooth, we estimate 0.17 W per tooth.

From these estimations we can predict a range of scattering rates dependent on each case. In either instance the laser is predicted to be focused down to 20 μm. As discussed in Ch. 5.1 the $|X, v = 0\rangle \leftrightarrow |B, v = 0\rangle$ saturation intensity $I_{sat}^{XB} = 55$ uW/mm^2. From this we can estimate the scattering rate and the time it takes to cause 11 (signal from just $|n = 1\rangle$) or 20 scatters (signal from all $|n > 0\rangle$) and the results are shown in Tab. 7.1.

We see the first two methods provide similar results, and scattering of 20 photons is on the order of 70 - 90 μs. For a pulse to pulse repetition rate of 1.72 MHz or time separation of 581 ns, an exposure of 50(100) μs would mean 86(172) pulses are incident on the ion. Recall from Sec. 7.2.1 that least twice the mean number of photon recoils are required, in the limit of low intensity, for the photon statistical treatment to be appropriate. These conditions are satisfied.

Table 7.1: **Estimated PRR rates:** For the ratio method, we assume zero detuning and for the 1.72 MHz and 80 MHz comb teeth methods we assume a worst case detuning of $\nu_{rep}/2$ where the resonance is located in between two comb teeth. The time for 11 or 20 scatters includes the time for one scatter and the wait time for the next pulse to arrive.

Method	$s_0 = \frac{I}{I_{sat}^{XB}}$	γ_s (1/s)	t($11\gamma_s$) (μs)	t($20\gamma_s$) (μs)
Ratio of Bandwidths	0.048	3.46×10^5	38	69
1.72 MHz Teeth	0.034	2.45×10^5	51	93
80 MHz Teeth	2.6	7.6×10^6	8	14

All of these provide an underestimation of the scattering rates. Using the ratio of bandwidths, we don't incorporate any off resonant power into that method, which would only increase the predicted scattering rates. Additionally, for the 1.72 MHz and 80 MHz comb structure, these were calculated using the largest detuning possible, $f_{rep}/2$. Expanding out to 100 comb teeth, with increasing detuning of $N \cdot f_{rep}$ the transition becomes saturated and the scattering rates approach $1/(2\tau_{XB}) \approx 7.5 \times 10^6$ s^{-1} meaning it would take only 14 us to achieve 20 photon recoils.

Experimentally, we can also estimate the power per comb tooth. This is accomplished when the 385 nm light is put through the spectral filtering set-up (see Ch. 5.3.1) and the spectrum is measured on the homebuilt spectrometer. As a result, we can selectively change the cut-off and measure the power. For example, if we set the cutoff to the R(2) line of the $|X, v = 0\rangle \leftrightarrow |B, v = 0\rangle$ transition and measure the power, we obtain 551 μW when pulse-picking at 1.72 MHz. Then we move the cut-off to the R(1) line and measure 543.3 μW. We know the spectral separation between those lines to be 42,514.77 MHz. At a comb tooth separation of 1.72 MHz that provides 0.3 nW of power per tooth. Scaling to a total 10 mW of power that gives 6 nW per comb tooth, which is a similar order of magnitude to the values given above in Table 7.1. This was done for several lines, all of which give about the same power per comb tooth at $f_{pp} = 1.72$ MHz.

In PRR, the fundamental limit of PRR laser excitation time, with sufficient laser power, is essentially $t_{min} \sim 2N/\nu_i$ where it takes N scatters to kick sufficient population out of the ground state of mode i at frequency ν_i. Recall that the spectroscopy state, which acts as a shelf state here, should have a lifetime longer than t_{min} so that population does not decay back to the PRR cycling transition. This is the reason for the factor of 2 in t_{min}. For a Ba^+ - SiO^+ crystal in our trap with an axial out-of-phase mode of 1.72 MHz, this puts the limit at a state lifetime of ~ 23 μs.

In summary, we find that using laser parameters typical to our experiment, we can estimate a necessary exposure time of no longer than 100 μs to excite our of the motional ground state to a detectable amount. These rates determine the spectroscopy state addressable for potential detection using PRR. In other words, PRR for spectroscopy works best when the shelved state lifetime is longer than the time needed for motional excitation.

7.4 Experimental Results

For our first demonstration, there was no need to spectral filter the ultrafast laser, whose set-up is described in Ch. 5 and demonstrated use previously in our group in Ref. [47], [130]. Regardless of where the population diffuses to while cycling on the X-B transition, the femtosecond laser has spectral components to address the transition. In addition, spectral filtering would only lower the available laser power (due to the 25 % loss of using the optical grating) and when trying something for the first time, you want as much power as possible. It is important to note though that this setup is available on this experiment and can easily be implemented if necessary.

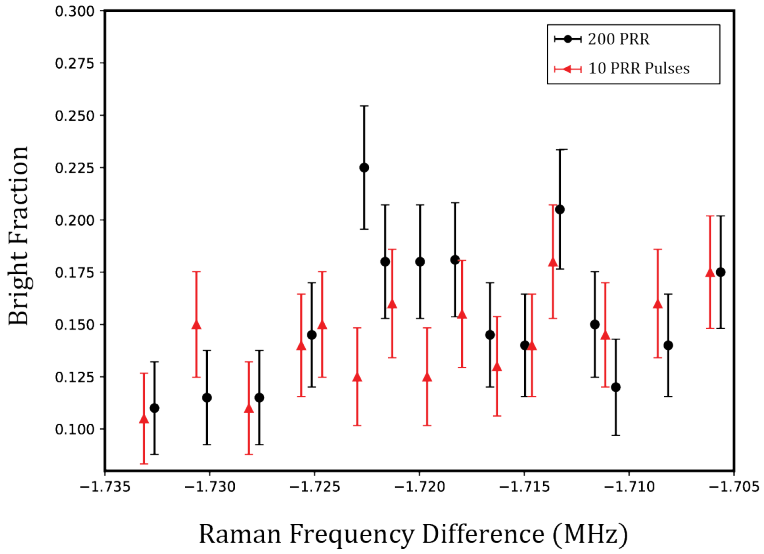

(a) **PRR Attempt Dataset Example 1:** Here, we scan over the axial out-of-phase RSB with a long (200 pulses) and brief (10 pulses) PRR laser exposure. Demonstration of PRR would appear as a clear peak in the black data points.

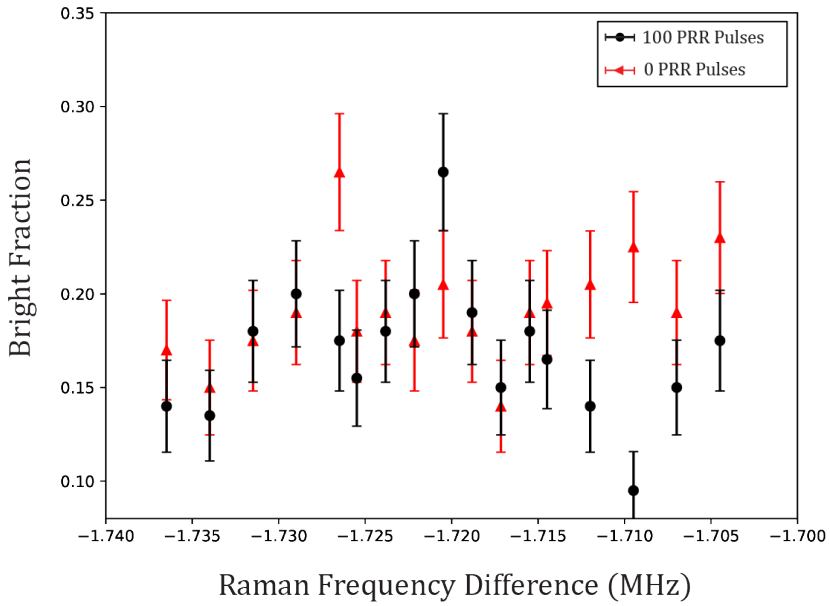

(b) **PRR Attempt Dataset Example 2:** Here, we scan over the axial out-of-phase RSB with (100 pulses) and without (0 pulses) PRR laser exposure. Demonstration of PRR would appear as a clear peak in the black data points.

Initial demonstrations of PRR were unsuccessful. While fits to the data shown in Fig. 7.14a and 7.14b may trick the user into believing there is an amplitude difference, the raw data shows that the values are within the error.

Most of the time, exposure of the fs laser to the trap created patch potentials due to the large electric fields of the focused laser. This is seen by a movement of the ion positions when the PRR laser is exposed. A measurement of micromotion afterwards showed an increase in excess micromotion which indicates a change in the trapping potential.

7.5 Future Work

Fig. 3.16 shows that the PRR beam enter the trap overlapped with the FOR-π, NR-π, 614 nm, 455 nm. This makes alignment to the single ion challenging and it may be advantageous to align the PRR beam into a less busy viewport, such as the one occupied by Doppler2. However, the resulting **k**-vector of the 385 nm would only excite radial modes. The experiment would greatly stand to gain by increasing the PRR signal with the implementation of Rapid Adiabatic Passage [59] using the 1.762 μm transition, similar to the STIRAP readout sequence in [152]. This type of scheme would allow for measurement of all the population in states $|n > 0\rangle$.

The datasets are taken by scanning over the RSB. As mentioned, the PRR light seems to influence the trapping conditions, which could potentially change the axial frequencies. To better understand this, further experiments should be taken by fixing the FOR laser detunings to measure the RSB peak over time. The results can show both the uncertainty in RSB amplitude and potential drifts in the peak over time. This experiment can then be conducted while the PRR is exposed to the trap, which would provide a better understanding of the influence that the PRR laser has on the trapping conditions.

If PRR is successfully demonstrated, we can potentially confirm rotational cooling by setting the cut-off to rotationally cool to N=0. Afterwards if PRR is attempted the molecule should not be motionally heated since no population is in $|X, v = 0, N > 0\rangle$. Because of the cut-off N=0 is a dark state, so the molecule should not be kicked. This same sequence can also measure the cooling rate by scanning the cooling exposure time.

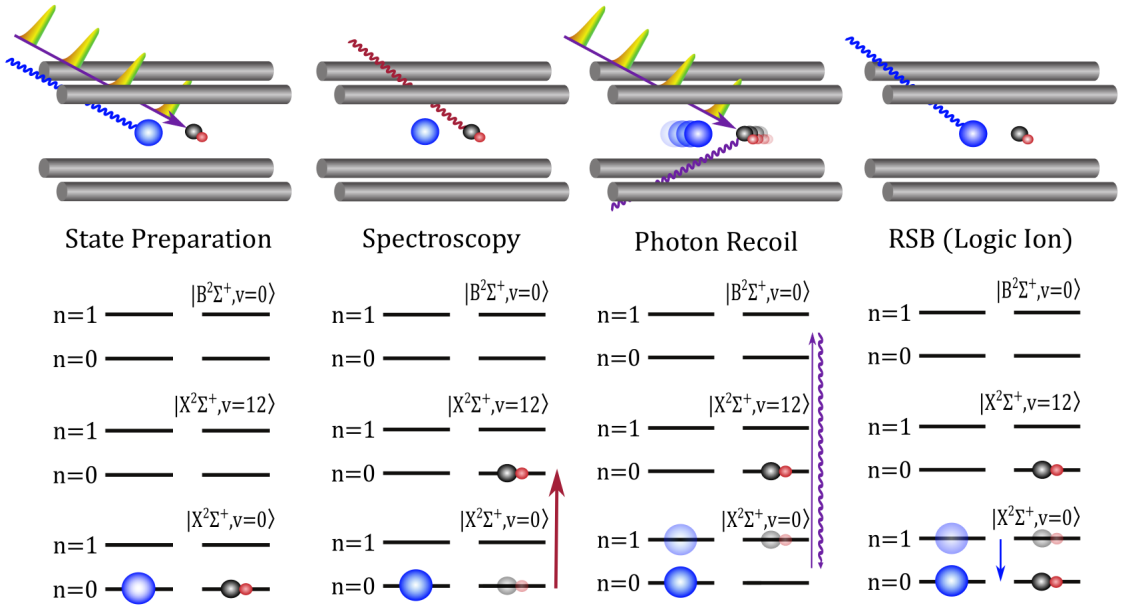

Figure 7.15: **PRR for Vibrational Overtone Spectroscopy in SiO^+:** The ultimate goal of this experiment would be to use PRR as a method of readout for spectroscopy. If our CW IR laser is resonant with the $|X, v = 0\rangle \rightarrow |X, v = 12\rangle$ transition, then the PRR laser will be transparent to the molecular ion and no momentum is added to the ion pair. If the spectroscopy laser is not resonant with a transition, then population can cycle between the X and B states with photon recoils resulting in removal of ground motional state population. The motional states listed correspond to the axial out-of-phase mode.

It would be quite a result to conduct spectroscopy on an overtone transition in SiO^+ using PRR. The relevant states involved and logical sequence is shown in Fig. 7.15. If a widely tunable CW OPO could address many overtone transitions (see Table 5.6), then spectroscopy of those lines, which have varying lifetimes, can demonstrate the broad potential that PRR has as a readout scheme.

References

[1] P. Hamilton and E. R. Hudson, "A Diatomic Molecule is One Atom too Few," *Physics*, vol. 10, Apr. 2017.

[2] J. M. Hutson, "Ultracold chemistry," *Science*, vol. 327, no. 5967, pp. 788–789, Feb. 2010.

[3] G. Quéméner and P. S. Julienne, "Ultracold molecules under control!" *Chemical Reviews*, vol. 112, no. 9, pp. 4949–5011, 2012.

[4] N. Balakrishnan, "Perspective: Ultracold molecules and the dawn of cold controlled chemistry," *Journal of Chemical Physics*, vol. 145, no. 15, p. 110 901, 2016.

[5] W. E. Perreault, N. Mukherjee, and R. N. Zare, "Cold quantum-controlled rotationally inelastic scattering of HD with H2 and D2 reveals collisional partner reorientation /639/638/440/950 /639/638/440/94 article," *Nature Chemistry*, vol. 10, no. 5, pp. 561–567, May 2018.

[6] Y. Liu, Y. Liu, D. D. Grimes, M. G. Hu, and K. K. Ni, "Probing ultracold chemistry using ion spectrometry," *Physical Chemistry Chemical Physics*, vol. 22, no. 9, pp. 4861–4874, Mar. 2020.

[7] S. Venkataramanababu, A. Li, I. Antonov, *et al.*, "Rotational control of reactivity: Hydrogen abstraction by SiO+ ions in extreme rotational states," *unpublished*, 2022.

[8] N. Gershenfeld and I. L. Chuang, "Quantum computing with molecules," *Scientific American*, vol. 278, no. 6, pp. 66–71, 1998.

[9] D. DeMille, "Quantum Computation with Trapped Polar Molecules," *Physical Review Letters*, vol. 88, no. 6, p. 4, 2002.

[10] K. A. B. Soderberg, N. Gemelke, and C. Chin, "Ultracold molecules: Vehicles to scalable quantum information processing," *New Journal of Physics*, vol. 11, no. 14pp, p. 55 022, 2009.

[11] E. R. Hudson and W. C. Campbell, "Dipolar quantum logic for freely rotating trapped molecular ions," *Physical Review A*, vol. 98, no. 4, 2018.

[12] M. Mills, H. Wu, E. C. Reed, *et al.*, "Dipole-phonon quantum logic with alkaline-earth monoxide and monosulfide cations," *Physical Chemistry Chemical Physics*, vol. 22, no. 43, pp. 24 964–24 973, 2020.

[13] E. R. Hudson and W. C. Campbell, "Laserless quantum gates for electric dipoles in thermal motion," *Physical Review A*, vol. 104, p. 42 605, 2021.

[14] C. Chin and V. V. Flambaum, "Enhanced sensitivity to fundamental constants in ultracold atomic and molecular systems near Feshbach resonances," *Physical Review Letters*, vol. 96, no. 23, 2006.

[15] D. DeMille, "Diatomic molecules, a window onto fundamental physics," *Physics Today*, vol. 68, no. 12, pp. 34–40, Dec. 2015.

[16] W. B. Cairncross, D. N. Gresh, M. Grau, *et al.*, "Precision Measurement of the Electron's Electric Dipole Moment Using Trapped Molecular Ions," *Physical Review Letters*, vol. 119, no. 15, 2017.

[17] M. S. Safronova, D. Budker, D. Demille, D. F. Kimball, A. Derevianko, and C. W. Clark, "Search for new physics with atoms and molecules," *Reviews of Modern Physics*, vol. 90, no. 2, p. 25 008, 2018.

[18] V. Andreev, D. G. Ang, D. DeMille, *et al.*, "Improved limit on the electric dipole moment of the electron," *Nature*, vol. 562, no. 7727, pp. 355–360, 2018.

[19] M. G. Kokish, P. R. Stollenwerk, M. Kajita, and B. C. Odom, "Prospects for a polar-molecular-ion optical probe of varying proton-electron mass ratio," *Physical Review A*, vol. 98, no. 5, pp. 1–7, 2018.

[20] J. Lim, J. R. Almond, M. A. Trigatzis, *et al.*, "Laser Cooled YbF Molecules for Measuring the Electron's Electric Dipole Moment," *Physical Review Letters*, vol. 120, no. 12, p. 123 201, 2018.

[21] R. Carollo, A. Frenett, and D. Hanneke, "Two-photon vibrational transitions in 16O+ 2 as probes of variation of the proton-to-electron mass ratio," *Atoms*, vol. 7, no. 1, 2019.

[22] M. Kajita and N. Kimura, "Prospects in rare-gas hydride ions for terahertz frequency standards," *Journal of Physics B: Atomic, Molecular and Optical Physics*, vol. 53, no. 13, p. 4, 2020.

[23] D. Mitra, K. H. Leung, and T. Zelevinsky, "Quantum control of molecules for fundamental physics," *Physical Review A*, vol. 105, no. 4, Apr. 2022.

[24] V. V. Flambaum and M. G. Kozlov, "Enhanced sensitivity to the time variation of the fine-structure constant and mp/me in diatomic molecules," *Physical Review Letters*, vol. 99, no. 15, 2007.

[25] T. Zelevinsky, S. Kotochigova, and J. Ye, "Precision test of mass-ratio variations with lattice-confined ultracold molecules," *Physical Review Letters*, vol. 100, no. 4, 2008.

[26] D. Demille, S. Sainis, J. Sage, T. Bergeman, S. Kotochigova, and E. Tiesinga, "Enhanced sensitivity to variation of me/mp in molecular pectra," *Physical Review Letters*, vol. 100, no. 4, 2008.

[27] L. D. Carr, D. Demille, R. V. Krems, and J. Ye, "New Journal of Physics Cold and ultracold molecules: science, technology and applications," *New Journal of Physics*, vol. 11, no. 87pp, p. 55 049, 2009.

[28] S. Kotochigova, T. Zelevinsky, and J. Ye, *Prospects for application of ultracold Sr2 molecules in precision measurements*, 2009.

[29] C. Chin, V. V. Flambaum, and M. G. Kozlov, "Ultracold molecules: New probes on the variation of fundamental constants," *New Journal of Physics*, vol. 11, no. 055048, p. 55 048, 2009.

[30] P. Jansen, L. H. Xu, I. Kleiner, W. Ubachs, and H. L. Bethlem, "Methanol as a sensitive probe for spatial and temporal variations of the proton-to-electron mass ratio," *Physical Review Letters*, vol. 106, no. 10, 2011.

[31] M. Kajita, G. Gopakumar, M. Abe, M. Hada, and M. Keller, "Test of mp / me changes using vibrational transitions in N2+," *Physical Review A - Atomic, Molecular, and Optical Physics*, vol. 89, no. 3, p. 32 509, 2014.

[32] J. Ye, L. S. Ma, and J. L. Hall, "Molecular iodine clock," *Physical Review Letters*, vol. 87, no. 27, pp. 270 801–270 801, 2001.

[33] S. Schiller, D. Bakalov, and V. I. Korobov, "Simplest molecules as candidates for precise optical clocks," *Physical Review Letters*, vol. 113, no. 2, 2014.

[34] C. W. Chou, C. Kurz, D. B. Hume, P. N. Plessow, D. R. Leibrandt, and D. Leibfried, "Preparation and coherent manipulation of pure quantum states of a single molecular ion," *Nature*, vol. 545, no. 7653, pp. 203–207, 2017.

[35] S. S. Kondov, C. H. Lee, K. H. Leung, *et al.*, "Molecular lattice clock with long vibrational coherence," *Nature Physics*, vol. 15, no. 11, pp. 1118–1122, 2019.

[36] S. Alighanbari, G. S. Giri, F. L. Constantin, V. I. Korobov, and S. Schiller, "Precise test of quantum electrodynamics and determination of fundamental constants with HD+ ions," *Nature*, vol. 581, no. 7807, pp. 152–158, 2020.

[37] I. Kozyryev, L. Baum, K. Matsuda, B. Hemmerling, and J. M. Doyle, *Radiation pressure force from optical cycling on a polyatomic molecule*, 2016.

[38] I. Kozyryev, L. Baum, K. Matsuda, *et al.*, "Sisyphus Laser Cooling of a Polyatomic Molecule," *Physical Review Letters*, vol. 118, no. 17, pp. 1–6, 2017.

[39] B. L. Augenbraun, Z. D. Lasner, A. Frenett, *et al.*, "Laser-cooled polyatomic molecules for improved electron electric dipole moment searches," *New Journal of Physics*, vol. 22, no. 2, 2020.

[40] D. Mitra, N. B. Vilas, C. Hallas, *et al.*, "Direct laser cooling of a symmetric top molecule," *Science*, vol. 369, no. 6509, pp. 1366–1369, 2020.

[41] N. R. Hutzler, "Polyatomic molecules as quantum sensors for fundamental physics," *Quantum Science and Technology*, vol. 5, no. 4, p. 044 011, Oct. 2020.

[42] C. E. Dickerson, H. Guo, G. Z. Zhu, *et al.*, "Optical Cycling Functionalization of Arenes," *Journal of Physical Chemistry Letters*, vol. 12, no. 16, pp. 3989–3995, Apr. 2021.

[43] C. Y. Lien, C. M. Seck, Y. W. Lin, J. H. Nguyen, D. A. Tabor, and B. C. Odom, "Broadband optical cooling of molecular rotors from room temperature to the ground state," *Nature Communications*, vol. 5, no. May, pp. 1–7, 2014.

[44] P. R. Stollenwerk, M. G. Kokish, A. G. de Oliveira-Filho, F. R. Ornellas, and B. C. Odom, "Optical pumping of TeH+: Implications for the search for varying mp/me," *Atoms*, vol. 6, no. 3, Sep. 2018.

[45] P. Huang, S. Kain, A. G. De Oliveira-Filho, and B. C. Odom, "Protocol for optically pumping AlH+to a pure quantum state," *Physical Chemistry Chemical Physics*, vol. 22, no. 42, pp. 24 423–24 430, 2020.

[46] P. R. Stollenwerk, I. O. Antonov, S. Venkataramanababu, Y. W. Lin, and B. C. Odom, "Cooling of a Zero-Nuclear-Spin Molecular Ion to a Selected Rotational State," *Physical Review Letters*, vol. 125, no. 11, p. 113 201, 2020.

[47] I. O. Antonov, P. R. Stollenwerk, S. Venkataramanababu, A. P. de Lima Batista, A. G. de Oliveira-Filho, and B. C. Odom, "Precisely spun super rotors," *Nature Communications*, vol. 12, no. 1, 2021.

[48] S. Venkataramanababu, "Application of Quantum Control of Diatomic Molecular Ions," Ph.D. dissertation, Northwestern University, 2022.

[49] P. Jansen, H. L. Bethlem, and W. Ubachs, *Perspective: Tipping the scales: Search for drifting constants from molecular spectra*, 2014.

[50] R. Lange, N. Huntemann, J. M. Rahm, *et al.*, "Improved Limits for Violations of Local Position Invariance from Atomic Clock Comparisons," *Physical Review Letters*, vol. 126, no. 1, Jan. 2021.

[51] J. Kobayashi, A. Ogino, and S. Inouye, "Measurement of the variation of electron-to-proton mass ratio using ultracold molecules produced from laser-cooled atoms," *Nature Communications*, vol. 10, no. 1, 2019.

[52] J.-S. Chen, "Ticking Near the Zero-Point Energy: towards 1 × 10-18 Accuracy in Al+ Optical Clocks," Ph.D. dissertation, University of Colorado, 2017.

[53] C. Monroe, D. M. Meekhof, B. E. King, *et al.*, "Resolved-sideband Raman cooling of a bound atom to the 3D zero-point energy," *Physical Review Letters*, vol. 75, no. 22, pp. 4011–4014, 1995.

[54] U. Bressel, A. Borodin, J. Shen, M. Hansen, I. Ernsting, and S. Schiller, "Manipulation of individual hyperfine states in cold trapped molecular ions and application to HD+ frequency metrology," *Physical Review Letters*, vol. 108, no. 18, May 2012.

[55] C. W. Chou, A. L. Collopy, C. Kurz, *et al.*, "Frequency-comb spectroscopy on pure quantum states of a single molecular ion," *Science*, vol. 367, no. 6485, pp. 1458–1461, Mar. 2020.

[56] F. Wolf, Y. Wan, J. C. Heip, F. Gebert, C. Shi, and P. O. Schmidt, "Non-destructive state detection for quantum logic spectroscopy of molecular ions," *Nature*, vol. 530, no. 7591, pp. 457–460, 2016.

[57] M. Sinhal, Z. Meir, K. Najafian, G. Hegi, and S. Willitsch, "Quantum-nondemolition state detection and spectroscopy of single trapped molecules," *Science*, vol. 367, no. 6483, pp. 1213–1218, 2020.

[58] M. Sinhal and S. Willitsch, "Molecular-ion quantum technologies," 2022.

[59] H. Metcalf and P. v. d. Straten, *Laser Cooling and Trapping*, Graduate T. Springer New York, 1999.

[60] C. Foot, *Atomic Physics*. New York: Oxford University Press, 2005.

[61] G. Herzberg and J. Spinks, *G. Herzberg and J. W. T. Spinks, Molecular Spectra and Molecular Structure: Diatomic molecules*. Prentice-Hall physics series; U. Condon, ed (Van Nostrand)., 1950.

[62] J. Brown and A. Carrington, *Rotational Spectroscopy of Diatomic Molecules*. Cambridge University Press, 2003.

[63] P. F. Bernath, *Spectra of Atoms and Molecules*. New York: Oxford University Press, 2005, vol. 49, pp. 94–94, ISBN: 9780195177596.

[64] B. Odom, D. Hanneke, B. D'urso, and G. Gabrielse, "New measurement of the electron magnetic moment using a one-electron quantum cyclotron," *Physical Review Letters*, vol. 97, no. 3, 2006.

[65] S. M. Brewer, J. S. Chen, A. M. Hankin, *et al.*, "Al+ 27 Quantum-Logic Clock with a Systematic Uncertainty below 10-18," *Physical Review Letters*, vol. 123, no. 3, Jul. 2019.

[66] H. Häffner, C. F. Roos, and R. Blatt, *Quantum computing with trapped ions*, Dec. 2008.

[67] P. E. Miller and M. B. Denton, "The quadrupole mass filter: Basic operating concepts," *Journal of Chemical Education*, vol. 63, no. 7, pp. 617–622, 1986.

[68] D. J. Wineland, C. Monroe, W. M. Itano, D. Leibfried, B. E. King, and D. M. Meekhof, "Experimental Issues in Coherent Quantum-State Manipulation of Trapped Atomic Ions," *Journal of Research of the National Institute of Standards and Technology*, vol. 103, no. 3, pp. 259–328, 1998.

[69] D. A. Tabor, V. Rajagopal, Y. W. Lin, and B. Odom, "Suitability of linear quadrupole ion traps for large coulomb crystals," *Applied Physics B: Lasers and Optics*, vol. 107, no. 4, pp. 1097–1104, 2012.

[70] D. F. V. James, "Applied Physics B Lasers and Optics Quantum dynamics of cold trapped ions with application to quantum computation," *Appl. Phys. B*, vol. 66, pp. 181–190, 1998.

[71] D. Leibfried, R. Blatt, C. Monroe, and D. Wineland, *Quantum dynamics of single trapped ions*, Jan. 2003.

[72] V. A. Alekseev, D. D. Krylova, and V. S. Letokhov, "Sympathetic cooling of two trapped ions," *Physica Scripta*, vol. 51, no. 3, pp. 368–372, Mar. 1995.

[73] J. B. Wübbena, S. Amairi, O. Mandel, and P. O. Schmidt, "Sympathetic cooling of mixed-species two-ion crystals for precision spectroscopy," *Physical Review A - Atomic, Molecular, and Optical Physics*, vol. 85, no. 4, Apr. 2012.

[74] M. G. Kokish, "Toward Molecular Detection of Drifting Fundamental Constants," Ph.D. dissertation, Northwestern University, 2018.

[75] J. E. Goeders, C. R. Clark, G. Vittorini, K. Wright, C. R. Viteri, and K. R. Brown, "Identifying single molecular ions by resolved sideband measurements," *Journal of Physical Chemistry A*, vol. 117, no. 39, pp. 9725–9731, Oct. 2013.

[76] B. Roth, P. Blythe, and S. Schiller, "Motional resonance coupling in cold multispecies Coulomb crystals," *Physical Review A - Atomic, Molecular, and Optical Physics*, vol. 75, no. 2, Jan. 2007.

[77] C. B. Zhang, D. Offenberg, B. Roth, M. A. Wilson, and S. Schiller, "Molecular-dynamics simulations of cold single-species and multispecies ion ensembles in a linear

Paul trap," *Physical Review A - Atomic, Molecular, and Optical Physics*, vol. 76, no. 1, Jul. 2007.

[78] K. Sheridan and M. Keller, "Weighing of trapped ion crystals and its applications," *New Journal of Physics*, vol. 13, no. 22pp, p. 123 002, 2011.

[79] Y. Wan, "Quantum logic spectroscopy of atomic and molecular ions," Ph.D. dissertation, Universität Hannover, 2014.

[80] M. Guggemos, D. Heinrich, O. A. Herrera-Sancho, R. Blatt, and C. F. Roos, "Sympathetic cooling and detection of a hot trapped ion by a cold one," *New Journal of Physics*, vol. 17, no. 10, p. 103 001, 2015.

[81] D. B. Hume, "Two-Species Ion Arrays for Quantum Logic Spectroscopy and Entanglement Generation," Ph.D. dissertation, University of Colorado, 2002.

[82] S. Ding, "Control of Trapped-ion Motion for Molecular Spectroscopy and Quantum Information Processing," Ph.D. dissertation, University of Singapore, 2015.

[83] S. A. King, L. J. Spieß, P. Micke, *et al.*, "Algorithmic Ground-State Cooling of Weakly Coupled Oscillators Using Quantum Logic," *Physical Review X*, vol. 11, no. 4, Dec. 2021.

[84] M. W. Van Mourik, P. Hrmo, L. Gerster, *et al.*, "Rf-induced heating dynamics of noncrystallized trapped ions," *Physical Review A*, vol. 105, no. 3, Mar. 2022.

[85] H. Walther, "Phase Transitions of Stored Laser-Cooled Ions," *Advances in Atomic, Molecular and Optical Physics*, vol. 31, no. C, pp. 137–182, 1993.

[86] W. M. Itano and D. J. Wineland, "Laser cooling of ions stored in harmonic and Penning traps," *Physical Review A*, vol. 25, no. 1, pp. 35–54, 1982.

[87] J. H. Wesenberg, R. J. Epstein, D. Leibfried, *et al.*, "Fluorescence during Doppler cooling of a single trapped atom," *Physical Review A - Atomic, Molecular, and Optical Physics*, vol. 76, no. 5, Nov. 2007.

[88] C. W. Chou, D. B. Hume, J. C. Koelemeij, D. J. Wineland, and T. Rosenband, "Frequency comparison of two high-accuracy Al+ optical clocks," *Physical Review Letters*, vol. 104, no. 7, Feb. 2010.

[89] J. P. Home, D. Hanneke, J. D. Jost, D. Leibfried, and D. J. Wineland, "Normal modes of trapped ions in the presence of anharmonic trap potentials," *New Journal of Physics*, vol. 13, Jul. 2011.

[90] F. Splatt, M. Harlander, M. Brownnutt, F. Zähringer, R. Blatt, and W. Haänsel, "Deterministic reordering of40Ca2 ions in a linear segmented Paul trap," *New Journal of Physics*, vol. 11, no. 17pp, p. 103 008, 2009.

[91] D. B. Hume, C. W. Chou, T. Rosenband, and D. J. Wineland, "Preparation of Dicke states in an ion chain," *Physical Review A - Atomic, Molecular, and Optical Physics*, vol. 80, no. 5, Nov. 2009.

[92] C. M. Seck, "Quantum State Control of Trapped Atomic and Molecular Ions," Ph.D. dissertation, Northwestern University, 2016.

[93] Y.-W. Lin, "Towards the Precision Spectroscopy of a Single Molecular Ion," Ph.D. dissertation, Northwestern University, 2016.

[94] P. R. Stollenwerk, "Rovibrational Control of a Diatomic Molecule," Ph.D. dissertation, Northwestern University, 2020.

[95] D. J. Berkeland, J. D. Miller, J. C. Bergquist, W. M. Itano, and D. J. Wineland, "Minimization of ion micromotion in a Paul trap," *Journal of Applied Physics*, vol. 83, no. 10, pp. 5025–5033, 1998.

[96] G. Morigi and H. Walther, "Two-species Coulomb chains for quantum information," *European Physical Journal D*, vol. 13, no. 2, pp. 261–269, 2001.

[97] C. F. Roos, T. Monz, K. Kim, *et al.*, "Nonlinear coupling of continuous variables at the single quantum level," *Physical Review A - Atomic, Molecular, and Optical Physics*, vol. 77, no. 4, Apr. 2008.

[98] X. R. Nie, C. F. Roos, and D. F. James, "Theory of cross phase modulation for the vibrational modes of trapped ions," *Physics Letters, Section A: General, Atomic and Solid State Physics*, vol. 373, no. 4, pp. 422–425, Jan. 2009.

[99] C. M. Seck, M. G. Kokish, M. R. Dietrich, and B. C. Odom, "Raman sideband cooling of a Ba + 138 ion using a Zeeman interval," *Physical Review A*, vol. 93, no. 5, p. 53 415, 2016.

[100] B. Merkel, K. Thirumalai, J. E. Tarlton, *et al.*, "Magnetic field stabilization system for atomic physics experiments," *Review of Scientific Instruments*, vol. 90, no. 4, Apr. 2019.

[101] T. Ruster, C. T. Schmiegelow, H. Kaufmann, C. Warschburger, F. Schmidt-Kaler, and U. G. Poschinger, "A long-lived Zeeman trapped-ion qubit," *Applied Physics B: Lasers and Optics*, vol. 122, no. 10, Oct. 2016.

[102] P. R. Stollenwerk, I. O. Antonov, and B. C. Odom, "IP determination and 1+1 REMPI spectrum of SiO at 210–220nm in an ion trap: Implications for SiO+ ion trap loading," *Journal of Molecular Spectroscopy*, vol. 355, pp. 40–45, Jan. 2019.

[103] W. F. McGrew, X. Zhang, H. Leopardi, *et al.*, "Towards the optical second: verifying optical clocks at the SI limit," *Optica*, vol. 6, no. 4, p. 448, Apr. 2019.

[104] C. F. Roos, D. Leibfried, A. Mundt, F. Schmidt-Kaler, J. Eschner, and R. Blatt, "Experimental Demonstration of Ground State Laser Cooling with Electromagnetically Induced Transparency," 2000.

[105] P. O. Schmidt, T. Rosenband, C. Langer, W. M. Itano, J. C. Bergquist, and D. J. Wineland, "Physics: Spectroscopy using quantum logic," *Science*, vol. 309, no. 5735, pp. 749–752, Jul. 2005.

[106] G. Marx, G. Tommaseo, and G. Werth, "Precise gJ- and gI-factor measurements of Ba+ isotopes," *European Physical Journal D*, vol. 4, no. 3, pp. 279–284, 1998.

[107] D. De Munshi, T. Dutta, R. Rebhi, and M. Mukherjee, "Precision measurement of branching fractions of Ba 138 +: Testing many-body theories below the 1% level," *Physical Review A - Atomic, Molecular, and Optical Physics*, vol. 91, no. 4, Apr. 2015.

[108] E. H. Pinnington, R. W. Berendsî, and M. Lumsden, "Studies of laser-induced fluorescence in fast beams of Sr+ and Ba+ ions," *Journal of Physics B: Atomic, Molecular and Optical Physics*, vol. 28, no. 11, pp. 2095–2103, Jun. 1995.

[109] N. Kurz, M. R. Dietrich, G. Shu, *et al.*, "Measurement of the branching ratio in the 6 P3/2 decay of Ba II with a single trapped ion," *Physical Review A - Atomic, Molecular, and Optical Physics*, vol. 77, no. 6, Jun. 2008.

[110] N. Yu, W. Nagourney, and H. Dehmelt, "Radiative Lifetime Measurement of the Ba+Metastable D3/2State," *Physical Review Letters*, vol. 78, no. 26, pp. 4898–4901, 1997.

[111] K. H. Knöll, G. Marx, K. Hübner, *et al.*, "Experimental gJ factor in the metastable 5 D3/2 level of Ba+," *Physical Review A*, vol. 54, no. 2, pp. 1199–1205, 1996.

[112] C. Auchter, T. W. Noel, M. R. Hoffman, S. R. Williams, and B. B. Blinov, "Measurement of the branching fractions and lifetime of the 5D5/2 level of Ba+," *Physical Review A - Atomic, Molecular, and Optical Physics*, vol. 90, no. 6, Dec. 2014.

[113] K. J. Arnold, R. Kaewuam, S. R. Chanu, T. R. Tan, Z. Zhang, and M. D. Barrett, "Precision Measurements of the Ba+ 1386sS21/2-5dD25/2 Clock Transition," *Physical Review Letters*, vol. 124, no. 19, May 2020.

[114] E. A. Dijck, M. Nuñez Portela, A. T. Grier, *et al.*, "Determination of transition frequencies in a single Ba + 138 ion," *Physical Review A - Atomic, Molecular, and Optical Physics*, vol. 91, no. 6, Jun. 2015.

[115] J. J. Curry, *Compilation of wavelengths, energy levels, and transition probabilities for Ba I and Ba II*, 2004.

[116] E. D. Black, "An introduction to Pound–Drever–Hall laser frequency stabilization," *American Journal of Physics*, vol. 69, no. 1, pp. 79–87, 2001.

[117] D. J. Berkeland and M. G. Boshier, "Destabilization of dark states and optical spectroscopy in Zeeman-degenerate atomic systems," *Physical Review A - Atomic, Molecular, and Optical Physics*, vol. 65, no. 3, p. 13, 2002.

[118] B. Shore, *THE THEORY OF COHERENT ATOMIC EXCITATION*. John Wiley & Sons, Inc, 1990.

[119] S. Webster, "Raman Sideband Cooling and Coherent Manipulation of Trapped Ions," Ph.D. dissertation, 2005.

[120] M. R. Dietrich, N. Kurz, T. Noel, G. Shu, and B. B. Blinov, "Hyperfine and optical barium ion qubits," *Physical Review A - Atomic, Molecular, and Optical Physics*, vol. 81, no. 5, May 2010.

[121] A. Kleczewski, M. R. Hoffman, J. A. Sherman, E. Magnuson, B. B. Blinov, and E. N. Fortson, "Coherent excitation of the 6S 1/2 to 5D 3/2 electric-quadrupole transition in 138Ba +," *Physical Review A - Atomic, Molecular, and Optical Physics*, vol. 85, no. 4, p. 043 418, Apr. 2012.

[122] A. D. Ludlow, "The Strontium Optical Lattice Clock: Optical Spectroscopy with Sub-Hertz Accuracy," *Thesis*, p. 251, 2008.

[123] R. W. Fox, C. W. Oates, and L. W. Hollberg, "Stabilizing diode lasers to high-finesse cavities," *Experimental Methods in the Physical Sciences*, vol. 40, no. C, pp. 1–46, Jan. 2003.

[124] M. R. Dietrich, "Barium Ions for Quantum Computation," Ph.D. dissertation, University of Washington, 2009.

[125] J. H. Nguyen and B. Odom, "Prospects for Doppler cooling of three-electronic-level molecules," *Physical Review A - Atomic, Molecular, and Optical Physics*, vol. 83, no. 5, pp. 1–7, 2011.

[126] S. D. Rosner, R. Cameron, T. J. Scholl, and R. A. Holt, "A Study of the X $2\Sigma+$ and a 2Π States of SiO+ Using Fast-Ion-Beam Laser Spectroscopy," *Journal of Molecular Spectroscopy*, vol. 189, no. 1, pp. 83–94, May 1998.

[127] Z. Qin, T. Bai, J. Zhao, and L. Liu, "Transition properties between low-lying electronic states of SiO+," *Journal of Molecular Spectroscopy*, vol. 370, p. 111 298, Apr. 2020.

[128] R. J. Le Roy, "RKR1: A computer program implementing the first-order RKR method for determining diatomic molecule potential energy functions," *Journal of Quantitative Spectroscopy and Radiative Transfer*, vol. 186, pp. 158–166, 2017.

[129] P. R. Stollenwerk, B. C. Odom, D. L. Kokkin, and T. Steimle, "Electronic spectroscopy of a cold SiO+ sample: Implications for optical pumping," *Journal of Molecular Spectroscopy*, vol. 332, pp. 26–32, Feb. 2017.

[130] P. R. Stollenwerk, "Rovibrational Control of a Diatomic Molecule," Ph.D. dissertation, Northwestern University, 2020.

[131] C. M. Western, "PGOPHER: A program for simulating rotational, vibrational and electronic spectra," *Journal of Quantitative Spectroscopy and Radiative Transfer*, vol. 186, pp. 221–242, 2017.

[132] Z. L. Cai and J. P. François, "Ab Initio Study of the Electronic Spectrum of the SiO+ Cation," *Journal of Molecular Spectroscopy*, vol. 197, no. 1, pp. 12–18, Sep. 1999.

[133] R. Li, X. Yuan, G. Liang, Y. Wu, J. Wang, and B. Yan, "Laser cooling of the SiO+ molecular ion: A theoretical contribution," *Chemical Physics*, vol. 525, no. December 2018, p. 110 412, 2019.

[134] R. Li, G. Y. Liang, X. H. Lin, Y. H. Zhu, S. T. Zhao, and Y. Wu, "Explicitly correlated configuration interaction investigation on low-lying states of SiO+ and SiO," *Chinese Physics B*, vol. 28, no. 4, 2019.

[135] W. C. Campbell and E. R. Hudson, "Dipole-Phonon Quantum Logic with Trapped Polar Molecular Ions," *Physical Review Letters*, vol. 125, no. 12, Sep. 2020.

[136] R. A. VanGundy, J. H. Bartlett, and M. C. Heaven, "Spectroscopy of the low-lying states of CaO+," *Journal of Molecular Spectroscopy*, vol. 344, pp. 17–20, Feb. 2018.

[137] L. Baum, N. B. Vilas, C. Hallas, *et al.*, "1D Magneto-Optical Trap of Polyatomic Molecules," *Physical Review Letters*, vol. 124, no. 13, 2020.

[138] B. L. Augenbraun, J. M. Doyle, T. Zelevinsky, and I. Kozyryev, "Molecular Asymmetry and Optical Cycling: Laser Cooling Asymmetric Top Molecules," *Physical Review X*, vol. 10, no. 3, p. 031 022, Jul. 2020.

[139] J. Kłos and S. Kotochigova, "Prospects for laser cooling of polyatomic molecules with increasing complexity," *Physical Review Research*, vol. 2, no. 1, Mar. 2020.

[140] J. Bagdonaite, M. Daprà, P. Jansen, *et al.*, "Robust constraint on a drifting proton-to-electron mass ratio at z=0.89 from methanol observation at three radio telescopes," *Physical Review Letters*, vol. 111, no. 23, Dec. 2013.

[141] J. E. Christensen, D. Hucul, W. C. Campbell, and E. R. Hudson, "High-fidelity manipulation of a qubit enabled by a manufactured nucleus," *npj Quantum Information*, vol. 6, no. 1, Dec. 2020.

[142] F. A. An, A. Ransford, A. Schaffer, *et al.*, "High fidelity state preparation and measurement of ion hyperfine qubits with I ¿ 1/2," Mar. 2022.

[143] N. B. Khanyile, G. Shu, and K. R. Brown, "Observation of vibrational overtones by single-molecule resonant photodissociation," *Nature Communications*, vol. 6, Jul. 2015.

[144] B. Lounis and C. Cohen-Tannoudji, "Coherent population trapping and Fano profiles," *Journal de Physique II*, vol. 2, no. 4, pp. 579–592, Apr. 1992.

[145] G. Morigi, J. Eschner, and C. H. Keitel, "Ground state laser cooling using electromagnetically induced transparency," *Physical Review Letters*, vol. 85, no. 21, pp. 4458–4461, Nov. 2000.

[146] C. Cohen-Tannoudji, *Dark resonances from optical pumping to cold atoms and molecules*, Aug. 2015.

[147] Y. Lin, J. P. Gaebler, T. R. Tan, *et al.*, "Sympathetic electromagnetically-induced-transparency laser cooling of motional modes in an ion chain," *Physical Review Letters*, vol. 110, no. 15, Apr. 2013.

[148] R. Lechner, C. Maier, C. Hempel, *et al.*, "Electromagnetically-induced-transparency ground-state cooling of long ion strings," *Physical Review A*, vol. 93, no. 5, May 2016.

[149] C. Di Fidio and W. Vogel, "Damped Rabi oscillations of a cold trapped ion," *Physical Review A - Atomic, Molecular, and Optical Physics*, vol. 62, no. 3, p. 4, 2000.

[150] T. Baba and I. Waki, "Laser-cooled fluorescence mass spectrometry using laser-cooled barium ions in a tandem linear ion trap," *Journal of Applied Physics*, vol. 89, no. 8, pp. 4592–4598, Mar. 2001.

[151] D. B. Hume, C. W. Chou, D. R. Leibrandt, M. J. Thorpe, D. J. Wineland, and T. Rosenband, "Trapped-ion state detection through coherent motion," *Physical Review Letters*, vol. 107, no. 24, Dec. 2011.

[152] Y. Wan, F. Gebert, J. B. Wübbena, *et al.*, "Precision spectroscopy by photon-recoil signal amplification," *Nature Communications*, vol. 5, Jan. 2014.

[153] M. Schulte, N. Lörch, P. O. Schmidt, and K. Hammerer, "Photon-recoil spectroscopy: Systematic shifts and nonclassical enhancements," *Physical Review A*, vol. 98, no. 6, p. 063 808, Dec. 2018.

[154] E. H. Clausen, V. Jarlaud, K. Fisher, S. Meyer, C. Solaro, and M. Drewsen, "Unresolved sideband photon recoil spectroscopy of molecular ions," 2020.

[155] L. Mandel and E. Wolf, *Optical Coherence and Quantum Optics*. Cambridge University Press, 1995.

Internal and External State Preparation of a Single Molecule

Approved by:

Brian Odom
Professor
Department of Physics and Astronomy

Andrew Geraci
Associate Professor
Department of Physics and Astronomy

Tim Kovachy
Assistant Professor
Department of Physics and Astronomy

Date Approved: August 19, 2022

APPENDIX A

Ion-Light Interactions

One should never do algebra in public
Prof. Bill Phillips
Quantum Science Seminar #12

A.1 Interaction Hamiltonian

While outlined in many papers and thesis [68], [71] we will briefly go over the Hamiltonian describing the interaction of light with an ion trapped in an ion trap. Consider a particle with an internal two-level structure of states $|g\rangle$ and $|e\rangle$ with energy separation of $\hbar\omega_0$ confined in a one-dimensional harmonic potential of trapping frequency ω_T. The Hamiltonian describing interaction of monochromatic light of frequency ω_L, and Rabi frequency of Ω_0, with the ion can be written as,

$$\hat{H} = \hat{H}_a + \hat{H}_m + \hat{H}_i \tag{A.1}$$

$$= \underbrace{\frac{\hbar\omega_0}{2}\hat{\sigma}_z}_{\hat{H}_a} + \underbrace{\hbar\omega_T\left(\hat{a}^\dagger\hat{a} + \frac{1}{2}\right)}_{\hat{H}_m} + \underbrace{\frac{\hbar\Omega_0}{2}\hat{\sigma}_+ \exp\left[i\eta(\hat{a} + \hat{a}^\dagger)\right]e^{-i\omega_L t} + \text{ h.c. }}_{\hat{H}_i}, \tag{A.2}$$

where $\hat{H}_a$, $\hat{H}_m$, $\hat{H}_i$ describes the Hamiltonian for the ions electronic states, ion's motion and for the ion-light interaction respectively. Here, $\hat{\sigma}_z = |e\rangle\langle e| - |g\rangle\langle g|$ is one of three Pauli matrices, $\hat{\sigma}_+ = |e\rangle\langle g|$ is the spin-flip raising operator, $\hat{\sigma}_- = |g\rangle\langle e|$ is the spin-flip lowering

operator, $\hat{a}$ is the motional lowering operator and $\hat{a}^\dagger$ is the motional raising operator. The Lamb-Dicke Parameter $\eta = kz_0 = 2\pi\frac{z_0}{\lambda} = \sqrt{\hbar k^2/(2m\omega)}$ is the ratio of the spatial extent z_0 of the ion's motional wavepacket in the ground state of a harmonic potential with frequency ω to the wavelength λ of the laser.

It is useful to point out that the ion-light interaction Hamiltonian can be rewritten in terms of the Displacement operator, $\hat{D}(\alpha) = \exp[\alpha\hat{a}^\dagger - \alpha^*\hat{a}]$ (see Sec. B.2). $\hat{D}(\alpha)$ describes a displacement in phase space by α where $\alpha = \mathrm{i}\eta$ here.

$$\hat{H}_i = \frac{\hbar\Omega_0}{2}\hat{\sigma}^+\hat{D}(i\eta)e^{-i\omega_T t} + \text{ h.c.} \tag{A.3}$$

We can transform into the interaction picture (into the frame of the atom and trap) by setting $\hat{H}_0 = \hat{H}_a + \hat{H}_m$ and with the interaction $\hat{V} = \hat{H}_i$. For $\hat{H}_{int} = \hat{U}^\dagger V\hat{U} - i\hbar\dot{\hat{U}}^\dagger\hat{U}$ where $\hat{U}_0 = \exp[-(i/\hbar)\hat{H}_0 t]$ the new interaction Hamiltonian is given by,

$$\begin{aligned}\hat{H}_{int} &= \hat{U}_0^\dagger\hat{H}_i\hat{U}_0 \\ &= \frac{\hbar}{2}\Omega_0(\sigma_+e^{-i\omega_0 t} + \sigma_-e^{i\omega_0 t})e^{(i/\hbar)\hat{H}_m t}\left[e^{i(k\hat{x}-\omega_L t+\phi)} + e^{-i(k\hat{x}-\omega_L t+\phi)}\right]e^{-(i/\hbar)\hat{H}_m t}\end{aligned} \tag{A.4}$$

The next step is to take the Rotating-Wave Approximation (RWA) and neglect the terms that include $\omega_0+\omega_L$ since they are rapidly oscillating and do little to effect the time evolution. Then the Hamiltonian becomes,

$$\hat{H}_{int} = \frac{\hbar}{2}\Omega_0\sigma_+\exp\left\{i\eta(\hat{a}e^{-i\omega_T t} + \hat{a}^\dagger e^{i\omega_T t})\right\}e^{i(\phi-\delta t)} + \text{h.c.}, \tag{A.5}$$

where $\delta = \omega_0 - \omega_L$ is the detuning of the laser from resonance. From this interaction Hamiltonian we find coupling between certain internal and external modes. Expanding Eq.

A.5 in orders of η there are terms that include $\sigma_{\pm}$, j $\hat{a}$-operators and k $\hat{a}^{\dagger}$-operators that rotate with a frequency of $(j-k)\omega_T = l\omega_T$. If the detuning is set such that $\delta = l\omega_T$ then there is a coupling of states $|g,n\rangle$ with $|e,n+l\rangle$. This as whats known as driving the l'th red (l < 0) or blue sideband (l > 0). The generalized Rabi frequency is [68], [71],

$$\begin{aligned}\Omega_{n,n+l} = \Omega_{n+1,n} &= \Omega_0 |\langle n+l|e^{i\eta(a+a^{\dagger})}|n\rangle| \\ &= \Omega_0 e^{-\eta^2/2}\eta^{|l|}\sqrt{\frac{n_<!}{n_>!}}L_{n_<}^{|l|}(\eta^2) \end{aligned} \tag{A.6}$$

where $n_<$ ($n_>$) is the lesser (greater) of $n+l$ and n, and,

$$\begin{aligned} L_{n_<}^{|l|}(\eta^2) &= \sum_{m=0}^{n_<}(-1)^m \binom{n_< + |l|}{n_< - m}\frac{(\eta^2)^m}{m!} \\ &= \sum_{m=0}^{n_<}(-1)^m \frac{(n_<+|l|)!}{(n_<-m)!(|l|+m)!}\frac{(\eta^2)^m}{m!} \end{aligned} \tag{A.7}$$

Going back to the interaction Hamiltonian, it can be further simplified if the ion is in the Lamb-Dicke regime, where the spatial extent of the ions motional wavefunction is much less the $1/k$, $\langle\psi_{motion}|k^2z^2|\psi_{motion}\rangle^{1/2} \ll 1$. In this regime, $\eta\sqrt{\langle(a+a^{\dagger})^2\rangle} \ll 1$ and we expand Eq. A.5 to lowest order in η and is expressed as,

$$\hat{H}_{LD} = \frac{\hbar}{2}\Omega_0\sigma_+\Big\{1 + i\eta(\hat{a}e^{-i\omega_T t} + \hat{a}^{\dagger}e^{i\omega_T t})\Big\}e^{i(\phi-\delta t)} + \text{h.c.}\ . \tag{A.8}$$

When $\delta = 0$ that is called the carrier transition, where no change of motional state occurs.

The carrier Rabi frequency is Ω_0 and the Hamiltonian has the form of,

$$\hat{H}_{car} = \frac{\hbar}{2}\Omega_0(\sigma_+ e^{i\phi} + \sigma_- e^{-i\phi}). \tag{A.9}$$

When $\delta = -\omega_T$ that is called the first red sideband (RSB). The Hamiltonian has the form,

$$\hat{H}_{RSB} = \frac{\hbar}{2}\Omega_0\eta(\hat{a}\sigma_+ e^{i\phi} + \hat{a}^\dagger\sigma_- e^{-i\phi}). \tag{A.10}$$

The RSB rabi frequency for such as transition, $|g,n\rangle \leftrightarrow |e,n-1\rangle$, is given by,

$$\Omega_{n,n-1} = \Omega_0\eta\sqrt{n}. \tag{A.11}$$

For $\delta = +\omega_T$, that is called the first blue sideband (BSB). This Hamiltonian is given by,

$$\hat{H}_{BSB} = \frac{\hbar}{2}\Omega_0\eta(\hat{a}^\dagger\sigma_+ e^{i\phi} + \hat{a}\sigma_- e^{-i\phi}). \tag{A.12}$$

This gives rise to transitions of $|g,n\rangle \leftrightarrow |e,n+1\rangle$ at a Rabi frequency of,

$$\Omega_{n,n+1} = \Omega_0\eta\sqrt{n+1} \tag{A.13}$$

For a RSB, when going to the excited state one quanta of motional energy (one phonon) is removed from the system. In the same way, a BSB adds one phonon of energy to the system. This implies that by driving either the RSB or BSB we entangle the internal state of the ion with it's motional state.

We can also rewrite the Hamiltonian in Eq. A.2 in the reference frame of the laser, which will remove the time dependence. Again, using a unitary transformations now of the form,

$$\hat{H}_L = \hat{U}V\hat{U}^\dagger + i\hbar\frac{\partial\hat{U}}{\partial t}\hat{U}^\dagger \tag{A.14}$$

$$\text{where, } \hat{U} = \exp\Big[-\frac{i}{\hbar}\hat{H}_0 t\Big]\ ,\ \hat{H}_0 = \frac{\hbar\omega_L t}{2}\hat{\sigma}_z, \text{ and } \hat{V} = \hat{H}_a + \hat{H}_m + \hat{H}_i \tag{A.15}$$

Note that $\hat{\sigma}_z$ commutes with $\hat{a}, \hat{a}^\dagger$ and itself so we only are concerned with its action of the $\hat{H}_i$ term, and the derivative term. Rewriting $\exp[i\eta(\hat{a}+\hat{a}^\dagger)] = \hat{D}(i\eta)$ and expanding out,

$$\hat{U}\hat{H}_i\hat{U}^\dagger = \frac{\hbar\Omega_0}{2}e^{\frac{i\omega_L t}{2}\hat{\sigma}_z}\Big[\hat{\sigma}_+\hat{D}(i\eta)e^{-i\omega_L t} + \hat{\sigma}_-\hat{D}(-i\eta)e^{i\omega_L t}\Big]e^{\frac{-i\omega_L t}{2}\hat{\sigma}_z} \tag{A.16}$$

$$= \frac{\hbar\Omega_0}{2}\Big[\hat{D}(i\eta)e^{-i\omega_L t}e^{\frac{i\omega_L t}{2}\hat{\sigma}_z}\hat{\sigma}_+e^{\frac{-i\omega_L t}{2}\hat{\sigma}_z} + \hat{D}(-i\eta)e^{i\omega_L t}e^{\frac{i\omega_L t}{2}\hat{\sigma}_z}\hat{\sigma}_-e^{\frac{-i\omega_L t}{2}\hat{\sigma}_z}\Big] \tag{A.17}$$

$$\text{use: } e^{\hat{X}}\hat{Y}e^{-\hat{X}} = \hat{Y} + \Big[\hat{X},\hat{Y}\Big] + \frac{1}{2!}\Big[\hat{X},\Big[\hat{X},\hat{Y}\Big]\Big] + \frac{1}{3!}\Big[\hat{X},\Big[\hat{X},\Big[\hat{X},\hat{Y}\Big]\Big]\Big] + \ ...$$

$$\text{where: } [\hat{\sigma}_z,\hat{\sigma}_+] = 2\sigma_+ \text{ and } [\hat{\sigma}_z,\hat{\sigma}_-] = -2\sigma_-$$

$$= \frac{\hbar\Omega_0}{2}\Big[\hat{\sigma}_+\hat{D}(i\eta) + \text{ h.c.}\Big]. \tag{A.18}$$

Here, we utilize the the properties of the Baker-Campbell-Hausdorff Formula [60] which returns,

$$\begin{aligned}
\alpha e^{\hat{X}}\hat{Y}e^{-\hat{X}} &\rightarrow e^{\frac{i\omega_L t}{2}\hat{\sigma}_z}\hat{\sigma}_+ e^{\frac{-i\omega_L t}{2}\hat{\sigma}_z} \\
&= \hat{\sigma}_+ + (2\frac{i\omega_L t}{2})\hat{\sigma}_+ \frac{(2\frac{i\omega_L t}{2})^2}{2!}\hat{\sigma}_+^2 + \frac{(2\frac{i\omega_L t}{2})^3}{3!}\hat{\sigma}_+^3 + \ ... \\
&= \hat{\sigma}_+\Big(1 + (2\frac{i\omega_L t}{2}) + \frac{(2\frac{i\omega_L t}{2})^2}{2!} + \frac{(2\frac{i\omega_L t}{2})^3}{3!}\Big) + \ ... \\
&= \hat{\sigma}_+ \exp\{i\omega_L t\} \qquad \text{(A.19)}
\end{aligned}$$

$$\text{(A.20)}$$

and we get a similar result for the $\hat{\sigma}_-$ term which effectively cancels out the time dependence in the equation. Finally with ,

$$i\hbar\frac{\partial\hat{U}}{\partial t}\hat{U}^\dagger = -\frac{\hbar\omega_L}{2}\hat{\sigma}_z, \qquad \text{(A.21)}$$

we can combine and find the Hamiltonian in the reference frame of the laser is , with δ = ω_L - ω_0 set as the detuning,

$$\hat{H}_L = \hat{H}_m - \frac{\hbar\delta}{2}\hat{\sigma}_z + \left[\frac{\hbar\Omega_0}{2}\hat{\sigma}_+ \exp[i\eta(\hat{a} + \hat{a}^\dagger)] + \ \text{h.c.}\right] \qquad \text{(A.22)}$$

We can again take the Lamb-Dicke approximation to first order and further simplify the Hamiltonian to,

$$\hat{H}'_L = \hat{H}_m - \frac{\hbar\delta}{2}\hat{\sigma}_z + \left[\frac{\hbar\Omega_0}{2}\hat{\sigma}_+\Big(1 + i\eta(\hat{a} + \hat{a}^\dagger)\Big) + \ \text{h.c.}\right] \qquad \text{(A.23)}$$

When the laser is off, the system evolves under the free Hamiltonian (in the reference frame of the laser) as,

$$\hat{H}_{NL} = \hat{H}_m - \frac{\hbar\delta}{2}\hat{\sigma}_z \tag{A.24}$$

A.2 States Dynamics of Multiple Modes

It is important to generalize the previous discussion to 3N modes, where N is the number of ions trapped. The Hamiltonian for the jth ion is given by

$$H_{0,j} = \hbar\omega_a\sigma_z^j + \sum_{k=1}^{3N} = \hbar\omega_k\hat{n}_k. \tag{A.25}$$

as with the last section, analysis in the interaction picture and under the RWA (see Ref. [68]), for ion j the transition from motional state $|n_k\rangle \rightarrow |n'_k\rangle$ has a Rabi frequency given by,

$$\Omega_{n'_k,n_k} = \Omega|\left\langle n_{p\neq k}, n'_k|\Pi_{l=1}^{3L} e^{i\eta(a_l+a_l^\dagger)}|n_{p\neq k}, n_k\right\rangle| \tag{A.26}$$

The above expression shows that the Rabi frequency of a given mode n_k depends on the population of other 'spectator modes' $n_{p\neq k}$. Their contribution to the Rabi frequency is known as the Debye-Waller factors (see Sec. 4.4.5 of Ref. [68]. If these spectator modes are not sideband cooled as well, their amplitudes likely match a distribution set by the particular Doppler cooling settings at the time and may vary from shot to shot. This creates a fluctuation in the Rabi frequency. To suppres these effects it is desirable to cool all motional modes. Note that for Raman transitions, only modes which motion parallel to $\mathbf{\Delta k}$ contribute to the Debye-Waller factors.

For a Raman transitions where Δk lies only along the $\hat{z}$-axis (true in our experiment) then in the Lamb-Dicke regime the Rabi frequency for mode 1 with spectator mode 2 is

given by,

$$\Omega_{n_1',n_1}(n_2) \approx \Omega_0 \eta_1 \sqrt{n_{1>}} e^{-(\eta_1^2 \eta_2^2)/2}(1 - n_2 \eta_2^2) \tag{A.27}$$

where Ω_0 is the carrier Rabi frequency and $n_{1>}$ is the greater number of n' or n. The effect is a reduction of the sideband Rabi frequency and a source of noise as each experimental repetition does not produce the same thermal distribution each time after Doppler cooling. In our trap, for a Ba^+ - SiO^+ crystal at the trap settings shown in Table 3.3, the out-of-phase Rabi frequency is reduced by 28% if the in-phase mode is populated at a Doppler, $\bar{n}_{ip,z} \approx$. If cooled to $\bar{n}_{ip,z} = 1$ then there is only a 2% change.

A.3 Analyzing Motional States

For a single ion initialized in the state $|\downarrow, n\rangle$ then the probability of finding the ion in that qubit state after time t is,

$$P_\downarrow(t) = |\cos(\Omega_{n',n} t)|^2 = \frac{1}{2}[1 + \cos(2\Omega_{n',n} t)] \tag{A.28}$$

with $\Omega_{n',n}$ given somewhere (obviously need to write this out better). Since the motional states follow a distribution, the resulting Rabi oscillations show interference between these different Rabi rates (n-dependence in the Rabi frequency formula). A better representation of the Rabi oscillations are then,

$$P_\downarrow(t) = \frac{1}{2}\left[1 + \sum_{n=0}^{\infty} p_n \cos\left(2\Omega_{n',n} t\right)\right] \tag{A.29}$$

With good resolution it is possible to use Fourier analysis of the rabi oscillations to yield the

probability distribution of $|n\rangle$ states.

When there are multiple modes of motion, the Rabi oscillations include terms of all the normal modes (a la Debye-Waller factors). The signal then becomes,

$$P_{\downarrow}(t) = \frac{1}{2}\left[1 + \prod_{l=1}^{3N_{ions}} \sum_{n_l=0}^{\infty} p_{n_l} \cos\left(2\Omega| \langle n_{p\neq k}, n'_k| \prod_{l=1}^{3N_{ions}} e^{i\eta_l(a_l + a_l^\dagger)} |n_{p\neq k}, n_k\rangle \, |t\right)\right] \tag{A.30}$$

Here, we have replaced the equation for $\Omega_{n',n}$ with that of the multi-mode case and the sum over the probability p_n with the sum over all products for the probability of the ion being in the state $|n_l\rangle$ for each normal mode l. For a typical situation addressing just the axial modes in a two-ion crystal we find,

$$P_{\downarrow}(t) = \frac{1}{2}\left[1 + \sum_{n=0}^{\infty}\sum_{m=0}^{\infty} p_n p_m \cos\left(2\Omega| \langle m, n'| e^{i\eta_m(a_m + a_m^\dagger)} e^{i\eta_n(a_n + a_n^\dagger)} |m, n\rangle \, |t\right)\right] \tag{A.31}$$

where the number states n and m are the two normal modes of motion, in-phase and out-of-phase, with respective populations p_n and p_m for a transition on the mode with states $|n\rangle$ and spectator mode $|m\rangle$.

To analyze the resulting distribution it is possible to either look at the Fourier transform of Rabi oscillations which give a distribution of p_n's that can be fit to find $\bar{n}$ or it is also possible to find $\bar{n}$ by looking at the ratio of sideband amplitudes in the frequency spectrum.

After an exposure time on a sideband of t_{sb}, the states evolve as,

$$P_{\downarrow}^{RSB} = \sum_{n=1}^{\infty} p_n \cos^2\left(2\Omega_{n-1,n} t_{sb}\right) \tag{A.32}$$

$$P_{\downarrow}^{BSB} = \sum_{n=0}^{\infty} p_n \cos^2\left(2\Omega_{n+1,n} t_{sb}\right) \tag{A.33}$$

Recall that $p_n = \frac{\bar{n}^n}{(\bar{n}+1)^{n+1}}$. Taking the ratio of the two gives,

$$R = \frac{\sum_{n=1}^{\infty} \frac{\bar{n}^n}{(\bar{n}+1)^{n+1}} \cos^2\left(2\Omega_{n-1,n} t_{sb}\right)}{\sum_{n=0}^{\infty} \frac{\bar{n}^n}{(\bar{n}+1)^{n+1}} \cos^2\left(2\Omega_{n+1,n} t_{sb}\right)} \tag{A.34}$$

$$= \frac{\bar{n}}{\bar{n}+1} \frac{\sum_{n=0}^{\infty} \frac{\bar{n}^n}{(\bar{n}+1)^{n+1}} \cos^2\left(2\Omega_{n,n+1} t_{sb}\right)}{\sum_{n=0}^{\infty} \frac{\bar{n}^n}{(\bar{n}+1)^{n+1}} \cos^2\left(2\Omega_{n+1,n} t_{sb}\right)} \tag{A.35}$$

$$= \frac{\bar{n}}{\bar{n}+1} \tag{A.36}$$

thus,

$$\bar{n} = \frac{R}{1-R} \tag{A.37}$$

for a thermal state. This also works in the presence of Debye-Waller factors as they

cancel out since the factors are common to both red- and blue-sidebands for a given mode (see Eq. A.26).

APPENDIX B

Motional Distributions

In the previous chapter, we have considered individual Fock states ($|n\rangle$). Here, lets consider the distribution of population among Fock states given certain conditions. Of importance to PRR are coherent states and these are discussed as well. For a discussion of other interesting states of motion and internal/motional-state entanglement including squeezed and cat states I refer the reader to Ref. [71].

B.1 Thermal Distribution

After Doppler cooling, we can expect that the motional distribution follows a thermal one centered around the Doppler cooling limit for a given transition. Additionally, when heating sources are treated as random kicks to the ion we expect the resulting motional states to follow a thermal distribution.

Treating the ion to be in contact with a thermal reservoir at temperate T, the probability a given motional state is occupied is given by,

$$p_n = \frac{e^{-\frac{E_n}{k_B T}}}{Z} = \frac{e^{\frac{-\hbar\omega}{k_B T}(n+\frac{1}{2})}}{Z} \tag{B.1}$$

Replacing$\beta = \frac{1}{k_B T}$, the partition function is,

$$
\begin{aligned}
Z &= \sum_{n=0}^{\infty} e^{-\beta\epsilon_n} = \sum_{n=0}^{\infty} e^{-\beta\hbar\omega(n+\frac{1}{2})} \\
&= e^{-\frac{\beta\hbar\omega}{2}} \sum_{n=0}^{\infty} \left(e^{-\beta\hbar\omega} \right)^n \\
&= \frac{e^{\frac{-\beta\hbar\omega}{2}}}{1 - e^{-\beta\hbar\omega}}
\end{aligned}
$$

Combining we find the zero-point energy cancels and we get,

$$
p_n = e^{-\beta\hbar\omega n}(1 - e^{-\beta\hbar\omega}) \tag{B.2}
$$

In the thermal distribution, the mean occupation number $\bar{n}$ is,

$$
\begin{aligned}
\bar{n} &= \sum_{n=0}^{\infty} n p_n \\
&= \left(1 - e^{-\beta\hbar\omega}\right) \sum_{n=0}^{\infty} n \left(e^{-\beta\hbar\omega}\right)^2 \\
&= (1-a) \sum_{n=0}^{\infty} n a^n \quad \text{where } a = e^{-\beta\hbar\omega} \\
&= (1-a) a \frac{d}{da} \sum_{n=0}^{\infty} a^n \\
&= (1-a) a \frac{d}{da} \left(\frac{1}{1-a}\right) = \frac{a}{1-a} \\
&= \frac{1}{e^{\beta\hbar\omega} - 1}
\end{aligned}
$$

Even after Doppler cooling, the thermal energy is larger than the harmonic energy and in this limit ($k_B T \gg \hbar\omega$), we find that for a single Ba^+ cooled to its doppler temperature in a trapping frequency of $2\pi = 670$ kHz,

$$\bar{n} \approx \frac{k_B T}{\hbar\omega} \approx 16.8 \tag{B.3}$$

We can also write p_n in terms of $\bar{n}$. First recall $a = e^{-\beta\hbar\omega}$ such that we can write $a = \frac{\bar{n}}{1+\bar{n}}$. Applying this substitution to p_n, we find,

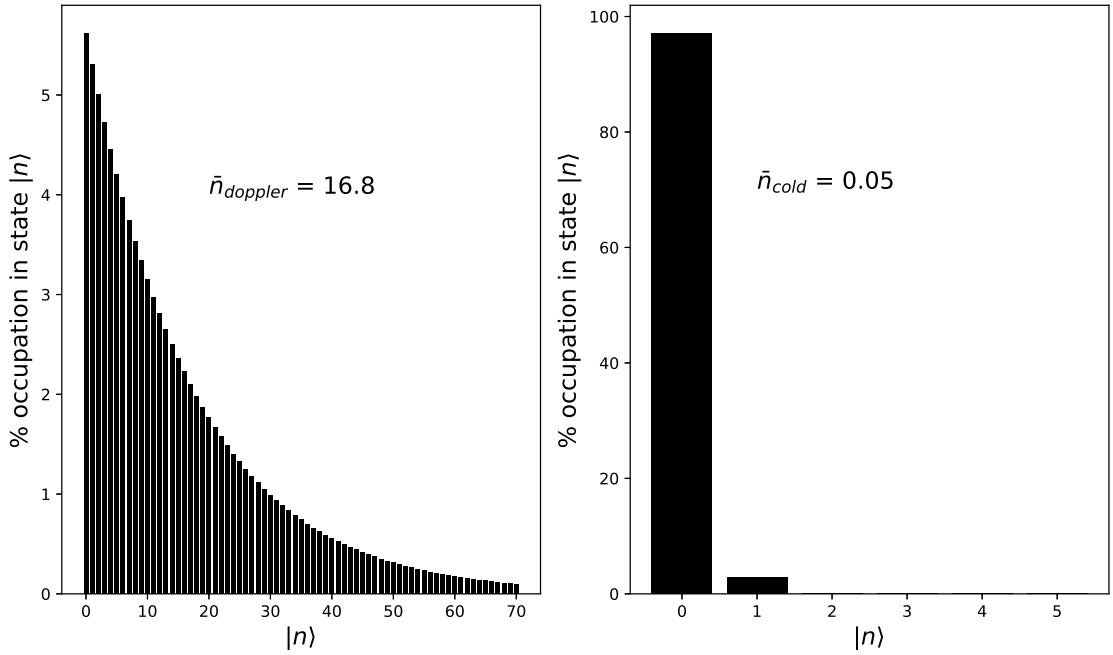

Figure B.1: **Distribution of Population in Motional States:** Here we plot p_n for an ion cooled to $\bar{n} = 16.8$ and one that has been sideband cooled to $\bar{n} = 0.05$. A $\bar{n}$ of 0.05 results in 95% occupation of the ground state $n = 0$ which we observe. Note the substantial population in high n states for the doppler cooled situation.

$$\begin{aligned} p_n &= a^n(1-a) \\ &= \frac{\bar{n}^n}{(1+\bar{n})^n}\left(1 - \frac{\bar{n}}{1+\bar{n}}\right) \\ &= \frac{\bar{n}^n}{(1+\bar{n})^{n+1}} \end{aligned}$$

This will be useful later when we want to characterize the resulting distribution after ground state cooling.

B.2 Coherent State

A coherent state is a minimal uncertainty state, $\sigma_x \sigma_p = \hbar/2$, of the ground state of a harmonic oscillator. Because of this, its dynamics most closely resembles a classical system. The coherent state describes a state where the ground-state harmonic oscillator wavefunction but shifted in momentum and position. Despite this, the Heisenberg uncertainty is unchanged. The coherent state is related to the classical solutions of the H.O by,

$$|\alpha| e^{-i\omega t} = \frac{1}{2}\left(\frac{z(t)}{z_0} + \frac{p(t)}{p_0}\right), \tag{B.4}$$

and the state $|\alpha\rangle$ is an eigenstate of the lowering operators given by, $\hat{a}\,|\alpha\rangle = \alpha\,|\alpha\rangle$ (note: $\langle\alpha|\,\hat{a}^\dagger = \langle\alpha|\,\alpha^*$) and related to the Fock states by,

$$|\alpha\rangle = e^{-|\alpha|^2/2} \sum_n \frac{\alpha^n}{\sqrt{n!}} |n\rangle \tag{B.5}$$

Note for any value α, the state still has minimal uncertainty. From this, the probability p_n to be in a Fock state $|n\rangle$ is,

$$p_n = |\langle n|\alpha\rangle|^2 = \frac{\bar{n}^n}{n!} e^{-\bar{n}} = \frac{(|\alpha|^2)^n}{n!} e^{-|\alpha|^2}. \tag{B.6}$$

This is a Poissonian distribution with mean value $\bar{n} = |\alpha|^2$ with variance $\sigma_n^2 = |\alpha|^2$.

Coherent states are created by application of the displacement operator, [68], [71],

$$\hat{D}(\alpha) = e^{\alpha a^\dagger - \alpha^* a}, \tag{B.7}$$

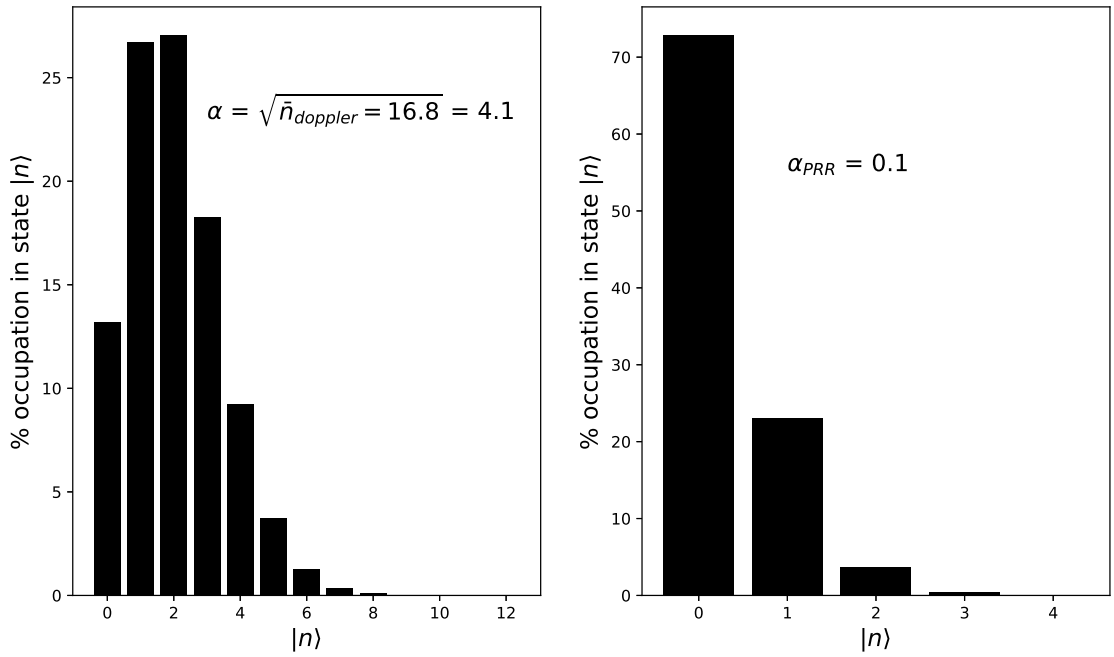

Figure B.2: **Distribution of Population in a Coherent State:** Here we plot p_n for two coherent states: the first (left) corresponding to a thermal distribution after doppler cooling ($\alpha = 4.1$) and the second (right) with $\alpha = 0.1$ which corresponds to the coherent state created after one photon recoil on the molecular ion with weight Lamb-Dicke parameter $\eta = 0.1$

on the zero state written as $\hat{D}(\alpha)\,|0\rangle = |\alpha\rangle$. Note: $\hat{D}(\alpha)^\dagger = \hat{D}(-\alpha)$ and $\hat{D}(\alpha)^\dagger\hat{D}(\alpha) = \hat{D}(\alpha)\hat{D}(\alpha)^\dagger = \mathbb{1}$.

The position expectation value (when rewriting the position operator in terms of creation and annihilation operators) of the coherent state is,

$$\begin{aligned}\langle\hat{x}\rangle &= \sqrt{\frac{\hbar}{2m\omega}}\,\langle\alpha|\hat{a}+\hat{a}^\dagger|\alpha\rangle \\ &= \sqrt{\frac{\hbar}{2m\omega}}(\alpha+\alpha^*)\,\langle\alpha|\alpha\rangle \\ &= \sqrt{\frac{2\hbar}{m\omega}}\mathfrak{R}[\alpha]. \end{aligned} \tag{B.8}$$

Similarly the position expectation value of the coherent state is,

$$\begin{aligned}\langle\hat{p}\rangle &= i\sqrt{\frac{\hbar m\omega}{2}}\,\langle\alpha|\hat{a}^\dagger-\hat{a}|\alpha\rangle \\ &= i\sqrt{\frac{\hbar m\omega}{2}}(\alpha^*-\alpha)\,\langle\alpha|\alpha\rangle \\ &= \sqrt{2\hbar m\omega}\mathfrak{Im}[\alpha] \end{aligned} \tag{B.9}$$

Subsequently, the energy expectation value is,

$$\begin{aligned}\left\langle\hat{E}\right\rangle &= \langle\alpha|\hat{H_{H.O.}}|\alpha\rangle \\ &= \langle\alpha|\hbar\omega\Big(\hat{a}^\dagger\hat{a}+\frac{1}{2}\Big)|\alpha\rangle \\ &= \hbar\omega\Big(|\alpha|^2+\frac{1}{2}\Big) = \hbar\omega\Big(\bar{n}+\frac{1}{2}\Big) \end{aligned} \tag{B.10}$$

Finally, consider the application of successive displacements, $\hat{D}(\alpha)\hat{D}(\beta)$. First recall the Baker-Campbell-Hausdorff formula [155],

$$e^{\hat{A}+\hat{B}} = e^{\hat{A}}e^{\hat{B}}e^{(-\left[\hat{A},\hat{B}\right]/2)}, \tag{B.11}$$

which is valid as long as $\left[\hat{A},\left[\hat{A},\hat{B}\right]\right] = 0 = \left[\hat{B},\left[\hat{A},\hat{B}\right]\right]$. From that (and making use of $\left[\hat{a},\hat{a}^{\dagger}\right]$=1) we can see,

$$\begin{aligned}
\hat{D}(\alpha)\hat{D}(\beta) &= e^{\alpha\hat{a}^{\dagger}-\alpha^{*}a}e^{\beta\hat{a}^{\dagger}-\beta^{*}a} \\
&= e^{\alpha\hat{a}^{\dagger}}e^{-\alpha^{*}\hat{a}}e^{-\frac{1}{2}|\alpha|^{2}}e^{\beta\hat{a}^{\dagger}}e^{-\beta^{*}\hat{a}}e^{-\frac{1}{2}|\beta|^{2}} \\
&= e^{(\alpha+\beta)\hat{a}^{\dagger}}e^{(\alpha^{*}+\beta^{*})a}e^{-\frac{1}{2}(|a|^{2}+|\beta|^{2})} \qquad \text{(B.12)} \\
&= \hat{D}(\alpha+\beta)e^{-\frac{1}{2}(\alpha^{*}\beta-\beta^{+}\alpha)}. \qquad \text{(B.13)}
\end{aligned}$$

Moving from the last two steps, we knew the desired final form of $\hat{D}(\alpha+\beta)$ in the three exponential form (Eq. B.2) and just needed to add that extra phase factor. From Eq. B.13 we see that successive displacements is represented by another displacement operator whose total displacement is the sum of the separate displacements. As seen in Sec. 7.2.1, each photon recoil acts as a displacement operator given by $\hat{D}(i\eta)$ and so that N photon recoils is represented by $\hat{D}(Ni\eta)$ and when acting on the ground state, results in a coherent state of amplitude $|\alpha = Ni\eta\rangle$.

If anyone has made it this far, to the annals of this thesis, I will buy you a cup of coffee, just email me at jdragan30@gmail.com

APPENDIX C

Effects of Pulse Picking on a Frequency Comb

C.1 Frequency Comb

It is important to understand the effects the pulse picker has on the frequency spectrum. I am referring to the frequency spectrum and not to the group-delay dispersion added, which can be handled with compressor, home-built or a commercial device such as a Swamp Optics BOA Compressor.

Let us begin by understanding that time between output pulses in a mode-locked laser is determined by the cavity length and given by $\tau = 2L/c$, which gives a repetition rate $\nu_{rep} = 1/\tau$ which is also the spacing between comb teeth. The overall frequency bandwidth of the laser is determined by the number of comb teeth, N, participating in the mode-lock and is given by Nf_{rep}. For a time-bandwidth product (TBP) limited pulse, assuming Gaussian shape comb teeth, then the individual pulse duration is $\Delta t = 0.441/N\nu_{rep} = 1\Delta\nu$, where $\Delta\nu$ is the frequency bandwidth. For pulses described by a $sech^2$ function, the TBP is 0.315. These are the minimum values for the TBP, and the values are typically larger as the femtosecond laser passes through optics and dispersion is added, enlongating the pulse duration. Plugging in typical parameters, a cavity length of $\approx$ 1.875 nm gives a pulse-to-pulse separation of τ =12.5 ns and ν_{rep} = 80 MHz. Assuming a typical temporal bandwidth of 100 fs pulse width, we find that there are $\approx$ 55,000 comb phase-locked and present in the spectrum. Note that as N increases, the spectral bandwidth ($\Delta\lambda$), increases and the temporal bandwidth decreases.

Assuming comb teeth represented by a Gaussian, a single pulse in time is given by,

$$f(t) = \frac{1}{\Delta t\sqrt{2\pi}} e^{-\frac{(t-\tau)^2}{2\Delta t^2}}. \tag{C.1}$$

The entire pulse train written as,

$$f(t) = \frac{1}{\Delta t\sqrt{2\pi}} \sum_n e^{-\frac{(t-n\tau)^2}{2\Delta t^2}}. \tag{C.2}$$

Taking the Fourier transform, to see the frequency spectrum we find,

$$F(\nu) = \mathcal{F}\{f(t)\} = \int_{-\infty}^{+\infty} f(t) e^{-2\pi i\nu t} dt \tag{C.3}$$

$$= \frac{1}{\Delta t\sqrt{2\pi}} \int_{-\infty}^{+\infty} e^{-\frac{(t-\tau)^2}{2\Delta t^2}} e^{-2\pi i\nu t} dt \tag{C.4}$$

$$= \frac{1}{\sqrt{2\pi}} e^{-2\pi i \frac{\nu}{\nu_{rep}}} e^{-2\pi^2 \left(\frac{\nu}{\Delta\nu}\right)^2}. \tag{C.5}$$

Here we used the shift theorem of the Fourier transform, which says $\mathcal{F}\{f(t-\tau)\} = F(t)e^{-2\pi i\nu\tau}$, between Eq. (A.4) and (A.5). Making use of the linearity of the Fourier Transform, we can then write the entire pulse train as,

$$F(\nu) = \mathcal{F}\Big\{\sum_n f(t - n\tau)\Big\} \tag{C.6}$$

$$= \sum_n \frac{1}{\Delta t\sqrt{2\pi}} \int_{-\infty}^{+\infty} e^{-\frac{(t-n\tau)^2}{2\Delta t^2}} e^{-2\pi i\nu t} dt \tag{C.7}$$

$$= \frac{1}{\sqrt{2\pi}} \underbrace{\sum_n e^{-2\pi i \frac{n\nu}{\nu_{rep}}}}_{\text{Comb Teeth separated by } \nu_{rep}} \times \underbrace{e^{-2\pi^2\left(\frac{\nu}{\Delta\nu}\right)^2}}_{\text{Envelope/Frequency Bandwidth}} \tag{C.8}$$

This describes a comb in the frequency domain.

C.2 Pulse Picker

There are several ways to write the function regarding the pulse picker, whether it be a repeated piece-wise function or the convolution between the Dirac comb and a box function. We will use the latter. Let us first define the ratio of the period between the frequency comb and the pules picker to be d $= \tau_{pp}/\tau = \nu_{rep}/\nu_{pp}$.

We can write the Dirac Comb as,

$$COMB\Big(\frac{t}{d\tau}\Big) = \sum_{n=-\infty}^{+\infty} \delta(t - kd\tau_{pp}). \tag{C.9}$$

This describes a repeated firing of the Pulse Picker whose pulses are separated in time τ. Since the firing is not instantaneous and occupies some timescale of being on, we can write a box function encasing k pulses, where k is an odd number, one TTL pulse can be written as,

$$RECT\Big(\frac{t}{k\tau}\Big) = \begin{cases} 1 & \text{for } -k\tau/2 \le t \le k\tau/2 \\ 0 & \text{otherwise} \end{cases} \tag{C.10}$$

In an attempt to form some semi-complete theory, we require k to be odd, for the pass port $k = 1$ and for the reject port $k = d - 1$. The Tsunami has $\nu_{rep} = 80$ MHz and if we want to pass pulses at $\nu_{pp} = 1$ MHz, then $d = f_{rep}/f_{pp} = 80$ for the pass port and $k_r = d - 1 = 79$ for the reject port.

Making the pulse picker periodic, with period $\tau_{pp} = d\tau$, the resulting function is $g(t) = COMB\Big(\frac{t}{d\tau}\Big) * RECT\Big(\frac{t}{k\tau}\Big)$. This gives a square function with period $\tau_{pp} = d\tau$ and width $k_i\tau$. Finding the frequency spectrum, we make use of the convolution property of the Fourier Transform which says that if $g(t) = a(t)*b(t)$ then $G(\nu) = \mathcal{F}\{a(t)*b(t)\} = \mathcal{F}\{a(t)\}\cdot\mathcal{F}\{b(t)\}$. This shows us,

$$\begin{aligned} G(\nu) &= \mathcal{F}\Big\{COMB\Big(\frac{t}{d\tau}\Big)\Big\} \cdot \mathcal{F}\Big\{RECT\Big(\frac{t}{k\tau}\Big)\Big\} \\ &= \frac{1}{d\tau}\sum_m \delta\Big(\nu - \frac{m}{d\tau}\Big) \cdot k\tau \ \ sinc(k\tau\nu) \\ &= \frac{k}{d}\sum_m \delta\Big(\nu - \frac{m}{d\tau}\Big) \cdot \ \ sinc(k\tau\nu) \\ &= \frac{k}{d} COMB\Big(\nu d\tau\Big) \cdot \ \ sinc(k\tau\nu). \end{aligned}$$

This follows our general understanding, the Fourier transform of a comb in time with mode spacing $d\tau$ gives another comb with frequency spacing $1/d\tau$. Additionally, the Fourier Trans-

form of a square wave is a *sinc* function.

C.3 Frequency Comb Through a Pulse Picker

We can now combine our understanding to see the output spectrum from the pulse picker on both the pass and reject ports. In the time domain, the action of the pulse picker gives a function written as $h(t) = f(t) \cdot g(t)$. In the frequency domain, $H(\nu) = \mathcal{F}\Big\{ f(t) \cdot g(t) \Big\} = F(\nu) * G(\nu)$, this is known as the modulation property of the Fourier Transform. Evaluating we find,

$$H(\nu) = F(\nu) * G(\nu) \tag{C.11}$$

$$= \int_{-\infty}^{+\infty} F(\nu - \nu') G(\nu') \delta\nu \tag{C.12}$$

$$= \frac{1}{2\pi} \frac{k}{d} \sum_n \sum_m \int_{-\infty}^{+\infty} e^{-2\pi i \frac{n}{\nu_{rep}} (\nu - \nu')} e^{-2\pi^2 \left(\frac{\nu - \nu'}{\Delta\nu} \right)^2} \delta\Big(\nu' - \frac{m}{d\tau} \Big) \; sinc\big(k\tau\nu' \big) \delta\nu' \tag{C.13}$$

$$= \frac{1}{2\pi} \frac{k}{d} \sum_n \sum_m \; sinc\left(m \frac{k}{d} \right) e^{-2\pi i \frac{n}{\nu_{rep}} \left(\nu - m\nu_{pp} \right)} e^{-2\pi^2 i \left(\frac{\nu - m\nu_{pp}}{\Delta\nu} \right)^2} \tag{C.14}$$

The above expression fully represents the effect of the pulse picker on a frequency comb where for the pass port $k = 1$ and for the reject port $k = d - 1$. To simulate this numerically takes many resources when plotted symbolically in Mathematica. Since the properties of the frequency comb are due to the coherent interaction between $\sim$ 55,000 frequency components it is important to sum over as many harmonics as possible to plot the behavior. As a result evaluation of this takes time.

C.4 Plots

We can plot these expressions in Python using only $\mathcal{O}(10^5)$ pulses to observe the basics of these spectral features. Here, we make use of the 'scipy.signal' library to easily plot square waves of a given duration and period. One interesting aspect that we find, is that in the reject ports, spectral components that are supposed to be blocked, i.e. 40 MHz components when $d = 2$ are present in the reject port. We find that as d increases, the amplitude of these features decreases. Intuitively this makes sense. For $d = 2$ only 1 out of 40 pulses are removed from the pulse train which we expect to have little effect on the resulting spectrum. Whereas for $d = 2$, every other pulse is passed, so in the reject port we have a strong modulation at that frequency due to half the spectrum missing.

C.4.1 For $\nu_{pp} = 40$ MHz

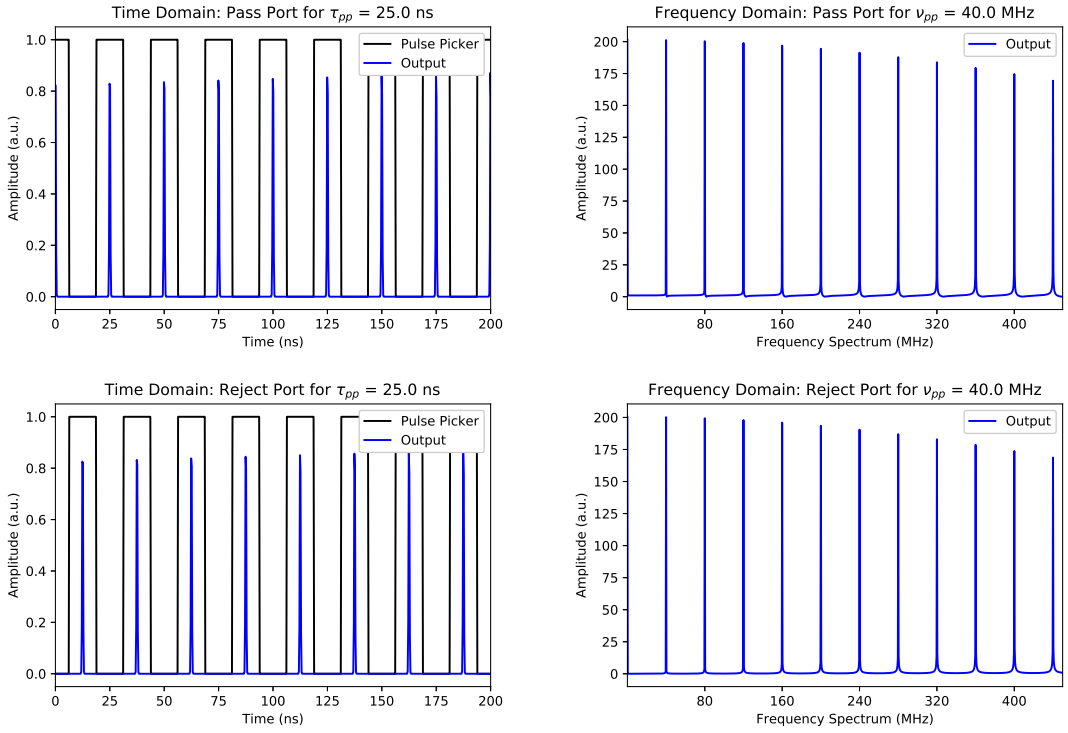

C.4.2 For $\nu_{pp} = 16$ MHz

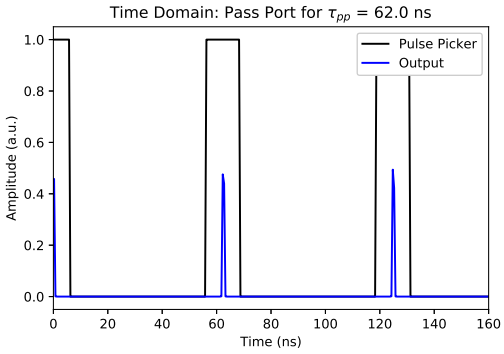

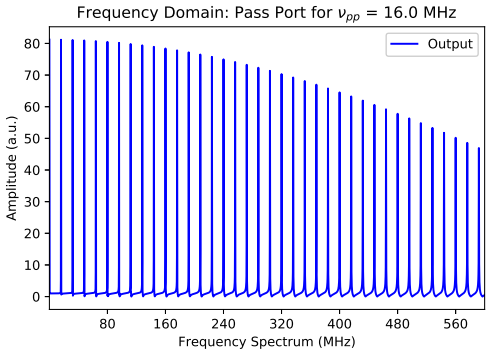

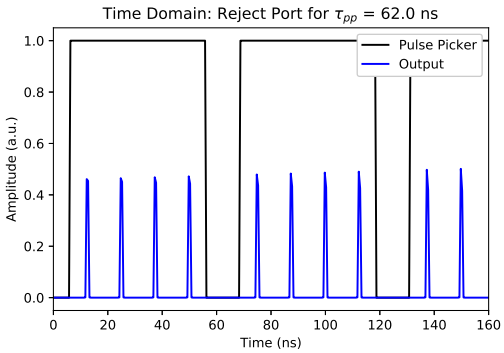

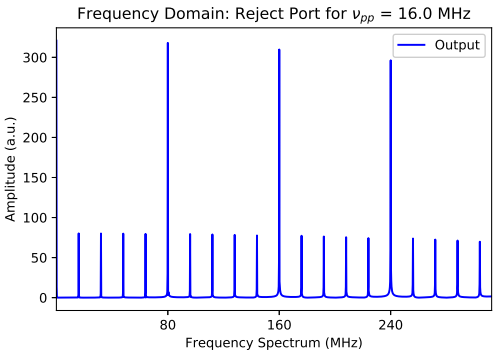

C.4.3 For $\nu_{pp} = 2$ MHz

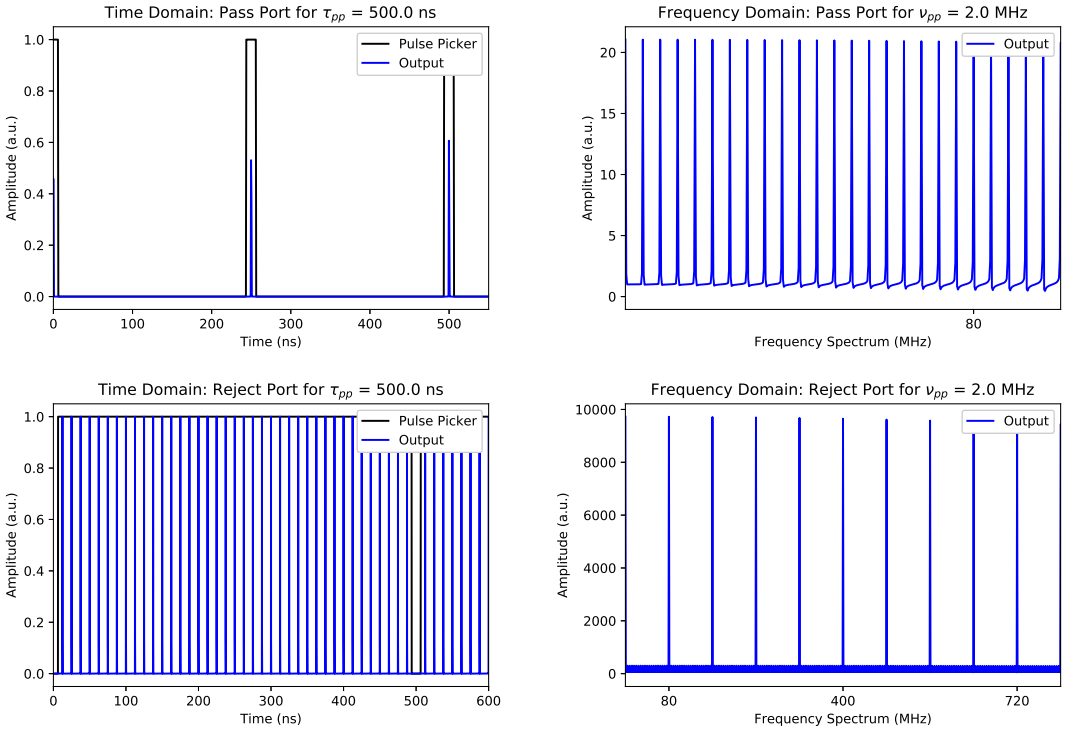

APPENDIX D

RF Circuit Design for LIF SiO^+ Trap

D.1 LIF Trap Resonator Design

This was one of my frist projects in the lab. The RF circuitry here drives the LIF trap [94] rods and allows for DC biasing of each of the four trap rods. Typical peak-to-peak voltages reached were ~ 900 V_{pp} and only limited by saturating effects on the toroid.

Figure D.1: **LIF Trap Circuitry**

APPENDIX E

Python Codes

E.1 Evaluation Board Control

The following code was found from `https://github.com/Schlabonski/evalcontrol` and modified to operate in our specific system. Thank you Fabian T. Schlabonski !

```
import usb
import time

import numpy as np

from .customhandler import DeviceHandle

class AD9959_0(object):
    """This class emulates the AD9959 evaluation board for python.

    An instance of the class will construct a handler for the cypress USB
    controler. Through this handler commands can be sent to the chip and
                                        piped
    to the DDS processor.
    """
    # FOR DDS
    def __init__(self, vid=0x0456, pid=0xee25, port_numbers= (14,4,1),
                                        bus_number=0x1, auto_update=True,
            rfclk=25e6, clkmtp=20, channel=0): #these bus # will specify
```

```
                                        the diffrent AD9959,
#port_numbers = (5,1)     when connected to front of computer
#port_numbers= (14,4,1)   when connected to long usb at experiment
"""Initializes a handler for the usb controler.

If more than one AD9959 are connected via USB, they are in
                                      principle indistinguishable.
                                      The only way
to identify them is by specifying their USB bus address.

vid : hex
    vendor ID of the device
pid : hex
    product ID of the device
bus_number: int
    Bus number of the connected device to distinguish between
                                        identical devices.
port_numbers: tuple
    Contains the port and subport numbers to distinguish between
                                        identical devices.
refclk: float
    Reference clock frequency in Hertz.
clkmtp: int
    Clock multiplier. The reference clock signal is internally
                                        multiplied by this value
                                        to generate
    the system clock frequency.
"""
self.channel = channel
```

```
# find all usb devices with matching vid/pid
devs = list(usb.core.find(idVendor=vid, idProduct=pid, find_all=
                                        True))
dev = None
dev_mess = 'No devices with matching vID/pID {0}/{1} found!'.
                                        format(hex(vid), hex(pid))
assert len(devs) > 0, dev_mess
# if more than one AD9959 is present, decide by usb port address
if len(devs) > 1:
    assert port_numbers is not None and bus_number is not None, '
                                            More than one AD9959
                                            present. Specify USB bus
                                            and port numbers!'
    for d in devs:
        #print(d)
        #print(d.port_numbers)
        #print(str(hex(d.bus)))
        if d.port_numbers == port_numbers and d.bus == bus_number:
            dev = d
            break
    assert dev is not None, 'No matching device was found. Check
                                            bus and port numbers!'

else:
    dev = devs[0]
#print(self.dev)
dev.set_configuration()
cnf = dev.configurations()[0]
```

```
        intf = cnf[(0,0)]
        self.dev = dev

        # retrieve important endpoints of usb controller
        self._ep1 = intf[0]
        self._ep81 = intf[1]
        self._ep4 = intf[3]
        self._ep88 = intf[5]

        # set default values for physical variables
        self.ref_clock_frequency = rfclk
        self.system_clock_frequency = rfclk

        # set default value for auto IO update
        self.auto_update = auto_update

        # try to access device, it might still be in use by another
                                                handler,
        #in this case, reset it
        try:
            self.set_clock_multiplier(clkmtp)
        except usb.USBError:
            self._reset_usb_handler()
            self.set_clock_multiplier(clkmtp)

    def __del__(self):
        usb.util.dispose_resources(self.dev)

    def _reset_usb_handler(self):
```

```
        """Resets the usb handler via which communication takes place.

        This method can be used to prevent USBErrors that occur when
                                                communication with the device
                                                 times out
        because it is still in use by another process.
        """
        self.dev.reset()

    def _write_to_dds_register(self, register, word):
        """Writes a word to the given register of the dds chip.

        Any words that are supposed to be written directly to the DDS
        chip are sent to endpoint 0x04 of the microcrontroler.

        :register: hex
            ID of the target register on the DDS chip.
        :word: bytearray
            word that is written to the respective register. Each byte in
            the bytearray should be either 0x00 or 0x01.

        """
        # express the register name as a binary. Maintain the format that
                                                is
        # understood by endpoint 0x04. The first bit signifies read/write,
        # the next 7 bits specify the register
        register_bin = bin(register).lstrip('0b')
        if len(register_bin) < 7:
            register_bin = (7-len(register_bin))*'0' + register_bin
```

```
        register_bin = ''.join(' 0' + b for b in register_bin)

        # construct the full message that is sent to the endpoint
        message = '00' + register_bin  + ' ' + word
        message = bytearray.fromhex(message)

        # endpoint 0x04 will forward the word to the specified register
        with DeviceHandle(self.dev) as dh:
            dh.bulkWrite(self._ep4, message)

    def _read_from_register(self, register, size):
        """Reads a word of length `size` from `register` of the DDS chip.

        :register: hex
            register of the DDS chip from which to read
        :size: int
            length of the word (in bytes) that is read from the register
        :returns: bytearray
            the readout of the register

        """
        # convert the size to hex
        size_hex = hex(size).lstrip('0x')
        if len(size_hex) < 2:
            size_hex = '0' + size_hex

        # set the controler to readback mode
        begin_readback = bytearray.fromhex('07 00 ' + size_hex)
```

```
        with DeviceHandle(self.dev) as dh:
            dh.bulkWrite(self._ep1, begin_readback)

        # construct the command to read out the register
        register_bin = bin(register).lstrip('0b')
        if len(register_bin) < 7:
            register_bin = (7-len(register_bin))*'0' + register_bin
        register_bin = ''.join(' 0' + b for b in register_bin)
        readout_command = bytearray.fromhex('01' + register_bin)
        with DeviceHandle(self.dev) as dh:
            dh.bulkWrite(self._ep4, readout_command)

        time.sleep(0.1)
        # read the message from endpoint 88
        with DeviceHandle(self.dev) as dh:
            readout = dh.bulkRead(self._ep88, size=size)

        # turn off readback mode
        end_readback = bytearray.fromhex('04 00')
        with DeviceHandle(self.dev) as dh:
            dh.bulkWrite(self._ep1, end_readback)
        return readout

    def _load_IO(self):
        """Loads the I/O update line (same as GUI load function).

        """
        load_message = bytearray.fromhex('0C 00')
        with DeviceHandle(self.dev) as dh:
```

```
            dh.bulkWrite(self._ep1, load_message)
            readout = dh.bulkRead(self._ep81, 1)
        return readout

    def _update_IO(self):
        """Updates the IO to the DDS chip (same as GUI function).

        """
        update_message = bytearray.fromhex('0C 10')
        with DeviceHandle(self.dev) as dh:
            dh.bulkWrite(self._ep1, update_message)
            readout = dh.bulkRead(self._ep81, 1)
        return readout

    def set_clock_multiplier(self, factor):
        """Sets the multiplier for the reference clock.

        The system clock frequency is given by
           f_sys = multiplier * f_ref
        where f_ref is the frequency of the reference clock.

        :factor: int
            Multiplying factor between 4 and 20. A `factor` of 1 disables
            multiplication.

        """
        # in case of a factor of one, we want to disable multiplication
        if factor == 1:
            factor -= 1
```

```
        self.system_clock_frequency = self.ref_clock_frequency

    else:
        assert factor in range(4, 21), "Multiplier should be integer
                                            between 4 and 20!"
        self.system_clock_frequency = self.ref_clock_frequency *
                                            factor

    # construct the multiplier word
    multi_bin = bin(factor).lstrip('0b')
    if len(multi_bin) < 5:
        multi_bin = (5-len(multi_bin))*'0' + multi_bin

    # get the current state of function register 1
    fr1_old = self._read_from_register(0x01, 24)
    fr1_old_bitstring = ''.join(str(b) for b in fr1_old)

    # update the multiplier section of the bitstring
    fr1_new_bitstring = fr1_old_bitstring[0] + multi_bin +
                                        fr1_old_bitstring[6:]
    if self.system_clock_frequency > 255e6:
        l = list(fr1_new_bitstring)
        l[0] = '1'
        fr1_new_bitstring = ''.join(l)
        #print("System clock exceeds 255 MHz, VCO gain bit was set to
                                            True")
    fr1_word = ''.join(' 0' + b for b in fr1_new_bitstring)[1:]

    # write the new multiplier to the register on dds chip
```

```
        self._write_to_dds_register(0x01, fr1_word)
        self._load_IO()
        if self.auto_update:
            self._update_IO()

    def _channel_select(self, channel):
        """Selects the chosen channels in the channel select register.

        :channels: int or list
            ID or list of the channel IDs to select e.g. [0,2,3]

        """
        if np.issubdtype(type(channel), np.integer):
            channels = [channel]
        else:
            channels = [c for c in channel]

        # set the channels in the channel select register
        channel_select_bin = list('0000')
        for ch in channels:
            channel_select_bin[ch] = '1'
        channel_select_bin = channel_select_bin[::-1] # we have inverse
                                                      order
        channel_select_bin = ''.join(channel_select_bin)
                                                           # in the register
        csr_old = self._read_from_register(0x00, 8)
        csr_old_bin = ''.join(str(b) for b in csr_old)
        csr_new_bin = channel_select_bin[:4] + csr_old_bin[4:]
```

```
        csr_word = ''.join(' 0' + b for b in csr_new_bin)
        csr_word = csr_word[1:]

        self._write_to_dds_register(0x00, csr_word)
    def set_amplitude(self, amplitude, channel=None, channel_word=0):
            """Sets a new amplitude for a given channel.

            :amplitude: float
                The new amplitude. Should not exceed 1.
            :channel: int or seq
                Channel(s) for which the frequency should be set.
            :channel_word: int
                Determines the channel_word to which the frequency is
                                                    written. Each
                                                    channel has 16
                channel_words that can be used.

            Amplitude has 10 bits of scalar resolution, as indicated by
                                                the AD9959 manual

            I believe the amplitude register is 0x06
            """
            asf = 1 #amplitude scale factor, default set to 1, it MUST
                                                be an integer
                    # I do not have this working for asf > 1
            #the amplitude out is multiples of asf * (1 / (2^10 - 1)) so
                                                we need to ensure this

            if channel is None:
```

```
    channel = self.channel
assert amplitude <= 0.5, ("Amplitude should not exceed 1,
                                    your going to break
                                    something silly! ")

assert channel_word < 16, ("Channel word cannot exceed 15,
                                    input was {0}".format(
                                    channel_word))

# select the chosen channels
self._channel_select(channel)

#Scale input amplitude to multipes of the ASF
ampscal = (asf / ((2**10) -1))
amp     = ampscal * round(amplitude/ampscal)
amp     = round(amp,5)

norm_amp = int(round((1/ampscal)*float(amp)))
amp_bin = bin(int(round(norm_amp ))).lstrip('0b')
                                                    #
                                    full range are 10 bit
if len(amp_bin) < 10:
    amp_bin = (10-len(amp_bin)) * '0' + amp_bin


# set the frequency word in the frequency register
amp_word = ''.join(' 0' + b for b in amp_bin)
amp_word = amp_word[1:]
#print(amp_word)
```

```
            #now add the 0x04 register for some random reason, can tell
                                                you need to do
            #this by looking at register 0x06 on the evaluation software
                                                'register map debug'
            r4 = 0x04
            register_bin = bin(r4).lstrip('0b')
            if len(register_bin) < 14:
                register_bin = (14-len(register_bin))*'0' + register_bin

            register_bin = ''.join(' 0' + b for b in register_bin)

            amp_word = register_bin  + ' ' + amp_word
            #print(amp_word)

            if channel_word == 0:
                self._write_to_dds_register(0x06, amp_word)
            else:
                register = channel_word - 1 + 0x0A
                self._write_to_dds_register(register, amp_word)

            # load and update I/O
            self._load_IO()
            if self.auto_update:
                self._update_IO()

    def precompute_frequency_word(self, channel, frequency):
        """Precomputes a frequency tuning word for given channel(s) and
                                                frequency.
```

```
    The current implementation of this method is repetitive and clumsy
                                                !

    :channel:  int or list
        Channel number or list of channel numbers.
    :frequency: float
        frequency to be set on channel(s)
    :returns: bytearray, bytearray
       The message to select the channels and set the frequency word,
                                                 which can both
       be sent to self._ep4

    """
    if np.issubdtype(type(channel), np.integer):
        channels = [channel]
    else:
        channels = [c for c in channel]

    # set the channels in the channel select register
    channel_select_bin = list('0000')
    for ch in channels:
        channel_select_bin[ch] = '1'
    channel_select_bin = channel_select_bin[::-1] # we have inverse
                                                  order
    channel_select_bin = ''.join(channel_select_bin)
                                                          # in the register
    # preserve the information that is stored in the CSR
    csr_old = self._read_from_register(0x00, 8)
```

```
csr_old_bin = ''.join(str(b) for b in csr_old)
csr_new_bin = channel_select_bin[:4] + csr_old_bin[4:]

csr_word = ''.join(' 0' + b for b in csr_new_bin)
csr_word = csr_word[1:]
word = csr_word

# express the register name as a binary. Maintain the format that
                                        is
# understood by endpoint 0x04. The first bit signifies read/write,
# the next 7 bits specify the register
register_bin = bin(0x00).lstrip('0b')
if len(register_bin) < 7:
    register_bin = (7-len(register_bin))*'0' + register_bin

register_bin = ''.join(' 0' + b for b in register_bin)

# construct the full message that is sent to the endpoint
message = '00' + register_bin  + ' ' + word
message_channel_select = bytearray.fromhex(message)

## Now compute the same message to select the frequency
assert frequency <= self.system_clock_frequency, ("Frequency
                                        should not"
        + " exceed system clock frequency! System clock frequency
                                                is {0}Hz".format(self
                                                .
                                                system_clock_frequency
                                                ))
```

```
# calculate the fraction of the full frequency
fraction = frequency/self.system_clock_frequency
fraction_bin = bin(round(fraction * (2**32 - 1))).lstrip('0b') #
                                        full range are 32 bit
if len(fraction_bin) < 32:
    fraction_bin = (32-len(fraction_bin)) * '0' + fraction_bin
closest_possible_value = (int(fraction_bin, base=2)/(2**32 -1) *
                            self.system_clock_frequency)
print('Frequency of channel {1} encoded as closest possible value
                                        {0}MHz'.format(
                                                closest_possible_value
```

```
# set the frequency word in the frequency register
frequency_word = ''.join(' 0' + b for b in fraction_bin)
frequency_word = frequency_word[1:]
word = frequency_word

# express the register name as a binary. Maintain the format that
                                        is
# understood by endpoint 0x04. The first bit signifies read/write,
```

```
        # the next 7 bits specify the register
        register_bin = bin(0x04).lstrip('0b') # 0x04 = frequency register
        if len(register_bin) < 7:
            register_bin = (7-len(register_bin))*'0' + register_bin

        register_bin = ''.join(' 0' + b for b in register_bin)

        # construct the full message that is sent to the endpoint
        message = '00' + register_bin  + ' ' + word
        message_frequency_word = bytearray.fromhex(message)

        return message_channel_select, message_frequency_word

    def set_precomputed_frequency(self, message_channel_select,
                                        message_frequency_word):
        """This method sets the frequency from precomputed byte-encoded
                                            words.

        The input for this method should be the ouput of self.
                                            precompute_frequency_word.
        This method only send the precomputed byte arrays to enpoint 4 of
                                            the USB handler and
        thus be faster than the self.set_frequency method.

        :message_channel_select: bytearray
            The bytearray that encodes a given channel selection.

        :message_frequency_word: bytearray
            Encodes the setting of the frequency word.
```

```
        """
        with DeviceHandle(self.dev) as dh:
            dh.bulkWrite(self._ep4, message_channel_select)
            dh.bulkWrite(self._ep4, message_frequency_word)

    def set_frequency(self, frequency, channel=None, channel_word=0):
        """Sets a new frequency for a given channel.

        :frequency: float
            The new frequency in Hz. Should not exceed `
                                                system_clock_frequency`.
        :channel: int or seq
            Channel(s) for which the frequency should be set.
        :channel_word: int
            Determines the channel_word to which the frequency is written.
                                                 Each channel has 16
            channel_words that can be used.

        """

        if channel is None:
            channel = self.channel

        assert frequency <= self.system_clock_frequency, ("Frequency
                                            should not"
                + " exceed system clock frequency! System clock frequency
                                                    is {0}Hz".format(self
                                                    .
```

```
                                                    system_clock_frequency
                                                    ))

assert channel_word < 16, ("Channel word cannot exceed 15, input
                                                was {0}".format(channel_word)
                                                )

# select the chosen channels
self._channel_select(channel)

# calculate the fraction of the full frequency
fraction = (frequency*1e6)/self.system_clock_frequency
fraction_bin = bin(int(round(fraction * (2**32 - 1)))).lstrip('0b'
                                                ) # full range are 32 bit
if len(fraction_bin) < 32:
    fraction_bin = (32-len(fraction_bin)) * '0' + fraction_bin
closest_possible_value = (int(fraction_bin, base=2)/(2**32 -1) *
                            self.system_clock_frequency)
#print('Setting frequency of channel {1}:{2} to closest possible
                                                value {0}MHz'.format(
 #
                                                 closest_possible_value/1e6,
                                                 channel, channel_word))

# set the frequency word in the frequency register
frequency_word = ''.join(' 0' + b for b in fraction_bin)
frequency_word = frequency_word[1:]
#print(frequency_word)
if channel_word == 0:
```

```
            self._write_to_dds_register(0x04, frequency_word)
        else:
            register = channel_word - 1 + 0x0A
            self._write_to_dds_register(register, frequency_word)


        # load and update I/O
        self._load_IO()
        if self.auto_update:
            self._update_IO()

    def set_phase(self, phase, channel=None):
        """Sets the phase offset for a given channel.

        :phase: float
            phase in degree, 0 < `phase` < 360
        :channels: int or list
            ID or list of IDs of the selected channels

        """
        if channel is None:
            channel = self.channel
        assert 0 <= phase <= 360,  'Phase should be between 0 and 360
                                                degree!'

        # select the channels
        self._channel_select(channel)

        # calculate the binary phase word
```

```
        phase_fraction = phase/360
        phase_fraction_bin = bin(round(phase_fraction * 2**14)).lstrip('0b
                                                '))
        if len(phase_fraction_bin) < 16:
            phase_fraction_bin = (16 - len(phase_fraction_bin)) * '0' +
                                                    phase_fraction_bin

        # construct the message for cypress chip
        phase_fraction_word = ''.join(' 0' + b for b in phase_fraction_bin
                                                ))
        phase_fraction_word = phase_fraction_word[1:]

        # write the phase word to the register
        self._write_to_dds_register(0x05, phase_fraction_word)

        # update I/O
        self._load_IO()
        if self.auto_update:
            self._update_IO()

    def toggle_autoclear_phase_accumulations(self):
        """Switches the autoclear phase accumulation bit on and off.

        """
        # load the current channel function register setting
        cfr = self._read_from_register(0x03, 24)
        print(cfr)

        # set the autoclear phase accumulator bit to 1 if old value was 0
```

```
                                                and
        # vice versa
        cfr[21] = (cfr[21] + 1) % 2
        print(cfr)

        # construct the command for the cypress chip
        cfr_new_bin = ''.join(' 0'+str(b) for b in cfr)
        cfr_new_bin = cfr_new_bin[1:]
        print(cfr_new_bin)

        # write new values to register
        self._write_to_dds_register(0x03, cfr_new_bin)

        # update I/O
        self._load_IO()
        if self.auto_update:
            self._update_IO()

    def _enable_channel_modulation(self, channel=None, modulation_type='
                                            frequency', disable=False):
        """Enables frequency modulation for selected channel(s).
        :channel: int or list
            channel ID or list of channel IDs that are selected
        :modulation_type: str
            can be 'frequency', 'phase' or 'amplitude'. Only frequency is
                                                    implemented so far.
        :disable: bool
            when True, modulation for this channel(s) is disabled.
```

```
    """
    if channel is None:
        channel = self.channel
    if np.issubdtype(type(channel), np.integer):
        channel = [channel]

    # we need to iterate over all channels, as the channel's
                                            individual function registers
    # might have different content
    for ch in channel:
        self._channel_select(ch)

        # the modulation type of the channel is encoded in register
                                                0x03[23:22].
        # 00 disables modulation, 10 is frequency modulation.
        if not disable:
            if modulation_type == 'frequency':
                modulation_type_bin = '10'
        else:
            modulation_type_bin = '00'

        # 1. read the old CFR content
        cfr_old = self._read_from_register(0x03, 24)
        cfr_old_bin = ''.join(str(b) for b in cfr_old)

        # 2. replace the modulation type
        cfr_new_bin = modulation_type_bin + cfr_old_bin[2:]

        cfr_word_new = ''.join(' 0' + b for b in cfr_new_bin)
```

```
        cfr_word_new = cfr_word_new[1:]

        self._write_to_dds_register(0x03, cfr_word_new)

        self._load_IO()
        if self.auto_update:
            self._update_IO()

def enable_modulation(self, level=2, active_channels=None,
                                    modulation_type='frequency'):
    """This method chooses the modulation level and type.

    :level: int
        Can be either 2, 4 or 16. The level determines the number of
                                            registers from
        which active channels can choose.
    :active_channels: int or list
        In 4- and 16-level modulation this determines which channels
                                            can be modulated.
        Note that as there is only a 4 bit input (P0-P3), in 4-level
                                            modulation only 2
                                            channels
        can be modulated, in 16-level modulation only one.
    :modulation_type: str
        'frequency', 'amplitude' or 'phase'

    """
    if active_channels is None:
        active_channels = self.channel
```

```
if np.issubdtype(type(active_channels), np.integer):
    active_channels = [active_channels]
active_channels.sort()

# 1. get the current content of (global) function register 1
fr_old = self._read_from_register(0x01, 24)
fr_old_bin = ''.join(str(b) for b in fr_old)

# 2. set the modulation level
level_bin = '00'
if level == 4:
    level_bin = '01'
elif level == 16:
    level_bin = '11'
# 3. replace the old level
fr_new_level = fr_old_bin[:14] + level_bin + fr_old_bin[16:]

# 3.1 if the level is 4 or 16, also the PPC bits need to be
                                        updated
if level != 2:
    # mappings are taken from the manual of the AD9959
    if level == 4:
        configurations = [[0,1], [0,2], [0,3], [1,2], [1,3], [2,3]
                                                ]
        ppcs_combinations = [bin(i)[2:] for i in range(6)]

    elif level == 16:
        configurations = [[i] for i in range(4)]
        ppcs_combinations = [bin(i)[2:] for i in range(4)]
```

```
            i = configurations.index(active_channels)
            PPC_bin = ppcs_combinations[i]
            if len(PPC_bin) < 3:
                PPC_bin = '0' * (3 - len(PPC_bin)) + PPC_bin

            # update PPC word
            fr_new_level = fr_new_level[:9] + PPC_bin + fr_new_level[12:]

        # write the new FR1 word to the register
        fr_new_word = ''.join(' 0' + b for b in fr_new_level)
        fr_new_word = fr_new_word[1:]
        #return fr_new_word, fr_new_level

        self._write_to_dds_register(0x01, fr_new_word)

        self._load_IO()
        if self.auto_update:
            self._update_IO()

        # we also make sure that the active channels are in correct
                                                modulation mode
        for ch in active_channels:
            self._enable_channel_modulation(channel=ch, modulation_type=
                                                    modulation_type)

    def _enable_channel_linear_sweep(self, channels=None, disable=False):
        """TODO: Docstring for _enable_channel_linear_sweep.
```

```
    :channel: int or list
        channel ID or list of channel IDs that are selected
    :disable: bool
        when True, modulation for this channel(s) is disabled.

    """
    if channels is None:
        channels = self.channel
    if np.issubdtype(type(channels), np.integer):
        channels = [channels]

    # the modulation type of the channel is encoded in CFR 0x03[14].
    # 0 disables linear sweep, 1 enables
    if not disable:
        ls_enable_bin = '1'
    else:
        ls_enable_bin = '0'

    # we need to iterate over all channels, as the channel's
                                            individual function registers
    # might have different content
    for ch in channels:
        self._channel_select(ch)

        # 1. read the old CFR content
        cfr_old = self._read_from_register(0x03, 24)
        cfr_old_bin = ''.join(str(b) for b in cfr_old)

        # 2. replace the CFR by one with updated LS enable bit
```

```
            cfr_new_bin = cfr_old_bin[:9] + ls_enable_bin + cfr_old_bin[10
                                                    :]

            cfr_word_new = ''.join(' 0' + b for b in cfr_new_bin) #
                                                    translate to bytes
            cfr_word_new = cfr_word_new[1:] # crop the first white space

            self._write_to_dds_register(0x03, cfr_word_new)

            self._load_IO()
            if self.auto_update:
                self._update_IO()

            # print summary message
            mes = ['Disabled', 'Enabled'][int(ls_enable_bin)]
            mes += ' linear sweep for channel {0}.'.format(ch)
            print(mes)
            print(cfr_old_bin, len(cfr_old_bin))
            print(cfr_new_bin, len(cfr_new_bin))

        return

    def configure_linear_sweep(self, channels=None, rsrr=0, fsrr=0, rdw=0,
                                            fdw=0, disable=False):
        """Configure the linear frequency sweep parameters for selected
                                                channels.

        The linear sweep ramp rate (lsrr) specifies the timestep of the
                                                rising ramp, falling sweep
```

```
                                        ramp rate
(fsrr) works accordingly.
Rising delta word specifies the rising frequency stepsize, falling
                                        delta works respectively.

:channels: int or list
    Channel ID(s) for channels to configure.
:lsrr: float
    Timestep (in seconds) of the rising sweep. Can be 1-256 times
                                        the inverse SYNC_CLK
                                        frequency.
    SYNC_CLK frequency is the SYSCLK divided by 4.
:fsrr: float
    Same as :lsrr:
:rdw: float
    Frequency step (in Hertz) of the rising sweep. Can be chosen
                                        similar to the channel
                                        frequency.
:fdw: float
    Same as :rdw:
:disable: bool
    If True, disable linear sweep for selected channels.
:returns: TODO

"""
if channels is None:
    channels = self.channel
if np.issubdtype(type(channels), np.integer):
    channels = [channels]
```

```
channels.sort()

# If desired, disable selected channels and return.
self._enable_channel_linear_sweep(channels, disable=disable)
if disable:
    return

# All linear sweep properties are in individual channel registers,
                                        so we
# can write all channels in one go
self._channel_select(channels)

########################################################
# 1. Set the new falling and rising sweep ramp rate
ramp_rate_word = ''
rr_name = ['Falling', 'Rising']
for i, rr in enumerate([fsrr, rsrr]):
    # 1.1 Compute RR word in binary
    rr_time_step = 4/self.system_clock_frequency
    fraction_bin = round(rr/rr_time_step)

    # 1.2 Check for correct bounds
    if fraction_bin < 1:
        print('Ramp rate below lower limit, choosing lowest
                                                possible value.')
        fraction_bin = 1
    elif fraction_bin > 256:
        print('Ramp rate above upper limit, choosing highest
                                                possible value.')
```

```
            fraction_bin = 256

        # align the fraction_bin with binary representation
        print('Setting {0} sweep ramp rate to {1:1.3e} s'.format(
                                                rr_name[i], fraction_bin*
                                                rr_time_step))
        fraction_bin -= 1
        rrw_bin = bin(fraction_bin)[2:]
        if len(rrw_bin) < 8:
            rrw_bin = (8-len(rrw_bin))*'0' + rrw_bin
        ramp_rate_word += rrw_bin
        print('Len RRW', len(ramp_rate_word))

    # write the new ramp rate word to the RR register
    ramp_rate_word = ''.join(' 0' + b for b in ramp_rate_word)
    ramp_rate_word = ramp_rate_word[1:]
    print('RRW: {0}'.format(ramp_rate_word), len(ramp_rate_word))
    self._write_to_dds_register(0x07, ramp_rate_word)
    print(self._read_from_register(0x07, 16))

    ################################################
    # 2. Set the falling and rising delta words.
    # calculate the fraction of the full frequency
    delta_word_registers = [0x09, 0x08]
    delta_words = [fdw, rdw]
    for i, dw in enumerate(delta_words):
        fraction = dw/self.system_clock_frequency
        fraction_bin = bin(int(round(fraction * (2**32 - 1)))).lstrip(
                                                '0b') # full range are 32
```

```
                                        bit
if len(fraction_bin) < 32:
    fraction_bin = (32-len(fraction_bin)) * '0' + fraction_bin
closest_possible_value = (int(fraction_bin, base=2)/(2**32 -1)
                                        *
                            self.system_clock_frequency)
print('Setting {2} delta word of channel {1} to closest
                                    possible value {0}MHz'.
                                    format(
                                              closest_possible_value
```

```
# set the frequency word in the frequency register
frequency_word = ''.join(' 0' + b for b in fraction_bin)
frequency_word = frequency_word[1:]
self._write_to_dds_register(delta_word_registers[i],
```

```
                                                    frequency_word)
            print(frequency_word)
            print(self._read_from_register(delta_word_registers[i], 32))
        return

class AD9959dev_0(AD9959_0):
    def __init__(self, experiment, *args, **kwargs):
        super(AD9959dev_0, self).__init__(*args, **kwargs)
        self.default_frequency = 80
        self.default_amp = 0.56

    def __set__(self, obj, value):
        """This sets the frequency of the channels. The method is needed
                                                to
        ensure compatibility with our experimental control.
        """
        self.set_frequency(value)
        #self.set_ampltude()

    def __get__(self, obj, value):
        """.
        """

        return self.default_frequency
        #return self.default_amp
```

E.2 Experimental Parameters (Dictionary)

Here, the experimental parameters are all kept in one file with a '.npy' extension. Then a single code loads the dictionary file using the

```
ExpParams = np.load('ExpParameterList.npy').item()
```

Where a specific parameter is defined by the following example:

```
expose_t = ExpParams['expose_t']
```

Below is the dictionary file used for booking. In this way, every code calls upon the same values and common mistakes are avoided.

```
# -*- coding: utf-8 -*-
"""
Stores a list of experimental parameters to be accessed by python
-5.6
This is for global variables. I included exposure times, etc also so that
things are consistent script to script.

@author: JBD
"""
import os
import numpy as np
#List of experimental parameters and constants
# c - carrer (ip)
# s - stretch (op)
# ---------------------------------- #
```

```
#           Important stuff           #
# ---------------------------------- #
Vec_s    = 59.95#60.8#58.7 #77.9#Labivew Vec setting to work at
Vec_ls   = 20  #Vec low voltage setting for recrystallization
Vrf      = -3.2#-3.2
rf_l     = -4.15 #where to recrystallize
D3       = 30
Vec_o    = 2.75 #0.95 # offset axial compensation voltage
D1       = 44 #62
D2_l     = 93   #62 for RF -4.2 and Vec = 20 V
D2_h     = 84   #At what Vec we take scans, 68 for 60 V, 71 for 80V
Vec_p    = 10 #push voltage to one side
# CW raman carrier
rsc_carrier_ax = -8.28#-8.36#-8.618
rsc_carrier_rad = -8.28#-8.4218
eit_cool_t = 10e-3
# FOR settings
for_ax_c_freq       = -8.659#-23.852#-23.622#-23.877#-23.665 #675
for_ax_c_pi_pulse_t = 3.4e-6 #3.4e-6

for_rad_c_freq      = -8.769
for_rad_c_pi_pulse_t = 15e-6
# ---- Second Ion Mass --- #
m2 = 44*1.66053904e-27
# ---- ---------------- --- #
# ------ pulse-picker ------------
tsunami_reprate = 80.846e6#80.9422e6#80.81824e6 #1.7987
pp_dial = 47
pp_numb_pulses = 100
```

```
pp_t = (pp_numb_pulses-1)/(tsunami_reprate/pp_dial)
# ---------------------------------- #
# ---------------------------------- #
# -------- General Constants ------------
hbar = 1.0545718e-34
mBa = 138*1.66053904e-27
e  = 1.602176565e-19
e0 = 8.8541878128e-12
kb = 1.380649e-23
q = 1*e
z0  = 0.00095
r0  = 0.000457
# ----------Trap Parameters continued ------------------
kap_ip = 0.187 #0.186 #error is 0.002 0.1885#0.1871
kap_op = 0.189#0.1863#0.18869#0.19 #0.193
kap = kap_op
Vec_is = (Vec_s + Vec_ls)/2 #intermdiate voltage setting
Vec = 0.96145*Vec_s + 0.09483 #0.96195476*Vec_s - 0.02742857
rf_h = Vrf
Vrfx = 219.8*Vrf + 1112  #221.07*Vrf + 1112
Vrfy = 218.25*Vrf + 1133 #added 7 v here to match current values
wrf = 2*np.pi*23306600
k   = 2*np.pi/(493.545e-9)
kz  = np.sqrt(2)*2*np.pi/(493.545e-9)
kz2 = np.pi*np.sqrt(2)/(385e-9)
omegaz  = np.sqrt(2*e*kap*Vec/mBa/z0**2)
# radial
wpx  = e*Vrfx/np.sqrt(2)/wrf/mBa/r0**2
epx = wpx/omegaz
```

```
wpy = e*Vrfy/np.sqrt(2)/wrf/mBa/r0**2
epy = wpy/omegaz
u0   = (e*2*kap*Vec)/(z0**2)
u0ip = (e*2*kap_ip*Vec)/(z0**2)
u0op = (e*2*kap_op*Vec)/(z0**2)
Z0 = 2*((e**2 / (16*np.pi*e0*u0))**(1/3))
ax = (4*q/mBa/wrf**2)*(-kap*Vec/z0**2)
ay = ax
qx = 2*q*Vrfx/mBa/r0**2 /wrf**2
qy = 2*q*Vrfy/mBa/r0**2 /wrf**2
#--
omegax = wrf/2 * np.sqrt(ax + qx**2 /2)
omegay = wrf/2 * np.sqrt(ay + qy**2 /2)
#omegax = 2*np.pi*1.027*1e6
#omegay = 2*np.pi*1.1043*1e6
#--
#Doppler cooling results
Gamma = 2*np.pi*22.1*1e6
Td = hbar*Gamma/(2*kb) #doppler cooling temperature
FOR_detuning = 57.437e6 #for 493.571 mode
# ------------------------------ #
print('Endcap voltage = ' + str(Vec))
print('The ion to ion spacing is ' + str(np.round(Z0*1e6,2)) + ' um')
print('Epsilon is ' + str(np.round(epx,3)))
print('Single Ba+ Axial Frequency is: ' + str(np.round(omegaz/2/np.pi/1e6,
                                        4)) + ' MHz')
print('Single Ba+ Axial RSB at : ' + str(np.round(for_ax_c_freq-omegaz/2/
                                        np.pi/1e6,3)) + ' MHz')
print('Single Ba+ Axial BSB at : ' + str(np.round(for_ax_c_freq+omegaz/2/
```

```
                                        np.pi/1e6,3)) + ' MHz')
print('Single Ba+ Radial-x RSB at : ' + str(np.round(for_rad_c_freq-omegax
                                        /2/np.pi/1e6,3)) + ' MHz')
print('Single Ba+ Radial-x BSB at : ' + str(np.round(for_rad_c_freq+omegax
                                        /2/np.pi/1e6,3)) + ' MHz')
print('Single Ba+ Radial-y RSB at : ' + str(np.round(for_rad_c_freq-omegay
                                        /2/np.pi/1e6,3)) + ' MHz')
print('Single Ba+ Radial-y BSB at : ' + str(np.round(for_rad_c_freq+omegay
                                        /2/np.pi/1e6,3)) + ' MHz')
print('----')
print('Axial Frequency is ' + str(np.round(omegaz/2/np.pi/1e6,3)) + ' MHz'
                                        )
print('Radial-x Frequency is ' + str(np.round(omegax/2/np.pi/1e6,3)) + '
                                        MHz')
print('Radial-y Frequency is ' + str(np.round(omegay/2/np.pi/1e6,3)) + '
                                        MHz')
print('----')

# --- Single Ion Lamb-Dicke parameter -----
# --- Axial ----
etaSqz = (hbar*kz**2/2/mBa)/omegaz
etaz = np.sqrt(etaSqz)
#etaz = 0.15
for_ax_sb_pi_pulse_t = for_ax_c_pi_pulse_t/(etaz)
print('Single Ba+ Axial Lamb-Dicke Parameter is ' + str(np.round(etaz,3)))
# --- Radial ---
kx = 0.679  #0.637 #found after measuring eta
ky = 0.182 #0.297# #found after measuring eta
etaSqx = (hbar*(2*kx*k)**2/2/mBa)/omegax
```

```
etaSqy = (hbar*(2*ky*k)**2/2/mBa)/omegay
etax   = np.sqrt(etaSqx)
etay   = np.sqrt(etaSqy)
#etax = 0.103
#etay = 0.0447
print('Single Ba+ Radial-x Lamb-Dicke Parameter is ' + str(np.round(etax,4
                                    )))
print('Single Ba+ Radial-y Lamb-Dicke Parameter is ' + str(np.round(etay,4
                                    )))
for_radx_sb_pi_pulse_t = for_rad_c_pi_pulse_t/etax
for_rady_sb_pi_pulse_t = for_rad_c_pi_pulse_t/etay
print('Single Ba+ Radial-x pi time is ' + str(np.round(
                                    for_radx_sb_pi_pulse_t*1e6,3)) + ' us
                                    ')
print('Single Ba+ Radial-y pi time is ' + str(np.round(
                                    for_rady_sb_pi_pulse_t*1e6,3)) + ' us
                                    ')


# ------------ TWO IONS ------------------------
print ('------')
print('Two Ion Frequencies:')
mu = m2/mBa
omegaz_c = np.sqrt(((u0ip/mBa)*(1+(1/mu)-np.sqrt(1-(1/mu)+(1/mu**2)))))/2/
                                    np.pi/1e6
omegaz_s = np.sqrt(((u0op/mBa)*(1+(1/mu)+np.sqrt(1-(1/mu)+(1/mu**2)))))/2/
                                    np.pi/1e6
print('IP omegaz: ' + str(np.round(omegaz_c,4)) + ' MHz')
print('OP omegaz: ' + str(np.round(omegaz_s,6))  + ' MHz')
ax = np.sqrt((epx**4)*(mu**2 -1)**2 -2*(epx**2)*((mu-1)**2)*mu*(1+mu)+(mu
```

```
                                        **2)*(1+(mu-1)*mu))
ay = np.sqrt((epy**4)*(mu**2 -1)**2 -2*(epy**2)*((mu-1)**2)*mu*(1+mu)+(mu
                                        **2)*(1+(mu-1)*mu))
b1x = (mu - mu**2 + (epx**2 * (mu**2-1)) + ax)/(2*ax) #eigenamplitude for
                                        stretch mode, x-direction for Ba+
b1y = (mu - mu**2 + (epy**2 * (mu**2-1)) + ay)/(2*ay) #eigenamplitude for
                                        stretch mode, y-direction for Ba+
b2x = 1-b1x #eigenamplitude for COM mode, x - direction for SiO
b2y = 1-b1y #eigenamplitude for COM mode, y- direction for SiO
b11z = (1- mu + np.sqrt(1-mu+mu**2))/(2*np.sqrt(1-mu+mu**2))
b21z = 1 - b11z
b12z = b21z/np.sqrt(mu)
b22z = b11z/np.sqrt(mu)

print('---------')
print(b1x)
print(b1y)
print(b2x)
print(b2y)
print('---------')

#omegax_ip = np.sqrt(-u0/mBa * (mu+mu**2 - ep**2*(1+mu**2)-a)/(2*mu**2))/2
                                        /np.pi
omegax1 = np.sqrt(-(mu+mu**2 - (1+mu**2)*epx**2 - ax)/(2*mu**2))*omegaz/2/
                                        np.pi/1e6
omegax2 = np.sqrt(-(mu+mu**2 - (1+mu**2)*epx**2 + ax)/(2*mu**2))*omegaz/2/
                                        np.pi/1e6
omegay1 = np.sqrt(-(mu+mu**2 - (1+mu**2)*epy**2 - ay)/(2*mu**2))*omegaz/2/
                                        np.pi/1e6
```

```
omegay2 = np.sqrt(-(mu+mu**2 - (1+mu**2)*epy**2 + ay)/(2*mu**2))*omegaz/2/
                                        np.pi/1e6
print('Omegax Mode 1: ' + str(np.round(omegax1,4)) + ' MHz')
print('Omegax Mode 2: ' + str(np.round(omegax2,4))  + ' MHz')
print('Omegay Mode 1: ' + str(np.round(omegay1,4)) + ' MHz')
print('Omegay Mode 2: ' + str(np.round(omegay2,4))  + ' MHz')

# roughly .... need to get these amplitudes better
eta_mBa_x1 = np.sqrt(b1x)*np.sqrt((hbar*((2*kx*k)**2)/2/mBa)/(omegax1*2*np
                                        .pi*1e6)) #x1 - Ba high freq mode
eta_mBa_x2 = np.sqrt(b2x)*np.sqrt((hbar*((2*kx*k)**2)/2/mBa)/(omegax2*2*np
                                        .pi*1e6)) #x2 - Ba low freq mode
eta_mBa_y1 = np.sqrt(b1x)*np.sqrt((hbar*((2*ky*k)**2)/2/mBa)/(omegay1*2*np
                                        .pi*1e6)) #y1 - m2 high freq mode
eta_mBa_y2 = np.sqrt(b2y)*np.sqrt((hbar*((2*ky*k)**2)/2/mBa)/(omegay2*2*np
                                        .pi*1e6)) #y2 - m2 low frequency mode

eta_m2_x1 = np.sqrt(b2x/np.sqrt(mu))*np.sqrt((hbar*((2*kx*kz2)**2)/2/m2)/(
                                        omegax1*2*np.pi*1e6)) #x1 - Ba high
                                        freq mode
eta_m2_x2 = np.sqrt(b1x/np.sqrt(mu))*np.sqrt((hbar*((2*kx*kz2)**2)/2/m2)/(
                                        omegax2*2*np.pi*1e6)) #x2 - Ba low
                                        freq mode
eta_m2_y1 = np.sqrt(b2x/np.sqrt(mu))*np.sqrt((hbar*((2*ky*kz2)**2)/2/m2)/(
                                        omegay1*2*np.pi*1e6)) #y1 - m2 high
                                        freq mode
eta_m2_y2 = np.sqrt(b1y/np.sqrt(mu))*np.sqrt((hbar*((2*ky*kz2)**2)/2/m2)/(
                                        omegay2*2*np.pi*1e6)) #y2 - m2 low
                                        frequency mode
```

```
print('----')
print('--m1 radial eta:-')
print(eta_mBa_x1)
print(eta_mBa_x2)
print(eta_mBa_y1)
print(eta_mBa_y2)
print('----')
print('----')
print('--m2 radial eta:-')
print(eta_m2_x1)
print(eta_m2_x2)
print(eta_m2_y1)
print(eta_m2_y2)
print('----')

for_rad_x1_sb_pi_pulse_t = for_rad_c_pi_pulse_t/eta_mBa_x1
for_rad_x2_sb_pi_pulse_t = for_rad_c_pi_pulse_t/eta_mBa_x2
for_rad_y1_sb_pi_pulse_t = for_rad_c_pi_pulse_t/eta_mBa_y1
for_rad_y2_sb_pi_pulse_t = for_rad_c_pi_pulse_t/eta_mBa_y2
print('Rad-x1 pi time: ' + str(np.round(for_rad_x1_sb_pi_pulse_t*1e6,2)) +
                                    ' us ')
print('Rad-x2 pi time: ' + str(np.round(for_rad_x2_sb_pi_pulse_t*1e6,2)) +
                                    ' us ')
print('Rad-y1 pi time: ' + str(np.round(for_rad_y1_sb_pi_pulse_t*1e6,2)) +
                                    ' us ')
print('Rad-x1 pi time: ' + str(np.round(for_rad_y2_sb_pi_pulse_t*1e6,2)) +
                                    ' us ')
```

```
# axial eigenmplitudes
Ap = (1/(1+((1-(1/mu)-np.sqrt(1-(1/mu)+(1/mu**2)))**2) * mu))**(1/2)
Am = (1/(1+((1-(1/mu)+np.sqrt(1-(1/mu)+(1/mu**2)))**2) * mu))**(1/2)
Bp = (1-(1/mu)-np.sqrt(1-(1/mu)+(1/mu**2)))*np.sqrt(mu)*Ap
Bm = (1-(1/mu)+np.sqrt(1-(1/mu)+(1/mu**2)))*np.sqrt(mu)*Am


print('----')
print('Axial eigenamplitudes000')
print(Ap**2)
print(Am**2)
print(Bp**2)
print(Bm**2)
print('----')
#etaSq_c          = (Am**2)*(hbar*(kz**2)/2/mBa)/(omegaz_c*2*np.pi*1e6)
#etaSq_s          = (Ap**2)*(hbar*(kz**2)/2/mBa)/(omegaz_s*2*np.pi*1e6)
#etaSq_c_m2       = (Bm**2)*(hbar*(kz2**2)/2/m2)/(omegaz_c*2*np.pi*1e6)
#etaSq_s_m2       = (Bp**2)*(hbar*(kz2**2)/2/m2)/(omegaz_s*2*np.pi*1e6)
etaSq_c          = (b11z)*(hbar*(kz**2)/2/mBa)/(omegaz_c*2*np.pi*1e6)
etaSq_s          = (b12z)*(hbar*(kz**2)/2/mBa)/(omegaz_s*2*np.pi*1e6)
etaSq_c_m2       = (b21z)*(hbar*(kz2**2)/2/m2)/(omegaz_c*2*np.pi*1e6)
etaSq_s_m2       = (b22z)*(hbar*(kz2**2)/2/m2)/(omegaz_s*2*np.pi*1e6)
#etaSq_c = (hbar*kz**2/2/mBa)/(omegaz_c*2*np.pi*1e6)
#etaSq_s = (hbar*kz**2/2/mBa)/(omegaz_s*2*np.pi*1e6)
eta_c        = np.sqrt(etaSq_c)
#eta_c = 0.125
eta_s        = np.sqrt(etaSq_s)
eta_c_m2     = np.sqrt(etaSq_c_m2)
eta_s_m2     = np.sqrt(etaSq_s_m2)
# Axial Lamb-Dicke Parameters
```

```
print('barium IP,OP then m2 IP,OP')
print(eta_c) #Ba+, IP mode
print(eta_s) #Ba+, OP mode
print(eta_c_m2) #m2, IP mode
print(eta_s_m2) #m2, OP mode
print ('----')
#Pi Times
for_ax_c_sb_pi_pulse_t = for_ax_c_pi_pulse_t/eta_c
for_ax_s_sb_pi_pulse_t = for_ax_c_pi_pulse_t/eta_s
print('Axial Single Ion Sideband pi time: ' + str(np.round(
                                    for_ax_sb_pi_pulse_t*1e6,2)) + ' us '
                                    )
print('Axial IP sideband pi time: ' + str(np.round(for_ax_c_sb_pi_pulse_t*
                                    1e6,2)) + ' us ')
print('Axial OP sideband pi time: ' + str(np.round(for_ax_s_sb_pi_pulse_t*
                                    1e6,2)) + ' us ')
#print(for_sb_pi_pulse_t)
#print(for_sb_pi_pulse_t)  #what it should be
#for_sb_pi_pulse_t = 30.2e-6#for_c_pi_pulse_t/eta # if ion appears warm

# -------------- Debye-Waller Factors --------------- #
# this is a test of the emergency Debye-Waller System #
#nb_1 = kb*Td/(hbar * omegaz)
#print('Estimated nbar of one ion in the axial direction is ' + str(np.
                                    round(nb_1,1)))

nb_x = kb*Td/(hbar * (omegax))
nb_y = kb*Td/(hbar * (omegay))
nb_z = kb*Td/(hbar * (omegaz))
```

```
print('Estimated nbar of Ba+ in the x-axis is ' + str(np.round(nb_x,3)))
print('Estimated nbar of Ba+ in the y-axis is ' + str(np.round(nb_y,1)))
print('Estimated nbar of Ba+ in the z-axis is ' + str(np.round(nb_z,1)))
nb_c = kb*Td/(hbar * (2*np.pi*1e6*omegaz_c))
nb_s = kb*Td/(hbar * (2*np.pi*1e6*omegaz_s))
nb_x1 = kb*Td/(hbar * (2*np.pi*1e6*omegax1))
nb_x2 = kb*Td/(hbar * (2*np.pi*1e6*omegax2))
print('Estimated nbar of two ions in the in-phase mode is ' + str(np.round
                                    (nb_c,1)))
print('Estimated nbar of two ions in the out-of-phase mode is ' + str(np.
                                    round(nb_s,1)))
print('Estimated nbar of two ions in the rad-x1 mode is ' + str(np.round(
                                    nb_x1,1)))
print('Estimated nbar of two ions in the rad-x2 mode is ' + str(np.round(
                                    nb_x2,1)))
##debye-waller factor on mode 1 (in-phase) with spectator mode 2 (out-of-
                                    phase) for 1st BSB on n=0 -> n=1
#dbwf_12 = eta_c*np.exp(-((eta_c**2)+(eta_s**2))/2)*(1-nb_s*eta_s**2)
#print(for_c_pi_pulse_t/dbwf_12)
#dbwf_21 = eta_s*np.exp(-((eta_s**2)+(eta_c**2))/2)*(1-nb_c*eta_c**2)
#print(for_c_pi_pulse_t/dbwf_21)
# -------------- Debye-Waller Factors --------------- #

# Places to store the dictionary #
pathscripts  = 'C:/Users/QLS/Documents/Python Scripts/STIRAP Control/'
pathtwoionscripts  = 'C:/Users/QLS/Documents/Python Scripts/STIRAP Control
                                    /twoions/'
pathanalysis = 'C:/Users/QLS/Documents/Python Scripts/Analysis/'
pathtwoionanalysis = 'C:/Users/QLS/Documents/Python Scripts/Analysis/
```

```
                                        twoions/'

omegaz = omegaz/2/np.pi/1e6
omegax = omegax/2/np.pi/1e6
omegay = omegay/2/np.pi/1e6
omegax1 = omegax1
omegax2 = omegax2
omegay1 = omegay1
omegay2 = omegay2

ExpParameters = {
            # useful constants
            'Vec' : Vec,
            'Vrf' : Vrf,
            'kappa': kap,
            'etaz' : etaz,
            'etax' : etax,
            'etay' : etay,
            'omegaz': omegaz,
            'omegaz_c': omegaz_c,
            'omegaz_s': omegaz_s,
            'omegax' : omegax,
            'omegay' : omegay,
            'omegax1': omegax1,
            'omegax2': omegax2,
            'omegay1': omegay1,
            'omegay2': omegay2,
            'FOR_detuning': FOR_detuning,
            #Trap & Laser Paramters for warm ions
```

```
'rf_low' : rf_l,
'rf_high': rf_h,
'Comp2'  : (D1 + D3)*0.025, #compensation rods labeled off of
                              labview block diagram
                            array
'Comp3_l': (D2_l+D3)*0.025,
'Comp3_h': (D2_h+D3)*0.025,
'Comp4_l': (D2_l+D1)*0.025,
'Comp4_h': (D2_h+D1)*0.025,
'Vec1_l' : (Vec_ls - Vec_o/2)*0.025, #EC 1 is dev3/ao0, EC
                                      box has 40x gain
'Vec2_l' : (Vec_ls + Vec_o/2)*0.025, #EC 2 is dev3/ao1, EC
                                      box has 40x gain
'Vec1_h' : (Vec_s - Vec_o/2)*0.025,
'Vec2_h' : (Vec_s + Vec_o/2)*0.025,
'Vec2_p' : (Vec_s + Vec_o/2 + Vec_p)*0.025,
'Vec_i'  : (Vec_is)*0.025,
#------- Lasers Parameters --------------------
'AM_493_cool': -2.2, #-0.4
'AM_493_detect': -2.2 , #-1.2
'FM_493_cool':  0.2,
'FM_493_detect': 0.2,
'AM_650_cool': -0.2,
'AM_650_detect':-0.2,
'FM_650_cool': 0.0,
'FM_650_detect': 0.0,
# ------- Raman laser powers -----------------
'for_sig_ax_pwr' : 0.5,  #DDS0 Channel 0
'for_sig_rad_pwr': 0.5,  #DDS0 Channel 1
```

```
'for_pi_ax_pwr'  : 0.35,  #DDS0 Channel 2
'for_pi_rad_pwr' : 0.5,  #DDS0 Channel 3
'nr_sig_ax1_pwr' : 0.145,  #134 DDS1 Channel 0 - OP mode
'nr_sig_ax2_pwr' : 0.118,  #DDS1 Channel 1 - IP mode
'nr_sig_rad1_pwr': 0.125,  #DDS1 Channel 2 - rad1 mode
'nr_sig_rad2_pwr': 0.128,   #DDS1 Channel 3 - rad2 mode
'nr_pi_ax_pwr'   : 0.12,     #DDS2 Channel 0
'nr_pi_rad_pwr'  : 0.3,    #DDS2 Channel 1
#Discriminators, assuming a exposure of 10 ms and recovery of
                                        10 ms
'disc': 7500,
'disch': 20000,
'disc_initial_state': 7500, # with curtain closed.
# ---------- Pulse-Picker Settings ------------
'tsunami_rep': tsunami_reprate,
'pp_dial': pp_dial,
'pp_numb_pulses': pp_numb_pulses,
'pp_t': pp_t,
#------ Script Parameters ----------------------
#------ Timings --------------------------------
'expose_t': 10e-3,
'recover_t': 10e-3,
'warm_recover_t': 20,
'safe': 1e-5,
'shutter_t': 1e-3,
'red_op_t': 2e-3,
'shelve_t': 5e-3,
'deshelve_t': 5e-3,
'op_t': 100e-6, #40 us for low 493 power
```

```
'protect_t': 6e-6,#3.45e-6,#4.5 us for low 493 power
# shutter safe times
'shut_open': 2e-3,
's_fsafe': 7.5e-3,
'shut_tog': 1e-3,
'shut_close': 3e-3,
'b_srs_fall_d': 2.5e-3, #delay from the trigger to acutal
                                    fall, 493
'b_srs_rise_d': 3e-3,
'r_srs_fall_d': 2e-3, #delay from the trigger to acutal fall,
                                     650
'r_srs_rise_d': 2.75e-3,
'shelve_srs_fall_d': 2.6e-3, #delay from the trigger to
                                    acutal fall, 650
'shelve_srs_rise_d': 2.2e-3,
'deshelve_srs_fall_d': 2.7e-3, #delay from the trigger to
                                    acutal fall, 650
'deshelve_srs_rise_d': 2.7e-3,
#------- Laser timings and Frequencies --------
#  NR
'rsc_cool_t': eit_cool_t,
'eit_cool_t': eit_cool_t,
'eit_rad_cool_t': eit_cool_t/2,
'eit_ax_cool_t': eit_cool_t/2,
'rsc_carrier_ax': rsc_carrier_ax,
'rsc_carrier_rad': rsc_carrier_rad,
#  FOR axial
'for_ax_c_freq': for_ax_c_freq,
'for_ax_rsb_freq': for_ax_c_freq-omegaz,
```

```
'for_ax_bsb_freq': for_ax_c_freq+omegaz,
'for_ax_c_pi_pulse_t': for_ax_c_pi_pulse_t,
'for_ax_sb_pi_pulse_t': for_ax_sb_pi_pulse_t,
#  FOR radial
'for_rad_c_freq': for_rad_c_freq,
'for_x_rsb_freq': for_rad_c_freq-omegax,
'for_x_bsb_freq': for_rad_c_freq+omegax,
'for_y_rsb_freq': for_rad_c_freq-omegay,
'for_y_bsb_freq': for_rad_c_freq+omegay,
'for_rad_c_pi_pulse_t': for_rad_c_pi_pulse_t,
'for_radx_sb_pi_pulse_t': for_radx_sb_pi_pulse_t,
'for_rady_sb_pi_pulse_t': for_rady_sb_pi_pulse_t,
# ------ 1.76 um settings -------
'1.7_shelve_t' : 1e-3,
'stretch_r' : 1.978,
# ------ two ions ------------
# --- COM ---
'for_c_rsb_freq': for_ax_c_freq-omegaz_c,
'for_c_bsb_freq': for_ax_c_freq+omegaz_c,
'for_c_sb_pi_pulse_t': for_ax_c_sb_pi_pulse_t,
# --- stretch ----
'for_s_rsb_freq': for_ax_c_freq-omegaz_s,
'for_s_bsb_freq': for_ax_c_freq+omegaz_s,
'for_s_sb_pi_pulse_t': for_ax_s_sb_pi_pulse_t,
# --- Radial ----
'for_x1_rsb_freq': for_rad_c_freq - omegax1,
'for_x1_bsb_freq': for_rad_c_freq + omegax1,
'for_rad_x1_sb_pi_pulse_t': for_rad_x1_sb_pi_pulse_t,
            #--
```

```
            'for_x2_rsb_freq': for_rad_c_freq - omegax2,
            'for_x2_bsb_freq': for_rad_c_freq + omegax2,
            'for_rad_x2_sb_pi_pulse_t': for_rad_x2_sb_pi_pulse_t,
                        #--
            'for_y1_rsb_freq': for_rad_c_freq - omegay1,
            'for_y1_bsb_freq': for_rad_c_freq + omegay1,
            'for_rad_y1_sb_pi_pulse_t': for_rad_y1_sb_pi_pulse_t,
                        #--
            'for_y2_rsb_freq': for_rad_c_freq - omegay2,
            'for_y2_bsb_freq': for_rad_c_freq + omegay2,
            'for_rad_y2_sb_pi_pulse_t': for_rad_y2_sb_pi_pulse_t
            }

#print(ExpParameters['for_bsb_freq'])
#Save this right here
print('Pulse Picker Exposure time is ' + str(np.round(ExpParameters['pp_t'
                                    ],8)))
print('CW NR Pi Detuning: ' + str(np.round(ExpParameters['rsc_carrier_ax']
                                    ,2)) + ' MHz')
print('---')
print('IP RSB: ' + str(np.round(ExpParameters['for_c_rsb_freq'],4)) + '
                                    MHz' +
      '   & IP BSB: ' + str(np.round(ExpParameters['for_c_bsb_freq'],4)) +
                                            ' MHz')
print('OP RSB: ' + str(np.round(ExpParameters['for_s_rsb_freq'],4)) + '
                                    MHz' +
      ' & OP BSB: ' + str(np.round(ExpParameters['for_s_bsb_freq'],4)) + '
                                            MHz')
print('---')
```

```
print('x2 RSB: ' + str(np.round(ExpParameters['for_x2_rsb_freq'],4)) + '
                                        MHz' +
      ' & x2 RSB: ' + str(np.round(ExpParameters['for_x2_bsb_freq'],4)) +
                                                ' MHz' )
print('y2 RSB: ' + str(np.round(ExpParameters['for_y2_rsb_freq'],4)) + '
                                        MHz' +
      '  & y2 RSB: ' + str(np.round(ExpParameters['for_y2_bsb_freq'],4)) +
                                                 ' MHz' )
print('x1 RSB: ' + str(np.round(ExpParameters['for_x1_rsb_freq'],4)) + '
                                        MHz' +
      ' & x1 RSB: ' + str(np.round(ExpParameters['for_x1_bsb_freq'],4)) +
                                                ' MHz' )
print('y1 RSB: ' + str(np.round(ExpParameters['for_y1_rsb_freq'],4)) + '
                                        MHz' +
      ' & y1 RSB: ' + str(np.round(ExpParameters['for_y1_bsb_freq'],4)) +
                                                ' MHz' )
print('---')

#Save the data
filename = 'ExpParameterList'
filenamescripts = os.path.normpath(pathscripts + filename)
filenameanalysis = os.path.normpath(pathanalysis + filename)
filenametwoions = os.path.normpath(pathtwoionscripts + filename)
filenametwoionanalysis = os.path.normpath(pathtwoionanalysis + filename)



np.save(filenamescripts,ExpParameters)
np.save(filenameanalysis,ExpParameters)
np.save(filenametwoions,ExpParameters)
```

```
np.save(filenametwoionanalysis,ExpParameters)
```

E.3 Example PRR Code

This code conducts a frequency scan over a desired frequency range of the FOR Raman beam detunings.

```
# -*- coding: utf-8 -*-
"""
Created on Mon Mar 22 15:09:02 2017

v1.1 - building off of PRR_freq_v51 but now with 3D cooling, new DDS'
v2   - added rotational cooling in the beginning alongside doppler cooling
v3   - adding ion swapping procedure
v4   - removing rot. cooling in the beginning
@author: MGK/JBD
"""
from OneShot import OneShot
from evalcontrol import ad9959DDS0 as eval_board0
from evalcontrol import ad9959DDS1 as eval_board1
from evalcontrol import ad9959DDS2 as eval_board2
from TrigControl import TrigControl
import time
import numpy as np
import os
import pdb
from plotoneshots import plotOneShots
from pmt import PMT
from AIWrite import AOWrite
```

```
import sys
import psutil
#Load dictionary of Parameters
ExpParams = np.load('ExpParameterList.npy').item()
begin = time.time()
proc = psutil.Process(os.getpid())
proc.nice(psutil.REALTIME_PRIORITY_CLASS)
# ------------------- What to do? ----------------------
delay_t = 0e-3 #e-3
#     !!!!!!!!!!!!!     #
carrier = False
RSB_c = False
RSB_s = False
BSB_c = False
BSB_s = True
twosidebands_c = False
twosidebands_s = False
# cooling two sidebands ?
# How much data to take at each setting
reps = 200
break_reps = 7 #number of times to attempt RC before breaking loop
#----------------Other parameteRS ----------------------
# If this is true, then plot the ctimes sequence
plot_me = False
# The path to save the data in
path = 'c:/data/PRR/Axial/Freq/'
# ------------ Eval Board ----------------------
dds0 = eval_board0.AD9959_0() #FOR DDS
dds1 = eval_board1.AD9959_1() #NR sig DDS
```

```
dds2 = eval_board2.AD9959_2() #NR pi DDS
dds0.set_frequency(80, channel=[0,1,2,3])
dds0.set_phase(0.0, channel = [0,1,2,3])
dds1.set_frequency(80, channel=[0,1,2,3])
dds1.set_phase(0.0, channel = [0,1,2,3])
dds2.set_frequency(80, channel=[0,1,2,3])
dds2.set_phase(0.0, channel = [0,1,2,3])
#saturates at 0.5
dds0.set_amplitude(ExpParams['for_sig_ax_pwr'], channel=[0])    #FOR sig
                                        axial
dds0.set_amplitude(0.0, channel=[1])    #FOR sig radial
dds0.set_amplitude(ExpParams['for_pi_ax_pwr'], channel=[2])    #FOR pi
                                        axial
dds0.set_amplitude(0.0, channel=[3])    #FOR pi radial
# saturates at 0.3
dds1.set_amplitude(ExpParams['nr_sig_ax1_pwr'], channel=[0]) #NR sig axial
                                         1
dds1.set_amplitude(ExpParams['nr_sig_ax2_pwr'], channel=[1])    #NR sig
                                        axial 2
dds1.set_amplitude(ExpParams['nr_sig_rad1_pwr'], channel=[2]) #NR sig
                                        radial 1
dds1.set_amplitude(ExpParams['nr_sig_rad2_pwr'], channel=[3])  #NR sig
                                        radial 2
#saturates at 0.3
dds2.set_amplitude(ExpParams['nr_pi_ax_pwr'],  channel=[0])  #NR pi axial
dds2.set_amplitude(ExpParams['nr_pi_rad_pwr'], channel=[1])   #NR pi
                                        radial
dds2.set_amplitude(0.0,  channel=[2])     #unconnected
dds2.set_amplitude(0.0,  channel=[3])    #unconnected
```

```
# ------------------------------------------------
# ------------------------------------------------
# Pulse-Picker Settings #
pp_time = ExpParams['pp_t']
print('This is the total pp exposure time ' + str(pp_time*1e6) + ' us')
#Set frequencies
#Frequency and length of time to do CW Raman cooling
cool_freq_ax = ExpParams['rsc_carrier_ax']#11.3 #-13.1
cool_freq_rad = ExpParams['rsc_carrier_rad']#11.3 #-13.1
omegaz_c = ExpParams['omegaz_c']
omegaz_s = ExpParams['omegaz_s']
#print(omegaz_s)
#print(omegaz)#1.031
 #for center scan range
if carrier:
    scan = 'carrier'
    for_pi_pulse_t = ExpParams['for_ax_c_pi_pulse_t']#+0.5e-6
    #for_pi_pulse_t = 1.1e-6
    #for_pi_pulse_t = 3e-6
    for_freq = ExpParams['for_ax_c_freq']
    #for_freq = -23.858
    freq_scan_range = 0.6
    freq_c_scan_range = 0.1
    freq_step = 0.01
    #range of freuqencies
    for_frequencies1 = np.linspace(for_freq-freq_c_scan_range-freq_step-
                                   freq_scan_range,for_freq-
                                   freq_c_scan_range-freq_step,5)
    for_frequencies2 = np.linspace(for_freq-freq_c_scan_range,for_freq+
```

```
                                        freq_c_scan_range,7)
    for_frequencies3 = np.linspace(for_freq+freq_c_scan_range+freq_step,
                                        for_freq+freq_c_scan_range+
                                        freq_step+freq_scan_range,5)
    for_frequencies = np.concatenate((for_frequencies1,for_frequencies2,
                                        for_frequencies3),axis=0)
    #for_frequencies = np.linspace(for_freq,for_freq+freq_scan_range,15)
    #for_freq = -23.3
    #for_freq = -6.7
    #for_frequencies = np.linspace(for_freq,for_freq,1)
# ------------scan over rsb -------------------------------------
elif RSB_c:
    scan = 'RSB_c'
    for_pi_pulse_t = 38e-6#ExpParams['for_s_sb_pi_pulse_t']
    for_freq = ExpParams['for_ax_c_freq']
    #omegaz_c = ExpParams['omegaz_c']
    freq_scan_range = 0.02
    freq_c_scan_range = 0.02
    scan_step = 0.005
    for_frequencies1 = np.linspace(for_freq-omegaz_c-freq_c_scan_range-
                                        scan_step-freq_scan_range,
                                        for_freq-omegaz_c-
                                        freq_c_scan_range-scan_step,3)
    for_frequencies2  = np.linspace(for_freq-omegaz_c-freq_c_scan_range,
                                        for_freq-omegaz_c+
                                        freq_c_scan_range,9)
    for_frequencies3  = np.linspace(for_freq-omegaz_c+freq_c_scan_range+
                                        scan_step,for_freq-omegaz_c+
                                        freq_c_scan_range+scan_step+
```

```
                                        freq_scan_range,3)

    for_frequencies = np.concatenate((for_frequencies1,for_frequencies2,
                                        for_frequencies3),axis=0)
    #for_frequencies = np.linspace(for_freq-freq_scan_range,for_freq+
                                        freq_scan_range,1)
    #for_frequencies = np.linspace(for_freq,for_freq,1)
    # ------------scan over rsb -------------------------------------
elif RSB_s:
    scan = 'RSB_s'
    for_pi_pulse_t = 110e-6#ExpParams['for_s_sb_pi_pulse_t']
    for_freq = ExpParams['for_ax_c_freq']
    #omegaz_s = 0.723
    freq_scan_range = 0.01
    freq_c_scan_range = 0.005
    scan_step = 0.001
    for_frequencies1 = np.linspace(for_freq-omegaz_s-freq_c_scan_range-
                                        scan_step-freq_scan_range,
                                        for_freq-omegaz_s-
                                        freq_c_scan_range-scan_step,5)
    for_frequencies2  = np.linspace(for_freq-omegaz_s-freq_c_scan_range,
                                        for_freq-omegaz_s+
                                        freq_c_scan_range,7)
    for_frequencies3  = np.linspace(for_freq-omegaz_s+freq_c_scan_range+
                                        scan_step,for_freq-omegaz_s+
                                        freq_c_scan_range+scan_step+
                                        freq_scan_range,5)
```

```
    for_frequencies = np.concatenate((for_frequencies1,for_frequencies2,
                                      for_frequencies3),axis=0)

    #------ Look at BSB at end! -----
#    for_freqbsb  = ExpParams['for_s_bsb_freq']
#    for_freqbsbs = np.linspace(for_freqbsb-0.002,for_freqbsb+0.002,3)  #
                                      scan over BSB frequency so that we
                                      know the ion is still SiO+
#    for_frequencies = np.concatenate((for_frequencies1,for_frequencies2,
                                      for_frequencies3,for_freqbsbs),axis=0
                                      )
    #---------------------------------

    #for_frequencies = np.linspace(for_freq-freq_scan_range,for_freq+
                                      freq_scan_range,1)
    #for_frequencies = np.linspace(-10.35,-10.325,10) #SiO+
    #for_frequencies = np.linspace(-10.373,-10.36,10) #SiOH+
    # ------------scan over bsb ------------------------------------
elif BSB_c:
    scan = 'BSB_c'
    for_pi_pulse_t = ExpParams['for_c_sb_pi_pulse_t']
    for_freq = ExpParams['for_ax_c_freq']
    freq_scan_range = 0.03
    freq_c_scan_range = 0.03
    scan_step = 0.005
    for_frequencies1 = np.linspace(for_freq+omegaz_c-freq_c_scan_range-
                                      scan_step-freq_scan_range,
                                      for_freq+omegaz_c-
                                      freq_c_scan_range-scan_step,5)
```

```
    for_frequencies2  = np.linspace(for_freq+omegaz_c-freq_c_scan_range,
                                    for_freq+omegaz_c+
                                    freq_c_scan_range,11)
    for_frequencies3  = np.linspace(for_freq+omegaz_c+freq_c_scan_range+
                                    scan_step,for_freq+omegaz_c+
                                    freq_c_scan_range+scan_step+
                                    freq_scan_range,5)

    for_frequencies = np.concatenate((for_frequencies1,for_frequencies2,
                                    for_frequencies3),axis=0)
# ------------scan over bsb -------------------------------------
elif BSB_s:
    scan = 'BSB_s'
    for_pi_pulse_t = 120e-6#ExpParams['for_s_sb_pi_pulse_t']
    for_freq = ExpParams['for_ax_c_freq']
    freq_scan_range = 0.015
    freq_c_scan_range = 0.005
    scan_step = 0.001
    for_frequencies1 = np.linspace(for_freq+omegaz_s-freq_c_scan_range-
                                    scan_step-freq_scan_range,
                                    for_freq+omegaz_s-
                                    freq_c_scan_range-scan_step,5)
    for_frequencies2  = np.linspace(for_freq+omegaz_s-freq_c_scan_range,
                                    for_freq+omegaz_s+
                                    freq_c_scan_range,7)
    for_frequencies3  = np.linspace(for_freq+omegaz_s+freq_c_scan_range+
                                    scan_step,for_freq+omegaz_s+
                                    freq_c_scan_range+scan_step+
                                    freq_scan_range,5)
```

```
    for_frequencies = np.concatenate((for_frequencies1,for_frequencies2,
                                      for_frequencies3),axis=0)

    #for_frequencies = np.linspace(-6.914,-6.894,9)   #SiOH+
    #for_frequencies = np.linspace(-6.921,-6.901,9)  #SiO+
    #for_frequencies = np.linspace(-6.94,-6.92,7)  #SiO+
    #for_frequencies = np.linspace(-6.97,-6.95,9)  #SiOH+
    #for_frequencies = np.linspace(-6.94,-6.94,1)

# -------- C.O.M Twosideband parameters ---------------------------------
elif twosidebands_c:
    scan = 'twosidebands_c'
    for_pi_pulse_t = ExpParams['for_c_sb_pi_pulse_t']
    #for_pi_pulse_t = ExpParams['for_sb_pi_pulse_t']
    for_freq = ExpParams['for_ax_c_freq']
    #omegaz_c = 0.658
    #for_pi_pulse_t = 21.5e-6
    freq_scan_range = 0.06
    freq_c_scan_range = 0.02 #0.03
    scan_step = 0.001

    #rsb
    rsb_peak_l = for_freq-omegaz_c-freq_c_scan_range
    rsb_peak_r = for_freq-omegaz_c+freq_c_scan_range
    bsb_peak_l = for_freq+omegaz_c-freq_c_scan_range
    bsb_peak_r = for_freq+omegaz_c+freq_c_scan_range
    #rsb
    rsb_l_bg = np.linspace(rsb_peak_l-scan_step-freq_scan_range,rsb_peak_l
```

```
                                        -scan_step,5)
    rsb_peak  = np.linspace(rsb_peak_l,rsb_peak_r,9)#13
    rsb_r_bg = np.linspace(rsb_peak_r+scan_step,rsb_peak_r+scan_step+
                                        freq_scan_range,5)
    #bsb
    bsb_l_bg = np.linspace(bsb_peak_l-scan_step-freq_scan_range,bsb_peak_l
                                        -scan_step,5)
    bsb_peak  = np.linspace(bsb_peak_l,bsb_peak_r,9)
    bsb_r_bg = np.linspace(bsb_peak_r+scan_step,bsb_peak_r+scan_step+
                                        freq_scan_range,5)

    for_frequencies = np.concatenate((rsb_l_bg,rsb_peak,rsb_r_bg,bsb_l_bg,
                                        bsb_peak,bsb_r_bg),axis=0)
    #for_frequencies = np.linspace(-23.02835,-23.02835,1)
# -------- Stretch Twosideband parameters
                                    ----------------------------------
elif twosidebands_s:
    scan = 'twosidebands_s'
    for_pi_pulse_t = 110e-6#ExpParams['for_s_sb_pi_pulse_t']
    #for_pi_pulse_t = ExpParams['for_sb_pi_pulse_t']
    for_freq = ExpParams['for_ax_c_freq']

    freq_scan_range = 0.01#0.024
    freq_c_scan_range = 0.007#0.01
    scan_step = 0.001

    #rsb
    rsb_peak_l = for_freq-omegaz_s-freq_c_scan_range
    rsb_peak_r = for_freq-omegaz_s+freq_c_scan_range
```

```
    bsb_peak_l = for_freq+omegaz_s-freq_c_scan_range
    bsb_peak_r = for_freq+omegaz_s+freq_c_scan_range
    #rsb
    rsb_l_bg = np.linspace(rsb_peak_l-scan_step-freq_scan_range,rsb_peak_l
                                        -scan_step,11)
    rsb_peak  = np.linspace(rsb_peak_l,rsb_peak_r,15)
    rsb_r_bg = np.linspace(rsb_peak_r+scan_step,rsb_peak_r+scan_step+
                                        freq_scan_range,11)
    #bsb
    bsb_l_bg = np.linspace(bsb_peak_l-scan_step-freq_scan_range,bsb_peak_l
                                        -scan_step,11)
    bsb_peak  = np.linspace(bsb_peak_l,bsb_peak_r,15)
    bsb_r_bg = np.linspace(bsb_peak_r+scan_step,bsb_peak_r+scan_step+
                                        freq_scan_range,11)

    for_frequencies = np.concatenate((rsb_l_bg,rsb_peak,rsb_r_bg,bsb_l_bg,
                                        bsb_peak,bsb_r_bg),axis=0)
    #for_frequencies = np.linspace(-6.9717,-6.9717,1)
    #for_frequencies = np.linspace(-6.73,-6.715,3)

# -------- Continue ----------------------------------

#check that we did things right
#print(for_freq)
print(scan)
print('FOR scan frequencies: ' + str(for_frequencies))
for_frequencies = np.random.permutation(for_frequencies)
# ---- take one point on the BSB to find it each scan
if RSB_s:
```

```
    bsbp = ExpParams['for_s_bsb_freq']
    bsbpar = np.linspace(bsbp,bsbp,1)
    for_frequencies = np.concatenate((for_frequencies,bsbpar),axis=0)
else:
    for_frequencies = for_frequencies

print('Delay time is set to be ' + str(delay_t*1e3) + ' ms')
print('FOR pi pulse time used: ' + str(np.round(for_pi_pulse_t*1e6,2)) + '
                                    us')

# ----------------       RSC            -------------------------------
#Frequency and length of time to do CW Raman cooling
Thcool_freq_ax = ExpParams['rsc_carrier_ax']#11.3 #-13.1
cool_freq_rad = ExpParams['rsc_carrier_rad']#11.3 #-13.1
eit_cool_t = ExpParams['eit_cool_t']
eit_ax_cool_t = ExpParams['eit_ax_cool_t'] #half total cool time
eit_rad_cool_t = ExpParams['eit_rad_cool_t']
print('NR Raman Beams ax detuning set to : ' + str(np.round(cool_freq_ax,3
                                    )) + ' MHz')
print('NR Raman Beams rad detuning set to : ' + str(np.round(cool_freq_rad
                                    ,3)) + ' MHz')
print('EIT cool time set to : ' + str(np.round(eit_cool_t*1e3,2)) + ' ms')
# --------------- Expose time of camera and PMT -------------------
expose_t = ExpParams['expose_t']
# Recovery time between cycles to allow ion to Doppler cool
recover_t = ExpParams['recover_t']
# ---------------- Doppler Settings -------------------------------
# Change the Doppler cooling settings for ion detection after shelving.
                                    This
```

```
# sets up the AO task.  It has to be defined as a single task to share the
# on-board clock.  AO1 = b_FM, AO4 = b_AM, AO5 = r_FM.
trigchan2_camera = b'/dev2/PFI7'
b_detect_FM_v = ExpParams['FM_493_detect']
b_cool_FM_v = ExpParams['FM_493_cool']
b_FM_voltages = np.array([b_detect_FM_v,b_cool_FM_v],dtype=np.float64)
b_detect_AM_v = ExpParams['AM_493_detect']
b_cool_AM_v = ExpParams['AM_493_cool']
b_AM_voltages = np.array([b_detect_AM_v,b_cool_AM_v],dtype=np.float64)
r_detect_AM_v = ExpParams['AM_650_detect']
r_cool_AM_v = ExpParams['AM_650_cool']
r_AM_voltages = np.array([r_detect_AM_v,r_cool_AM_v],dtype=np.float64)
# PRR Info
print('Number of PRR pulses used ' + str(ExpParams['pp_numb_pulses']))
print('PRR Exposure time set to ' + str(np.round(ExpParams['pp_t']*1e6,3))
                                        + ' us')
AO_detect_voltages = np.concatenate((b_FM_voltages,b_AM_voltages,
                                     r_AM_voltages))
AO_detect_control = AOWrite(b"/dev2/ao1,/dev2/ao4:5")
AO_detect_control.setTrig(1/expose_t,2,trigchan2_camera)
AO_detect_control.voltSequence(3,AO_detect_voltages)


#PMT info
pmtc = b'/dev1/ctr7'
pmt = PMT(pmtc)
pmtc_condition = b'/dev6/ctr7'
pmt_condition = PMT(pmtc_condition)


#Trigger info
```

```
trigchan1 = b'/dev1/PFI14'
trigchan2 = b'/dev2/PFI6'
trigchan5 = b'/dev5/PFI13'
trigchan6 = b'/dev6/PFI14'
trigchan7 = b'/dev7/PFI14'
trigsource = b'/dev5/port0/line0'

# ---------------- Recrystallization Setup ---------------
# triggers
warmtrigsource = b'/dev5/port0/line1'
warmtrig = TrigControl(warmtrigsource)
warmtrigchan5 = b'/dev5/PFI33'
warmtrigchan1 = b'/dev1/PFI37'
warmtrigchan6 = b'/dev6/PFI37'
warm_recover_t = ExpParams['warm_recover_t']
# trap settings
rf_v = AOWrite(b'/dev3/ao2')
rf_l = ExpParams['rf_low']
rf_h = ExpParams['rf_high']
Vec1_v = AOWrite(b'dev3/ao0')
Vec2_v = AOWrite(b'dev3/ao1')
Vec1_l = ExpParams['Vec1_l']
Vec2_l = ExpParams['Vec2_l']
Vec1_h = ExpParams['Vec1_h']
Vec2_h = ExpParams['Vec2_h']
Vec2_p = ExpParams['Vec2_p']
Vec_i = ExpParams['Vec_i']
Comp2 = ExpParams['Comp2']
Comp3_l = ExpParams['Comp3_l'] #Need to change D2 when ReCry
```

```
Comp3_h = ExpParams['Comp3_h']
Comp4_l = ExpParams['Comp4_l']
Comp4_h = ExpParams['Comp4_h']
Comp2_v = AOWrite(b'dev3/ao3') #D1 + D3
Comp3_v = AOWrite(b'dev3/ao4') #D2 + D3
Comp4_v = AOWrite(b'dev3/ao5') #D1 + D2
# ------------------------------------------------------------
#Start Timings
# A 'safe interval', which is a period added in to various places to
                                        ensure
# the light has actually turned off, or on.
safe = ExpParams['safe']
# The amount of time to allow for the mechanical shutter to close or open
shutter_t = ExpParams['shutter_t']
# amount to time to pump out of D3/2 at start
red_op_t = ExpParams['red_op_t']
# The amount of time to optically pump for.  Can safely be long.
op_t = ExpParams['op_t']
#amount of time to protect information stored in spin down state
protect_t = ExpParams['protect_t']
#The amount of time to use 455 nm light to shelve any remaining ions into
                                        D(5/2)
shelve_t = ExpParams['shelve_t']
# Deshelving time
deshelve_t = ExpParams['deshelve_t']
# SRS shutter delays
b_srs_fall_d = ExpParams['b_srs_fall_d']
b_srs_rise_d = ExpParams['b_srs_rise_d']
r_srs_fall_d = ExpParams['r_srs_fall_d']
```

```
r_srs_rise_d = ExpParams['r_srs_rise_d']
shelve_srs_fall_d = ExpParams['shelve_srs_fall_d']
shelve_srs_rise_d = ExpParams['shelve_srs_rise_d']
deshelve_srs_fall_d = ExpParams['deshelve_srs_fall_d']
deshelve_srs_rise_d = ExpParams['deshelve_srs_rise_d']

# Start PMT task.
pmt = PMT(pmtc)

if __name__ == '__main__':
    # Setup trigger out
    trig = TrigControl(trigsource)

## Prepare all the shutters (open them)
# NR leakage proven not to do anything, but others have effect
    try:
        del clist
    except NameError:
        print
    oneshots = {}
    clist = {
              'raman_shutter': [b'/Dev1/Ctr2',trigchan1,True], #turns on
              'NR_pi' : [b'/Dev5/Ctr5',trigchan5,False], #turns off
              'red_blue_shutters': [b'/Dev6/ctr1',trigchan6,True], #turns
                                                    off}
              'FOR_mode_ttl':[b'/Dev7/ctr2',trigchan7,False] \# Want TTL L
                                                    for axial RF line
                                                    selector
```

```
ctimes = {
          'raman_shutter': [0.0, 2*shutter_t],
          'NR_pi': [0.0, 2*shutter_t],
          'red_blue_shutters': [0.0,2*shutter_t],
          'FOR_mode_ttl':      [0.0,shutter_t]}


try:
    for k in ctimes.keys():
        oneshots[k] = OneShot(*(clist[k]+ctimes[k]))
    for k in oneshots.keys():
        oneshots[k].begin()
except:
    for k in oneshots.keys():
        oneshots[k].stop()
    sys.exit(1)
trig.setHigh()
#make sure the trap voltage is set right to start the script.
time.sleep(1e-3)
rf_v.setVoltage(rf_h)
Vec1_v.setVoltage(Vec1_h)
Vec2_v.setVoltage(Vec2_h)
Comp2_v.setVoltage(Comp2)
Comp3_v.setVoltage(Comp3_h)
Comp4_v.setVoltage(Comp4_h)
time.sleep(2*shutter_t)
#not related to recrystallization but good to set
trig.setLow()
time.sleep(3)
#time.sleep(5) #new in v2
```

```
    for k in oneshots.keys():
        oneshots[k].stop()
    del oneshots
    del clist

    # ---------------- Set up warm ion oneshots
    warm_clist = {'red_blue_shutter':[b'/Dev6/Ctr1',warmtrigchan6,True]}

    warm_shuton = 0.0
    warm_shutoff = warm_shuton + warm_recover_t - 3e-3

    warm_ctimes = {'red_blue_shutter': [warm_shuton,warm_shutoff]}

    oneshots_warm = {}
    for k in warm_ctimes.keys():
        oneshots_warm[k] = OneShot(*(warm_clist[k]+warm_ctimes[k]))
    for k in oneshots_warm.keys():
        try:
            oneshots_warm[k].begin()
        except:
            pdb.post_mortem()

## Continue young one

    shut_open = ExpParams['shut_open']    #shutter safety time (open SRS
                                          this time early before AOM)
    s_fsafe =ExpParams['s_fsafe']         #time that light is off from
                                          rising edge of trigger
    shut_tog = ExpParams['shut_tog']      #time to keep the shutters 'open
```

```
                                        ', only for shelve and deshelve
                                        lasers
    shut_close = ExpParams['shut_close'] #time it takes for shutters to
                                        close after trigger
    shut_buf   = 1e-3                   # fall time of shutter

  # Here, we scan the pi
  #toggle blue shutters and keep red on to pump out of D3/2
    # " Raman Cooling " , and optical pumping
    dds1.set_frequency(80.0 - cool_freq_ax/4 , channel=[0]) #v17 change
    dds1.set_frequency(80.0 - cool_freq_ax/4 , channel=[1]) #v17 change
    dds1.set_frequency(80.0 - cool_freq_rad/4 , channel=[2]) #v17 change
    dds1.set_frequency(80.0 - cool_freq_rad/4 , channel=[3]) #v17 change
    dds2.set_frequency(80.0 + cool_freq_ax/4 , channel=[0])  #v17 change
    dds2.set_frequency(80.0 + cool_freq_rad/4, channel=[1])  #v17 change
    time.sleep(3)

    #rotationally cool?
    b_doppler_s_b = 0e-3 #it will trigger 2.5 ms later, and close 1 ms
                                        after that
    b_doppler_a_b = 3e-3

#     rot_cool_b = 0.0
#     rot_cool_e = b_doppler_a_b #DOUBLE CHECK WE DO NOT NEED THIS AT ALL

#     b_doppler_s_b = 0e-3 #it will trigger 2.5 ms later, and close 1 ms
                                    after that
#     b_doppler_a_b = b_doppler_s_b + 3e-3
#
```

```
#     rot_cool_b = 0.0
#     rot_cool_e = b_doppler_a_b
    # " Raman Cooling " , and optical pumping
    ramancool_NR_sigma_b = b_doppler_a_b + 10*safe  #0.0
    ramancool_NR_sigma_e = ramancool_NR_sigma_b + op_t + eit_cool_t #+
                                        op_t # optical pumping

    ramancool_NR_pi_rad_b = ramancool_NR_sigma_b #0.0
    ramancool_NR_pi_rad_e = ramancool_NR_pi_rad_b + eit_rad_cool_t #cool
                                        radially for half the time

    ramancool_NR_pi_ax_b = ramancool_NR_pi_rad_e + 10e-6 #0.0
    ramancool_NR_pi_ax_e = ramancool_NR_pi_ax_b + eit_ax_cool_t    #cool
                                        axially for half the time

    nr_mode_ttl_b = ramancool_NR_sigma_b + eit_rad_cool_t/2
    nr_mode_ttl_e = nr_mode_ttl_b + eit_rad_cool_t

    nr_axis_ttl_b = ramancool_NR_pi_rad_e
    nr_axis_ttl_e = ramancool_NR_sigma_e + 5e-3 #keep on long enough for
                                        the NR sig ax1 parameters to
                                        protect

    r_doppler_s_b = ramancool_NR_sigma_e - r_srs_fall_d + 10*safe #-
                                        shut_buf#25*safe
    r_doppler_a_b = ramancool_NR_sigma_e + 5*safe #+ 2*shut_buf #toggle
                                        when red shutter has closed

    #pulse_picker
```

```
pp_b = r_doppler_a_b + 5*safe #+ shutter_t #unclear if it response
                                    time of PD or AOM, 1 ms delay
                                    here to turn off red
pp_e = pp_b + pp_time
# Pi pulse
pi_pulse_b = pp_e + 10*safe #turn FOR raman beams on after PRR beams
pi_pulse_e = pi_pulse_b + for_pi_pulse_t # #pi_time

for_shutter_b = 0.0
for_shutter_e = pi_pulse_e #- 2*shutter_t #2.5 ms delay from trig to
                                    off #

# Protect
protect_b = pi_pulse_e + 10*safe #+ 1e-3# shutter_t # Optical pumping
                                    shouldnt be on during shelving
protect_e = protect_b + protect_t

shelve_s_b = protect_e - shelve_srs_rise_d + 10*safe #-
                                    shelve_srs_rise_d + 10*safe #-
                                    shut_buf #shelve_s_b is the SRS
                                    shutter begin time  ##CHANGE! 12/
                                    03
shelve_s_e = shelve_s_b + shut_tog#shelve_t - 1.5*shelve_srs_fall_d

shelve_a_b = protect_e  + 10*safe #+ shelve_srs_rise_d # + 10*safe#
                                    protect_e + shutter_t    #
                                    shelve_a_b is the aom begin time
shelve_a_e = shelve_a_b + shelve_t
```

```
r_doppler_s_e = shelve_a_e + 2*shut_buf #10*safe #+ 5e-3 #-2e-3#-
                                        r_srs_rise_d  #- shut_open #- 1e-
                                        3
r_doppler_a_e = r_doppler_s_e + r_srs_rise_d   #shelve_a_e + shut_buf#
                                        shelve_s_b + s_fsafe - 0.5e-3

b_doppler_s_e = r_doppler_s_e #- 2e-3 #b_srs_rise_d  #- shut_open #-
                                        1e-3
b_doppler_a_e = r_doppler_a_e #shelve_a_e + shut_buf #shelve_s_b +
                                        s_fsafe - 0.5e-3

camera_b = r_doppler_a_e #+ shutter_t
camera_e = camera_b + expose_t

deshelve_s_b = camera_e #- 2e-3#deshelve_srs_rise_d #- 1e-3
deshelve_s_e = deshelve_s_b + shut_tog #+ deshelve_t -
                                        deshelve_srs_fall_d

deshelve_a_b = camera_e + 10*safe
deshelve_a_e = deshelve_a_b + deshelve_t

clist = {'b_doppler': [b'/Dev5/Ctr6',trigchan5,True],
         'b_shutter': [b'/Dev5/Ctr2',trigchan5,False],
         'r_doppler': [b'/Dev1/Ctr4',trigchan1,True],
         'r_shutter': [b'/Dev5/Ctr3',trigchan5,False],
         'NR_sigma':  [b'/Dev5/Ctr4',trigchan5,False],
         'NR_pi_ax' : [b'/Dev5/Ctr5',trigchan5,False],
         'NR_pi_rad': [b'/Dev7/Ctr5',trigchan7,False],
         'NR_sig_mode': [b'/Dev7/Ctr0',trigchan7,False],
```

```
            'NR_sig_axis': [b'/Dev7/Ctr1',trigchan7,False],
            'NR_sigma_protect': [b'/Dev1/Ctr1',trigchan1,False],
            'FOR_sigma' : [b'/Dev5/Ctr7',trigchan5,False],
            'FOR_pi' : [b'/Dev1/Ctr0',trigchan1,False],
            'FOR_shutter':[b'/Dev6/Ctr6',trigchan6,True],
            'shelve': [b'/Dev1/Ctr5',trigchan1,False],
            'shelve_shutter': [b'/Dev1/Ctr3',trigchan1,True],
            'deshelve': [b'/Dev1/Ctr6',trigchan1,False],
            'deshelve_shutter': [b'/Dev6/Ctr0',trigchan1,True],
            'pulsepicker': [b'/Dev7/Ctr4',trigchan7,False],
#            'rotationalcooling': [b'/Dev7/Ctr7',trigchan7,False],
            'camera': [b'/Dev5/Ctr1',trigchan5,False]}

    ctimes = {'b_doppler': [b_doppler_a_b, b_doppler_a_e],
              'b_shutter': [b_doppler_s_b, b_doppler_s_e],
              'r_doppler': [r_doppler_a_b, r_doppler_a_e],
              'r_shutter': [r_doppler_s_b, r_doppler_s_e],
              'NR_sigma' : [ramancool_NR_sigma_b, ramancool_NR_sigma_e],
              'NR_pi_ax' : [ramancool_NR_pi_ax_b, ramancool_NR_pi_ax_e],
              'NR_pi_rad': [ramancool_NR_pi_rad_b, ramancool_NR_pi_rad_e],
              'NR_sig_mode':[nr_mode_ttl_b,nr_mode_ttl_e],
              'NR_sig_axis':[nr_axis_ttl_b,nr_axis_ttl_e],
              'NR_sigma_protect': [protect_b,protect_e],
              'FOR_sigma' : [pi_pulse_b,pi_pulse_e],
              'FOR_pi' : [pi_pulse_b,pi_pulse_e],
              'FOR_shutter':[for_shutter_b,for_shutter_e],
              'shelve': [shelve_a_b, shelve_a_e],
              'shelve_shutter': [shelve_s_b, shelve_s_e],
              'deshelve': [deshelve_a_b, deshelve_a_e],
```

```
            'deshelve_shutter': [deshelve_s_b, deshelve_s_e],
            'pulsepicker': [pp_b, pp_e],
#             'rotationalcooling': [rot_cool_b,rot_cool_e],
            'camera': [camera_b, camera_e]}
    ctimes_exp = ctimes
    oneshots = {}
    for k in ctimes.keys():
        oneshots[k] = OneShot(*(clist[k]+ctimes[k]))
    for k in oneshots.keys():
        oneshots[k].begin()
    if plot_me:
        hold = plotOneShots(ctimes)

        # ----------------
#     warm_clist = {'red_blue_shutter':[b'/Dev6/Ctr1',warmtrigchan6,True]}
#     warm_shuton = 0.0
#     warm_shutoff = warm_shuton + warm_recover_t - 3e-3 #so that the SRS
                                        shutter if off for the next rep
#     warm_ctimes = {'red_blue_shutter': [warm_shuton,warm_shutoff]}
#
#     oneshots_warm = {}
#     for k in warm_ctimes.keys():
#         oneshots_warm[k] = OneShot(*(warm_clist[k]+warm_ctimes[k]))
#     for k in oneshots_warm.keys():
#         try:
#             oneshots_warm[k].begin()
#         except:
#             pdb.post_mortem()
#
```

```
    # -----------------

    #freq scan
    break_tf = False
    data = np.zeros((for_frequencies.shape[0],reps+1))
    stillDark = np.zeros((for_frequencies.shape[0],reps+1))
    for (i,for_freq) in enumerate(for_frequencies):
    #pi pulse time scan
#         data = np.zeros((pi_times.shape[0],reps+1))
    #for (i,pi_time) in enumerate(pi_times):

        # Set the dds frequencies.  I am making Raman A be the negative
                                                one.
        # Also, I am making them be symmetric around 80, because I can.
        dds0.set_frequency(80.0 + for_freq/4, channel=[0]) #for sig ax
        dds0.set_frequency(80.0 - for_freq/4, channel=[2]) #for pi ax
        dds0.set_frequency(80.0 + for_freq/4, channel=[1]) #for sig rad
        dds0.set_frequency(80.0 - for_freq/4, channel=[3]) #for pi rad
        time.sleep(1)

        data[i,0] = for_freq
        rc_counts = np.zeros(int(break_reps)) # of the same RC attempts
        rc_counts[0] = 1
        print('----')
        print('Data point: ' + str(np.round(for_freq,4)))
        for j in range(reps):
            #print(j)
            #first check if the script keeps trying to repeat the same rep
                                                    , cus something is wrong
```

```
if int((sum(rc_counts))/(len(rc_counts)*rc_counts[0])) == 1:
    break_tf = True
    break
# ------- start normal experiment
# ------- Set cooling and detect voltages
AO_detect_control.start()
# ------- start experiment and exposure
time.sleep(100e-6)
pmt.startRead()
trig.setHigh()
time.sleep(deshelve_a_e)
trig.setLow()
res = pmt.getRead()
data[i,j+1] = res
# --------- start recovery/condition read
pmt_condition.startRead()
time.sleep(recover_t)
stillDark = pmt_condition.getRead()
recover_counts = stillDark/recover_t
AO_detect_control.stop()
#print(recover_counts)
# ----- start recovery if decrystallization occurs -----
if recover_counts < ExpParams['disc_initial_state']:
    #time.sleep(1e-3) #new in v2 ?
    #counts of how many times a
    rep_count = 1
    if j == 0:
        rep_count = j + 1 #only need to step j at the
                                                beginning so
```

```
                                                    there is no /0 in
                                                     the code
else:
    rep_count == j
for k in range(0,len(rc_counts)):
    if rc_counts[0] != rep_count:
        rc_counts = np.zeros(break_reps)
        rc_counts[0] = rep_count
        break
    if rc_counts[k] == rep_count:
        k =+ 1
    else:
        rc_counts[k] = rep_count
        break #break when array is ammended

print('Its Happening!')
print(recover_counts)
#make sure the trap voltage is set right to start the
                                        script.
warmtrig.setHigh()
Vec1_v.setVoltage(Vec1_l)
Vec2_v.setVoltage(Vec2_l)
Comp3_v.setVoltage(Comp3_l)
Comp4_v.setVoltage(Comp4_l)
time.sleep(1) #must wait this time otherwise ion will be
                                        ejected
rf_v.setVoltage(rf_l)
time.sleep(10)
# --- set everything back -----
```

```
            rf_v.setVoltage(-4)
            Vec1_v.setVoltage(Vec1_h)
            Vec2_v.setVoltage(Vec2_h)
            Comp3_v.setVoltage(Comp3_h)
            Comp4_v.setVoltage(Comp4_h)
            time.sleep(10e-3)
            rf_v.setVoltage(-3.8)
            Vec2_v.setVoltage(Vec2_p)
            time.sleep(5)
            Vec2_v.setVoltage(Vec2_h)
            rf_v.setVoltage(rf_h)
            time.sleep(4)

            warmtrig.setLow()
            time.sleep(50e-6) #This is 100% neccesary, otherwise the
                                                    next line will clear
                                                    the memory before
                                                    updated
            #erase data from this run
            data[i,j+1] == 0
            #repeat rep
            j = j-1

    print('% of Scan Completed: ' + str(np.round((i+1.0)/
                                            for_frequencies.shape[0]*100.
                                            0,2)))


    if break_tf: # break out of loop if RC occurs too much, so data
```

```
                                        can be saved
        print('------------ SOS ----------------')
        print('Something is wrong, the ions are dark and they are not
                                            coming back. \n'
              'I (the self-aware computer) am stopping and saving')
        print('------------ SOS ----------------')
        break
    else:
        continue #young one
 # Build a suitable filename
t = time.localtime()
filename = "{}{:02g}{:02g}".format(t.tm_year,t.tm_mon,t.tm_mday)+ "
                                    _PRR_Axial_freq"
i = 0
while os.path.exists(os.path.normpath(path + filename + "_{}.npy".
                                    format(i))):
    i = i + 1
filenamen = os.path.normpath(path + filename + "_{}.npy".format(i))
ExpParamsFilen = os.path.normpath(path + filename + "_ExpParams_{}.txt
                                    ".format(i))
total_t = time.time() - begin
print()
with open(ExpParamsFilen, "w") as f:
    f.write('%s --> %s\n' % ('Scan ',scan))
    f.write('%s --> %s\n' % ('Did the scan stop early due to an issue
                                        ? ',break_tf))
    f.write('%s --> %s\n' % ('Number of reps per datapoint ',reps))
    f.write('%s --> %s\n' % ('Number of datapoints ',len(
                                        for_frequencies)))
```

```
        f.write('%s --> %s\n' % ('Time Begin ',time.strftime('%Y-%m-%d (H,
                                                M,S) %H-%M-%S', time.
                                                localtime(begin))))
        f.write('%s --> %s\n' % ('Time End ', time.strftime('%Y-%m-%d (H,M
                                                ,S) %H-%M-%S', time.localtime
                                                (time.time()))))
        f.write('%s --> %s\n' % ('Time per data point (s)',np.round(
                                                total_t/len(for_frequencies),
                                                3)))
        f.write('%s --> %s\n' % ('Number of reps ',reps))
        f.write('%s --> %s\n' % ('Number of reps before break ',break_reps
                                                ))
        f.write('%s --> %s\n' % ('EIT time ',eit_cool_t))
        f.write('%s --> %s\n' % ('ax EIT freq ',cool_freq_ax))
        f.write('%s --> %s\n' % ('rad EIT freq ',cool_freq_rad))
        f.write('%s --> %s\n' % ('delay time (s) ',delay_t))
        for key, value in ExpParams.items():
            f.write('%s:%s\n' % (key,value))
    # And save the data
    np.save(filenamen,data)

    #filename_initial_states = os.path.normpath(path + filename + "
                                            _initial_states" + "_{}.npy".
                                            format(i))
    #np.save(filename_initial_states,stillDark)

    for k in oneshots.keys():
        oneshots[k].stop()
    del oneshots
```

```
for k in oneshots_warm.keys():
    oneshots_warm[k].stop()
del oneshots_warm
warmtrig.stop()
del warmtrig
del ctimes
del clist
time.sleep(10)
oneshots = {}

clist = {'b_shutter': [b'/Dev5/Ctr2',trigchan5,False],
         'r_shutter': [b'/Dev5/Ctr3',trigchan5,False],
         'deshelve' : [b'/Dev1/Ctr6',trigchan1,False],
         'deshelve_shutter': [b'/Dev6/Ctr0',trigchan6,True],
         'raman_shutter': [b'/Dev1/Ctr2',trigchan1,True],
         'FOR_shutter':[b'/Dev6/Ctr6',trigchan6,True],
         'red_blue_shutters': [b'/Dev6/ctr1',trigchan6,False]}

ctimes = {'b_shutter': [0.0, 2*shutter_t],
          'r_shutter': [0.0, 2*shutter_t],
          'deshelve' : [0.0,10*shutter_t],
          'deshelve_shutter': [0.0,10*shutter_t],
          'raman_shutter': [0.0,2*shutter_t],
          'FOR_shutter':[0.0,2*shutter_t],
          'red_blue_shutters': [0.0,2*shutter_t]}

try:
    for k in ctimes.keys():
```

```
            oneshots[k] = OneShot(*(clist[k]+ctimes[k]))
        for k in oneshots.keys():
            oneshots[k].begin()
    except:
        for k in oneshots.keys():
            oneshots[k].stop()
        sys.exit(1)
    #time.sleep(3) #change of v2
    trig.setHigh()
    time.sleep(3*shutter_t)

    Vec1_v.setVoltage(Vec_i)
    Vec2_v.setVoltage(Vec_i)
    time.sleep(0.5)
    Vec1_v.setVoltage(Vec1_l)
    Vec2_v.setVoltage(Vec2_l)
    Comp3_v.setVoltage(Comp3_l)
    Comp4_v.setVoltage(Comp4_l)
    time.sleep(1)
    rf_v.setVoltage(rf_l)
    trig.setLow()
    time.sleep(recover_t)

    for k in oneshots.keys():
        oneshots[k].stop()
    del oneshots
    del clist
    trig.stop()
    del trig
```

```
    pmt.stop()
    del pmt
    pmt_condition.stop()
    del pmt_condition
    AO_detect_control.clear()
    del AO_detect_control

    print('Im Done! I took: ', total_t, ' seconds')
```